



Department of Mechanical, Materials and  
Manufacturing Engineering

**REPRESENTATIVE FRETTING FATIGUE TESTING AND  
PREDICTION FOR SPLINED COUPLINGS**

**DEAN HOUGHTON, BEng.**

**Thesis submitted to the University of Nottingham for  
the degree of Doctor of Philosophy**

**October 2009**

## ABSTRACT

---

Spline couplings are a compact and efficient means for transferring torque between shafts in gas turbine aeroengines. With competition in the aerospace market and the need to reduce fuel burn from the flight carriers, there is an ever-present requirement for enhanced performance, leading to increasing demands on the coupling. Aeroengine spline couplings, particularly mainshaft, low pressure (LP) splines, are complex components that can fail from a variety of mechanisms, and are particularly susceptible to fretting wear and fretting fatigue (FF), as a result of small oscillatory relative movements between the highly-loaded teeth. Due to the expensive nature of full-scale spline testing, this thesis investigates the use of the representative specimen concept for predicting fretting-induced damage between spline teeth.

A combined experimental and computational representative specimen (RS) methodology is developed, using a uniaxial representative specimen (URS) concept and a multiaxial representative specimen (MRS) concept, with differing degrees of complexity, to address different aspects of the spline fretting wear-fatigue problem. The URS test rig consists of two pairs of specimens in contact and simulates spline major torque and axial loads from the overall flight cycle and the associated damage. The MRS rig consists of a fretting bridge arrangement that simulates the combination of the same major loads and with the addition of high-cycle bending loads from in-flight fluctuations (gyroscopic and carcass flexing) and the associated damage. The URS was successfully employed for experimental characterisation of a range of candidate aeroengine transmission and spline material combinations, including coated and uncoated combinations. The MRS concept was successfully implemented to characterise the multiaxial FF behaviour of the

current material of choice for mainshaft triple-spool gas turbine spline couplings. An inverse method was applied to the URS, based on measured and predicted displacements, to identify the coefficient-of-friction (COF) for the material combination tests.

The key novelty of the computational facet of the methodology related to the development of a finite element-based, multi-axial, total fatigue life (crack nucleation and propagation) capability which was successfully validated against the MRS and the URS for the complete load range. The methodology was achieved via the development of a global sub-modelling technique, to capture the steep stress gradients associated with the contact geometry, along with (i) a volume-averaged, critical-plane Smith-Watson-Topper (SWT) fatigue parameter for crack nucleation, using 10  $\mu\text{m}$  length crack nucleation, (ii) two-dimensional El Haddad short crack growth and (iii) a weighted function approach for long crack growth.

An additional contribution was the investigation and implementation of an FF damage parameter,  $D_{\text{fret}}$ , to incorporate the combined effects of relative slip and surface shear traction (which are key parameters in contact interface damage mechanisms), in conjunction with the critical-plane (multiaxial) SWT parameter, with volume-averaging, for life prediction. A least-squares optimisation approach was developed to identify the required material constants and thus to successfully capture (i) the measured effect of relative slip on a titanium alloy and (ii) the measured effect of contact size on an aluminium alloy.

## LIST OF PUBLICATIONS

---

- [1] Houghton D, Wavish PM, Williams EJ, Leen SB. Improved correlation of measured and predicted hysteresis loops in a multiaxial fretting fatigue test rig for spline couplings. *Advances in Experimental Mechanics V, Vol. Applied Mechanics and Materials*, Manchester, UK: Trans Tech Publications, 2007, pp. 37-42.
  
- [2] Wavish PM, Houghton D, Ding J, Leen SB, Williams EJ, McColl IR. A multiaxial fretting fatigue test for spline coupling contact. *Fatigue & Fracture of Engineering Materials & Structures* 2009; 32(4): pp. 325-345.
  
- [3] Houghton D, Wavish PM, Williams EJ, Leen SB. Multiaxial fretting fatigue testing and prediction for splined couplings. *International Journal of Fatigue* 2009; 31(11-12): pp. 1805-1815.

## ACKNOWLEDGEMENTS

---

The author is very grateful to Professor Sean Leen and Dr Edward Williams for providing supervision, guidance and support throughout the project. The contributions to the work that were made by Dr Ian McColl, who sadly passed away on the 30<sup>th</sup> November 2005, are also acknowledged.

The financial support of the EPSRC and Rolls-Royce plc. is recognised and also the assistance provided by Scott Wood, Emma Booth and Nina Banerjee of Rolls-Royce. The author is very thankful to Keith Dinsdale, Tom Buss and Aubrey Martin for sharing their significant experimental expertise and always being willing to help. Additionally, the work of Barrie Hanson and Bob Stables towards the re-design of the uniaxial representative specimen is appreciated and the experimental contributions made by Brian Webster, Roger Smith, Graham Malkinson, Barry Holdsworth and Jeff Bexon are recognised. The prompt manufacture of test specimens by G T G Engineering Company of Loughborough also made the work possible.

My colleagues within the UTC improved me personally and technically, including Dr Paul Wavish, Dr Jian Ding, Dr Sabesan Rajeratnam, Dr Graham Johnson, Dr Chris Bennett, Dr Jason Madge, Dr Yaw Lee, Dr David Tanner, Dr Joanne Williams, Dr Steve Rapley, Steven Baxter and numerous others.

The assistance provided by the undergraduate students Calvin Stewart, Daksh Agarwal (of the Indian Institute of Technology Kanpur) and Daniel Sullivan is acknowledged, and Riza Kahn during his Masters project.

Finally, I am indebted to my family for always being there and for supporting me throughout many years of education.

# TABLE OF CONTENTS

---

<b>1</b>	<b>Introduction</b>	<b>1</b>
1.1	Spline couplings	1
1.2	Representative specimen concept	4
1.3	Scope of thesis	6
1.4	Tables	9
1.5	Figures	10
<b>2</b>	<b>Literature Review</b>	<b>12</b>
2.1	Introduction	12
2.2	Fatigue	12
2.2.1	Cyclic definitions	13
2.2.2	Fatigue mechanisms	16
2.3	Fretting fatigue	18
2.3.1	Friction	19
2.4	Experimental	22
2.4.1	Variables	22
2.4.2	Fretting maps	23
2.4.3	Contact pressure	24
2.4.4	Contact slip	24
2.4.5	Interaction of variables	26
2.4.6	Surface damage and stress concentration effects	27
2.5	Experimental test setups	27
2.5.1	General	27
2.5.2	Bridge-type setups	28
2.5.3	Simplified geometries	29
2.5.4	Representative testing	29
2.6	The initiation of fretting fatigue cracks	30
2.6.1	Micro-modelling of fretting fatigue initiation	33
2.6.2	Macro-mechanics of fretting fatigue	33
2.7	Fretting fatigue lifing	38
2.7.1	Fretting fatigue damage parameters	38
2.7.2	Stress and strain-based (Cauchy) approaches	39
2.7.3	Multiaxial fatigue methods	40
2.7.4	Volume averaging	43
2.7.5	Asymptotic approaches	43
2.8	Fracture mechanics approaches	44
2.8.1	Crack-notch analogues	45
2.8.2	Short crack growth	45
2.9	Fretting wear	47

2.9.1	General.....	47
2.9.2	Wear modelling.....	49
2.9.3	Debris effects.....	51
2.10	The analysis of spline couplings.....	51
2.11	Representative specimens for spline couplings.....	53
2.11.1	Laboratory-scaled spline coupling.....	53
2.11.2	Uniaxial representative specimen.....	55
2.11.3	Multiaxial representative specimen.....	55
2.12	Summary of chapter.....	56
2.13	Figures.....	58
<b>3</b>	<b>Methodology.....</b>	<b>74</b>
3.1	Introduction.....	74
3.2	Representative specimen methodology.....	74
3.3	Material data.....	79
3.4	URS experimental test rig.....	80
3.4.1	Ranking material fretting performance.....	82
3.5	Experimental methods for the URS.....	83
3.5.1	Data acquisition.....	83
3.5.2	Profilometry.....	83
3.6	MRS experimental test rig.....	85
3.7	Experimental methods for the MRS.....	87
3.8	Finite element modelling.....	87
3.8.1	URS finite element modelling.....	88
3.8.2	MRS finite element modelling.....	89
3.9	Comparison with scaled spline modelling.....	90
3.10	Summary of chapter.....	91
3.11	Tables.....	92
3.12	Figures.....	93
<b>4</b>	<b>Experimental Results.....</b>	<b>101</b>
4.1	Introduction.....	101
4.2	URS Experimental results.....	101
4.2.1	Optical microscope images.....	102
4.2.2	SEM and EDX analysis.....	103
4.2.3	Surface profilometry results.....	104
4.2.4	Relative displacements.....	106
4.3	MRS experimental results.....	107
4.3.1	SC1.....	107
4.3.2	SC2.....	107
4.3.3	SC3.....	108
4.3.4	NL1.....	108

4.3.5	BR1 .....	108
4.3.6	Overall test observations.....	109
4.3.7	Relative displacements and wear .....	111
4.3.8	Measurement of the friction force .....	111
4.3.9	Spline comparison.....	113
4.4	Discussion .....	113
4.5	Summary of chapter .....	114
4.6	Tables .....	116
4.7	Figures .....	118
<b>5</b>	<b>Finite Element Modelling.....</b>	<b>130</b>
5.1	Introduction .....	130
5.2	URS FE modelling and results .....	131
5.2.1	Inverse calculation of COF .....	132
5.2.2	Wear coefficient for S/CMV.....	135
5.3	MRS major cycle FE analysis.....	136
5.3.1	In-plane force-displacement loops .....	136
5.3.2	Contact slip distributions.....	138
5.4	MRS minor cycle FE analysis .....	138
5.4.1	Frictionless analysis .....	139
5.4.2	Out-of-plane force-displacement loops .....	140
5.4.3	Contact slip distributions.....	141
5.5	Development of MRS FE sub-model.....	141
5.6	MRS stress and strain distributions.....	142
5.7	The effect of varying the parameters .....	144
5.7.1	Bridge gap .....	144
5.7.2	COF .....	144
5.8	Summary of chapter .....	145
5.9	Tables .....	147
5.10	Figures .....	148
<b>6</b>	<b>Fretting Fatigue Lifting.....</b>	<b>159</b>
6.1	Introduction .....	159
6.2	Fretting fatigue lifting methodology .....	160
6.3	Initiation life prediction .....	161
6.3.1	Smith-Watson-Topper (SWT) relation .....	162
6.3.2	Back-calculating Basquin constants.....	164
6.3.3	Short crack behaviour.....	165
6.3.4	Strain-controlled fatigue tests .....	166
6.3.5	Critical-plane implementation of SWT .....	167
6.3.6	Stress gradient effects.....	169
6.3.7	SWT URS results .....	170

6.3.8	SWT MRS results.....	171
6.3.9	FE-predicted critical-plane orientation .....	173
6.4	Fracture mechanics methodology.....	174
6.5	Determination of the SIFs .....	177
6.5.1	Weight functions .....	178
6.6	Fracture mechanics results .....	181
6.7	Total fretting fatigue life predictions .....	182
6.8	Discussion .....	182
6.9	Summary of chapter .....	184
6.10	Tables .....	186
6.11	Figures .....	187
<b>7</b>	<b>Slip-based Lifting Parameters.....</b>	<b>198</b>
7.1	Introduction .....	198
7.2	Ruiz parameter .....	198
7.3	Surface damage parameter $D_{fret}$ .....	200
7.4	Application of $D_{fret}$ .....	201
7.4.1	Effect of slip .....	201
7.4.2	Application of $D_{fret}$ to the size effect.....	206
7.4.3	Effect of COF.....	210
7.5	Discussion .....	212
7.6	Summary of chapter .....	214
7.7	Tables .....	215
<b>8</b>	<b>Conclusions and Recommendations .....</b>	<b>226</b>
8.1	Conclusions.....	226
8.2	Recommendations for future research.....	231
	<b>References .....</b>	<b>232</b>

# NOMENCLATURE

---

$\alpha$	Correction factor for axial variation in contact pressure along representative specimen model
$\alpha_{\text{mixity}}$	Mode mixity parameter
$\beta_p$	Helix angle at pitch circle diameter
$\delta$	Contact slip
$\delta_{\text{aes}}$	Allowable elastic slip
$\delta_{\text{hom}}$	Hooke's law out-of-plane displacements of MRS
$\delta_{\text{app}}^*$	Applied global tangential displacement
$\epsilon_y$	Yield strain
$\epsilon_{ij}$	Strain components
$\epsilon_f'$	Fatigue ductility coefficient
$\Delta\epsilon_e$	Elastic strain range
$\Delta\epsilon_p$	Plastic strain range
$\Delta\epsilon_T$	Total strain range
$\theta_x, \theta_z$	Rotations about the $x$ -axis and $z$ -axis, respectively
$\mu$	Coefficient of friction
$\mu_d$	Dynamic coefficient of friction
$\mu_s$	Static coefficient of friction
$\nu$	Poisson's ratio
$\rho$	Integrating variable divided by crack length
$\sigma_a$	Stress amplitude
$\sigma_e$	Fatigue limit
$\sigma_m$	Mean stress
$\sigma_y$	Yield stress
$\sigma_{\text{am}}$	Fatigue strength for given life with zero mean stress
$\sigma_{ij}$	Stress components
$\sigma_f'$	Fatigue strength coefficient
$\Delta\sigma_{\text{th}}$	Threshold stress range for crack growth
$\tau$	Shear stress
$\tau\delta$	Frictional work
$\tau\delta_{\text{SP}}$	Value of frictional work at stationary point
$(\tau\delta)_{\text{th}}$	Threshold frictional work for $D_{\text{fret}}$ parameter
$A$	Cross-sectional area
$A_{\nu\mu}$	Influence coefficients of the weight function
$a$	Contact half-width
$a_0$	Intrinsic crack length

$a_1$	Spline axial direction contact width
$a_2$	Spline tooth contact width in flank direction
$A, n$	Paris law empirical constants
$B$	Total bending moment
$B_n$	Non-dimensionalised bending moment
$B_{yp}^m$	Bending moment capacity of the nominal externally splined shaft
$b$	Fatigue strength exponent
$b_1$	Axial contact width of the MRS
$b_2$	Axial contact width of the URS
$C$	Palmgren-Miner law constant
$C, n$	Empirical constants for $D_{fret}$
$c$	Fatigue ductility exponent, size of the stick zone
$D_{fret}$	Empirical fretting fatigue damage parameter
$d_{av}$	Average wear depth
$E$	Young's modulus
$E^*$	Composite elastic modulus
$e$	Offset of the centre of the stick zone from centre of contact
$F$	Axial force
$F_1, F_2$	Ruiz parameters
$F_g$	Force inferred from strain gauge
$F_i$	In-plane applied force in simplified test
$F_n$	Non-dimensionalised axial force
$F_o$	Out-of-plane applied force in simplified test
$F_{sp}$	Total force along tooth flank contact width
$F_0^{nom}$	Nominal spline contact force per unit width
$F_{yp}^m$	Axial load capacity of the nominal externally splined shaft
$F-\delta$	Force-displacement
$h_I$	Mode I weight function
$h_{II}$	Mode II weight function
$\Delta K$	Stress intensity factor range
$\Delta K_0$	Crack growth threshold SIF range
$\Delta K_{eff}$	Effective stress intensity factor range
$\Delta K_{th}$	Crack growth threshold stress intensity factor
$K_I, K_{II}, K_{III}$	Mode I, II and III stress intensity factors
$k$	Dimensional wear coefficient
$m$	Walker exponent
$N$	Number of teeth in the spline coupling
$N_f$	Number of cycles to failure
$N_i$	Predicted number of cycles of crack initiation

$N_p$	Predicted number of cycles of crack propagation
$N_{SCG}$	Predicted number of cycles of short crack growth
$N_T$	Predicted total number of cycles to failure
$n$	Number of sampled data points
$P$	Normal load
$p$	Contact pressure
$p_0$	Mean contact pressure for spline contact surface, peak Hertzian contact pressure
$Q$	Shear traction
$Q_{\text{minor}}$	Out-of-plane force generated by friction
$R$	Relative radius of curvature
$R_\epsilon$	Strain ratio (minimum to maximum strain)
$R_\sigma$	Stress ratio (minimum to maximum stress)
$R_a$	Surface roughness
$R_x, R_z$	Rotation matrix for rotation about the $x$ -axis and $z$ - axis respectively
$r_p$	Pitch circle radius
$S$	Total accumulated sliding distance
$T$	Torque
$T_c$	Traction coefficient
$T_n$	Non-dimensionalised torque
$T_{yp}^m$	Maximum elastic torque capacity of the nominal externally splined shaft
$V$	Total worn volume
$w$	Width of specimen
$x$	Transverse length coordinate
$\gamma$	Geometrical correction of SIF for finite specimen dimensions
$z$	Axial length coordinate
$\frac{da}{dn}$	Crack growth rate
CAD	Computer-aided design
CMV	Chromium Molybdenum Vanadium
COF	Coefficient of friction
CT	Compact tension
DAQ	Data acquisition
EDX	Energy dispersive X-Ray
EPFM	Elastic-plastic fracture mechanics
ESH	Electro servo-hydraulic
F-S	Fatemi-Socie
FE	Finite element
FF	Fretting fatigue

FFDP	Fretting fatigue damage parameter
HCF	High-cycle fatigue
HT	Heat treated
IMechE	Institution of Mechanical Engineers
IP	In-plane
K-T	Kitagawa-Takahashi
LCF	Low-cycle fatigue
LEFM	Linear elastic fracture mechanics
LP	Low pressure
LVDT	Linear variable differential transformer
MRFM	Material response fretting map
MRS	Multiaxial representative specimen
MPC	Multi-point constraint
OP	Out-of-plane
PCD	Pitch circle diameter
PSB	Persistent slip bands
RCFM	Running condition fretting map
RS	Representative specimen
SEM	Scanning electron microscopy
SIF	Stress intensity factor
S-N	Stress-life
SWT	Smith-Watson-Topper
URS	Uniaxial representative specimen
VBA	Visual Basic for Applications

## Introduction

### 1.1 Spline couplings

The jet or gas turbine engine has become increasingly popular for flight propulsion since its invention by Sir Frank Whittle in 1937. This is due to its favourable thrust to weight ratio, giving it a higher efficiency than alternative power sources. The triple-spool gas turbine aeroengine produced by Rolls-Royce and used extensively for civil aircraft applications is shown in Figure 1.1. The three-shaft design allows the independent connection of the low, intermediate and high pressure sets that consist of the compressors and the turbines in the core of the engine. This makes it easier to scale the shafts for specific airframe requirements compared with traditional two-shaft designs and allows the optimum rate of shaft rotation. The use of one shaft for each pressure set is impractical due to the shaft lengths that would be required and the difficulty associated with assembly and reassembly of the modules that make up the full aeroengine [1]. A spline coupling is commonly used as a joint for transferring the torque between shafts. It is a compact feature, also able to accommodate axial thrust and axial misalignment and allows easy assembly / disassembly. The most highly loaded coupling is the low-pressure (LP) one (indicated in Figure 1.1), and is thus the focus of the work of this thesis.

The spline coupling is critical for engine integrity and hence conservative designs are necessary to ensure passenger safety. With competition in the aerospace market and the need to reduce fuel burn from the flight carriers, there is an ever-present requirement for enhanced performance in gas turbine

aeroengines. The requirement to reduce the environmental impact of aeroengines has also been recognised, providing an extra drive for improved engine efficiency. As a result, increases in torque density (torque transmitted for a given shaft diameter) via increasing bypass-ratios puts increasing demands on the coupling in the form of amplified contact pressures and stresses. These demands will be met through developments in materials [2] and improved understanding of the mechanical life-limiting conditions.

A spline coupling is a complex engineering component, that consists of externally and internally splined parts. Barrelling, sometimes referred to as crowning, may be applied to high-performance couplings in order to reduce the edge-of-contact pressure peaks. This is a technique that reduces the thickness of the spline teeth at the axial ends of engagement, leading to more uniform torque application [3], and is shown schematically in Figure 1.2. The spline teeth are usually involute in form, and axially they may follow a helical profile in order to accommodate axial loads. During a flight, the coupling undergoes the following loadings:

- Varying torque and axial load associated with each phase in the flight cycle; take-off, climb, cruise, etc.,
- Rotating bending moments due to gyroscopic effects during flight manoeuvres and engine carcass deformations,
- Fluctuating torque,
- Fluctuating centrifugal and thermal loads.

Due to the complex loading history and tooth geometry, the local contact pressure, sub-surface bulk stress and contact slip at points under the contact area and in the spline root can vary significantly during the loading cycle. As a result, a spline coupling may fail from a variety of mechanisms and

understanding these processes is of critical importance for their future development and optimisation. The potential failure modes include the following:

- Bursting failure,
- Pitch-circle diameter shear failure,
- Low cycle fatigue,
- High cycle fatigue,
- Fretting fatigue (FF),
- Fretting wear.

A bursting failure of a coupling is shown in Figure 1.3. This is associated with a sudden torque overload and is therefore a static failure mode. Volfson [4] presented a useful analytical work on calculations of stresses in a splined shaft subjected to torsional, bending and axial loads. The analysis was for non-involute, non-helical spline couplings. The importance of considering the different sources of elastic stress concentrations was highlighted and they were listed as:

- Spline root torsional stress concentrations,
- Spline fillet bending stress concentrations,
- Frictional contact stress concentrations.

The analysis also indicated that failure can occur in either the externally or internally-splined component.

In addition to static failure, the cyclic nature of the loads means that spline couplings are susceptible to fatigue damage. The combined loads lead to both low and high cycle fatigue effects; the overall flight cycle leads to low frequency loads (low-cycle fatigue), such as studied in Ref. [3], whilst in-flight

fluctuations associated with once-per-revolution shaft events (e.g. bending loads from gyroscopic moments) occur at a greater frequency (high-cycle fatigue) [5, 6]. The high amplitude LCF loads are often termed “major cycle” loads, whilst the higher frequency, lower magnitude HCF loads are termed “minor cycles”. The presence of a contact interface introduces the possibility of fretting, whereby small relative displacements occur between the contact surfaces. This can be a highly damaging form of fatigue and introduces additional difficulty in understanding in comparison with conventional fatigue processes. This thesis primarily focuses on the fretting fatigue of spline couplings. Fretting wear can occur in conjunction with the fretting fatigue process and is a form of surface damage that will also be investigated in this work.

## **1.2 Representative specimen concept**

The critical nature of the coupling in the engine requires that a full-scale rig test be conducted as part of the development of each new engine. Owing to the cost of such testing, they are run to demonstrate that the shaft will be safe throughout its design life. As a result, there was a lack of data for the ultimate life-limiting conditions for spline couplings, in particular, their fretting fatigue failure behaviour. This led in turn to the use of inherently conservative design approaches, such as that of Volfson [4] that was outlined above.

To address this deficiency, earlier experimental testing work at the University of Nottingham employed a coupling specimen that had 18 teeth on a reduced diameter [7]. This used the same spline geometry together with torque, axial and bending loads that replicated the tooth contact conditions as on full-size engine couplings. Several fretting fatigue failures occurred and the results from this so-called laboratory-scaled spline test programme are discussed in more detail in Chapter 2.

Although this programme produced some very valuable data, the laboratory-scaled spline specimens are still expensive to manufacture. The representative specimen (RS) concept was developed to address this and allows more comprehensive experimental investigations to be undertaken [8]. This combined experimental and computational approach involves the development of a test specimen (usually of a smaller-scale than the actual component) to replicate the key fretting fatigue variables of a chosen spline location. The design of an RS is necessarily conducted by matching the finite element (FE) predicted variables of both the RS and of the spline coupling. Parallel work at the University of Nottingham focused on the FE modelling of the scaled spline coupling, the results of which are presented in the following chapter.

A uniaxial representative specimen (URS) was initially developed that is capable of representing the spline behaviour under major cycle loading [9]. The rig consists of four fretting specimens and is shown schematically in Figure 1.4, where the contact coordinate conventions are also defined. The relative slip is generated by deflection of the load arms and occurs in the  $x$ -direction of Figure 1.4. In reality, the spline coupling experiences a complex multi-axial state of contact slip due to the combination of major and minor cycle loading. With the URS able to simulate spline behaviour under major cycle loading, a multi-axial representative specimen (MRS) was also developed [10] that is capable of superimposed major and minor cycle loading. The MRS consists of a fretting-bridge arrangement, and is shown schematically in Figure 1.5, where the coordinate conventions are defined. The direction of loading is also indicated in Figure 1.5, and this generates a multi-axial state of slip between the specimen and fretting bridges. Additionally, cylinder-on-flat testing (introduced in detail in Chapter 2) complements the RS approach by

generating relevant experimental fretting data. The relation between the various fretting test geometries is summarised in Table 1.1.

### **1.3 Scope of thesis**

The aim of the present work is to develop and demonstrate the representative specimen methodology for fretting fatigue life prediction of spline couplings. This thesis is focused on utilising the uniaxial and multiaxial representative specimens with a combination of experimental testing and finite element modelling. With the spline coupling commonly manufactured from the alloy steel Super CMV (S/CMV), emphasis will be placed on the study of this material, although other spline materials will also be investigated.

A suitable lifing methodology will be developed for the prediction of fretting fatigue in the representative specimens, and therefore by implication, the scaled spline coupling. This will permit the prediction of the number of cycles to failure and of the crack initiation location of the experimental tests. Additionally, the inclusion of surface damage effects will be investigated for the simplified cylinder-on-flat geometry, using a recently introduced fretting fatigue damage parameter.

In summary, this thesis aims to address the following:

- Evaluation of the fretting performance of different material combinations under representative spline conditions,
- Determination of the coefficient of friction (COF) of material combinations,
- Separation of the crack initiation and propagation regimes,
- What are the conditions for crack initiation in spline couplings?

- For a given spline geometry and loading history, can the life-limiting conditions of plain fatigue, fretting fatigue and wear be predicted?
- The inclusion of surface damage effects in a lifing methodology.

An outline of the thesis is given below:

Chapter 2 reviews the literature that is pertinent to the understanding of fatigue, fretting fatigue and fretting wear processes in the study of spline couplings.

Chapter 3 outlines the combined experimental and computational methodology that is pursued in this thesis for the investigation of fretting in spline couplings. The experimental details of the uniaxial representative specimen (URS) and multiaxial representative specimen (MRS) test rigs are given. Additionally, the finite element method for the two test rigs is described. A global approach is pursued for both the URS and MRS, which models more of the rig components, combined with a refined local sub-model approach for the MRS. The representative nature of the specimens is demonstrated via comparison with previous spline FE modelling.

Chapter 4 details the experimental findings from testing with the representative specimens. The fretting wear performance of different material combinations is compared using the URS. The results of the multiaxial fretting fatigue tests of the MRS are also presented. The failure surfaces are examined, allowing the location of crack initiation to be determined. The MRS tests allow a comparison of the number of cycles of failure to be made with the scaled spline test results.

Chapter 5 contains the results of the finite element modelling of the representative specimens. Experimental and computational data is compared in order to validate the approach. An inverse method is used to infer the COF under representative spline fretting conditions for various material combinations, from the experimental results of the URS. The FE sub-model of the MRS is also used to obtain important stress distributions for the analysis of fretting fatigue.

Chapter 6 is concerned with the fretting fatigue lifing of the URS and MRS. A lifing methodology is presented that quantifies the crack initiation and crack propagation regimes. The number of cycles of the initiation regime is predicted using the critical-plane fatigue approach with the Smith-Watson-Topper (SWT) relation. The crack propagation phase of the MRS is quantified using the Paris law, with short crack effects included. Comparisons are subsequently made between the experimental findings and computational predictions.

Chapter 7 explores the use of a recently introduced semi-empirical lifing parameter [11] that includes the effect of surface damage (hence contact slip) on fretting fatigue life. The damage parameter is combined with the SWT parameter in order to predict the fretting fatigue life of the cylinder-on-flat geometry using data from the literature. The technique is also used to provide a possible explanation of the size effect in fretting fatigue.

Finally, Chapter 8 offers the conclusions of the work. As a result, recommendations for future work are offered.

## 1.4 Tables

Table 1.1. The various geometries for the investigation of the fatigue and fretting fatigue behaviour of an aeroengine spline coupling.

	<b>Contact</b>	<b>Profile</b>	<b>Loading</b>	<b>Cost</b>	<b>Representation</b>
Full-scale engine spline	Radially conforming	Involute, barrelled	Flight loads	High	Actual component
Laboratory scaled spline	Radially conforming	Involute, barrelled	Major and minor cycles	↓	↓
Multiaxial representative specimen	Conforming	Flat	Major and minor cycles		
Uniaxial representative specimen	Conforming	Involute	Major cycles		
Cylinder-on-flat	Non-conforming	-	-	Low	Least representative

## 1.5 Figures

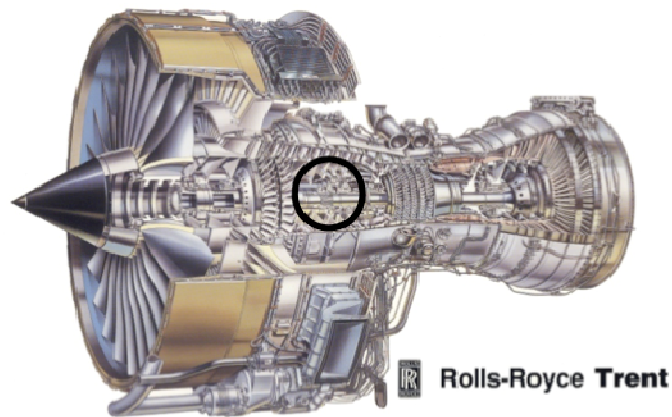


Figure 1.1. A triple-spool gas turbine aeroengine, indicating the location of the low-pressure spline coupling.

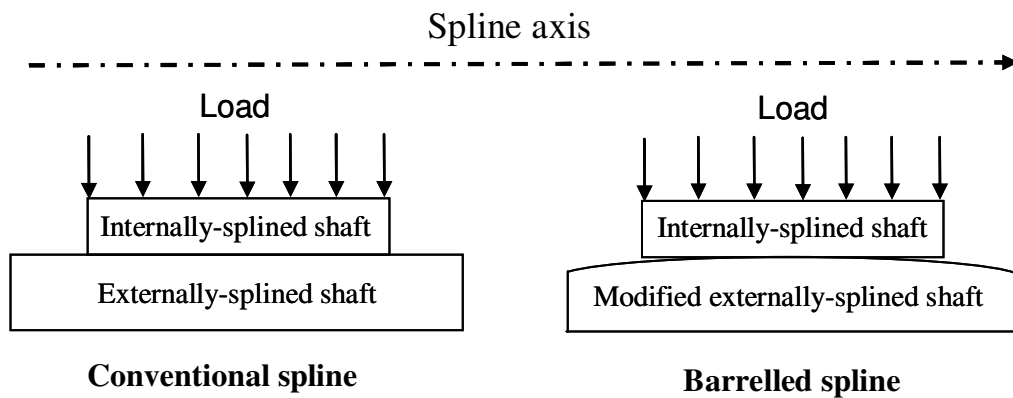


Figure 1.2. Schematic showing a comparison of a conventional spline coupling with a barrelled coupling that is modified by changing the geometry of the externally-splined shaft.

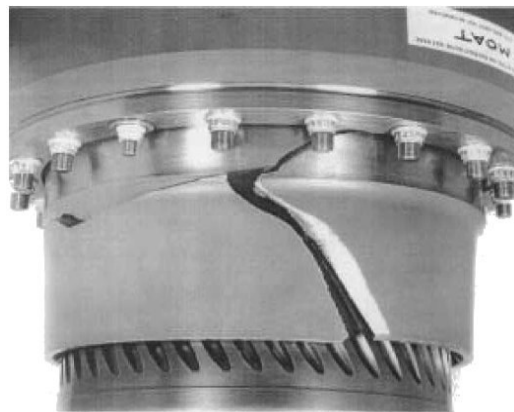


Figure 1.3. Bursting failure of the internally-splined component of a typical aeroengine low pressure spline coupling.

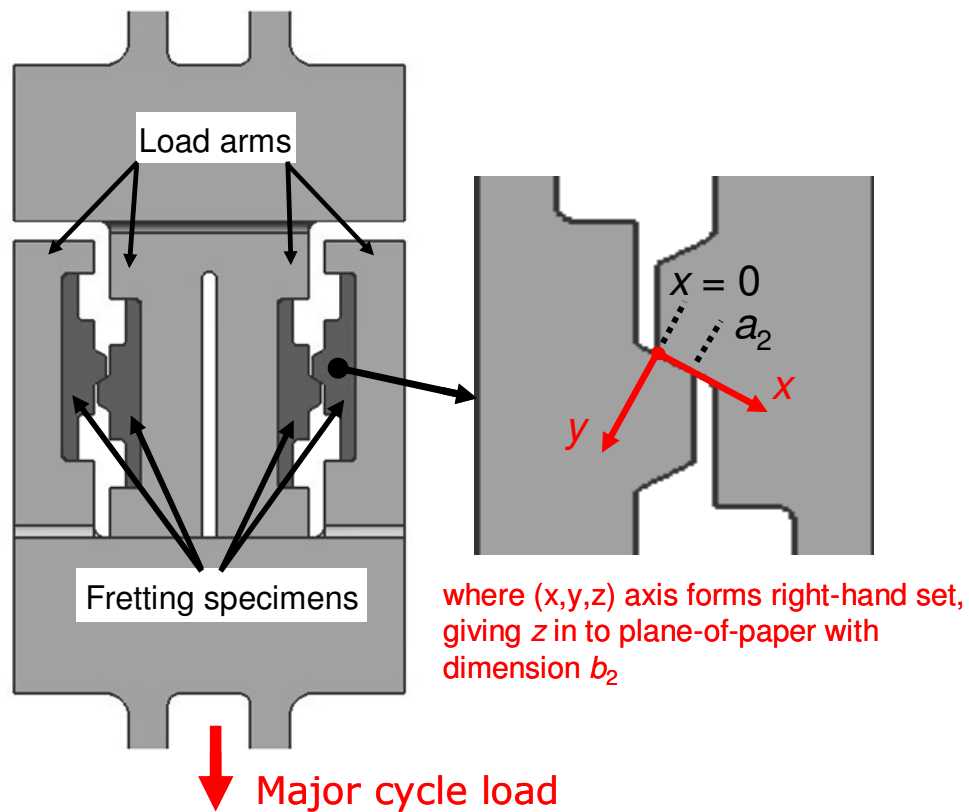


Figure 1.4. Schematic of the uniaxial representative specimen, indicating the loading and coordinate conventions.

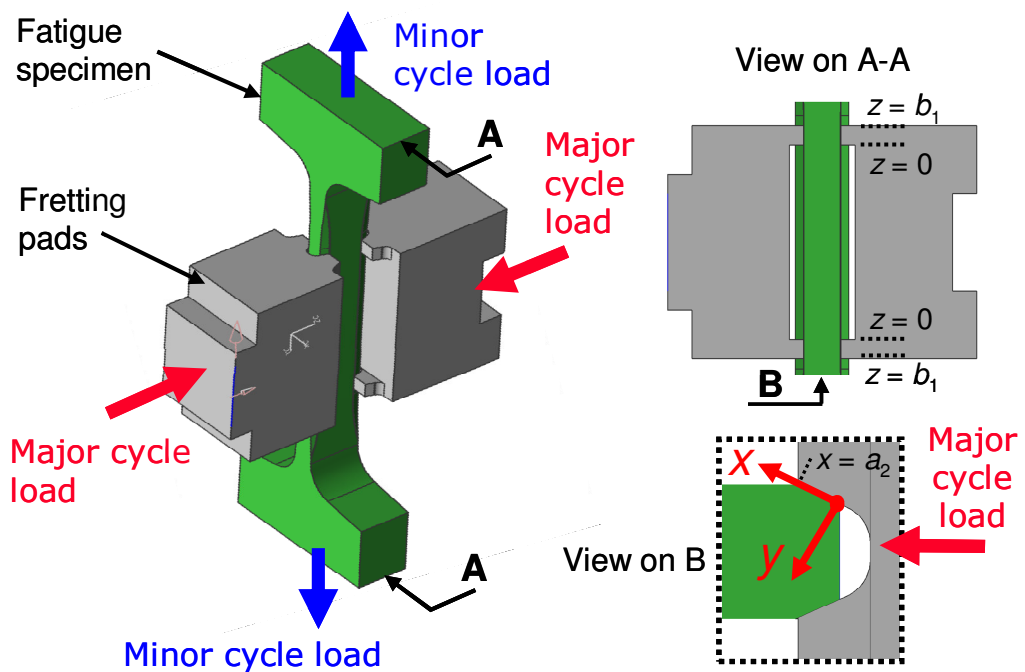


Figure 1.5. Schematic of the multiaxial representative specimen, indicating the multiaxial loading and coordinate conventions.

### Literature Review

#### 2.1 Introduction

This chapter reviews the current state of knowledge concerning fretting fatigue (FF). Firstly, a brief historical review of plain fatigue (i.e. conventional fatigue without fretting) is conducted. The subject of fretting is introduced, followed by the key analysis techniques that can be applied to the fretting problem. Fracture mechanics approaches and the subject of wear are then reviewed in the context of fretting fatigue. The results of numerical analyses of a complex aeroengine spline coupling are subsequently examined. The representative specimen concept as applied to the spline geometry is presented, including details of the various experimental setups utilised. Finally, a summary is offered highlighting the key developments that are required in order to understand fretting fatigue in spline couplings, which will be addressed in this thesis

#### 2.2 Fatigue

Many engineering failures have caused catastrophic damage and loss of life. The majority of mechanical failures can be attributed to fatigue [12]. Fatigue is the localised progressive damage to a material that undergoes cyclic stresses or strains, and which may cause cracks and lead to eventual fracture. The study of fatigue is an extensive field and many factors contribute to a fatigue failure. The following represents a brief overview of the key findings with respect to metal fatigue.

Wilhelm Albert is credited with the first article on fatigue in 1837 following his work with iron conveyor chains used in mining [13]. The industrial revolution drove the need for an improved understanding of the phenomenon. Sir William Fairbairn conducted experimental investigations using riveted wrought iron girders [14]. His work led him to conclude that the girders would fail when experiencing cyclic loads up to one third of the ultimate tensile strength.

An early breakthrough in the emerging field was made by the German engineer August Wöhler. During the 1840's he observed the phenomenon in steel railway axles, ending his work in 1869. Wöhler pioneered the systematic experimental study of fatigue, introducing the widely used rotating bending moment test. Consequently, he was the first to recognise the importance of the stress range on component life. He concluded that the cyclic stress range was more important than the peak stress in the material [15]. His studies led him to introduce stress amplitude-life (S-N) curves and the belief that a fatigue endurance limit exists for a particular material.

### 2.2.1 Cyclic definitions

Under cyclic loading it is helpful to separate the loading into mean stress ( $\sigma_m$ ) and stress amplitude ( $\sigma_a$ ) components as defined in Figure 2.1. In addition to the stress amplitude, the mean stress was found to have an effect on fatigue life and was first quantified by Gerber in 1884 [16]. The mean stress ratio ( $R_\sigma$ ) is given as:

$$R_\sigma = \frac{\sigma_{\min}}{\sigma_{\max}} \quad (2.1)$$

Gerber developed an empirical relationship that is often visualised on a constant life curve (Figure 2.2). A tensile mean stress is harmful to fatigue life

and, whilst compressive mean stress effects are usually neglected, an increase in fatigue resistance is sometimes found under those loadings. Other researchers, most notably Goodman [17] and Soderberg, also made significant contributions in this area (Figure 2.2). Goodman's relationship is generally recognised as giving good estimates for brittle materials, and a conservative prediction for ductile materials.

An important empirical lifing method is the stress-life approach. Uniaxial fatigue testing is carried out at various applied stress amplitudes and component life recorded. In 1910 O.H. Basquin [18] introduced a method to quantify the stress-life relationship, typically arising from low cyclic stresses. The primarily cyclic elastic deformations (macroscopic response) bring about a large number of cycles to failure; hence this fatigue regime is termed high-cycle fatigue (HCF). The Basquin relationship formulated in terms of elastic strain amplitude is given as:

$$\frac{\Delta\varepsilon_e}{2} = \frac{\sigma'_f}{E} (2N_f)^b \quad (2.2)$$

where  $\Delta\varepsilon_e$  is the elastic strain range,  $N_f$  the number of cycles to failure and the empirically determined constants are the fatigue strength coefficient,  $\sigma'_f$ , and  $b$ , the fatigue strength exponent. It was recognised that formulating the life in terms of the strain range would allow a wider applicability than the stress range, and the fatigue crack growth process is governed by the constraining deformation of the surrounding material [19].

Coffin [20] and Manson [21] independently quantified material life in the presence of high cyclic stresses and strains. Macroscopic plastic strain is observed and failure occurs after a relatively low number of cycles. This

behaviour is designated low-cycle fatigue (LCF). The fatigue life is characterised by the plastic strain range. The Coffin-Manson relationship is given by:

$$\frac{\Delta\varepsilon_p}{2} = \varepsilon_f' (2N_f)^c \quad (2.3)$$

where  $\Delta\varepsilon_p$  is the plastic strain range,  $\varepsilon_f'$  is the fatigue ductility coefficient, and  $c$  is the fatigue ductility exponent.

The stress and strain-life approaches are widely used, although they are not theoretical methods. Initially, experimental testing must be conducted, and the designer must be sure of the applicability of the data in relation to the actual component. For components with stress gradients (e.g. notches) and those undergoing multiaxial loadings (three-dimensional effects), the data obtained from uniaxial tests should be as representative as possible for use with more complex components.

In 1924, A. Palmgren first suggested a linear damage rule to quantify the effects of variable amplitude loading [22]. A. Miner subsequently brought about its widespread use in 1945 [23], creating the Palmgren-Miner law or Miner's rule:

$$\sum_{i=1}^k \frac{n_i}{N_i} = C \quad (2.4)$$

where  $k$  is the number of load levels,  $n_i$  is the number of completed cycles at a specific load magnitude,  $N_i$  is the number of cycles to failure at the prescribed stress amplitude, and  $C$  is experimentally determined (typically  $C = 1$  for design purposes). The law attributes the fatigue damage from each loading

condition as taking up a proportion of the total life in a linear manner. It is an approximation and also there is sometimes an effect in the order in which the reversals occur, that is not taken into account. Despite its shortcomings, the Palmgren-Miner law is still in widespread use today because of its simplicity. Non-linear rules have been shown to be more successful under certain conditions [24]. For components undergoing complex loadings that cannot be reduced to a simplified set of cycles, techniques such as the rainflow-counting algorithm have been developed [25].

### **2.2.2 Fatigue mechanisms**

According to Ref. [12], in 1849 the Institution of Mechanical Engineers (IMechE) became interested in exploring the underlying mechanisms behind fatigue failures. Initially it was believed that crystallisation of the metal was the origin of fatigue having a detrimental effect on component life. Sir James Ewing and his colleagues revealed the underlying fatigue mechanism as the forming of microscopic cracks, leading to gross material rupture or brittle cleavage fracture. In a 1900 lecture by Ewing and Rosenhain it was clearly shown that plastic deformation takes place by slip of the crystals and that the structure of the metal is preserved. The fatigue process can be broken down into the four general stages, and is schematically shown in Figure 2.3 [26]. Initially, slip by dislocations within the grain structures causes a crack initiation site. A persistent slip band then develops, and the crack growth across the grains is slow (stage I growth). A distinction is sometimes made between initiation and nucleation of a crack, with the term nucleation applied for an initiated crack that is of a detectable length. Once greater than the microstructural dimensions of the metal, crack growth is dominated by the bulk material properties (stage II growth). During crack growth it is commonly believed that striations are formed on the fracture surface, which corresponds to the propagation from individual load cycles. The final stage of

fatigue is failure of the material (usually complete specimen separation), with the material unable to accommodate the given load. Low cycle failures are generally termed ductile, whilst high cycle failures are designated as brittle failures.

The research into linear elastic fracture mechanics (LEFM) has yielded significant breakthroughs in the study of fatigue [27]. The stress intensity factor (SIF), denoted by  $K$ , describes the elastic stress field around the tip of a crack. Crack loading can then be separated into three components, and they are listed as:

- Mode I ( $K_I$ ) - the opening mode (tensile),
- Mode II ( $K_{II}$ ) - the sliding mode (in-plane shear),
- Mode III ( $K_{III}$ ) - the tearing mode (anti-plane shear).

These are illustrated in Figure 2.4 for the commonly employed compact tension (CT) specimen. LEFM approaches can be applied to quantify the growth of a fatigue crack, as described by P. C. Paris [28]. The log of crack growth rate against log stress intensity factor range shows a sigmoidal behaviour, with three distinct regions. There is a linear portion above the threshold for crack growth ( $\Delta K_{th}$ ), up until the region of high crack growth rate. This linear region can be quantified by using the relation for mode I loading:

$$\frac{da}{dN} = A(\Delta K_I)^n \quad (2.5)$$

where  $\frac{da}{dN}$  is the crack growth rate,  $\Delta K_I$  the opening mode stress intensity factor range and  $A$  and  $n$  are empirically determined constants. This relation is known as the Paris 'law.' It has gained widespread use in the analysis of

fatigue, although attention must be paid to periods of crack growth that occur outside the bounds described by the relation.

The applied mean stress affects the crack propagation rate. Walker developed an empirical relationship to quantify this effect by observing the crack growth behaviour of aluminium alloys [29]. The resulting Walker method is then used to correct the stress range for  $R$  ratio, where the fitting constant,  $m$ , is determined experimentally:

$$\Delta K_{effective} = \Delta K_{actual} (1 - R)^{m-1} \quad (2.6)$$

Different philosophies for the safe design against fatigue have been proposed. The appropriate criterion must be applied for the specific application. The infinite life approach was originally developed. This specifies that the component must not suffer from a fatigue failure by ensuring that the design stresses are below the endurance limit of the material. One of the other common approaches is the damage tolerant methodology to enable less conservative designs. The component is designed so that any cracks that grow will not develop into a critical flaw before the next period of inspection. This assumption is based on fracture mechanics and is often used in safety-critical fields, such as the gas turbine industry.

### 2.3 Fretting fatigue

Fretting is defined as the small amplitude (typically 1-100  $\mu\text{m}$ ) oscillatory relative motion between two surfaces in contact. Fretting occurs in many nominally static mechanical arrangements undergoing vibrations or cyclic stresses. The microslip causes damage to the surfaces and eventual failure is by means of fretting fatigue (catastrophic failure) or fretting wear (loss of fit). The slip condition in fretting is often described as:

- Complete stick,
- Partial slip,
- Full (gross) sliding.

Fretting was first observed in the grips of a plain fatigue test by Eden and Rose in 1911 [30]. The presence of fretting is often unexpected and causes reduction in life in comparison to plain fatigue, emphasising the importance of recognising and avoiding the phenomenon for practical design cases. The understanding of fretting is complicated by the presence of friction at the contact interface.

### **2.3.1 Friction**

A metallic surface is not perfectly flat and increased magnification reveals the roughness of the surface profile. The individual surface protrusions are termed asperities. When two surfaces are brought into contact, the asperities of the individual surfaces interact and junctions of contact are formed. This interaction creates a resistance to tangential motion and this force is termed 'friction.'

Leonardo da Vinci is credited as the first to attempt a systematic study of friction, with the investigations later rediscovered by Guillaume Amonton. The so-called laws of friction, formulated from empirical observations, are often stated as:

- The friction force is proportional to the normal load (Amonton's 1<sup>st</sup> law),
- The friction force is independent of the apparent area of contact (Amonton's 2<sup>nd</sup> law),
- The friction force is independent of the sliding velocity (Coulomb's law).

These ‘laws’ are not observed across all experimental conditions and were formulated for ‘dry’ conditions where no lubricant is applied. Amonton’s 1<sup>st</sup> law leads to the relation:

$$F = \mu N \quad (2.7)$$

where  $F$  is the friction force,  $N$  is the normal load and  $\mu$  is termed the coefficient of friction. The coefficient of friction (COF) can vary widely between different material combinations, from as low as 0.001 to around 10 in a vacuum. Most metals tested in air lie in the range 0.1 to 1.0 [31]. It has often been observed that the COF is greater under static ( $\mu_s$ ) than dynamic conditions ( $\mu_d$ ), but frequently found that  $\mu_d$  is essentially independent of sliding velocities for most practical situations encountered (Coulomb’s law). In addition to the commonly employed Coulomb friction law, different friction laws have been formulated and are detailed in Ref. [32].

It was initially believed that the frictional force principally arose from the interaction of asperities [33]. The Coulomb model describes the contact between two surfaces with simplified wedge-shaped asperities, by applying a normal contact load and displacing the two surfaces relative to each other. The model indicates that the work done is fully recovered (no net energy dissipation) as the surfaces slide, inferring that no frictional force is generated if the model is followed exactly. This leads to the conclusion that another mechanism is responsible for the generation of the frictional force. In metallic materials this is attributed to the plastic deformation experienced by the asperities, and is denoted  $F_{\text{def}}$ . It has also been proven that adhesion between the two surfaces ( $F_{\text{adh}}$ ), caused by the inter-atomic forces contributes to the total friction force.

The groundbreaking work of Bowden and Tabor [33] offered a key explanation of the behaviour of friction. They stated that the ‘real’ area of contact is significantly less than the apparent area. Their work, at first, seemed to be in discrepancy with Amonton’s laws, but they showed that with an increase in normal load, a subsequent increase in the ‘real’ area of contact is obtained. This may be investigated by approximating the asperity contacts as cylindrical, with the assumption that asperities are usually blunt. This leads to the application of the mathematical theory of Hertzian contact, which is introduced in Section 2.6.2 of this review. Assuming plastic behaviour of the asperities, the total real area of contact is found to be proportional to the normal load, thereby attaining approximate agreement with Amonton’s laws.

The adhesive force originates from the inter-atomic attractive forces at the asperity junctions. By investigating the real area of asperity contact and assuming asperity failure is governed by the shear stress of the material, the contribution of the adhesion force, for conventionally processed metals, to the COF is approximated by [31]:

$$\mu_{adh} \approx 0.2 \quad (2.8)$$

From an assumption of an idealised rigid conical asperity, the contribution of deformation processes is estimated by:

$$\mu_{def} = \cot \alpha \quad (2.9)$$

where  $\alpha$  is defined in Figure 2.5 and is generally greater than  $80^\circ$ , giving  $\mu_{def} < 0.1$ . This suggests that the total coefficient for two metals in sliding contact should not be greater than around 0.3. It is usually observed that the experimentally estimated COF is significantly greater than this. Junction growth (dependence of real contact area on tangential load) and work-

hardening effects are thought to contribute to the discrepancy between the predicted and measured COF.

The COF is often difficult to quantify and its determination remains one of the biggest challenges in fretting research. Experimentally, it is commonly observed that the COF is initially low (as low as  $\sim 0.1$ ), followed by a rapid increase. This is attributed to the beneficial (lubricating) surface layer films that are present during the initial stages of the test, which are quickly eliminated during the sliding motion, leading to metal-on-metal contact. The initial sliding motion can also increase surface roughness, leading to an increased COF. The standard approach is to establish the bulk variables (friction force and normal load) by measurement or calculation. A complexity encountered is that, under partial slip conditions, the bulk approach is an approximation due to the presence of stick zones. One approach taken is to interrupt a test to determine the mean coefficient. This is conducted by increasing the tangential force until full sliding occurs. From the mean value, the distribution of the COF was analytically determined for the Hertzian and rounded-flat cases in Ref. [34]. An additional obstacle is that the local distribution of the COF will vary across the contact surface. This effect is usually neglected in the analysis of FF, although an attempt to account for it was pursued in Ref. [35].

## **2.4 Experimental**

### **2.4.1 Variables**

In the early period of fretting research, experimental data was extensively interpreted with the aid of S-N curves. Plain fatigue testing would be conducted and the subsequent FF results compared. This allowed the determination of strength reduction ('knock-down') factors that quantified the

effect of FF on life. It was subsequently recognised that a significant number of variables affect fretting fatigue life and that greater rigor was necessary for further understanding. It has been cited that as many as fifty variables can influence the fretting process [36], highlighting the complexity. It was suggested that the factors could be separated and that they can be categorised into primary and secondary sets of variables. The primary variables were listed as:

- Contact pressure (normal load),
- Coefficient of friction (COF),
- Slip amplitude.

It was put forward that the COF is the most important of all of the factors. The secondary variables consist of factors that are arguably accounted for by their effect on the primary variables. These include: contact geometry, material, surface conditions (roughness, hardness etc.), residual stress, temperature and test frequency amongst others.

#### **2.4.2 Fretting maps**

The introduction of fretting maps by Vingsbo and Soderberg was an important development [37] in quantifying the effects of the variables. A fretting map is usually a two-dimensional representation of two fretting variables. The majority of fretting maps involve plotting the normal contact load or contact pressure against displacement or relative slip [38]. One type of fretting map is termed the material response fretting map (MRFM) and is shown in Figure 2.6 for the fretting analysis of an aluminium alloy from Ref. [39]. It is separated into three domains viz. no detachment, particle detachment and the cracking and wear domain. The following sections describe the influence of the contact pressure and contact slip.

### **2.4.3 Contact pressure**

The effect of the contact pressure on fretting fatigue life has been debated in the literature. It has generally been observed that there is a decrease in life with increasing contact pressure as found in Ref. [40]. These findings are of significant practical importance, indicating that a designer ought to minimise contact pressure in order to reduce the likelihood of an FF failure. One difficulty with the interpretation of the results of contact pressure studies is that other variables are also varied (notably shearing traction and contact slip). Iyer and Mall [41] studied the interaction for a titanium alloy (Ti-6Al-4V) for a cylinder-on-flat configuration. They suggested that decreasing FF lives with increasing contact pressure was solely due to the increased contact pressure and increased stress magnitudes associated with higher normal loads and was independent of the other fretting parameters. This is unlikely to be the case, given the importance of slip amplitude for fretting [42] and the interaction between all of the parameters.

### **2.4.4 Contact slip**

The magnitude of contact slip has been shown to be a key parameter with respect to FF life, although it has persistently been challenging to experimentally determine. It is typically small and therefore prone to experimental error. Researchers have used linear-variable differential transformers (LVDTs) [43], and extensometers [44, 45] near the contact surfaces in an attempt to quantify its magnitude. It is almost universally found that the measurements are significantly greater than the analytically or numerically-predicted values (e.g. by finite element analysis such as in Ref. [46]). Nevertheless, Nishida et al. [47] obtained a good correlation with FE-predicted values by utilising a novel experimental approach. They used a test setup in-situ with scanning electron microscopy (SEM) to measure the displacement of a point on the fretting pads in relation to the fretting

specimen. They found that their SEM measured displacements were significantly less than those measured using an extensometer.

It is generally accepted that a significant proportion of the discrepancy between measured and predicted displacements is due to the compliance of the testing fixture. Attempts have been made to include the compliance in the models, although the actual contributions from the individual test parts have not to date been fully modelled. Including more of the test fixtures in models will typically help to better quantify the compliance effects.

The three regimes that are used to describe the contact slip state are: complete stick, partial slip and full (gross) sliding. These are often plotted on a running-condition fretting map (RCFM) as shown, for example, in Figure 2.7. The contact slip regime can be inferred from analysis of the dynamic experimental force-displacement ( $F$ - $\delta$ ) loops. Figure 2.8 shows the characteristic shapes of the loops for each of the fretting regimes [38]. For complete stick, the relationship is linear. Under partial slip, a hysteresis loop is observed due to energy dissipation. For full sliding conditions, the hysteresis loop is opened up and portions of the curve are parallel to the displacement axis. A drawback of inferring the slip regime from bulk measurements is that the technique is unable to discern the variation of contact slip across the surface. To overcome this, Jin and Mall used the FE method to discern the variation of the slip across the surface [48], calibrating it against the measured global relative displacements. An alternative method of determining the slip regime was offered by Varenberg [49], introducing a non-dimensional 'slip index.' It was argued that this provides a more accurate description of the fretting condition. However the approach has not, to date, received widespread use in the field.

Vingsbo and Soderberg [37] examined various experimental data from the literature for the cylinder-on-flat geometry. They usefully represented the effect of slip amplitude on FF life as in Figure 2.9. For complete stick behaviour, or low amplitude slip, component life may be interpreted as the plain fatigue life in the presence of a stress concentration and associated gradient. They crucially showed that there exists a critical slip amplitude which yields the minimum FF life. This is often in the partial slip regime. For larger slip amplitudes (gross sliding regime) the life is seen to recover, possibly due to wear mechanisms becoming more dominant. It has been postulated that embryonic cracks are 'worn' out before they have chance to propagate. An additional explanation was offered following a numerical wear simulation methodology [50, 51] and is detailed in Section 2.9.2. It was shown that the stress field is amplified during partial slip and attenuated during gross sliding conditions. The quantitative determination of the competition between fatigue cracking and wear mechanisms offers promise in the understanding of FF. A difficulty with the Hertzian cylinder-on-flat geometry (see Section 2.6.2 for mechanics of the geometry) is encountered in interpreting the effect of slip amplitude in the partial slip regime, as the shearing traction also increases along with the slip amplitude.

#### **2.4.5 Interaction of variables**

The effect of each of the variables has yet to be determined, and it is a difficult task to separate out their influences in a test setup. The main obstacle with the approach is that there is often a synergistic inter-relationship between the variables. This is highlighted when investigating the primary variables, for example. For the cylinder-on-flat geometry (Section 2.6.2), a change in the contact pressure also directly modifies the shear traction and contact slip state. Even if the contact slip were to be kept constant, then the tangential load required to maintain the slip would have to be increased.

### **2.4.6 Surface damage and stress concentration effects**

The understanding of FF is complicated by the high stress concentration and associated stress gradients created by the contact. It is clear that contact slip also induces surface damage [52]. One key barrier to be overcome in the solution of the fretting problem is the determination of the relative significances of stress gradient effects and surface damage effects. The separation of the two is difficult, but a simple approach was pursued in Ref. [53], whereby an equivalent stress state for a rounded-flat geometry was obtained using the root-bisector of a notch. More experimental tests are required to determine the influence of surface damage and stress gradient effects. The testing of monolithic components also offers promise. This is where a component is designed as a replica of the geometry of the fretting specimen and pad, whereby there is no frictional contact interface and therefore no surface damage.

## **2.5 Experimental test setups**

### **2.5.1 General**

A unified fundamental theory for predicting FF has not currently been found and therefore experimental testing is essential for improved understanding. Fretting tests have been carried out for many decades, but it was recognised that the methods and approaches needed to be standardised in order to obtain universal findings [54].

The geometry of the contact can play an important role in the fretting process. Contacts may be separated into complete and in-complete contacts. Incomplete contacts are geometries where the extent of the contact is dependent upon the applied normal load, whereas incomplete contacts yield a contact patch that is normal load independent. Some applications and

research studies have utilised contacts classified as nearly-complete, in which there is a radius introduced at the edge of contact [55]. A further classification is also made according to the conformality of the geometry. An analysis of FF must therefore consider the geometry of the problem, a challenge being the unification of analysis techniques across different geometries. This section will outline the main experimental setups used for FF testing, which are: i) bridge-type, ii) fundamental geometries, iii) and representative testing.

### **2.5.2 Bridge-type setups**

The most common test set up in fretting research was originally the bridge-type arrangement, such as was utilised by Switek [56] and Lindley [57]. This involves a fatigue specimen in contact with two bridges, with each bridge comprising two feet, typically as in Figure 2.10. A normal force is applied to the bridges to enforce contact. Most test apparatus' apply an in-plane bulk fatigue load (or displacement) to the specimen, although an out-of-plane load can also be applied as in Ref. [10]. The relative slip is generated by the difference in the strain of the fatigue specimen in relation to the specimen pads, and therefore the pads should be of minimal height. The characterisation of the contact stress field for the complete contacts often used in these test set ups is complicated the presence of a theoretical elastic stress singularity at the edges-of-contact. This could mean that manufacturing tolerances and small variations become significant. It is also inevitable that the conditions at each of the bridge feet will not be identical. This means that one pair of feet may be sliding, whilst the other pair accommodates the load [58]. It is often found that fretting fatigue failures occur at the location where the wear is not at its maximum. The significant advantage of using these test geometries is that many real engineering components have sharp-edged or near sharp-edged contacts, such as the spline coupling in a gas turbine aeroengine.

### **2.5.3 Simplified geometries**

The use of simplified geometries in FF testing is common. Nishioka and Hirakawa [59] were the first to make use of the incomplete, conforming cylinder-on-flat geometry. This arrangement has gained popularity due to pad alignment being less critical in comparison with bridge set ups. Also, a closed-form analytical solution exists for the geometry (presented in Section 2.6.2). Other investigators have employed the spherical-on-flat arrangement and the rounded-punch-on-flat in an attempt to make the findings more applicable to complex engineering geometries. These geometries are useful for probing the theoretical aspects of FF. The location of cracking in the cylinder-on-flat arrangement has been studied extensively. Cracks are usually observed at the edge of contact or within the slip zone up to the stick-slip interface [60]. Additionally, FF cracks may be orientated at an inclined angle relative to the specimen normal [61].

### **2.5.4 Representative testing**

A major limitation of simplified test geometries is in their inability to readily reproduce the complex fretting conditions undergone by a real component. Representative testing attempts to overcome this by testing a laboratory specimen that is designed to reproduce the key variables of the in-service component. The factors influencing FF life were detailed in Section 2.4.1, and include: geometry, material, loadings and frequency in addition to the key fretting variables that should be reproduced in the vicinity of the contact interface.

Ruiz [62] notably devised a biaxial test rig to simulate the dovetail-root connection of the fan blades in a gas turbine aeroengine. The contacts were idealised with a two-dimensional rounded punch-on-flat geometry. Figure 2.11 shows a failed representative dovetail specimen from such a test rig [63],

with the critical crack emanating from the edge of the contact flank. The rig was capable of high and low frequency loading that leads to fretting from centrifugal loading or in-flight fluctuations. Following from the experimental work conducted, Ruiz and his colleagues devised an empirical FF damage parameter (see Section 2.7.1). The development of a dovetail fretting test arrangement was also detailed by Golden [64].

With the focus of this thesis on representative testing for aeroengine spline couplings, more detail on this geometry is presented in Section 2.11 of this review.

## **2.6 The initiation of fretting fatigue cracks**

Although significant advances in knowledge have been made, the initiation of cracks in polycrystalline metals is still not fully understood. In plain fatigue, cracks initiate along persistent slip bands (PSB) or at material defects. For a cylindrical bar, (plain) fatigue cracks occur on the plane of maximum shear stress at an angle of  $45^\circ$  to the axis. In FF, there are additional length scales that influence the problem [65], with the usually severe stress state induced by the contact an important factor to consider.

There has been debate in the literature as to when FF cracks initiate during a FF test. Many investigators hold the view that initiation is a gradual process that involves the accumulation of microstructural damage. Following from this, some researchers state that cracks initiate after a small number of cycles [66], whilst on the other hand, others found that the majority of the total life is occupied with initiating a crack [67]. This discrepancy is likely to arrive from two sources. Firstly, an ambiguity encountered is the definition of the transition from the initiation to propagation phases. The definition of initiation is strongly dependent on the scale of the observation. On the micro-

scale, nucleation may be defined as the development of persistent slip bands (across 1-3 grains for example), whilst at the bulk scale nucleation may be defined as detection of the smallest detectable flaw (typically  $\sim 100 \mu\text{m}$ ). This dependence on detection equipment can make it difficult to interpret results across different studies. The second factor that is likely to be significant in the determination of the relative initiation and propagation phases is the magnitude of the applied bulk stress, meaning that the loading must be examined for each situation encountered [58].

Converse to the idea of initiation as a gradual process, Miller argued that the initiation phase does not exist at all [68]. It was claimed that the initial stress concentrations (dislocations, grain boundaries etc.) at the surface suggests the presence of a crack. It was therefore surmised that the fatigue behaviour should be characterised solely in terms of fracture mechanics concepts. The difficulty with this approach is that elastic-plastic fracture mechanics (EPFM) techniques must be applied at a smaller scale than of the individual grains, for which the scientific method is not adequately advanced.

FF crack initiation shows some differences compared to the initiation of plain fatigue cracks. Crack initiation often arises from an initial flaw in plain fatigue and thus its location is often not easily predicted for cases without stress concentration features. Advantageously in comparison with plain fatigue, the location of FF crack initiation is usually well predicted. Fretting cracks invariably initiate at the surface and are usually observed to occur at the site of maximum stress concentration. The factors that influence crack initiation are separated into the following [58]:

- Material factors,
- Environmental factors,

- Mechanical factors.

Material factors include the grain size, morphology and the bulk properties. The environmental factors consist of surface temperature, debris and oxidation effects. The mechanical factors include the loading and the slip amplitude (determining the number of asperity passes).

It is of important practical interest to minimise the potential harmful consequences of FF. Most methods intended to improve fretting fatigue life inhibit the crack initiation phase, but may also reduce the crack propagation rate. Some commonly employed palliatives for FF include:

- Nitriding,
- Coatings (e.g. nitride),
- Shot peening.

A difficulty is encountered in the minimisation of fretting and fatigue damage when referring to the COF. Lowering the COF can significantly reduce the sub-surface stress state near the contact, resulting in a beneficial effect in terms of total life. At the same time, it is likely that an increase in relative slip will occur, leading to increased surface damage, which can promote initiation of a crack.

The complete quantitative understanding of the initiation process would be a paradigm shift in the analysis of fretting fatigue. Fundamental experimental tests will undoubtedly contribute towards this goal, in addition to the advancements in modelling of the process. The modelling of initiation is separated into approaches that consider the bulk or microstructure perspective.

### **2.6.1 Micro-modelling of fretting fatigue initiation**

The realisation of full-scale micro-mechanical modelling of components is difficult to imagine in the near to long-term future. It would require knowledge of the microstructure of the material and a validated scientific methodology that is capable of capturing the physical behaviour of the individual grains etc. Nevertheless, attempts have been made to model local behaviour at the microscale using simplified finite element (FE) analyses. Polycrystalline FE simulations were conducted in Ref. [69], whereby multiple grain orientations were included. This allows the simulation of local plasticity effects. The approach has the advantage that the fundamental mechanisms can be investigated and allows the ranking of material fatigue performance that would provide practical guidelines to improving fatigue resistance.

### **2.6.2 Macro-mechanics of fretting fatigue**

The first stage in the macro-analysis of FF is the solution of the contact problem. This was originally carried out analytically, but with developments in computational processing, numerical methods became increasingly popular. The approximate finite element method is commonly employed, although the less developed boundary element method has also been utilised. Analytical methods usually yield a rapid solution once the original problem has been solved, but their applicability can be limited with respect to the geometry. Nevertheless, analytical procedures have shed valuable light into the fretting fatigue process, and are thus described below. The following equations in this section are reproduced from Refs. [70] and [58].

The cylinder-on-flat geometry has become important in the study of FF due to the readily available closed-form analytical solution. A two-dimensional schematic of the arrangement is shown in Figure 2.12. Hertz [71] was the first to solve the elastic contact problem (the theory taking his name) by analysing

the contact of two cylinders or a cylinder contacting a half-plane. Caution must be taken when the fretting specimen is of finite width, but the half-plane assumption is usually deemed to be suitably accurate when [72]:

$$\frac{w}{a} > 5 \quad (2.10)$$

where  $w$  is the width of the fretting specimen and  $a$  the semi-width of contact. It is also assumed that the cylinders are of infinite length, the radius of curvature large compared to the contact width and a plane strain simplification applicable (therefore neglecting end-effects). The theory yields the contact pressure distribution under an applied normal load and gives:

$$p(x) = p_0 \sqrt{1 - (x/a)^2} \quad (2.11)$$

In addition, the peak pressure,  $p_0$ , is related to the normal load,  $P$ , and the pad radius,  $R$ , by:

$$p_0 = \sqrt{\frac{PE^*}{\pi R}} \quad (2.12)$$

where  $E^*$  is the composite modulus of the indenter-substrate system for a given material pair and for a similar material pair is given by [70]:

$$E^* = \frac{E}{2(1 - \nu^2)} \quad (2.13)$$

where  $R$  is the relative radius of curvature of the two contacting bodies and for the general case is:

$$\frac{1}{R} = \frac{1}{R_1} + \frac{1}{R_2} \quad (2.14)$$

where the subscripts refer to the two contacting bodies. The semi-width of contact,  $a$ , is then given by:

$$a = \sqrt{\frac{4PR}{\pi E^*}} \quad (2.15)$$

A major inference from Hertzian theory is in the prediction of partial slip (as shown in Figure 2.12). For partial slip to occur (assuming Coulomb friction behaviour) the total shear traction,  $Q$ , must be less than the limiting value:

$$Q \leq \mu N \quad (2.16)$$

where  $N$  is the normal load. Mindlin [73] and Cattaneo [74] independently obtained the surface shear traction distribution for the partial slip case, with the solution conventionally named the Cattaneo-Mindlin solution and is given by:

$$q(x) = \mu p_0 \sqrt{1 - \left(\frac{x}{a}\right)^2} + q'(x) \quad (2.17)$$

where  $q'(x)$  represents the perturbation in the slip zone and is zero for  $|x| < c$  and  $c$  is the size of the stick zone. With a bulk stress present:

$$q'(x) = -\mu p_0 \left(\frac{c}{a}\right) \sqrt{1 - \left(\frac{(x-e)}{c}\right)^2} \quad (2.18)$$

where  $e$  is the offset of the centre of the stick zone from the centre of contact. The determination of the stick zone size is realised via tangential equilibrium and gives:

$$\frac{c}{a} = \sqrt{1 - \left| \frac{Q}{\mu P} \right|} \quad (2.19)$$

The offset of the stick zone,  $e$ , is determined by:

$$e = \frac{\sigma a}{4\mu p_0} \quad (2.20)$$

where  $\sigma$  is the applied bulk stress. The shear traction distribution with an applied bulk stress is shown in Figure 2.13. The effect of a bulk stress is to shift the stick zone by the distance  $e$ . If the bulk stress is high enough in magnitude, reverse slip will occur at one edge of the contact.

In order to determine the elastic stress state under the contact analytically, the Muskhelishvili potential [75] may be found (incompressible substrate assumed) and superposition of the stress components performed. The presence of a bulk stress acts to increase the stress magnitude, particularly the in-plane axial component [58].

A significant implication of Hertzian theory is that the peak pressure is proportional to  $\sqrt{\frac{P}{R}}$ , and  $a$  is proportional to  $\sqrt[3]{PR}$ . The consequence of this is that the extent of the contact stress field can be varied, whilst the magnitude kept constant. This was first noted by Bramhall [76]. In the groundbreaking work, Bramhall found that larger contact sizes gave finite FF lives, whilst the smaller contact sizes gave effectively infinite lives. These findings were later confirmed by Nowell [52], whereby a series of tests were conducted on an aluminium alloy (Al4%Cu) and the results are shown in Figure 2.14. The size effect was also confirmed for the commonly used aerospace titanium alloy Ti-6AL-4V [77]. The observable size effect is attributed to the stress gradients

produced by the contact, meaning the smaller the contact radii, the steeper the stress gradient. It is thought that at low contact sizes, the rapidly decaying stress field is not sufficient for a crack to form and/or propagate. From the work of Miller [68], a physical hypothesis for this is that the strongest microstructural barrier must be overcome for a crack to initiate.

Another common geometry that is encountered in the study of FF is the punch-on-flat arrangement, which is schematically shown in Figure 2.15. With a frictionless, elastic half-plane assumption, the analytical pressure distribution is given as:

$$p(x) = \frac{P}{\pi\sqrt{a^2 - x^2}} \quad (2.21)$$

The distribution is plotted in Figure 2.16. It is apparent that at the edges of contact, there is a singularity, with the magnitude tending towards infinity. This severe edge-of-contact condition is found practically in many engineering assemblies, such as spline couplings or shrink-fit assemblies and therefore an understanding of this geometry is of paramount importance in the study of FF. The analysis of a tilted punch was conducted in Ref. [78], a condition that can also arise in real engineering assemblies.

Switek analysed the bridge-type geometry by computing the sub-surface stress and strain state of the fretting specimen when in contact with a fretting pad [56]. A parabolic normal stress distribution was assumed that was deemed to be less than 5% in error in comparison with the theoretical elastic half-space prediction. It was found that frictional stresses contributed significantly to the stress system and reached a maximum at the trailing edge of contact. Contours of constant strain energy from Switek's analysis are shown plotted in Figure 2.17. An early-stage crack initiation criterion was

utilised that specified initiation governed by the maximum strain energy release rate. Figure 2.17 indicates that an initiated crack would be orientated at approximately 45° into the fretting specimen for this configuration according to the assumed criterion. Knowledge of the local stress and strain state is of significant importance for the application of life prediction techniques, as discussed in the following section.

## 2.7 Fretting fatigue lifing

The field of FF lifing still presents significant challenges. The number of factors involved and the lack of understanding of their interaction adds complexity in relation to plain fatigue. In addition, a unified FF lifing methodology would be required to be equally applicable to conforming and non-conforming contacts. The ultimate aim for fretting research is to be able to predict the FF life of complex realistic engineering couplings or contacts.

### 2.7.1 Fretting fatigue damage parameters

Due to the clear added complexity that fretting involves in comparison to plain fatigue, various fretting specific parameters have been investigated. Ruiz devised a relation, the Ruiz parameter, based on experimental observations to predict the most likely site for crack initiation and the most commonly used form is given by [62]:

$$F_2 = (\sigma_T \tau \delta)_{\max} \quad (2.22)$$

where  $\sigma_T$  is the tangential stress and the frictional work ( $\tau \delta$ ) dissipated during one load cycle. Although, the parameter has seen some success in predicting the location of crack initiation, it does have significant shortcomings. Firstly, the physical reasoning behind the parameter has never been satisfactorily demonstrated. The product  $\tau \delta$  is a measure of the frictional work for a

particular point along the contact throughout the load cycle. This was, somewhat arbitrarily, combined with the tangential stress at the contact, as Ruiz hypothesised that a local tensile stress be required for the initiation and propagation of a crack. An adequate correlation of the Ruiz parameter with the number of cycles to initiate an FF crack has not adequately been demonstrated to date. In addition, the mean stress is known to affect the crack initiation period and is not included in the formulation. Other factors known to affect FF life are also not accounted for; for example, surface roughness effects are only considered indirectly via the value of the surface parameter ( $\tau\delta$ ).

### 2.7.2 Stress and strain-based (Cauchy) approaches

Attempts have been made to predict FF life using plain fatigue data, with the attractiveness that substantial experimental data has been gathered for plain fatigue cases. Initially, effective strain parameters were used, although they had significant shortcomings. These approaches are typically based on the Basquin and the Coffin-Manson relationships, which were developed from empirical observations.

Smith, Watson and Topper [79] introduced a stress-strain function with the intention of including the effect of mean stress. They combined this function with the strain-life relation in order to predict fatigue life. The Smith-Watson-Topper (SWT) formula is given below:

$$\sigma_{\max} \Delta \varepsilon_a = \frac{(\sigma'_f)^2}{E} (2N_f)^{2b} + \sigma'_f \varepsilon'_f (2N_f)^{b+c} \quad (2.23)$$

where the symbols have the same meaning in relation to plain fatigue. The maximum stress term in the SWT parameter attempts to include the effects of mean stress on fatigue life. This is based on the maximum stress ( $\sigma_{\max}$ ) being

equal to the stress amplitude ( $\sigma_a$ ) for a fully reversed test. The parameter is applied to tensile loading, and is set to zero for compressive stresses. The SWT parameter is applied to a stabilised hysteresis loop and therefore care must be taken to ensure that no significant ratchetting occurs.

The Fatemi-Socie (F-S) parameter is an alternative parameter that arose from the observation that the life of specimens in shear was usually found to be greater than that with axial loading [80].

$$\frac{\Delta\gamma}{2} \left( 1 + \alpha \frac{\sigma_{\max}}{\sigma_y} \right) = \frac{\tau'_f}{G} (2N_f)^b + \gamma'_f (2N_f)^c \quad (2.24)$$

where  $\gamma$  is the shear strain amplitude,  $G$  is the shear modulus and the constants are the same as in the SWT parameter but obtained in torsion.

### 2.7.3 Multiaxial fatigue methods

Originating from experimental observations of multiaxial loadings, Brown and Miller [19] suggested the existence of two cases of specimen loading and subsequent crack growth: case A and case B (Figure 2.18). It was suggested that case A cracks grew predominantly under torsion and case B under equibiaxial loading. Following from this, Fatemi and Socie [80] suggested the use of different life assessment criteria for tensile cracking and shear cracking failure modes. They argued that the critical-plane should be determined as the plane with the maximum principal strain amplitude and the maximum normal stress on the plane for tensile cracking modes (case B). For this case, the SWT parameter is therefore appropriate. For shear cracking modes (case A), the maximum shear strain amplitude and the maximum normal stress on the plane should be considered, leading to the application of the F-S parameter. The use of the critical-plane technique with empirical fatigue parameters has become a popular FF life methodology.

Lykins et al. evaluated the performance of various lifing parameters for the titanium alloy, Ti-6Al-4V, for the cylinder-on-flat geometry [67, 81]. They conducted an FE analysis to obtain the stress and strain distributions and then argued that the FF data could be collapsed onto the FF data with the SWT and F-S parameters. A plot of the SWT parameter against the number of cycles to initiation is shown in Figure 2.19 for plain fatigue and FF tests. A reasonable correlation was obtained, although some experimental scatter was observed for the FF results. They found that the predicted angles using the SWT parameter were not in agreement with experimental observations, but the maximum shear stress range parameter showed better correlation of the angles. It was suggested that initiation in Ti-6Al-4V is governed by the maximum shear stress range on the critical plane.

Navarro et al. applied various multiaxial fatigue parameters to the cylinder-on-flat and sphere-on-flat geometries and combined the initiation and propagation lives (from an analytically determined stress state) to give a total predicted life [82]. Tests were analysed for a titanium and aluminium alloy. A method of determining the initiation 'length' was offered in order to overcome the difficulties associated with this as discussed in Section 2.6. It was suggested that intersection of the Basquin fatigue curve with the propagation rate (as a function of distance into the specimen) would yield the transition from initiation to propagation and the associated length scale involved. This concept is shown in Figure 2.20. Nevertheless, an initial defect (given as the grain size) must still be specified in order to define the propagation curve as governed by LEFM. It was argued that the method was better able to predict fretting fatigue life compared to using a fixed initiation length. The method, however, relies on the questionable assumption that the material is acting to minimise endurance by undergoing the mechanism that furnishes the highest rate of damage.

The Dang Van criterion was formulated as an alternative fatigue parameter and can be applied for multiaxial loadings. It was postulated that plastic strain occurs locally at the grain level when the bulk state is nominally elastic [83]. Plastic shakedown may also occur at the grain level, and it was hypothesised that crack initiation will occur when there remains cyclic plasticity persists at the scale of the grains. However, the Dang Van criterion can only distinguish between finite life and infinite life. A relationship between the Dang Van and bulk fatigue properties was demonstrated in Ref. [84], bringing into doubt the distinctiveness of the approach.

Opinion differs as to whether FF can be predicted from plain fatigue data. A significant limitation is that all of the methodologies do not account for the experimentally observed effect of slip amplitude on FF life. Neglecting wear, the stress-state under the limiting partial slip condition is predicted to equal that of the full sliding condition [46], due to saturation of the shear force at the limiting value. A life prediction obtained using stress and strain-based parameters in the gross sliding regime can therefore be regarded as a conservative estimate.

For the cylinder-on-flat geometry, cracking is almost invariably predicted to occur at the trailing edge-of-contact. It has been observed that cracks initiate in the slip zone or at the stick-stick interface. The wear simulation methodology of Madge et al. (introduced in Section 2.9.2), has been shown to capture this effect [51].

An additional shortcoming of such approaches is that real materials usually contain inherent flaws, and total life methods are not able to predict self-arrest of flaws or nucleated cracks that is sometimes experimentally observed. Crack

arrest occurs due to the high stress gradients induced by the fretting contact, meaning that the stress field rapidly decays with distance from the contact.

#### **2.7.4 Volume averaging**

In order to incorporate the effects of high stress gradients (including the size effect), averaging of the stress and strain data can be conducted over a specified dimension. The methods arose from the study of notch fatigue. Point, line, area or volume methods may be applied depending on the test geometry. The rationale behind the averaging approach is that a high stress and strain state must be sustained over a 'critical' volume, in order to initiate a fatigue crack. This dimension has been suggested to be that of the material grain size or greater. Many researchers have applied this technique to the cylinder-on-flat geometry [77, 85, 86], and although some correlations of the life have been obtained, there is not complete agreement in the literature as to the dimension that should be applied *a priori*. The averaging process can be conducted numerically using FE, by varying the element size [60, 87].

#### **2.7.5 Asymptotic approaches**

Hills and co-workers, e.g. see Ref. [88], have investigated the application of asymptotic approaches to the initiation problem. Bounded asymptotics were formulated by Dini et al. for the rounded punch-on-flat and Hertzian geometries [89]. It is argued that this technique is able to completely capture the crack nucleation process zone, although it is only valid in a small region close to the edge-of-contact. The solution neglects plasticity and wear effects and a dimensionally consistent form has yet to be found for all geometries. The approach is useful in quantifying whether crack nucleation will occur or not, but doesn't predict life in the finite regime. Other mechanical factors such as oxidation and heat effects are neglected.

## 2.8 Fracture mechanics approaches

Significant insight has been gained into the fretting problem from the application of fracture mechanics techniques. Once a crack has initiated and has a length of the order of several grain sizes then, depending on the process zone, the problem reduces to an LEFM analysis. The crack tip stress state, via the SIFs, can completely describe the propagation behaviour. There is added complexity, relative to the plain fatigue case, in that the contact introduces high stress gradients, whereby the crack grows into a reducing stress field (with the possibility of crack arrest). In addition, the stress state will usually be multiaxial. A noteworthy benefit of fracture mechanics modelling is that stress gradient effects are directly addressed. A useful review of the problems to be solved in relation to the application of fracture mechanics to the fretting problem is given in Ref. [66].

Much work has been conducted to predict crack growth behaviour using analytical, semi-analytical and numerical techniques (e.g. the distributed dislocation technique [52], or the finite element method). Analytical solutions exist for the SIFs of many simple geometries. One difficulty encountered is in the specification of the initial flaw size and its orientation. It is often observed that FF cracks are oriented at an oblique angle to the contact, although many methods introduce a perpendicular flaw. Solutions for the SIFs of kinked cracks have been developed e.g. Cotterell and Rice [90], but the discrepancy with perpendicular cracks is often found to be small.

A substantial obstacle with the fracture mechanics approach is the difficulty of experimentally determining crack growth rates under fretting conditions in order to validate the predictions. The DC potential drop method was used in Ref. [91] as a way of estimating crack propagation rates in fretting, although

the calibration of crack length is almost always conducted for the non-fretting case, bringing into question the advantage of the approach.

### **2.8.1 Crack-notch analogues**

The equivalence of the elastic stress state between the punch-on-flat fretting contact and at the tip of a crack was first recognised by Giannakopoulos et al. [92] and applied in Ref. [93]. This significant observation allowed the use of standard LEFM stress intensity factor solutions for the analysis of the complete contact. A schematic of the equivalence is shown in Figure 2.21. A ‘fictitious’ crack is initially orientated horizontally to realise the analogue, and subsequently is allowed to kink using standard solutions. The limited geometries for which the analogue can be formed is a drawback of this approach. Furthermore, the technique is limited to cases where the process zone is small and the complicated variation of the frictional stress state during a fretting cycle also raises questions as to its applicability. This idea was further explored and extended to a crack-like notch analogue by Ciavarella [94], following from the work of Atzori et al. [95].

### **2.8.2 Short crack growth**

It has been commonly observed that small fatigue cracks propagate at a faster rate than long cracks under the same nominal  $\Delta K$ . This can lead to non-conservative fatigue life predictions. Below a certain size, continuum and LEFM principles are not applicable as the crack-tip plastic zone has a considerable influence on propagation behaviour. Crack retardation occurs at grain boundaries, leading to it being postulated that threshold conditions are different for short cracks than for long cracks. The Kitagawa-Takahashi (K-T) diagram [96] is shown in Figure 2.22. It represents the variation of  $\Delta K_{th}$  with (short) crack length, below a threshold value of crack length defined as:

$$a_0 = \frac{1}{\pi} \left( \frac{\Delta K_0}{\sigma_e} \right)^2 \quad (2.25)$$

where  $\Delta K_{th} = \Delta K_0$  for  $a > a_0$  and  $\Delta \sigma_{th} = \sigma_e$  for  $a < a_0$  in a constant stress field, where  $\sigma_e$  is the fatigue limit. In a varying stress field, it is more convenient to express the behaviour below the threshold in terms of the stress intensity factor as follows:

$$\Delta K_{th} = \Delta K_0 \sqrt{\frac{a}{a_0}} \quad (2.26)$$

An alternative approach was pursued by El Haddad et al [97]. An intrinsic crack length was defined,  $a_0$ , as the smallest crack size for which LEFM is applicable. It is often called the El Haddad dimension. The correction acts to increase the crack driving force for small cracks, assuming constant  $\Delta K_{th}$ , and is given by:

$$\Delta K = Q \Delta \sigma^\infty \sqrt{\pi(a + a_0)} \quad (2.27)$$

where  $\Delta \sigma^\infty$  is the far-field stress range and Q a geometrical correction factor. The El Haddad approach implies that the threshold remains constant with crack length. Alternatively, the crack driving force may be regarded as constant, but the threshold is reduced, giving:

$$\Delta K_{th} = \Delta K_0 \sqrt{\frac{a}{a + a_0}} \quad (2.28)$$

This leads to a more gradual transition from short to long crack behaviour than the K-T approach.

## 2.9 Fretting wear

### 2.9.1 General

The occurrence of fretting leads to surface wear. Sliding wear describes the condition of relative motion between two surfaces and is primarily caused by adhesive wear. Abrasive wear describes the wear caused by hard particles, which can also be present in fretting wear, due to the presence of debris. Wear plays an important role in the FF process. The accumulation of wear modifies contact pressure and sub-surface stress state, directly influencing both the crack initiation and nucleation processes.

A common way of experimentally measuring wear is by using profilometry. A stylus is traced across a surface and the resulting displacements recorded. The pin-on-disk arrangement is often used as a simple wear test. A flat disk is rotated and a small cylindrical 'pin' is subjected to a normal load to enforce contact. If the pin and disk are of different materials, then the pin is usually the softer material, enabling rapid replacement. Caution must be exercised when transferring wear data from simple tests for application to more complex components. It is important to ensure that the wear mechanism is the same across both tests and other conditions such as sliding speed and contact stresses are kept constant, for example. Also, as pointed out by Kauzlarich and Williams, the test geometry will be modified during the test, possibly significantly modifying the wear variables [98].

A simple but important quantitative analysis of wear can be conducted by employing the linear Archard equation [99]. The equation is derived from a sliding wear perspective with the assumptions that the real area of contact is proportional to the normal load and that local asperity behaviour is plastic. It is interesting to note that the same relation can also be derived from an

abrasive wear perspective, starting from different initial assumptions. The Archard equation is given as:

$$k = \frac{V}{SP} \quad (2.29)$$

where  $k$  is the dimensional wear coefficient,  $V$  is the total worn volume,  $S$  is the total accumulated sliding distance and  $P$  the applied normal load.

The dimensional wear coefficient (usually measured in  $\text{mm}^3/\text{Nm}$ ) represents the volume of material removed per unit sliding distance per unit normal load and is usually determined empirically. It is of fundamental importance for comparing the wear performance of different materials. There is usually a 'running-in' or 'bedding-in' period during the early stages of a test, followed by a stable region that is described by the Archard equation. It often found that the worn volume is proportional to sliding distance. The assumption that wear rate is proportional to normal load is found to be less well adhered to. The Archard equation assumes that wear rate is independent of the:

- Apparent area of contact,
- Sliding velocity.

For most materials this is seen to be true, although a sharp transition in wear rate occurs for some materials with an increase in sliding velocity [31]. It is sometimes observed that the dimensional wear coefficient can vary during an individual test, sometimes up to three times an order of magnitude. This has been attributed to the changing component geometry [98]. Even if local material behavior is well predicted by the Archard equation, the relation applied to the bulk scale is significantly complicated by the variation of wear across the geometry and subsequent evolving geometry. The bulk pressure

distribution is modified with time, calling into question the use of the original pressure magnitude.

The use of fretting fatigue damage parameters has been investigated in an attempt to capture the effect of wear on fretting fatigue life. Ding et al. [11] recently suggested a modified SWT approach, which introduced the empirical fretting damage parameter  $D_{\text{fret}}$ . The addition of the FFDP to the SWT relation emphasises the importance of frictional work,  $\tau\delta$ , for the crack nucleation process. A similar approach was also pursued in Ref. [100], creating an enhanced Ruiz parameter. The use of the  $D_{\text{fret}}$  parameter will be addressed later in this thesis.

### **2.9.2 Wear modelling**

Whilst the importance of wear for FF was demonstrated in Section 2.9 of this chapter, it is often neglected in analyses. The following is a summary of the work conducted to date that attempts to account for wear in conjunction with FF.

Following from the work of Ref. [101], Madge et al. conducted an FE simulation to model the Hertzian cylinder-on-flat geometry in the presence of wear [51] for a titanium alloy (Ti-6Al-4V). The methodology they offered is summarised as follows:

1. Initial model preparation with application of loads and material properties,
2. FE solution to furnish local nodal contact pressure, traction and slips,
3. Calculation of the critical-plane SWT parameter in conjunction with Miner's rule to determine the FF damage fraction,
4. Algorithms for calculation of the wear (modified Archard's equation),

5. Re-meshing of the model to account for 'worn' nodal geometry,
6. Repeating from Step 2 until failure is deemed to have occurred (Miner's rule).

To ease the computational cost, a cycle jumping technique was used, whereby the wear was assumed to be constant over the number of 'jump' cycles specified. It was found that the methodology was capable of capturing the key effect of slip amplitude on FF life. The gross sliding regime was seen to increase the contact patch, decreasing the contact pressure and fatigue-pertinent stresses, strains and SWT parameter, therefore producing an associated increase in FF life. In contrast, the partial slip regime was found to reduce the contact patch and cause an amplification of contact pressure at the stick-slip interface, thus highlighting the damaging effect of partial slip on FF life that is often observed experimentally.

A further development by Madge et al. [102] incorporated a number of key phenomena that are significant in FF, namely crack nucleation combined with crack propagation in the presence of wear. Mixed-mode fracture mechanics techniques along with the El Haddad correction for short crack growth were accounted for. It was concluded that the reduction in stresses caused by gross sliding could cause self arrest of a nucleated crack, highlighting the potential benefit of wear for the increase of component life.

Explicit FE wear modelling is still in relative infancy and some challenges exist in the future application of the technique. The main drawback is the heavy computational cost of the analyses, requiring significant resources and, with current technology, still requiring solution times in the order of days. Some simplifications, therefore, usually have to be made with respect to the level of mesh refinement for example. Even with the difficulties associated

with wear modelling, it will undoubtedly play an important role in the development of lifing techniques for simplified and complex engineering components.

### **2.9.3 Debris effects**

The fretting wear process removes particles from the contacting bodies that are termed debris. The debris in fretting wear is predominantly made-up of oxides. The generation of debris complicates the understanding of fretting, as the particles can either be released or become trapped under the contact (possibly causing seizure) and directly affect the mechanical response. The theories of third-body layer tribology and velocity accommodation have been applied to study debris. A full understanding of the behaviour of debris is a considerable task though, especially given that the problem is difficult to be amenable to traditional solid mechanics techniques. It is known, for example, that orientation of test geometry affects the rate of debris ejection, as may be expected, but an effect that is usually neglected. Ding et al. attempted to model the presence of debris for the cylinder-on-flat geometry [103], by incorporating a debris layer in an FE simulation, via the specification of the altered (anisotropic) mechanical properties of the layer. A better correlation with the experimental  $F$ - $\delta$  loops was obtained with the inclusion of the debris layer, although the theory is still in development.

## **2.10 The analysis of spline couplings**

Initially, the study of the mechanics of spline couplings was limited to simple analytical methods. Volfson [4] presented a useful analytical work on calculations of stresses in a splined shaft subjected to torsional, bending and axial loads. The analysis was for non-involute, non-helical spline couplings. The importance of considering the different sources of elastic stress concentrations was highlighted and they were listed as:

- Spline root torsional stress concentrations,
- Spline fillet bending stress concentrations,
- Frictional contact stress concentrations.

The following relation was derived by Volfson from analytical considerations:

$$\frac{F_E}{F_I} = \frac{I_E}{I_I} \quad (2.30)$$

where  $F_E$  and  $F_I$  represent the externally and internally splined tooth contact forces at the open end of the coupling respectively and  $I_E$  and  $I_I$  represent the torsional moduli of the two splined bodies. The load transfer between the two shafts reaches a maximum at one axial end of contact position. This is determined by the relative torsional stiffness between the internally and externally splined shafts and leads to the anticipation that when  $I_I > I_E$ , failure will occur at section *A-A* as shown in Figure 2.23. Conversely, failure would be expected to occur at section *B-B* of Figure 2.23 when  $I_E > I_I$ .

The development of numerical techniques allowed the spline geometry to be studied further. The boundary element method was employed in Ref. [104], capturing the experimental trend for the torsional stress distribution. This result is shown in Figure 2.24. Boundary analyses were also conducted in Ref. [105] to determine the contact pressure and slip distribution experienced by the individual teeth. It was suggested that the mis-alignment effects could provide a good correlation with the observed wear trends. For computational reasons, a coarse mesh was used and therefore the results must be interpreted with caution.

## 2.11 Representative specimens for spline couplings

The introduction of this work (Chapter 1) outlined the representative concept for spline couplings that is to be pursued in this thesis. The following sections detail the findings from the various geometries that have been studied to date. Initially the scaled spline is introduced, which is used as the basis for the representative specimen approach.

### 2.11.1 Laboratory-scaled spline coupling

The series of tests that were conducted at the University of Nottingham with the scaled spline coupling are documented in Ref. [7]. The externally-splined component of this is shown in Figure 2.25, with a schematic of the coupling geometry shown in Figure 2.26. The schematic includes the engagement coordinate conventions, which are normalised for commercial reasons. The spline coupling was manufactured from a high-strength CrMoV (CMV) steel, based on BS 3S 132, but subjected to cleaner processing. After final machining, the spline was vacuum gas nitrided to a minimum hardness of 820 HV30. The surface layer created by the gas nitriding process is often termed the white layer. This was approximately 6-7  $\mu\text{m}$  and was not removed. In order to simplify the complex fluctuating loads, the loading is separated into major and minor cycles. The major cycles (LCF) represent the take-off condition that constitutes torque and axial loads. The minor cycles (HCF) replicate the in-flight fluctuations that give rise to rotating bending moments. It is deemed that there are 500 minor cycles (cycled at a frequency of 5 Hz) per major cycle, which is termed one loading block. This simplified experimental loading is shown in Figure 2.27.

A mixture of plain fatigue and fretting fatigue failures were found to occur from the experimental tests. It was concluded that major cycles led to plain fatigue cracking in the spline root of the externally-splined component,

whereas bending moment overloads led to fretting fatigue cracking under the contact of the externally-splined component. The total fretting fatigue life increased with decreasing bending moment. An optical image of the failure zone from a fretting fatigue failure of the externally-splined component is shown in Figure 2.28. It is evident that fretting damage is present on the spline, with the presence of debris clearly observed. The axial position of  $z/a_1 = 0.75$  (as defined in Figure 2.26a) corresponded to the observed location of FF crack initiation for the loading condition. This axial position is therefore deemed a critical position in the study of such couplings.

A full 360°, three-dimensional FE model of the spline was described in Ref. [11], that featured mesh refinement on one tooth pair. This is shown in Figure 2.29, and highlights the applied loadings. The rotating bending moment leads to a critical tooth undergoing the highest loads. This tooth can be chosen as the critical position to evaluate the fretting variables in the representative concept. The SWT parameter was applied and correctly predicted a change in failure mechanism with increasing bending moment; viz. a switch from plain fatigue failure in the spline root, to FF failure under the contact. The life predictions were also in good agreement with experimental observations. The wear methodology (using the FE method neglecting crack propagation) of Section 2.9.2 was also applied to a complex aerospace spline coupling in Refs. [106-108]. Due to the complex behaviour of the aerospace spline coupling, Leen et al. [8] suggested a combined testing and modelling methodology (as described in Chapter 1) for the coupling. Limmer et al. [109] subsequently suggested a methodology akin to that of Leen et al. [8], however it was based on the rounded punch-on-flat geometry and minor cycle bending moment effects were not addressed. The work of Ref. [8] was based on the matching of FE-predicted critical variables of the scaled spline (neglecting wear) with a new representative test specimen as described below.

### 2.11.2 Uniaxial representative specimen

T.R. Hyde [8, 9] developed a uniaxial representative specimen (URS) that was designed to simulate conditions induced by the major cycles (torque and axial load) of the scaled spline and the original test specimen and rig is schematically shown in Figure 2.30. The approach was based on a reasonable representation (at spline location of  $z/a_1 = 0.75$ ) of the following:

- Contact pressure,
- Local contact region fatigue-dominant stress,
- Relative contact slip.

A mixture of plain fatigue failures and fretting cracking under the contacts were produced. A limitation of the results is that the wear behaviour was not studied and a high-strength CMV steel was the only material tested. More detail of the URS will be given in Chapter 3.

### 2.11.3 Multiaxial representative specimen

The multiaxial representative specimen (MRS) was designed and implemented by Wavish [10] at the University of Nottingham and is shown in Figure 2.31. The test set up consists of a fretting specimen in contact with a pair of fretting bridges, whereby a profile is machined onto the bridge feet to imitate the spline tooth form. As with the URS, the MRS was designed to provide a reasonable representation of the key fretting variables (listed above) of the scaled spline at the critical location of crack initiation ( $z/a_1 = 0.75$ ). The key novelty of the test rig is that it is capable of simulating the combined major and minor cycle loading of the spline coupling. The importance of this is highlighted in Ref. [7], where it was shown that the minor cycles, in addition to the major cycles, contribute significantly to the fretting fatigue process. The initial test series of Ref. [10] consistently produced fretting

fatigue failures, and the non-dimensionalised experimental stress-life curve is shown in Figure 2.32. A key development of the present work will be to further enhance the MRS and to develop a lifing methodology.

## **2.12 Summary of chapter**

This chapter has summarised the current knowledge in the field of fretting fatigue. Much progress has been made in understanding the phenomenon since its discovery, although a unified theory has yet to be formed. Several challenges remain to be overcome in the problem, including both the basic scientific understanding and its application to complex components. The representative concept is expected to provide considerable insights into the fretting behaviour of high-performance engineering components. This thesis explores the use of representative specimens for spline couplings and aims to address the issues outlined below.

This review has indicated that a validated methodology for predicting fretting fatigue failure for spline couplings has not yet been developed. The application of FE techniques have shown promise, but are always likely to require experimental data such as COF, wear coefficient etc. as inputs for the analysis. This experimental data must be representative of the spline coupling i.e. correct contact pressure distribution, contact geometry and slip etc. The representative specimen concept is an inexpensive approach that allows for more detailed experimental and computational study of the key phenomena important to the understanding and development of complex spline couplings.

The MRS is capable of simulating the combined major and minor cycles of the spline coupling and will be employed in this thesis. A fretting fatigue lifing methodology will be developed and applied to this geometry that has not

previously been conducted. The lifing methodology will also be applied to the URS, which can also be used as a 'look and see' method to assess candidate spline materials. More generally, the approaches undertaken in this thesis aim to advance the validation of methods that assess: spline designs, loading conditions and surface treatments etc, without expensive rig testing or even scaled spline testing. Finally, it is expected that simplified representative testing will be required in order to validate numerical prediction techniques.

## 2.13 Figures

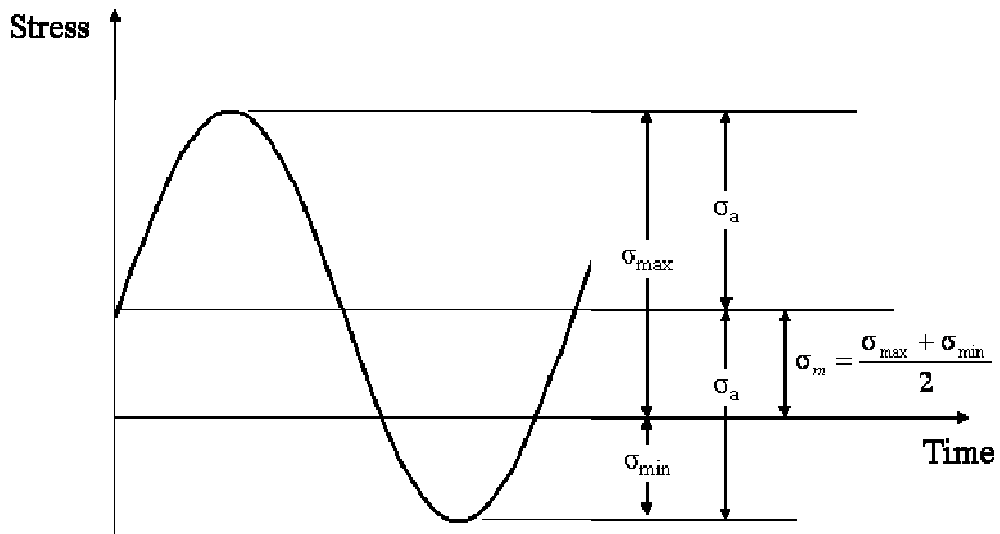


Figure 2.1. The cyclic loading definitions with a non-zero mean stress.

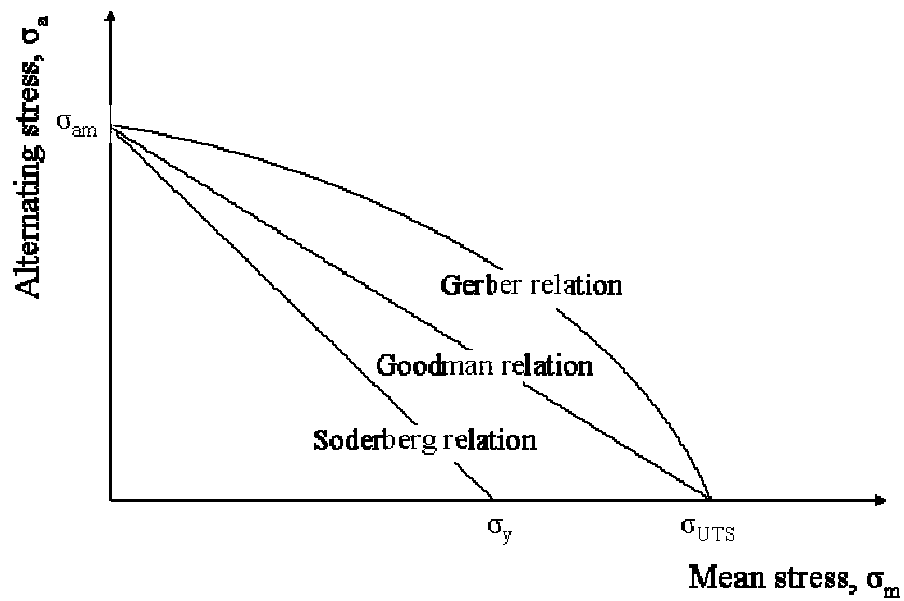


Figure 2.2. Constant life diagram showing the empirical relations quantifying the effect of a mean stress.

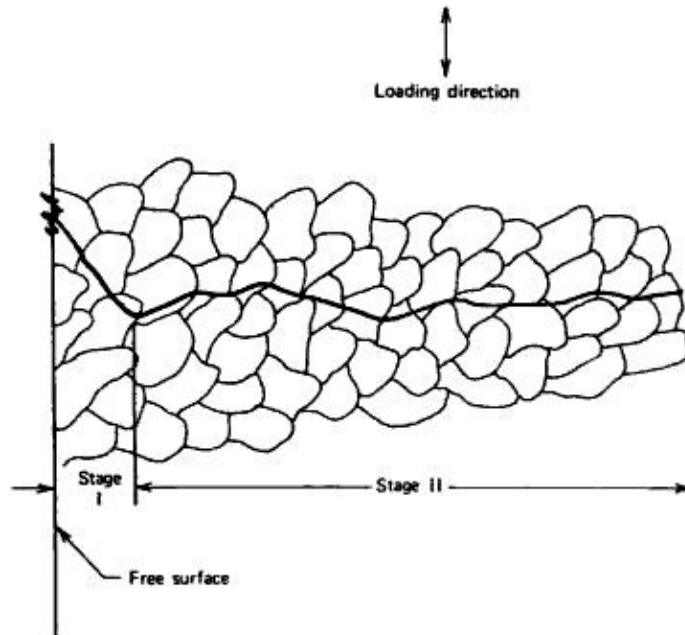


Figure 2.3. Schematic of the stages of fatigue crack growth for a polycrystalline metal [26].

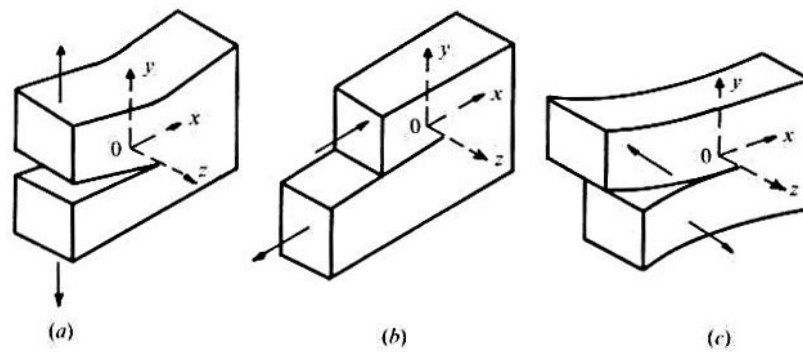


Figure 2.4. The fracture mechanics modes for a) mode I; b) mode II and c) mode III [12].

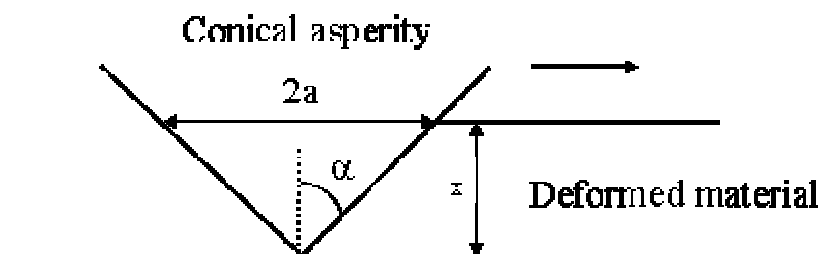


Figure 2.5. The model for the deformation component of friction, reproduced from [31].

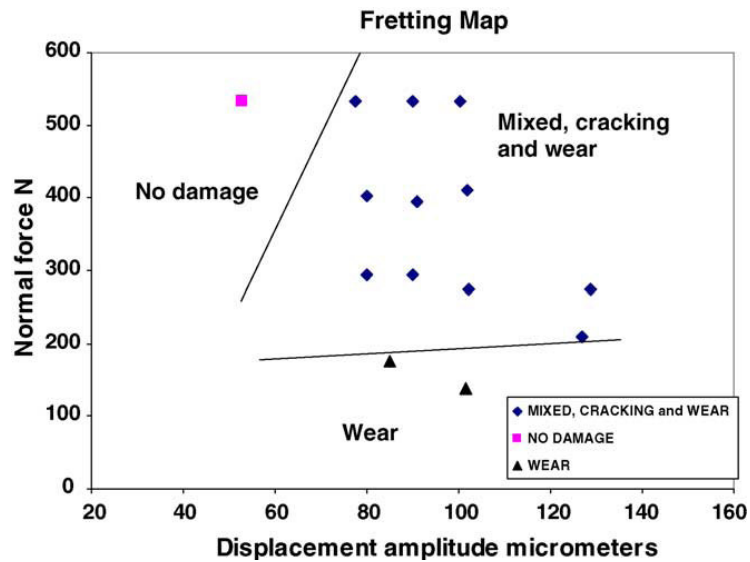


Figure 2.6. A material response fretting map for an aluminium alloy [39].

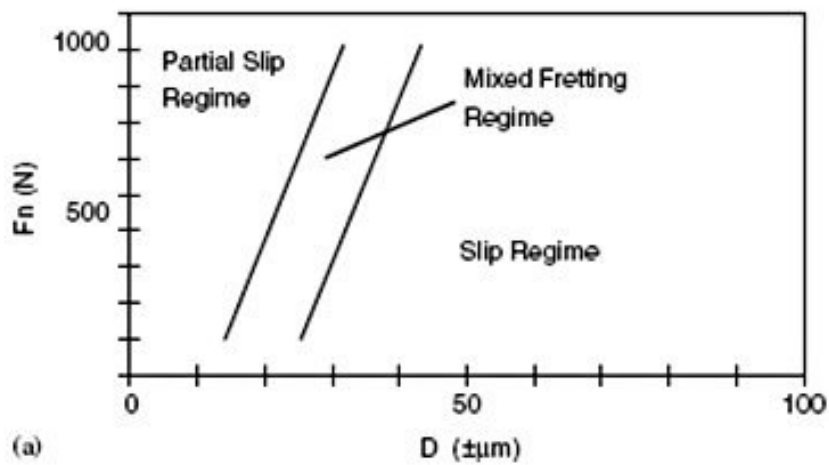


Figure 2.7. A running condition fretting map [38].

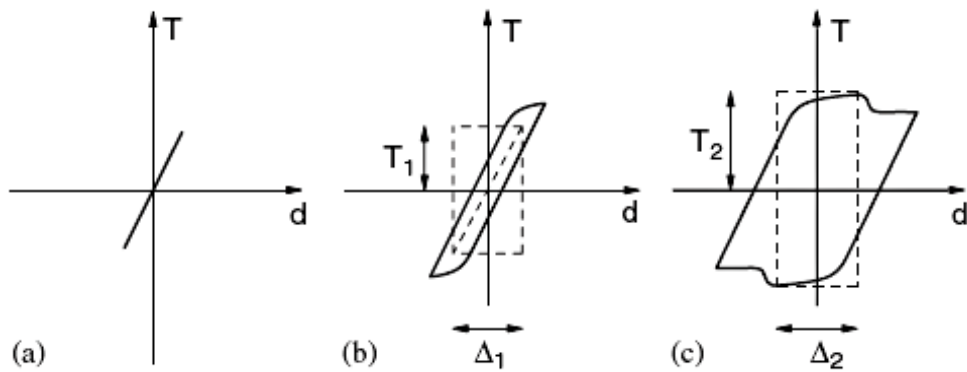


Figure 2.8. The characteristic shape of the fretting  $F$ - $\delta$  loops for a) stick b) partial slip c) gross sliding [38].

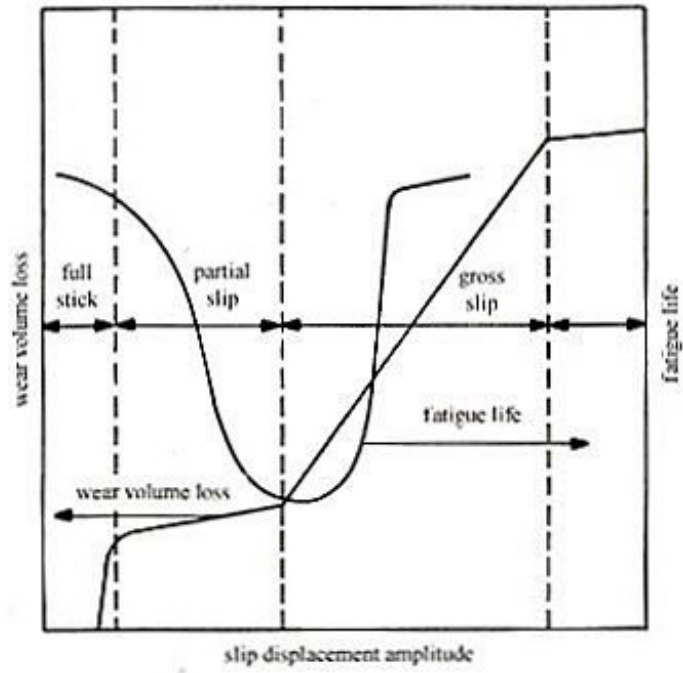


Figure 2.9. The effect of slip amplitude on fretting fatigue life and wear rate [37].

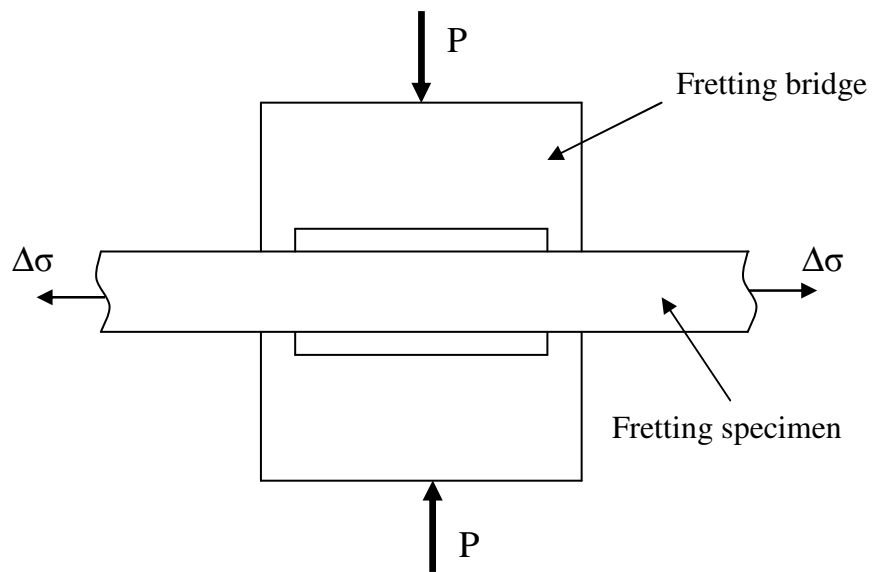


Figure 2.10. A schematic of a typical bridge-type experimental setup.

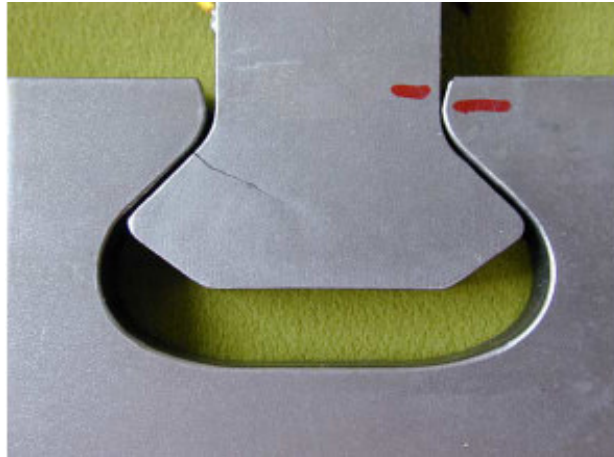


Figure 2.11. The dovetail-root connection fretting failure [110].

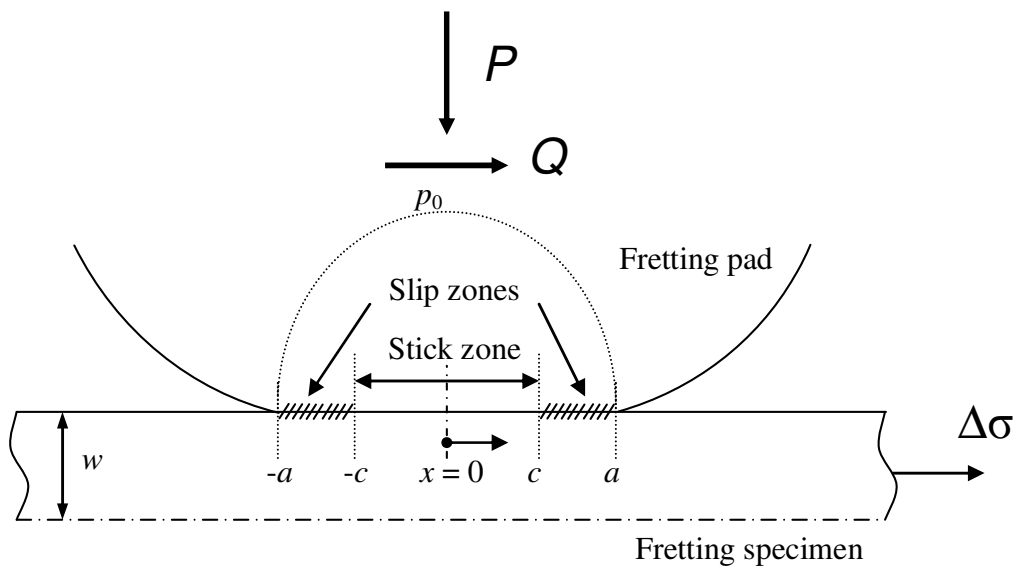


Figure 2.12. Schematic of the cylinder-on-flat arrangement.

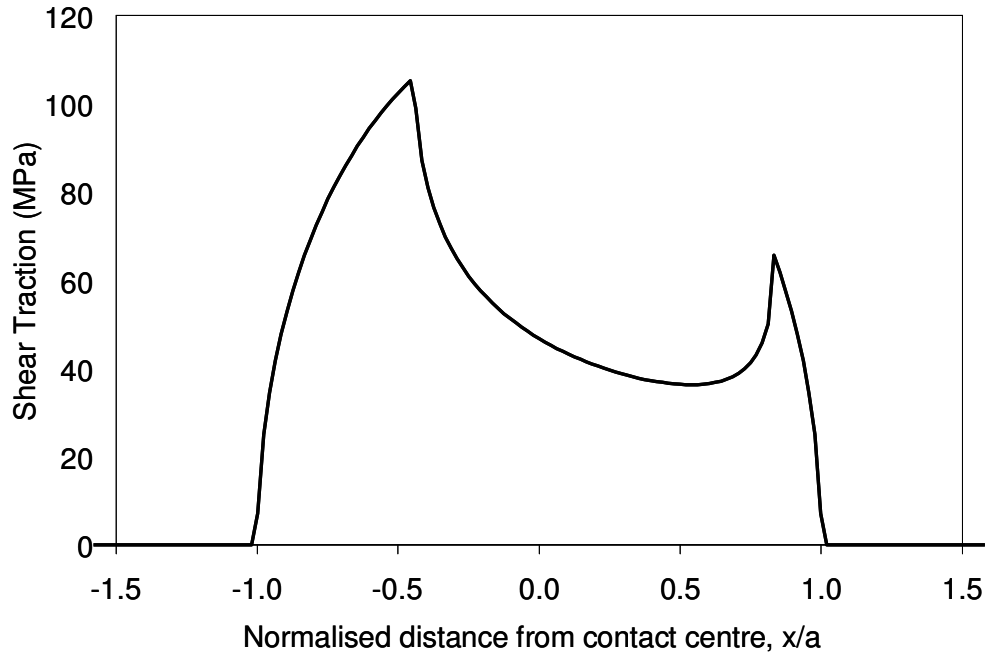


Figure 2.13. The shear traction distribution for the Hertzian cylinder-on-flat geometry, with a bulk stress applied.

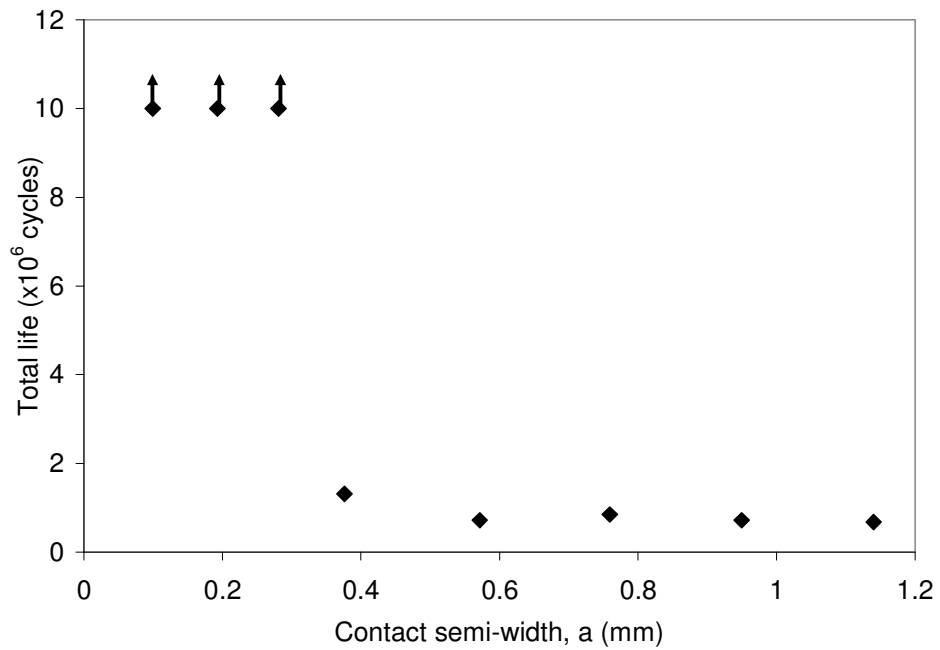


Figure 2.14. The contact size effect on total life for a Hertzian contact for the Al-Cu4 alloy [77].

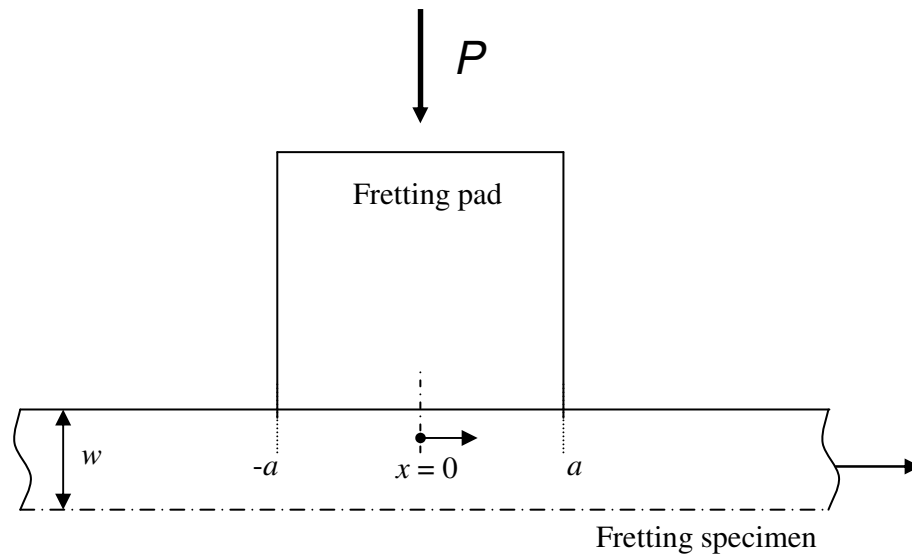


Figure 2.15. Schematic of the punch-on-flat arrangement.

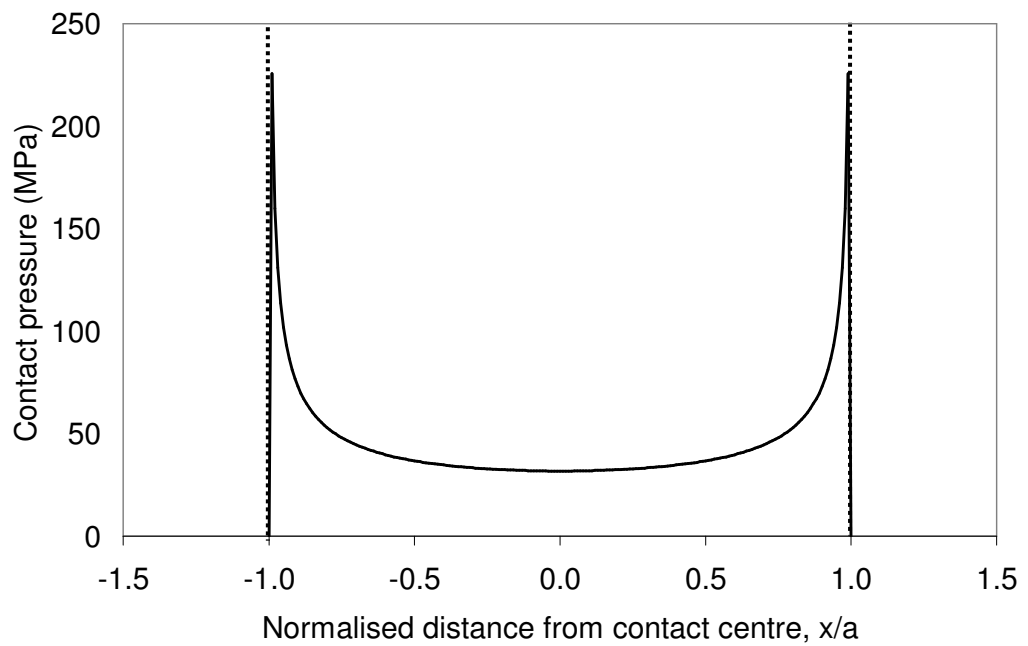


Figure 2.16. Contact pressure distribution for the punch-on-flat geometry.

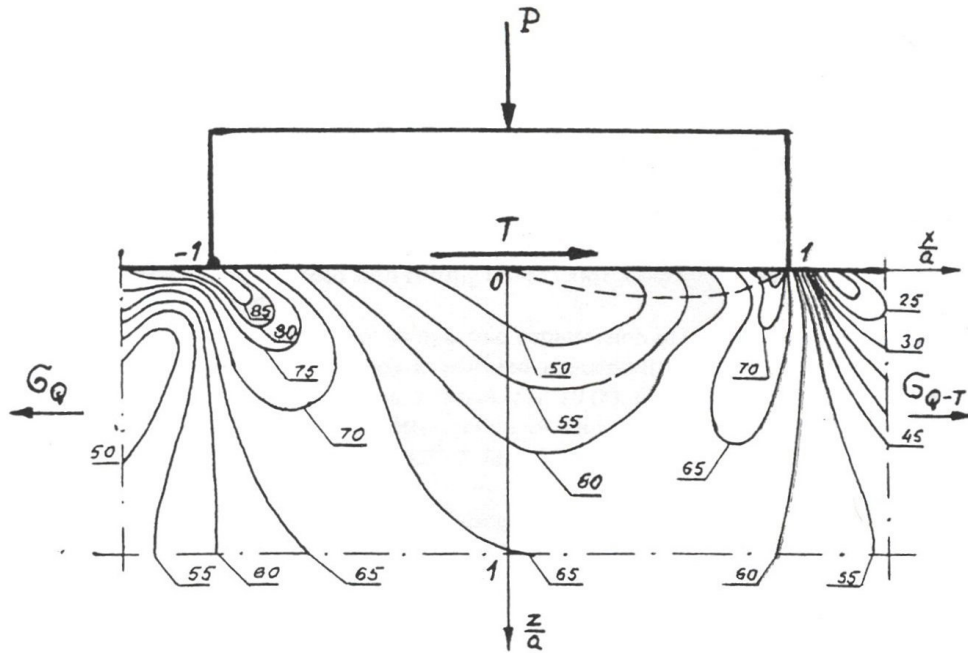


Figure 2.17. Contours of constant strain energy under the fretting pad [56], assuming an initial parabolic normal stress distribution.

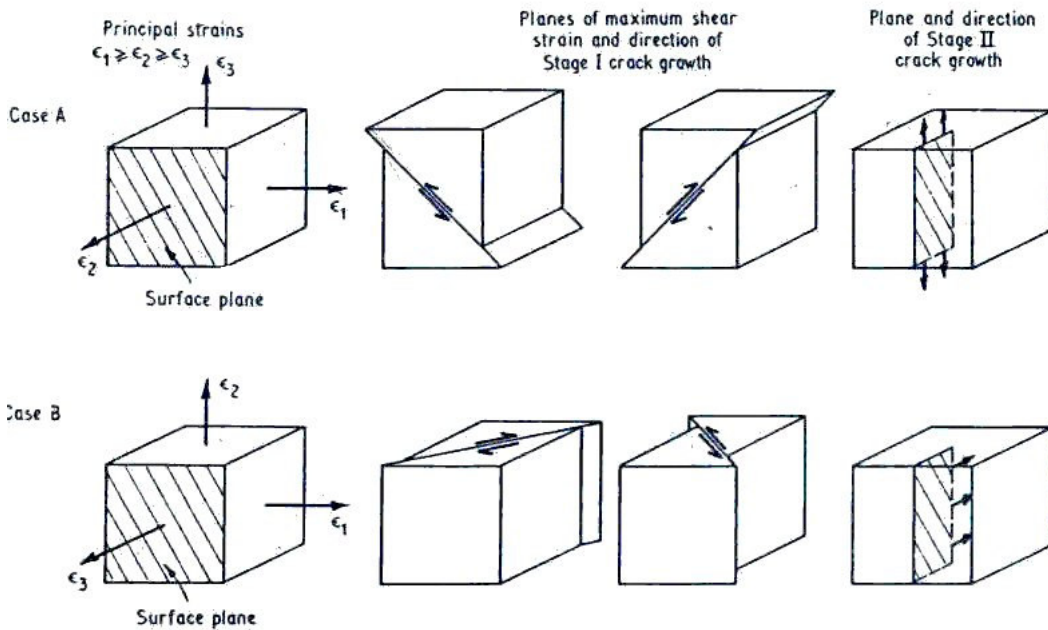


Figure 2.18. The two-types of loading and crack growth as suggested by Brown and Miller [19].

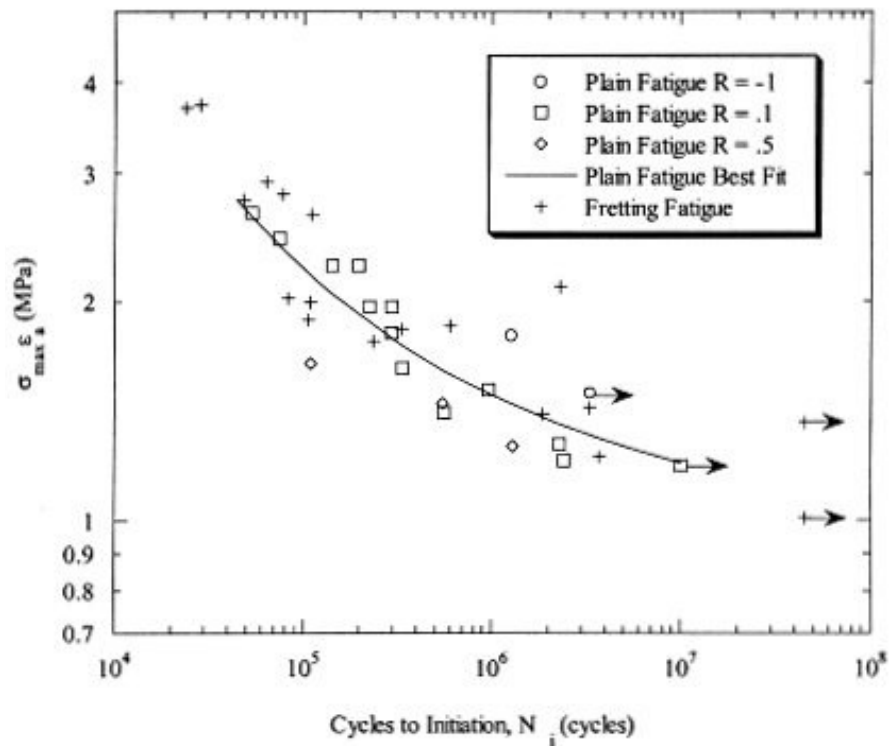


Figure 2.19. The SWT parameter against number of cycles to initiation [67].

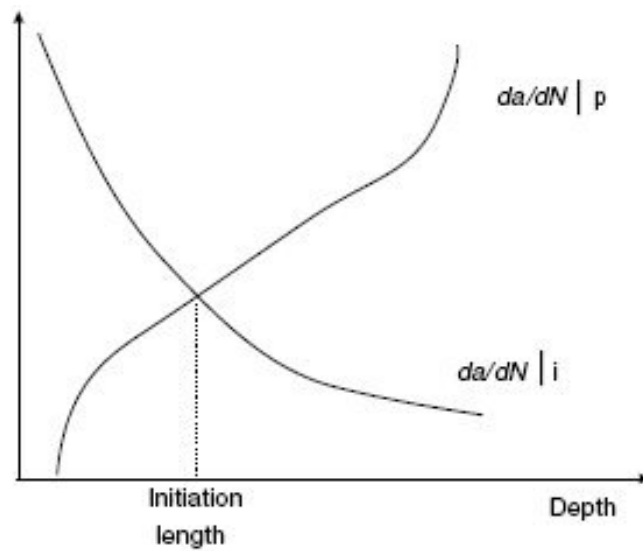


Figure 2.20. The intersection of the initiation and propagation regimes in order to determine the initiation length [82].

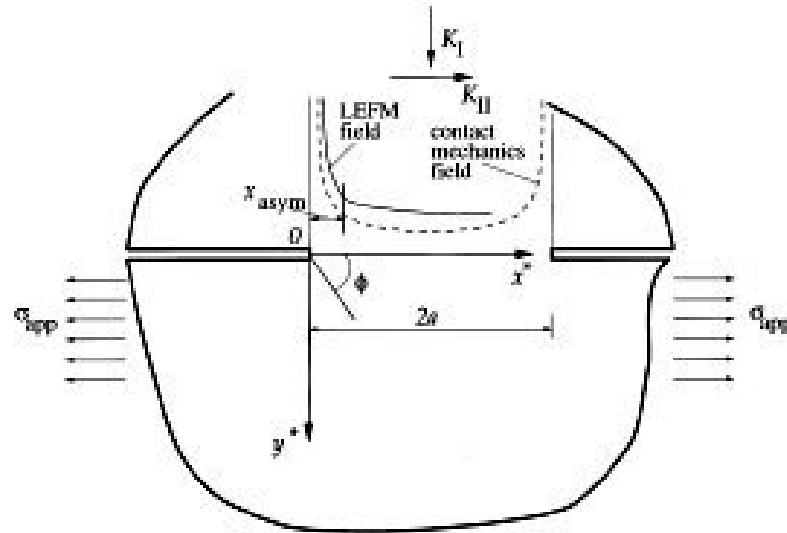


Figure 2.21. The crack analogue concept for fretting fatigue [92].

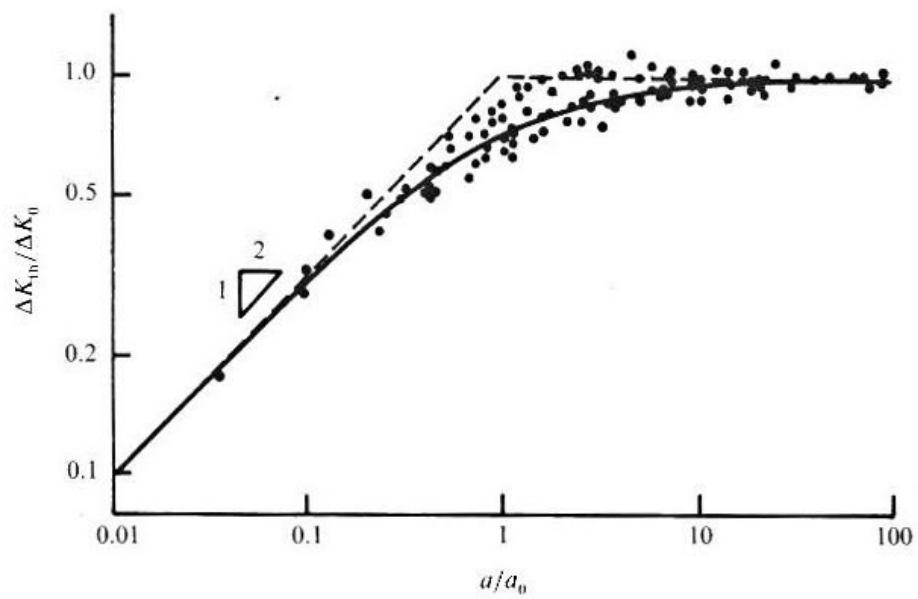


Figure 2.22. The Kitagawa-Takahashi diagram for the short crack threshold [96].

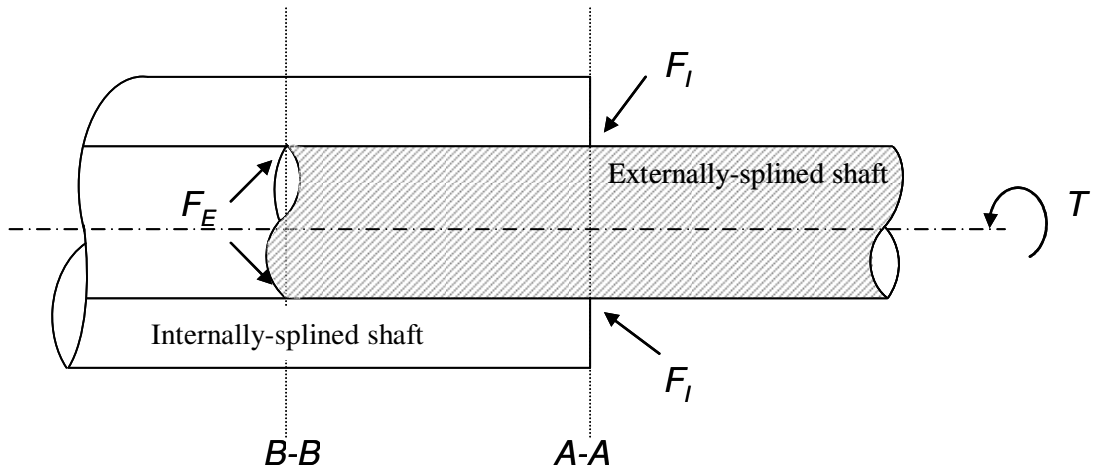


Figure 2.23. An axial schematic of a spline coupling, showing tooth contact force locations, adapted from [7].

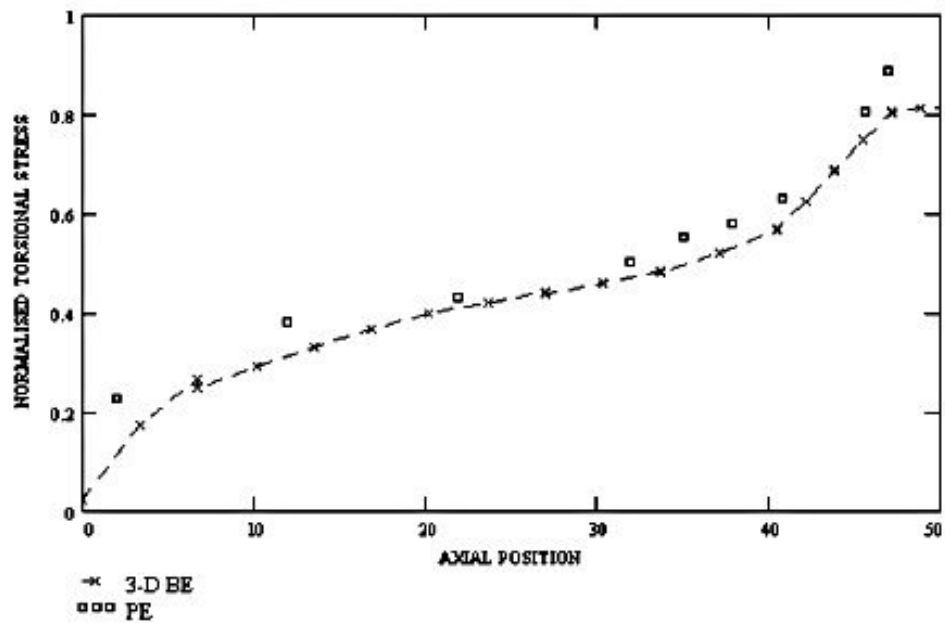


Figure 2.24. A comparison of the normalised torsional stress distribution from a boundary element (BE) simulation and photoelastic (PE) experimental measurements [104].



Figure 2.25. The externally-splined laboratory-scaled coupling.

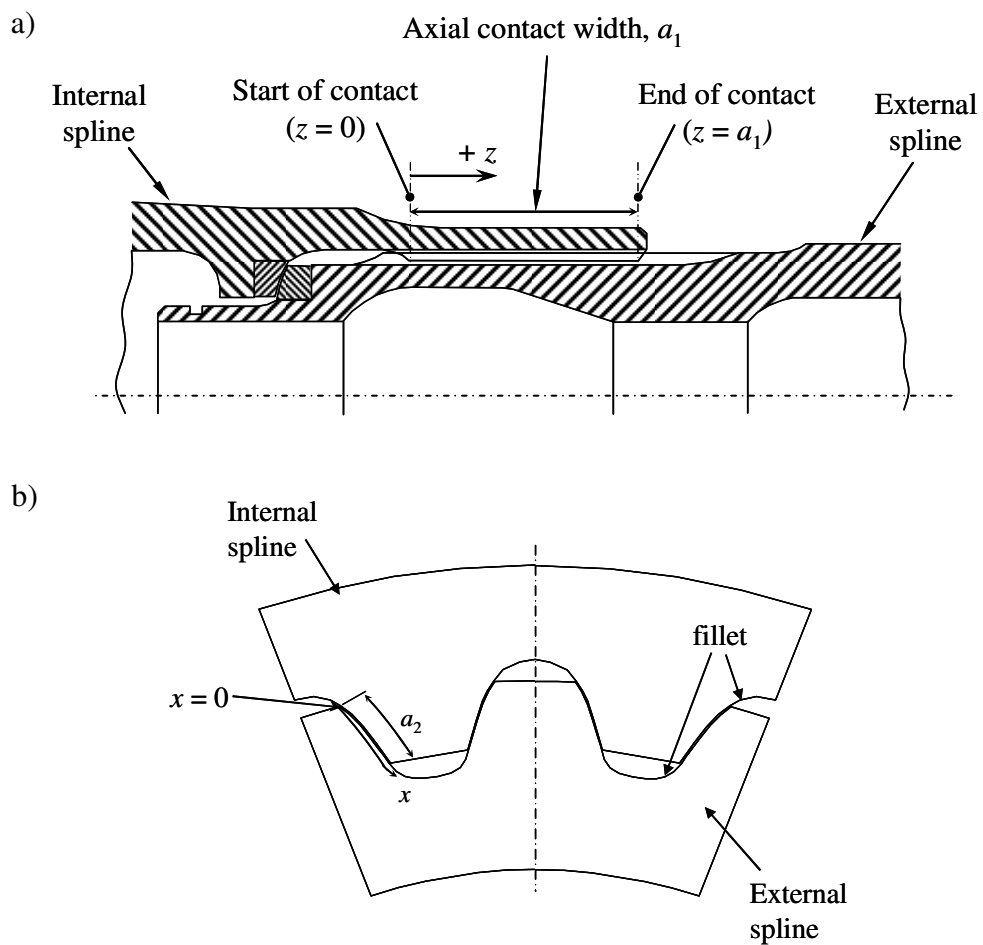


Figure 2.26. a) Axial and b) transverse sections of the spline, with the coordinate system definition for the externally-spline component [111].

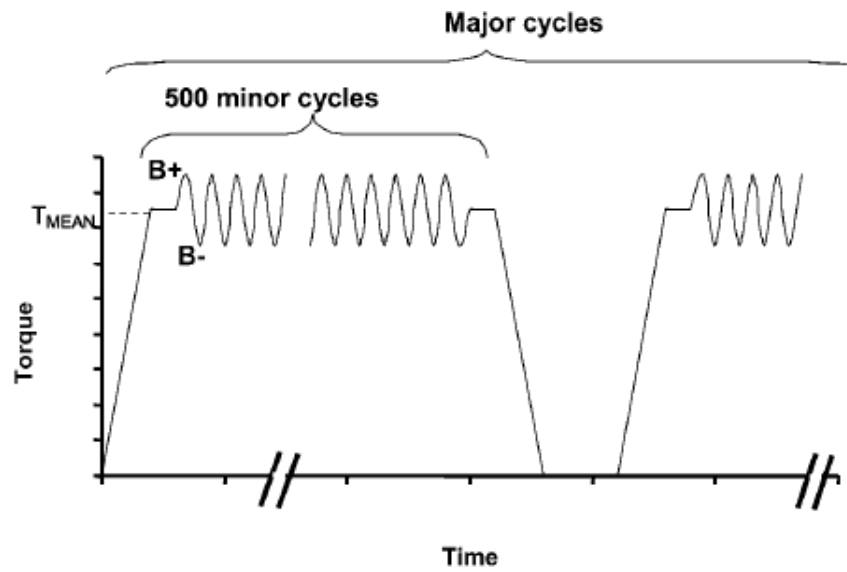


Figure 2.27. The loading of the laboratory-scaled spline, where one major cycle with the superimposed minor cycles represents one loading block.

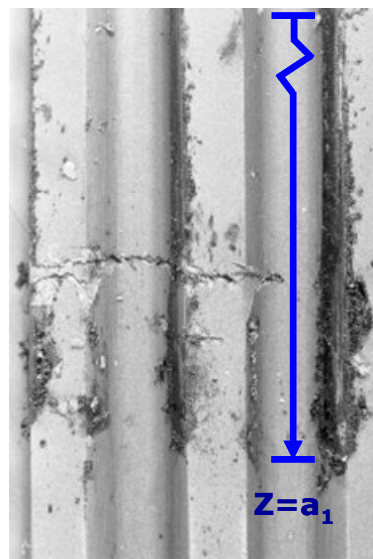


Figure 2.28. The fretting damage from a scaled spline test, showing the location of cracking on the externally-splined component [7].

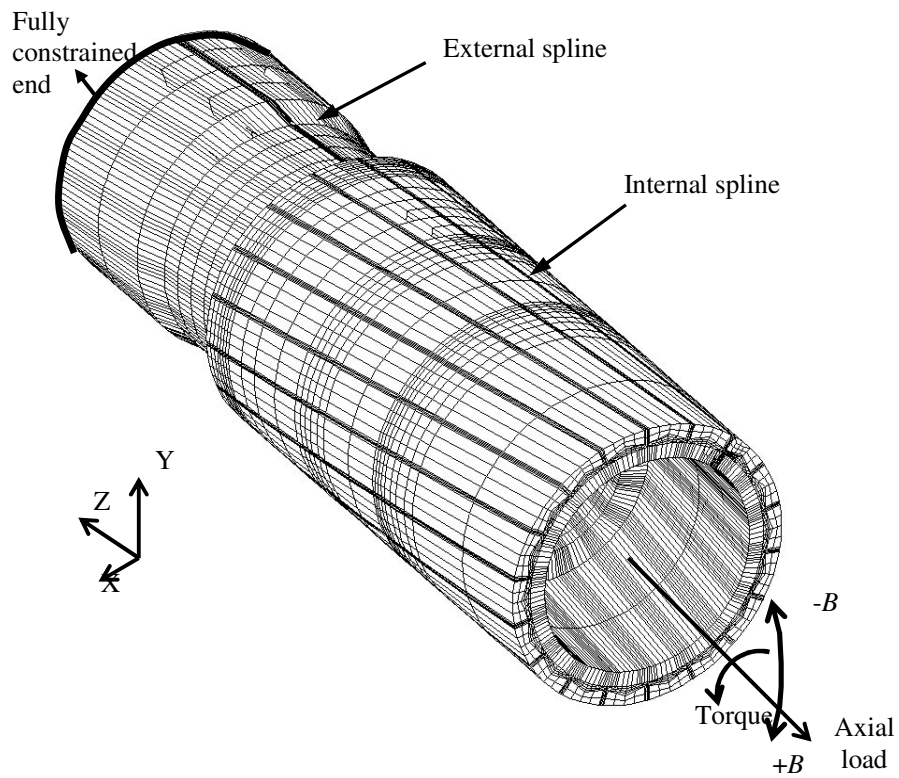


Figure 2.29. FE model of the spline coupling showing the constraints on the external spline and the combined torque, axial and bending moment loads applied to the internal spline [11].

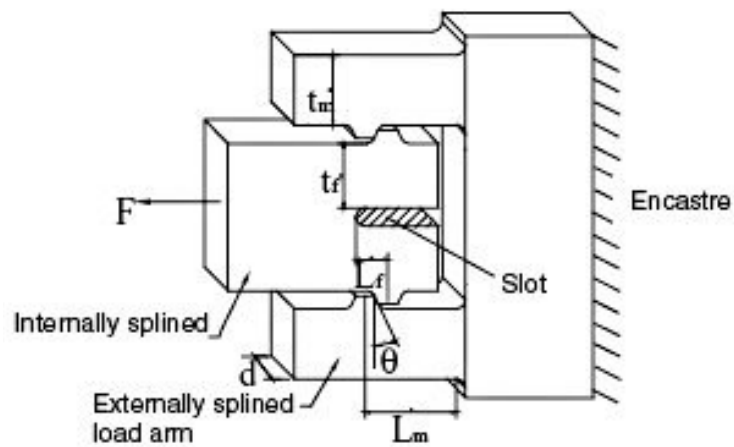


Figure 2.30. Schematic of the uniaxial representative specimen [43].

a)



b)

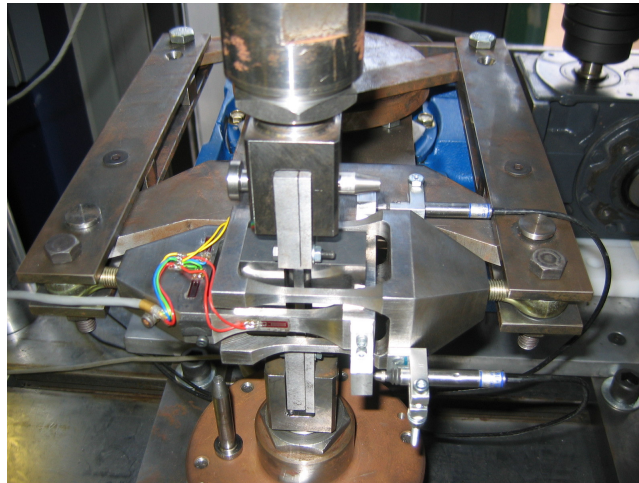


Figure 2.31 (a) The multi-axial representative specimen test assembly in-situ and (b) close-up of complete test assembly. Designed and implemented in Ref. [10].

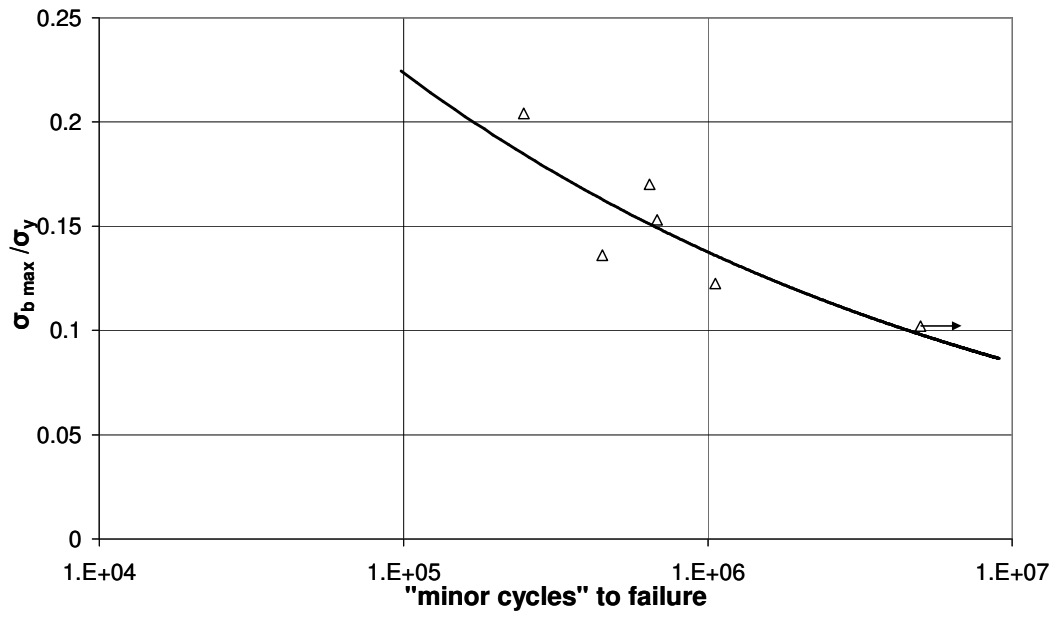


Figure 2.32. The experimental minor cycle stress-life curve of the multiaxial representative specimen [10].

# Methodology

## 3.1 Introduction

The importance of increased understanding of the fretting fatigue behaviour of spline couplings was highlighted in the previous chapters. This chapter outlines the methodology pursued in this thesis in order to meet this aim. The combined experimental and computational approach is introduced, and the experimental procedures given. A redesigned version of the uniaxial representative specimen (URS), originally developed by Hyde [9], is described below. The rig mimics the major cycle contact pressure (from torque and axial load), pertinent fatigue stress and contact slip experienced by a typical low pressure (LP) spline coupling. The multiaxial representative specimen (MRS), which also includes the effect of spline rotating bending loading, is then described and the modifications detailed.

The numerical methodology utilises the finite element (FE) method for the simulation of the two representative specimens. A global FE model is developed for the analysis of both the URS and MRS, which include the significant rig components. The representative nature of the specimens is subsequently examined via comparison with previous scaled spline FE modelling.

## 3.2 Representative specimen methodology

Figure 3.1 shows the methodology developed in the present thesis for the representative specimen (RS) concept. It is a combined experimental and computational approach. The FE modelling of the scaled spline coupling is

the first step in the procedure. This was conducted at the University of Nottingham in parallel with the current work and the results from this were discussed in Chapter 2. The key fretting variables output from the model (label 1 of Figure 3.1) are then used as the basis for the design of a new RS, as indicated in number 2 of the same figure. This was conducted in the original works of Refs. [9, 10], but will be demonstrated below for the contact pressure of the newly developed FE models. Given the primary fretting fatigue variables, the approach is based on a reasonable representation of the following:

1. Spline contact pressure,
2. Spline local contact region fatigue-dominant stress,
3. Spline relative slip.

These parameters govern the fatigue behaviour and failure mechanisms of the component. The contact pressure is predominantly controlled by the spline torque and axial load, the fatigue-dominant stress is influenced by the spline or shaft bending moment and the relative slip is primarily bending induced. The fatigue-dominant stress is taken to be the axial stress, owing to the observation from the scaled spline testing that the main fretting fatigue crack propagated transverse to the shaft axis [7]. Matching of the full-field stress field, whilst beneficial for replication of scaled spline behaviour, would introduce considerable complexity to the approach. Additionally, recent work by Dini and Hills [88] aims to quantify the crack nucleation process zone with the use of bounded asymptotics. The approach completely captures the local stress state and could be used to further enhance the replication of the local behaviour of the representative prototype to the actual component. The technique is still in development and therefore will not be applied here.

The representative test specimens are capable of replicating the fretting conditions experienced by the LP coupling (which in turn replicates the full-scale engine spline) for arbitrary locations along the axial direction,  $z$ , of the coupling. As discussed in Chapter 2, experimental studies of the scaled spline geometry indicated that the axial position of  $z/a_1 = 0.75$  on the externally-splined component was the critical failure location [7], where the coordinate convention is given in Figure 3.2. This thesis will therefore utilise the representative specimens that mimic the spline behaviour at this location, as in the original studies using the URS [9] and the MRS [10]. Attention was focused on the matching of the variables at the critical location for a load condition of design torque and axial load, and 3x design bending moment, where  $T_n$ ,  $F_n$  and  $B_n$  are non-dimensionalised loads (for commercial reasons) defined as follows:

$$T_n = \frac{T}{T_{yp}^m} \quad (3.1)$$

$$F_n = \frac{F}{F_{yp}^m} \quad (3.2)$$

$$B_n = \frac{B}{B_{yp}^m} \quad (3.3)$$

with the design values of  $T_n$ ,  $F_n$  and  $B_n$  for the scale coupling equal to 0.818, 0.032 and 0.039, respectively.  $T_{yp}^m$ ,  $F_{yp}^m$ ,  $B_{yp}^m$  are the maximum elastic torque, axial load and bending capacities for a shaft with outer diameter equal to the minor diameter of the externally-splined shaft and inner diameter equal to  $0.52 \times$  pitch circle diameter (PCD) of the externally-splined shaft, respectively. The calculations of  $T_{yp}^m$ ,  $F_{yp}^m$ ,  $B_{yp}^m$  are based on the yield stress (0.1% proof stress) of the spline material,  $\sigma_y$ .

The required force applied to the representative specimens in order to replicate the spline major cycle load may be calculated via static equilibrium considerations at the contact interface using the following equations:

$$F_{sp} = x_l \sum_{j=1}^{n-1} \frac{(p_j + p_{j+1})}{2} \quad (3.4)$$

$$F_i = 2b\alpha(\cos\theta + \mu \sin\theta)F_{sp} \quad (3.5)$$

where  $F_{sp}$  is the total force along the tooth-flank contact width, per unit thickness of slice for a given axial position in the spline coupling FE model, calculated by integration of the FE-predicted contact pressures over the contact width.  $F_i$  is the corresponding force on the fretting pads required to give the same contact pressure distribution,  $b$  is the width of the fretting contact,  $x_l$  is the length of the contact elements and  $p_j$  is the contact pressure at node  $j$  along the contact.  $\theta$  is the tooth flank angle relative to the vertical. The parameter  $\alpha$  ( $0 < \alpha < 1$ ) compensates for slight variation in contact pressure across the width of contact. This is due to the reduction of contact pressure at the edges of contact when both contacting bodies have coincident sharp edges, as caused by plastic deformation [70].

The next stage in the concept of Figure 3.1 is the application of a lifing methodology (labelled as process 3 in the figure). This can be applied to the scaled spline and the representative specimens. A lifing methodology should be able to predict fatigue and fretting failure failures, as were found to occur from the scaled spline testing. The lifing methodology adopted for the URS and MRS in the present thesis will be presented in Chapter 6, along with the resulting findings. An indicator of the success of the lifing approach is the comparison of the life predictions across the different geometries.

The complementary experimental approach facilitates the further investigation of spline behaviour by comparison with the RS test results; namely the number of cycles to failure, the failure mechanisms and failure locations. The objective is to obtain consistent test results between the geometries to provide validation. If there is a discrepancy, then the original computational design concept should be reviewed. The experimental results from the URS and MRS are given in Chapter 4.

The comparison of the computational and the experimental branches is the key indicator of the RS methodology (labelled 4 in Figure 3.1). When they are in agreement, the representative specimen approach is said to be fully validated (labelled 5 in Figure 3.1) and allows the efficient evaluation of spline behaviour with the use of a simplified specimen. This would also implicitly validate the lifing methodology, meaning that the number of experimental tests could be significantly reduced, although small-scale representative tests are still likely to be required in order to obtain relevant material parameters.

The present study will utilise the redesigned URS to produce additional fretting test results under spline major cycle loading. In the original study of Hyde et al. [43], the alloy steel Super CMV was solely considered. This work will investigate the comparative behaviour of a range of candidate spline materials that are listed as:

- High strength CMV steel,
- Ti-6Al-4V (Ti-6/4),
- Ti-6Al-4V with a surface coating of Balinit C Star (Ti-6/4c),
- AerMet 100,
- Inconel 718 (Inco).

The MRS will be employed to further investigate the multiaxial fretting fatigue behaviour of S/CMV (the current spline material of choice for triple-spool gas turbine aeroengines) under combined major and minor cycle loading.

### 3.3 Material data

The mechanical properties of a material are known to influence the fretting fatigue behaviour. Therefore, with a range of materials to be investigated using the URS and the behaviour of S/CMV to be investigated using the MRS, this section gives the relevant material properties. The elemental compositions of the ferrous and nickel materials are shown in Table 3.1, and the room temperature mechanical material properties are tabulated in Table 3.2 (from Refs. [111-113]). All of the materials were tested in their final heat treated (HT) form. A pre-heat treatment allowance to account for the decarburisation of the CMV and AerMet specimens was specified prior to final grinding.

The HT process conducted for the CMV steel samples was as follows in order to produce a Vickers hardness of 460-490 HV30:

- 45 minutes in a pre-heated furnace at 940 °C and oil quenched,
- Within 2 hours of oil quench, temper for 2 hours 15 minutes at 570°C,
- Air cool.

For the AerMet samples, the HT process to give the desired properties is given as:

- Anneal: 670°C / 5 hrs followed by air cool,
- Harden: 895°C / 1 hr,

- Quench to 66°C in 2 hrs,
- Cold Treatment: -73°C within 1 hr of attaining room temperature following harden and quench,
- Followed by air warm,
- Age: 482°C / 5 hrs followed by air cool.

The titanium was used in its final plate form (BS TA59:1980). The HT process of the Inconel samples can be found by consulting the Special Metals [112] datasheet (publication number SMC-045). The Balinit C-Star coating from Oerlikon Balzers is a metal containing (CrN) carbon coating (tungsten diamond-like carbon).

Gas nitriding is a surface modification technique that results in an increased hardness due to the infusion of nitrogen particles. This aims to reduce fretting fatigue damage and prolong total life. For one test series, the fatigue specimens of the MRS were gas nitrided (the fretting bridges were unmodified) with the specification summarised as:

- Temperature of  $525 \pm 10^\circ\text{C}$ ,
- 4:1 parts nitrogen to hydrogen,
- 72 hour cycle,
- Resulting with a hardening up to 0.5 mm depth.

### **3.4 URS experimental test rig**

The uniaxial representative specimen test arrangement consists of four fretting specimens (two sets of tooth contacts) and is shown in Figure 3.3. The fretting inserts are removable and are bolted to the test rig, and are shown schematically in Figure 3.4. A number were manufactured from different materials in order to facilitate the testing of various material combinations,

and they have two contact faces, enabling two tests per specimen. Figure 3.5 shows a schematic of the rig and gives the numbering convention that was used to identify the specimens, the local contact coordinate conventions and the contact dimensions  $b_2$  and  $a_2$ . The transverse dimension,  $a_2$ , refers to the outer specimen in the figure, beginning at the tooth tip and extending into the tooth root. The axial contact dimension,  $b_2$ , represents an axial slice of the spline. The outer specimens are intended to mimic conditions of the externally-spline component. The contact geometry was designed to nominally match that of the spline e.g. the surface roughness of the contacts of the two geometries were designed to match ( $R_a \sim 15 \mu\text{m}$ ), although a flat surface profile was used along the  $x$ -direction, in comparison to the involute geometry of the spline coupling [7] and previous testing of the URS [9]. However it has been shown, for example in Ref. [10], that the difference between the contact pressure state of the two profiles is small for the typical load conditions encountered here. More detail of the manufacturing process and implementation may be found by consulting Ref. [9].

Some design changes were implemented from the original design, of Ref. [9], most notably, the addition of two adjustable screws to aid symmetrical alignment of the two contact pairs (as seen in Figure 3.3 and Figure 3.5). The rig alignment was also ensured using slip gauges, which are accurately machined blocks that are dimensioned to engineering standards. The rig is designed to fit into a standard Instron uniaxial servo-hydraulic test machine ( $\pm 50 \text{ kN}$ ). A sinusoidal load waveform was applied by a Rubicon control system (Denison Mayes Group) and all tests were conducted with a nominal stress ratio ( $R_\sigma$ ) of 0.1 at a cyclic frequency of 5 Hz. The load was calibrated via a proving ring under a compressive load. The calibration curve can be seen in Figure 3.6, giving an output of 10 V at full-scale load. For the experimental tests, the applied tensile load deflects the load-arms, creating

relative slip between the contacts that therefore leads to the possibility of cyclic fretting damage.

The applied load may be determined according to the methodology given in Section 3.2, giving a peak value of  $F_i = 10.9 F_0^{nom}$  as representative of scaled spline major cycle loading, with:

$$F_0^{nom} = p_0 a_2 \quad (3.6)$$

where  $F_0^{nom}$  is a nominal spline contact force for a unit width and  $p_0$  is the mean contact pressure for normalisation. The calculation of  $p_0$  is realised by assuming that the applied torque per tooth ( $T$ ) has its centre of action at the PCD, and dividing the associated force value by the nominal tooth contact area:

$$p_0 = \frac{T \cos \beta_p}{N r_p a_1 a_2} \quad (3.7)$$

where  $N$  is the number of spline teeth,  $r_p$  is the pitch circle radius,  $a_1/\cos \beta_p$  is the helical (nominal) contact length and  $a_2$  is the tooth flank (nominal) contact width.

### 3.4.1 Ranking material fretting performance

With the aim of assessing the fretting performance of the various materials, the following is to be considered:

- Wear scar appearance - optical and scanning electron microscopy (SEM),
- Energy dispersive X-Ray (EDX) analysis to determine element compositions of the scar and level of oxidation,

- Surface profilometry of the wear scar,
- The slip amplitude and coefficient of friction (COF).

### 3.5 Experimental methods for the URS

#### 3.5.1 Data acquisition

Two linear variable differential transformers (LVDTs) were attached to the test rig in order to measure relative displacements during the test and their location is indicated in Figure 3.5. The figure also indicates the terminology used for the two arms and LVDTs; namely the inner and outer. The relative displacement data aids the characterisation of the COF and contact slip. The LVDTs were calibrated using a custom micrometer jig in order to give a 10 V output at a full-scale of 500  $\mu\text{m}$ . A data acquisition (DAQ) system was used to record the data and a LabVIEW program was created in order to acquire and process the data. The load and LVDT signals were processed by a National Instruments SCC signal conditioning interface, via SCC-FT01 feed-through analogue input modules. The analogue signals were digitised via a National Instruments E-series board.

#### 3.5.2 Profilometry

Surface profilometry is an important technique for the quantification of fretting wear. Wear scars were measured using a Mitutoyo SurfTest SV-600 along with the Surfpak-SV (v1.002) software. The accuracy of the profilometry is limited by the dimensions of the stylus tip and the sampling rate. A resolution of 0.05  $\mu\text{m}$  was obtained using a stylus diameter of 1.2 mm, with a 90° cone tip and a radius of 5  $\mu\text{m}$ .

Surface profiles were obtained for each tested specimen of the experimental tests. A trace was taken midway across the width of the face ( $z/b_2 = 0.5$  position, Figure 3.5), beginning at the tooth root, and extending beyond the

tooth tip ( $x/a_2 = 0$ ). The surface was profiled before the test to obtain the un-worn profile and after testing to obtain the worn profile. No attempt was made to remove compacted debris created by the fretting.

The data analysis was automated via a Microsoft Excel Visual Basic for Applications (VBA) macro, which was created in conjunction with Daniel Sullivan. The data of the un-worn and worn profiles were read in and aligned. Any difference in spatial position of the profiles was corrected for, in order to produce an overlay. The worn profile could be transformed via a translation (2 degrees of freedom) and a rotation (about a specified point). The beginning and end of contact was then specified from visual inspection of the data. To calculate the volume per unit face width of material removed (or added), an incremental distance was firstly determined by dividing the length of contact by the number of acquired data points,  $n$ . The volume change per unit face width was then computed for each increment, and the total summed. A positive value represents material loss from the specimen (i.e. wear), and a negative value represents material gain (i.e., net material transfer from the mating specimen). The sensitivity of the volume calculation was investigated and it was estimated that the error induced from the misalignment of the profiles was less than 5 %. For dissimilar material combinations, the calculated volume / unit width was averaged for the two specimens of the same material. For similar material combinations, the results from all four specimens were averaged. The average wear depths were calculated using the lengths of the worn profiles from the individual tests, identified within the Excel dataset and conducted as:

$$d_{av} = \frac{\sum_{i=1}^n d_i}{n} \quad (3.8)$$

where  $d_i$  are sampled wear depths and  $n$  is the number of samples.

### 3.6 MRS experimental test rig

The multiaxial representative specimen is a bridge-type fretting fatigue test arrangement which consists of a fatigue specimen and two fretting bridges, and is shown schematically in Figure 3.7. The transverse contact coordinate system ( $x$ ) begins at the tip of the fatigue specimen, and the axial convention ( $z$ ) begins at the outer edge of contact and has a dimension of  $b_1$ . This geometry represents an axial slice of the spline. In this experimental arrangement the applied loads are commonly referred to as either in-plane (IP) or out-of-plane (OP). For the MRS, the load that represents the spline major cycles will be termed the IP load and is denoted  $F_i$ , whilst the OP load replicates the spline minor cycles and is denoted  $F_o$ . With an applied bending moment, the scaled spline response is no longer cyclically symmetric, meaning that different spline teeth experience different conditions. The OP load is designed to simulate the damage induced from the positive bending half-cycle of the critical spline tooth, as this is the most severe case. This is due to the effect of the combined, in-phase maximum torque and bending moment. A peak magnitude for  $F_i$  of  $10.9 F_0^{nom}$  was applied as a representative load, as determined in Section 3.4.

The IP (major cycle) loads are realised via a motor and torque converter, whereas the OP loads are implemented via an electro servo-hydraulic (ESH) machine. The ESH applies a sinusoidal load waveform and is capable of cycling safely at a maximum load of  $\pm 50$  kN and at a frequency of up to 10 Hz. The IP load is initially ramped up to enforce contact, and is then held constant during the cyclic application of the 500 minor cycles ( $F_o$ ); the minor cycle load is out-of-plane, via the cyclic fatigue load. A load ratio ( $R_\sigma$ ) of 0.1 was utilised for both loads to avoid alignment/buckling difficulties associated

with compressive loadings. One loading block consists of 500 minor cycles, at a frequency of 5 Hz, for every major cycle.

The method of manufacture employed for the specimens, is summarised as follows:

1. Heat treatment of material blanks,
2. Wire erosion of blanks,
3. Spark erosion of specimen edges,
4. Low-stress grinding of chamfers.

The specimen chamfers are ground to produce a flat profile, which match the flat profile ground into the fretting bridges. The low-stress grinding of the chamfers ensures that the residual stresses generated from the machining process are minimised. The final finish produces a surface roughness of  $R_a = 0.15 \pm 0.03 \mu\text{m}$ . More details of the manufacturing process and the operation of the test rig are given by Wavish [10]. A modification was made to the original design of the bridge pads in order to provide better alignment of the contacts, and a comparison with the original design is shown in Figure 3.8. The modified pad geometry involves a new grinding wheel profile, which creates a flat recess on the fretting pad to ensure that the mating fatigue specimen does not contact the fillet radius. There are eight contact surface pairs in total (four from each bridge), and the numbering convention is given in Figure 3.9, where the four teeth that are behind (into plane of the paper) are denoted second. The axial contact position of  $z = b_1$  is also defined in the figure.

### **3.7 Experimental methods for the MRS**

The IP load was calibrated using an Instron uniaxial tensile test machine and the resulting calibration curve is shown in Figure 3.10. A new LabVIEW (v8.2) data acquisition (DAQ) program was developed to display and record the following data: a) the IP cyclic load, inferred from the attached strain gauges, b) the OP cyclic load from the load cell, c) relative displacement under IP cyclic loading from two LVDTs attached to the loading clasps, d) relative displacements under OP cyclic loading from the LVDTs e) the frictional force generated at the contacts using a pair of active strain gauges bonded to the mid-section of the fretting specimen.

A Talysurf using a stylus profilometer with a 40 nm contact stylus was employed for the post-test surface measurements. The software TalyMap Universal was used to post process the measured surface data.

### **3.8 Finite element modelling**

Finite element analysis can be utilised to simulate the mechanical behaviour of the representative specimens. A significant advantage of FE analysis over analytical approaches is that analytical techniques are usually limited to an elastic half-space assumption. The FE technique is also able to accommodate tilting of the punch and determination of stick/slip interfaces, for which analytical methods are still under development (such as in Ref. [114]). This section introduces the FE modelling of the representative specimens, in order to demonstrate the representative nature of the specimens. Additional details of the FE modelling are given in Chapter 5, where the results are also examined further.

### 3.8.1 URS finite element modelling

A three-dimensional, quarter-symmetry solid model of the test rig was created using the Unigraphics (NX3) computer-aided-design (CAD) software. The Structures module in NX3 was used for the preparation of the FE model, which included the mesh generation. The FE model includes the two load arms and test specimens and is shown in Figure 3.11. The bolts that fastened the specimens onto the load arms were not included in the model, although only a nominal pre-tension was experimentally applied, therefore this assumption is deemed not to significantly affect the stress state. The elastic-plastic isotropic material model was specified, with a Young's modulus of 206.8 GPa and Poisson's ratio of 0.28, as used in Ref. [111]. The use of this material model inherently assumes homogeneous macroscopic material behaviour. From the on-set of yield, the plastic material properties were implemented using a user-defined stress-strain curve that was experimentally determined [111], and is shown in Figure 3.12. The curve has been non-dimensionalised using the 0.2 percent proof stress and the maximum strain value.

The FE model was solved using the commercial general-purpose non-linear solver ABAQUS [115]. The mesh is a combination of linear hexahedral (C3D8) and tetrahedral (C3D4) elements, resulting in a total of 56,306 nodes and 177,473 elements. Linear elements are used because of the incorrect calculation of the mid-side node forces for quadratic elements in contact. The contact region and near contact-region between the fretting specimens is meshed with hexahedral elements due to their favourable behaviour under contact conditions in comparison with tetrahedral elements. The mesh is also biased towards the contact surface to enable suitable resolution of the stress field, giving an element size of  $215.2 \times 143.9 \times 20.1 \mu\text{m}$ .

Symmetry boundary constraints were applied to the model. A fixed boundary condition (encasté) was specified on the upper surface of the model of the inner arm. Additionally a spring element (SPRING1) with a small modulus was attached to the outer load arm (where the load is applied) in order to prevent rigid body motion in the axial direction. This is especially necessary for the case of full sliding between the two specimens. Contact was specified for the contacting surfaces of the rig. The finite sliding formulation was employed for the specimen to specimen contact, but the remaining surfaces (e.g. specimen to load arm) were tied as it was found that an insignificant amount of relative displacement occurred on these surfaces. Friction was introduced into the model according to the Coulomb friction law and the constraints enforced using the penalty method with an allowable elastic slip of  $\delta_{aes}/a_2 = 2.8 \times 10^{-4}$ . This value was arrived at from a convergence study that is demonstrated in Chapter 5.

The load was applied to the lower surface of the FE model on the outer load arm, with the magnitude chosen to match that of the rig tests. It was distributed via the use of multi-point constraints (MPC) with \*EQUATION in ABAQUS. The load was ramped to the maximum value in Step 1, and then reduced to 0.1 of the maximum in the following step. A total of two complete load cycles were simulated, to allow for frictional shakedown to occur. A range of FE analyses were solved, with a variation in the COF, and the results are presented in more detail in Chapter 5.

### **3.8.2 MRS finite element modelling**

A half-symmetry model of the MRS test rig was also developed using the solid modelling capability in the computer-aided design (CAD) software Unigraphics (NX3). This model is termed the global model as it includes the rig support structures and is shown in Figure 3.13. ABAQUS [115] was again

used as the FE solver. The mesh is a combination of linear brick (C3D8) and linear wedge (C3D6) elements in the contact regions. Following mesh refinement there is an element size of  $677 \times 400 \times 195 \mu\text{m}$  in the fretting contact region. The remaining regions are meshed with linear tetrahedral elements (C3D4) due to the low stress gradients. A matching mesh in the contact zones was used to aid the solution process.

Symmetry boundary conditions were applied to the model. The upper support points were also fully constrained (encastré). Some experimental bridge-type arrangements fix the location of the bridges, whilst others have them floating [57]. The bridges of the MRS are supported using loading clasps that are connected to the motor. This arrangement will have a small value of stiffness. Additionally, in order to fully constrain the loading clasps in the FE model, a spring element (SPRING1) was used in the axial direction. The frictional constraints for the MRS were implemented as for the URS.

The applied load was chosen to match that of the rig tests. The ABAQUS command \*EQUATION was used to remove the vertical degrees of freedom to distribute the load. The loading cycle applied to the FE model is shown schematically in Figure 3.14. The IP load is ramped up linearly during step 1 of the analysis. The OP load is then ramped to the maximum and minimum value during the following analysis steps respectively ( $R_\sigma = 0.1$ ). The solution was run to three complete minor cycles, ensuring that a stabilised loading block was captured. Inertia effects were not included, as it was deemed that at a cyclic frequency of 5 Hz, these effects would be insignificant.

### **3.9 Comparison with scaled spline modelling**

A comparison of the FE-predicted contact pressure distributions from the scaled spline (at  $z = 0.75a_1$ ), MRS (at  $z = b_1$ ) and URS (at  $z = b_2$  of outer arm) test

set ups is shown in Figure 3.15. The design major cycle torque ( $T_n = 0.818$ ) was applied for the scaled spline, an IP load of  $10.9 F_0^{nom}$  for the URS and MRS. It is observed that although an exact match is not achieved for both the URS and MRS, the mean values are close enough to be representative. The largest discrepancy is seen to occur at the contact edges. There is a theoretical elastic singularity at the edges of a complete contact [70], meaning that there is increased sensitivity to mesh density. In reality, small manufacturing tolerances mean that a perfectly square pad does not exist, weakening the singularity. The severity of the edge-of-contact stress gradient will also be lowered due to plasticity and wear processes. It is therefore deemed that matching of the average contact pressures is adequate to demonstrate broadly representative spline conditions. It was also demonstrated in Ref. [116] that the fatigue stress and contact slip are broadly similar between the MRS and the scaled spline, therefore validating the representative approach.

### **3.10 Summary of chapter**

This chapter has given the methodology that will be pursued in this thesis for the study of fretting fatigue in complex spline couplings. The combined experimental and computational approach utilises simplified specimens that mimic the behaviour of the scaled spline coupling. The finite element method was used to demonstrate the representative nature of the specimens by obtaining a reasonable agreement of the contact pressure. The experimental details of the uniaxial representative specimen and the multiaxial representative specimen were outlined and the modifications to the rigs described. The following chapter reports the experimental results from the two representative test specimen test rigs.

### 3.11 Tables

Table 3.1. The elemental compositions of the ferrous and nickel alloys (%mass).

Element	S/CMV	Inconel 718	AerMet 100
Ni	<0.3	53.63	0.05
Cr	3.0-3.5	19.05	3.16
C	0.35-0.43	0.028	0.4
Mo	0.8-1.10	3.05	0.89
Si	0.1-0.35	0.07	0.26
Mn	0.4-0.7	0.08	0.56
V	0.15-0.25	-	0.21
P	<0.007	0.007	0.007
S	<0.002	<0.001	0.001
Al	-	0.47	0.01
Cu	-	0.03	0.04
Nb	-	5.23	-
Co	-		0.17
Fe	Remainder	17.2	Remainder

Table 3.2. Selected room temperature mechanical material properties [111-113], including measured hardness values.

Material	Modulus (GPa)	Poisson's ratio	Yield stress (MPa)	UTS (MPa)	Vickers hardness (0.3HV)
Ti-6/4	~120	0.31	~920	~990	318
Inco718	200	0.29	1126	1422	455
AerMet100	194	0.30	1670	~2000	628

### 3.12 Figures

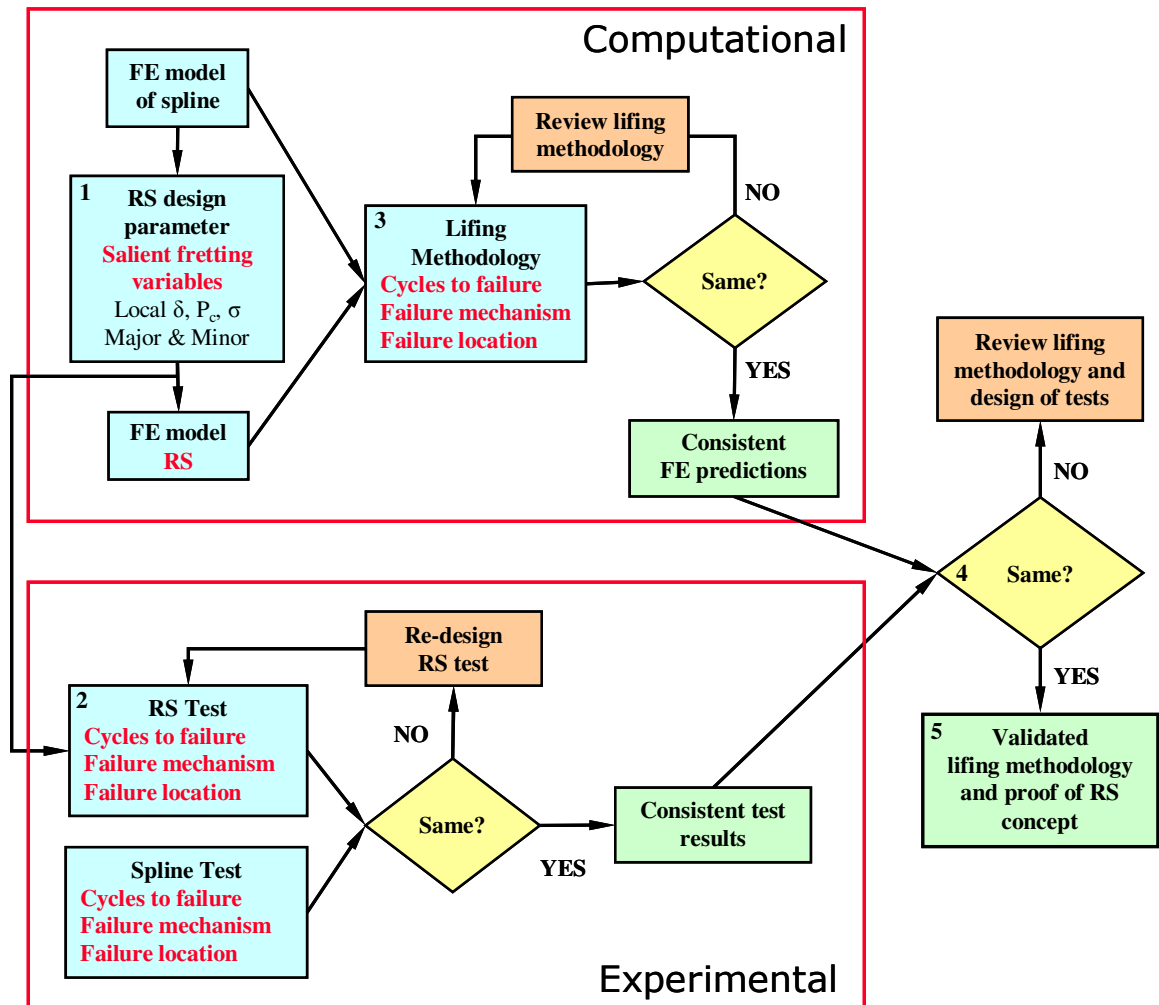


Figure 3.1. The representative specimen concept flowchart.

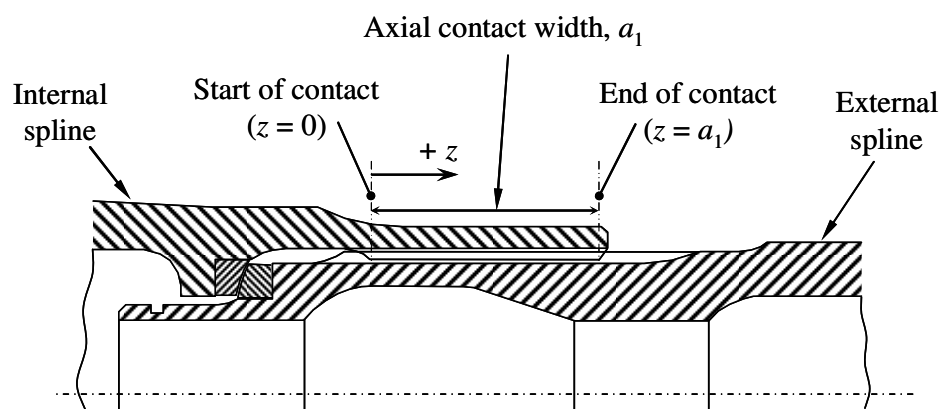


Figure 3.2. a) Axial section of the spline, with the coordinate system definition [111].

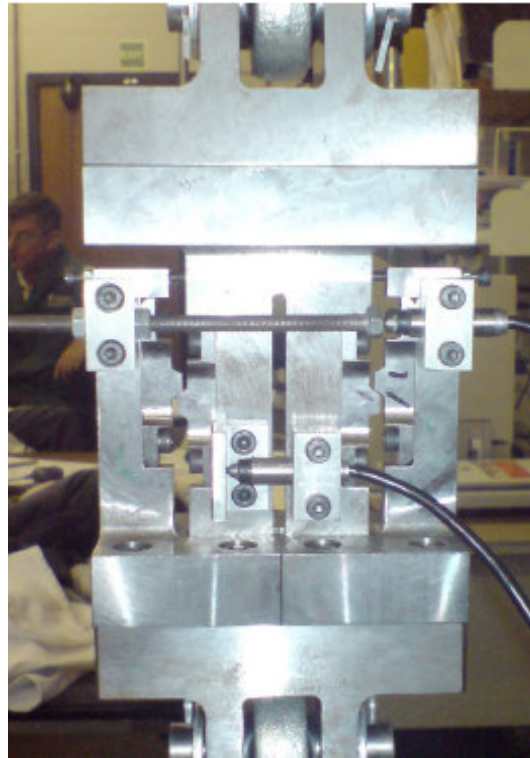


Figure 3.3. Photograph of the uniaxial representative specimen rig.

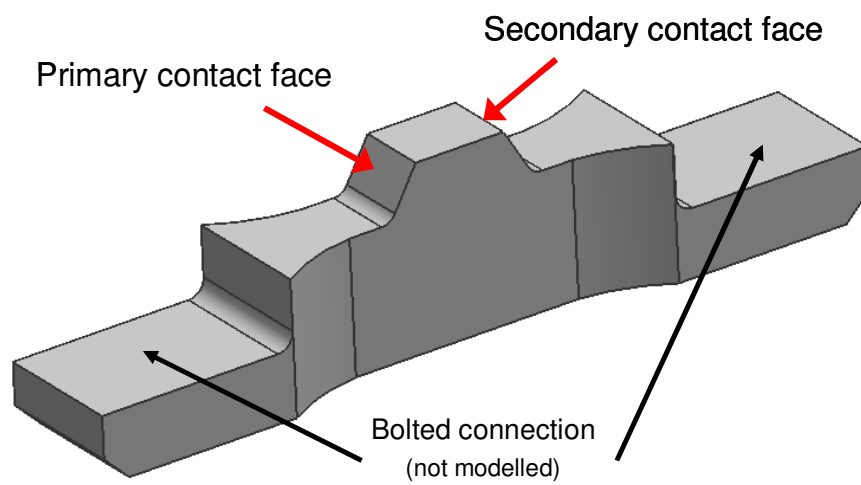


Figure 3.4. The URS fretting specimen insert.

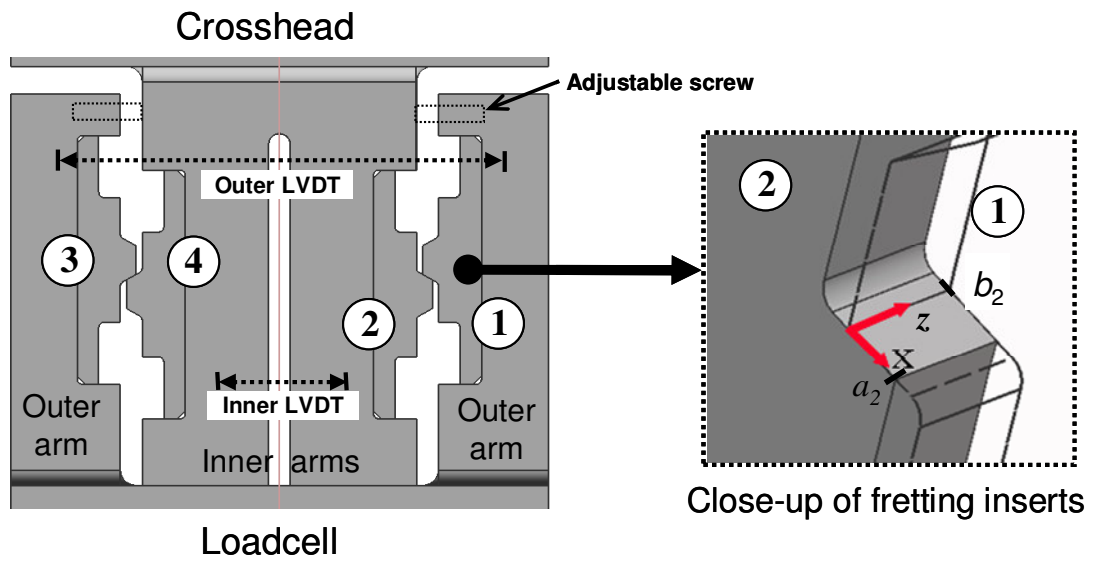


Figure 3.5. A schematic of the uniaxial representative specimen, showing the tooth numbering conventions. The local contact geometry is also shown, with the superimposed outer specimen (1) contact coordinate convention.

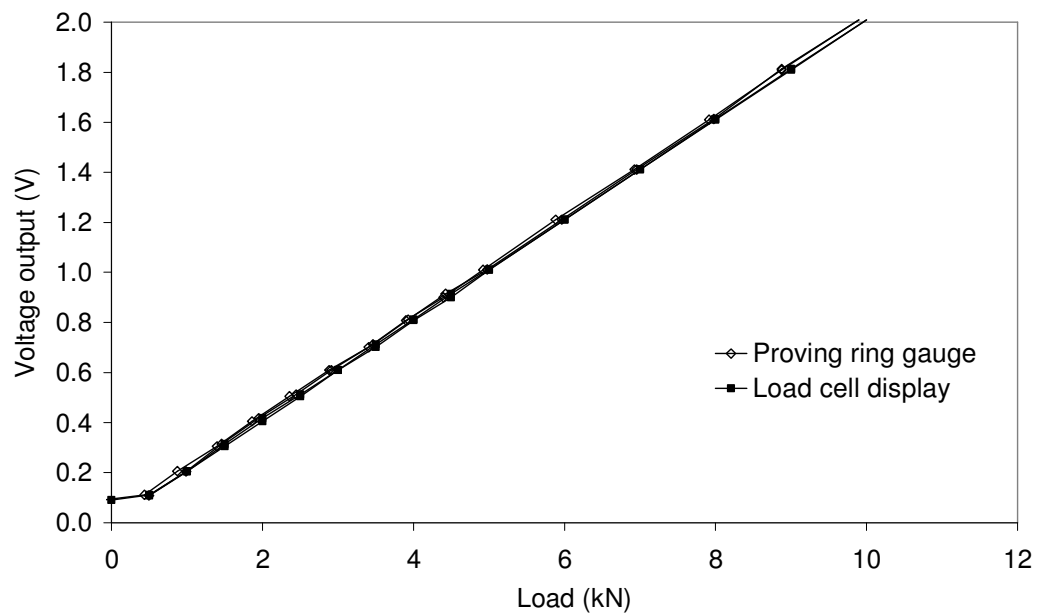


Figure 3.6. The load calibration curve, comparing the load cell with the proving ring output.

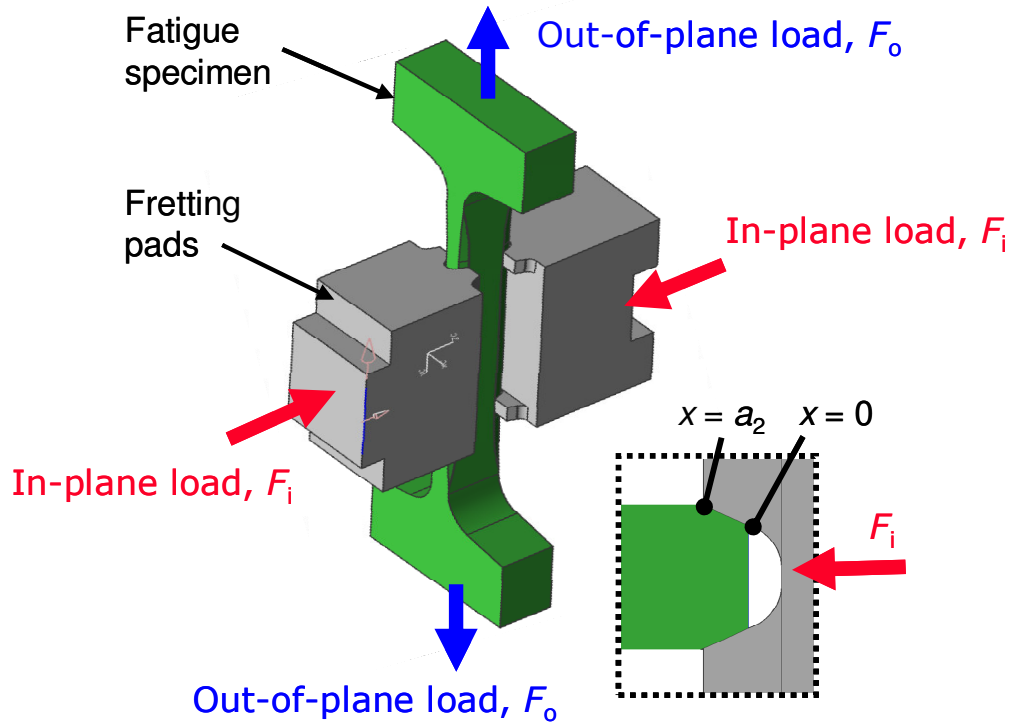


Figure 3.7. Schematic of the multiaxial representative specimen, indicating the applied multi-axial loading. The contact coordinate convention refers to the fatigue specimen.

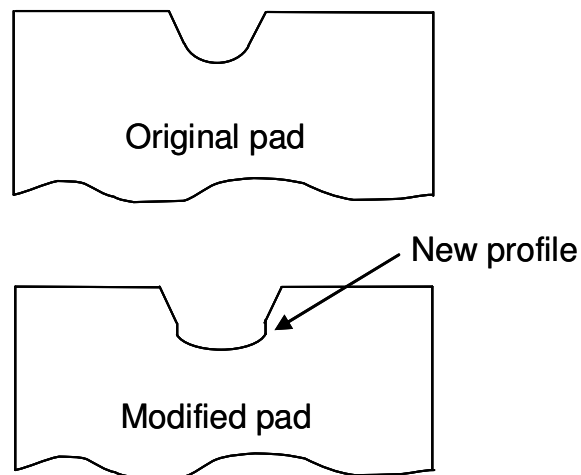


Figure 3.8. A comparison of the original and modified bridge pads of the MRS.

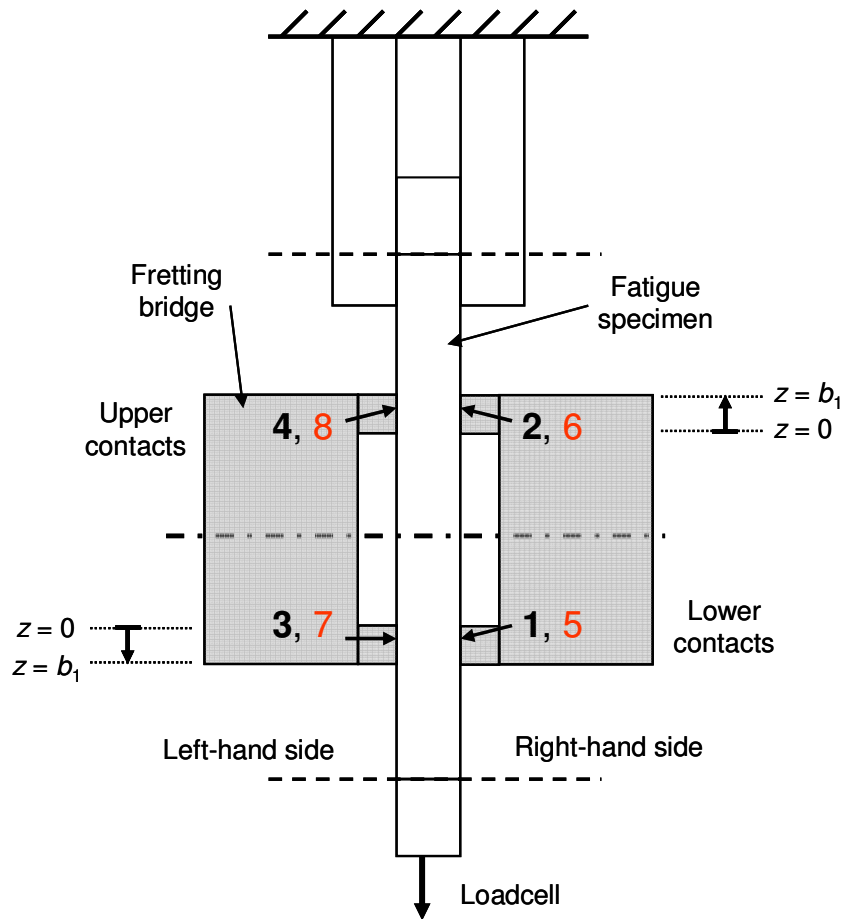


Figure 3.9. The MRS tooth numbering convention. Bold numbering indicates contact at the front of the rig, whereas the red numbering indicates the contacts at the back of the rig (into the page).

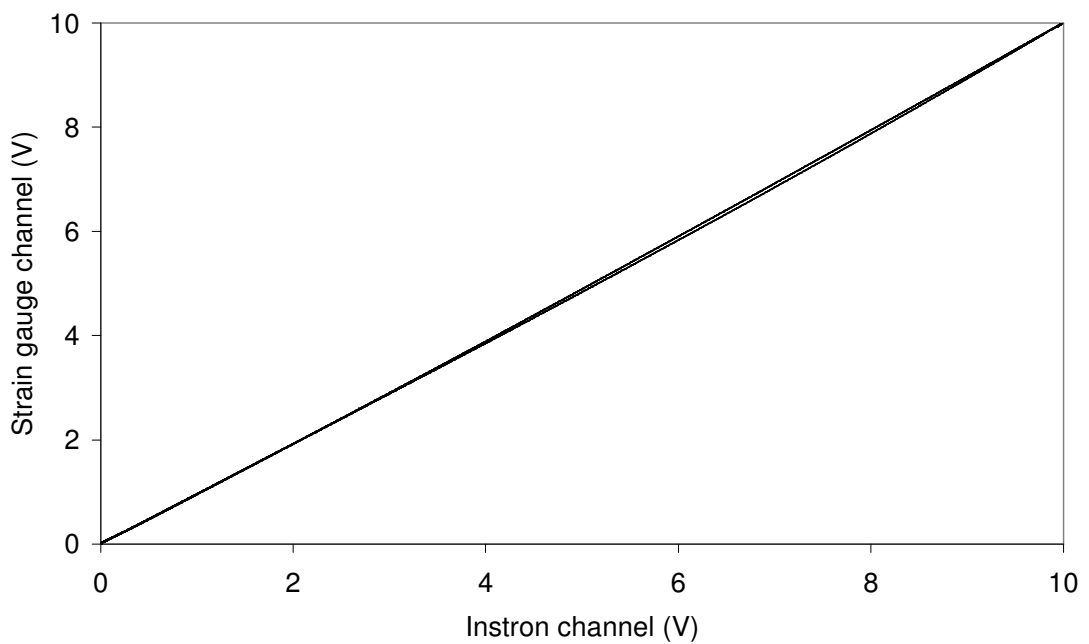


Figure 3.10. The calibration of the major cycle strain gauge.

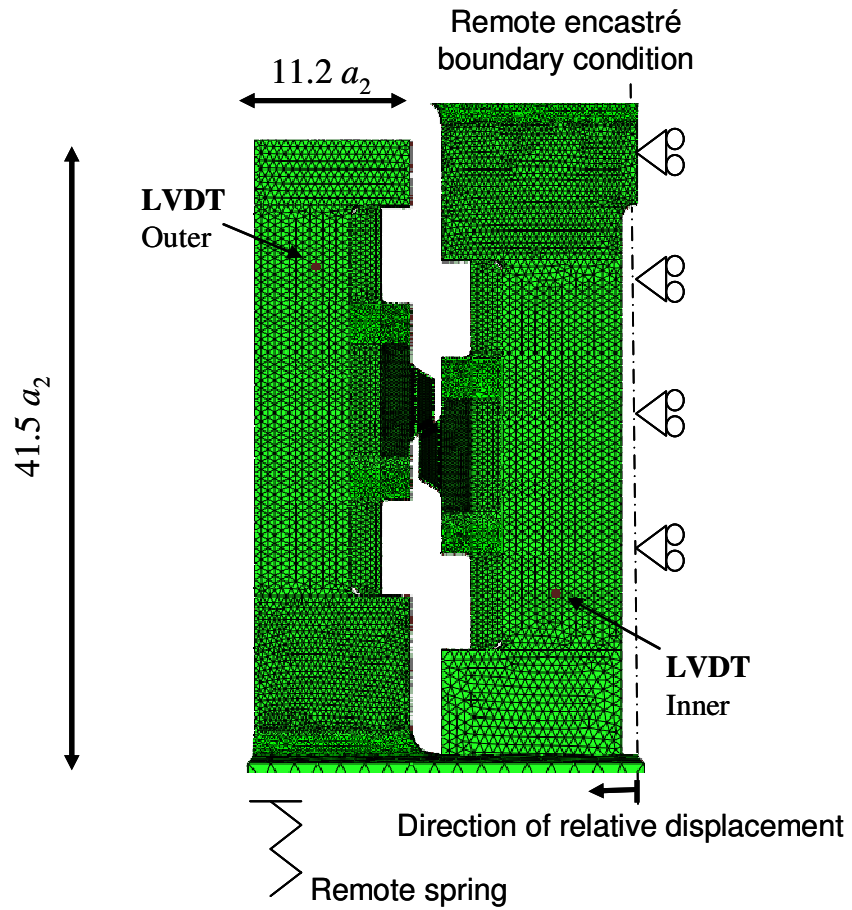


Figure 3.11. The FE model of the URS, showing the location of the nodes for evaluation of the relative displacements for 2 LVDTs.

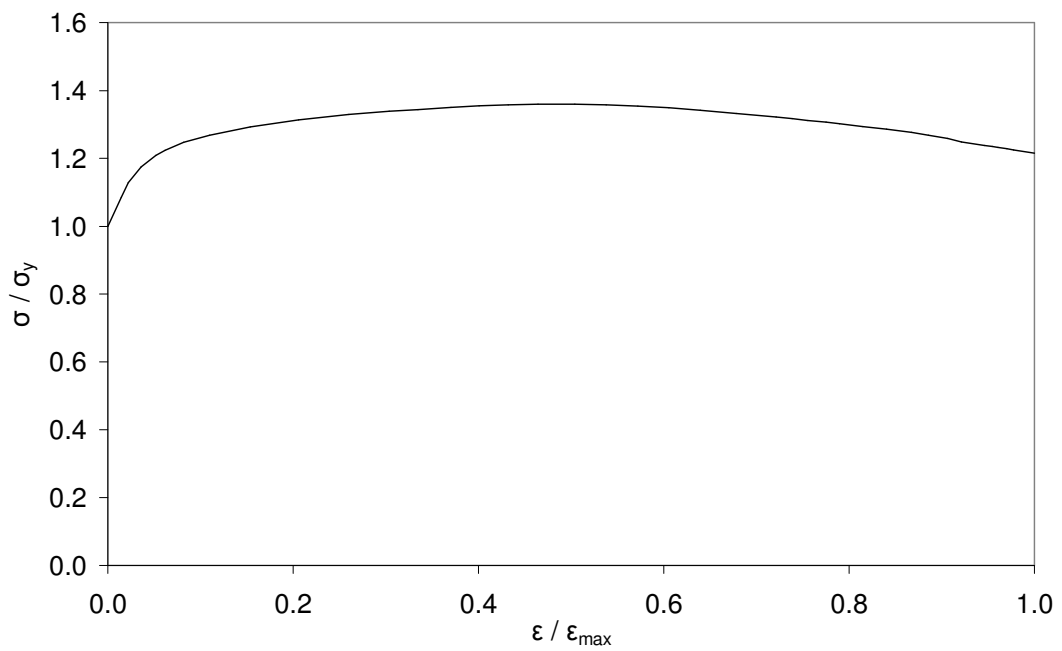


Figure 3.12. The non-dimensionalised true plastic stress-strain curve for S/CMV, obtained from Ref. [111].

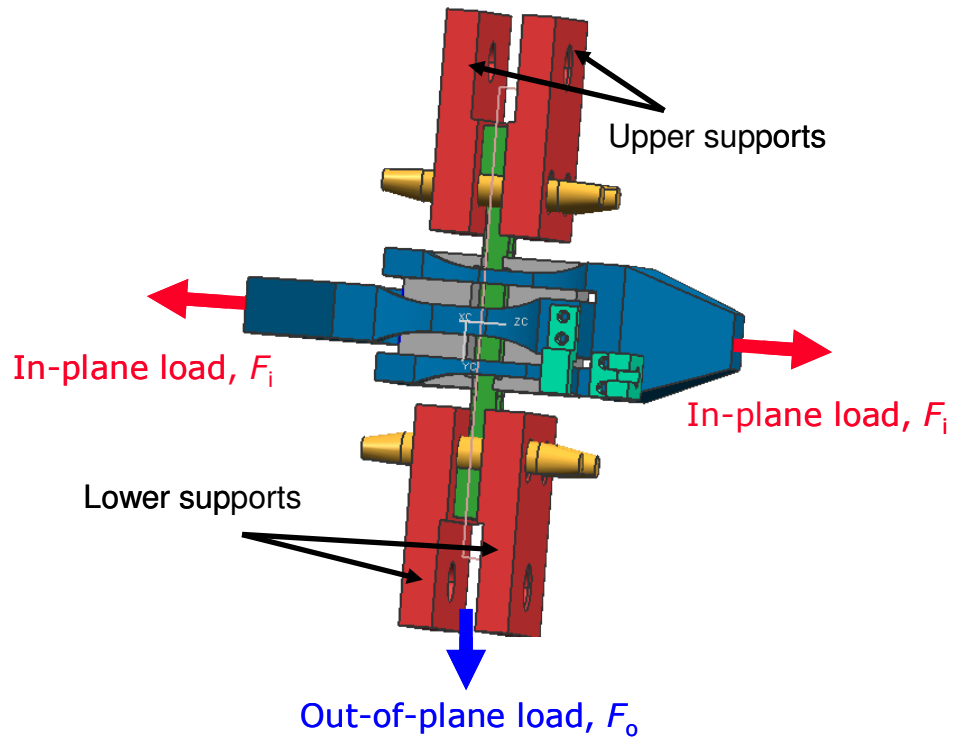


Figure 3.13. The global FE model of the MRS.

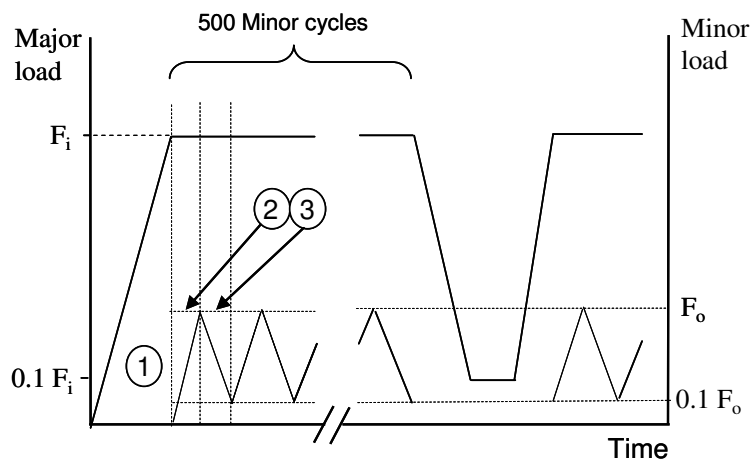


Figure 3.14. The simplified FE loading cycles of the MRS, where one major cycle with superimposed minor cycles represents one loading block.

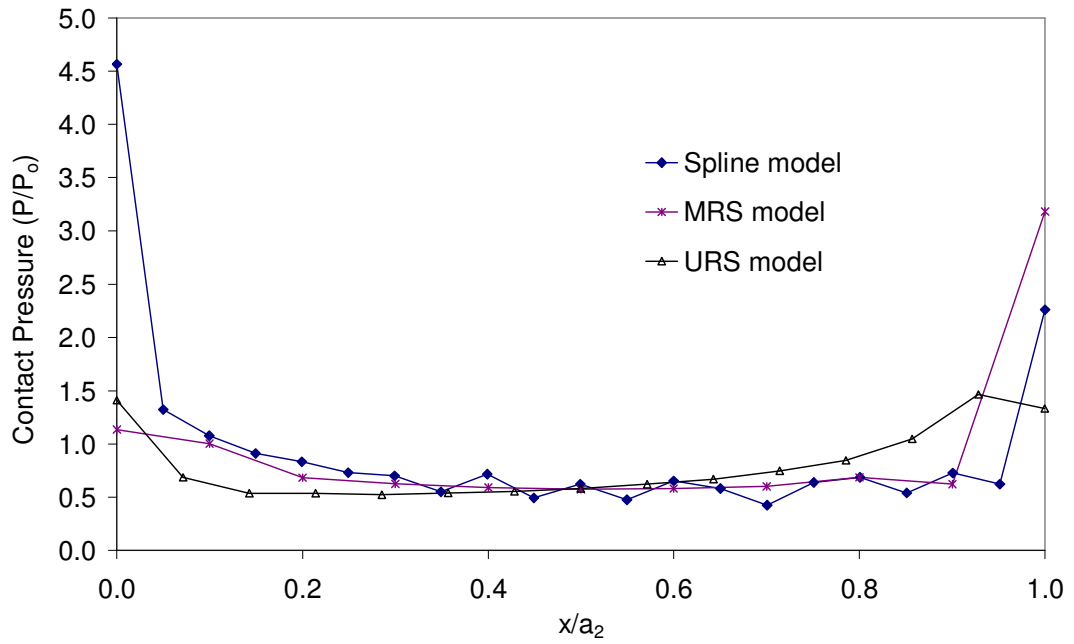


Figure 3.15. Comparison of the FE-predicted contact pressure distributions between the URS ( $z = b_2$  of outer arm), MRS ( $z = b_1$ ) and scaled spline ( $z = 0.75a_1$ ). For load conditions  $T_n = 0.818$ ,  $F_i = 10.9 F_0^{nom}$ ).

# Experimental Results

## 4.1 Introduction

The required increases in torque carrying capability of the spline coupling will be met by advances in materials and improved understanding of the life-limiting conditions. This chapter experimentally investigates both of these factors, by assessing the fretting performance of candidate spline materials using the uniaxial representative specimen (URS) and generating multiaxial fretting fatigue data with the multiaxial representative specimen (MRS).

A number of representative fretting tests were conducted on different material combinations using the URS. The tests are then examined using various experimental techniques. The experimental work of the URS was also contributed to by Daksh Agarwal and Daniel Sullivan (both undergraduate students), under the author's joint supervision. Multiaxial fretting tests were conducted using the MRS on the aeroengine material S/CMV. Further insight into the fretting fatigue behaviour of the spline is gained by identifying the specific load cases of the MRS tests that match the spline tests.

## 4.2 URS Experimental results

The URS allows the comparative fretting behaviour of a range of candidate spline materials to be investigated, that are listed as:

- High strength CMV steel,
- Ti-6Al-4V (Ti-6/4),
- Ti-6Al-4V with a surface coating of Balinit C Star (Ti-6/4c),

- AerMet 100,
- Inconel 718 (Inco).

Each material was tested against itself and against each of the other materials, with one test per combination. The tests were to run either until specimen failure (with propagating fatigue cracks) or 20,000 major cycles, whichever occurred first. 20,000 major cycles represents the typical service life of civil aeroengine spline couplings. The tests were conducted in load-control with an applied load of  $F_i = 10.9 F_0^{nom}$ , generating a representative spline contact pressure.

It was found that there were no complete plain fatigue or fretting fatigue failures from the experimental tests. The presence of wear and wear debris was clearly observed visually, suggesting the occurrence of fretting. In order to investigate this further, various experimental techniques can be utilised, as elucidated below.

#### **4.2.1 Optical microscope images**

Inspection of the fretted surfaces under an optical microscope can help to reveal the extent of the fretting damage. An optical image of the S/CMV versus S/CMV combination is shown in Figure 4.1, showing all four fretted contacts. The fretting damage is easily identifiable and a red oxide powder was formed. Good consistency is observed with respect to the wear scars of the contacts, providing confidence as to the alignment of the test rig. A significant finding from the optical microscope images concerned the Ti-6/4c specimens. In particular, the technique identified the partial removal of the coating on these specimens. All of the tests with the coated titanium specimens involved the removal or partial removal of the coating, such as evident in the image of Figure 4.2a, where the titanium substrate can be

clearly observed from the Ti-6/4c against S/CMV test. The partial removal of the coating is attributed to differing contact pressure and slip across the surfaces, which would be amplified by any small initial mis-alignment between the two contacting specimens. Figure 4.2b shows the corresponding mating specimen (S/CMV) from this material combination test. It is clear from this image that some of the coating material has been transferred onto the corresponding S/CMV specimen. Figure 4.3 shows the resulting wear scars on the coated titanium samples. Two distinct regions of deformation are visible, corresponding to the edges-of-contact, where the contact pressure is at a maximum.

#### **4.2.2 SEM and EDX analysis**

Scanning electron microscopy (SEM) enables examination of the fretted surfaces in additional detail in comparison with optical microscopy. As an example, SEM images of the Inco vs. Ti-6/4 combination are shown in Figure 4.4. For this test, the most significant wear occurred around the centre of contact, with less wear at the contact edges. Significantly, the use of SEM allowed the identification of surface cracking that was otherwise not visible using other visualisation techniques. SEM micrographs of the S/CMV sample, when tested against Inco are shown in Figure 4.5. Small surface cracking is observed on both the S/CMV and Inco samples. The cracks did not propagate into the main substrate. The test of this combination was run with additional cycles and it was found that no cracks were then visible. This suggests that the cracking is in the debris layer. Some materials had volume loss associated with wear and some had volume gain associated with material transfer from the mating specimen, as determined from surface profilometry.

SEM in conjunction with energy dispersive X-ray (EDX) analysis is an important technique in order to determine elemental compositions of

materials. This can be conducted on a fretted surface and allows the presence of oxides to be detected and can confirm when material transfer has taken place. The EDX analyses of the un-tested and tested surfaces of the Inco sample from the Inco vs. Ti-6/4 combination are shown in Figure 4.6. It is seen that there is a large peak of titanium detected on the fretted Inco sample, thus indicating that material was transferred from the contacting specimen. A peak of oxygen also indicates the presence of an oxide that can contribute to the fretting wear process. Figure 4.7 shows the results of EDX analyses of the pre and post-tested specimens of the AerMet for AerMet vs. Ti-6/4c combination. It is observed for the unfretted Ti-6/4c surface (Figure 4.7a) that there is evidence of tungsten (chemical symbol W), an element that is found in the coating. The fretted surface from AerMet vs. Ti-6/4c tests (Figure 4.7b) indicates a significant presence of titanium on the specimen, confirming that the coating on the Ti-6/4c specimen was removed, causing the Ti-6/4 substrate beneath to come into contact with the AerMet, thus transferring titanium. The presence of an oxide is also observed for the fretted AerMet sample.

### **4.2.3 Surface profilometry results**

The fretting wear performance of the materials and their combinations can be scrutinised using surface profilometry. The surface profiles of the test samples were measured for each combination before and after the test. The results from one contact pair at tooth 1 (outer arm) and tooth 2 (inner arm) of the S/CMV vs. S/CMV test are shown in Figure 4.8 and Figure 4.9 respectively. It is noted that the position of  $x/a_2 = 0$  of tooth 1 makes contact with the mating tooth at  $x/a_2 = 1$  of tooth 2. It is seen that the unaltered (not in contact) portion of the profiles show good consistency with respect to the pre and post-tested measurements. From examination of tooth 1 (Figure 4.8), the original profile does not appear to be flat, but contains a ridge at the tip ( $x/a_2 = 0$ ) of contact. This was formed during the manufacturing process. The ridge was found to

be present for the S/CMV, AerMet, Ti-6/4 and Ti-6/4c samples and results in a modified contact pressure distribution in comparison with the designed condition. Although this will influence the local fretting action, the overall representative average contact pressure still means that the results are valuable.

The average wear volume per unit face width of each material when in contact with each of the others was determined by subtracting the worn profile from the unworn profile (as described in Chapter 3), with the results given in Table 4.1 (calculated by averaging the results from the two specimens of the same material, as two pairs of specimens were tested together). The measured wear of a material in Table 4.1 is found by identifying it in the list of primary materials and finding the intersection with the secondary material that corresponds to the desired material combination. For example, S/CMV had a wear volume per unit face width of  $824 \mu\text{m}^2$  when tested against Ti-6/4. The corresponding wear volume per unit face width for the Ti-6/4 in the same test was  $15,606 \mu\text{m}^2$ . Figure 4.10 shows the average wear depth of each material when in contact with each of the others. These values were obtained by dividing the wear data in Table 4.1, by the length of contact that was calculated from each test. The combination highlighted in the figure in red indicates that cracks were observed in the test. From the measured profile data, a ranking of the different material combinations was conducted, according to the most worn material of the combination. As a result, the combinations are ordered from least wear to most wear in Figure 4.10.

For easy interpretation of the results of Figure 4.10, the results have been categorised into low wear, medium wear and high wear ranges. Although the choice of these ranges is subjective, it still serves to highlight the differing wear responses of the material combinations. It was found that dissimilar

material combinations generally produced higher wear than the like-on-like tests. For instance, the like-on-like coated and uncoated titanium combinations exhibited lower wear rates than the mixed combinations of Ti-6/4 and Ti-6/4c. Ti-6/4c shows the highest average wear of all, which is attributed to partial or complete loss of the coating during the test. Ti-6/4 (uncoated) also has a relatively high average wear rate against the other materials. S/CMV, AerMet and Inco exhibit much lower wear rates in comparison and all three accumulate material (negative wear) when tested against titanium. Inco generally experienced the least wear and it is noted that it was the hardest of the materials tested.

#### **4.2.4 Relative displacements**

The relative displacement behaviour was measured and recorded for each test using the inner and outer linear variable differential transformers (LVDTs). The plot from the S/CMV against S/CMV test is shown in Figure 4.11. There is an initial short period of higher relative displacement followed by a stabilised period for the remainder. The initial period is apparently a 'bedding-in' period, where there is a low COF (attributed to the presence of surface films and initial asperity contact) leading to higher relative displacements. It is observed that the relative displacements fluctuate at a smaller range than the applied *R*-ratio of 0.1. This is due to frictional effects at the specimen contacts. The result from the coated Ti-6/4c against S/CMV test is shown in Figure 4.12. There is a longer duration phase early in the test with higher relative displacements than in the stabilised region. This is attributed to the low friction effect of the surface coating before coating breakdown (see Figure 4.2). The transition from higher to lower relative displacements indicates coating removal and occurred for this test after approximately 3,000 cycles. The recorded ranges of the relative displacements obtained from the LVDTs from the individual combination tests are given in Table 4.2.

### 4.3 MRS experimental results

A schematic of the MRS is given in Figure 4.13, defining the bridge gap and indicating the loading. All of the experimental tests with the MRS were conducted at room temperature (20°C) and the fretting bridges and fatigue specimens were manufactured from S/CMV and used in the final heat-treated form. Additionally, the applied load cycle consisted of 500 sinusoidal out-of-plane (OP) cycles at a frequency of 5 Hz, for every one in-plane (IP) cycle, which represents one loading block. The IP cycles replicate the spline major cycles, whilst the OP cycles simulate the spline minor cycles. A nominal load ratio of  $R_\sigma = 0.1$  was used for both the IP and OP cycles. The test load conditions and the resulting number of OP cycles to failure are summarised in Table 4.3. More details of the experimental procedures are given in Ref. [10]. The following sections report the results of the individual experimental tests of the MRS.

#### 4.3.1 SC1

The first MRS test was conducted at an IP load of  $F_i = 10.9 F_0^{nom}$ , and an applied maximum OP stress of  $0.201\sigma_y$ . This provided a repeat test of one reported in Ref. [10]. The bridge gap was maintained at the reference value of 40 mm. It was found that the test specimen failed from fretting fatigue after 558 IP cycles and 279,000 OP cycles at the upper set of contacts. Visual inspection of the specimen indicated that the critical fretting fatigue crack initiated at the left hand side of the test rig, which is defined in the schematic of the test rig in Figure 3.9. The original study of Ref. [10] found that the fatigue specimen failed after 1,286 IP cycles and 643,000 OP cycles.

#### 4.3.2 SC2

The next experimental test was also used to investigate the scatter with respect to the number of cycles to failure. The test was run at an IP load of  $F_i =$

$10.9 F_0^{nom}$ , and a maximum applied OP stress of  $0.144\sigma_y$ . The bridge gap of 40 mm was maintained. The test specimen failed from fretting fatigue after 4,065 IP cycles and 2,032,500 OP cycles. The critical fatigue crack was observed to originate from the upper set of contacts, with nucleation occurring from the left hand side of the test rig. This test result compares with the test result from the original study of Ref. [10], where it was found that the fatigue specimen failed after 2,116 IP cycles and 1,058,000 OP cycles.

### **4.3.3 SC3**

The final test to investigate the scatter was carried out at an IP load of  $F_i = 10.9 F_0^{nom}$ , and a maximum applied OP stress of  $0.201\sigma_y$ . A bridge gap of 40 mm was utilised, meaning that test conditions were the same as for test SC1. It was found that the specimen failed from fretting fatigue after 746 IP cycles and 373,000 OP cycles. The critical fretting fatigue crack nucleated from the lower set of contacts and from the left hand side of the test rig.

### **4.3.4 NL1**

With the previous tests quantifying the scatter of the number of cycles to failure with a constant IP load, an additional test was conducted in order to investigate the influence of the IP load. The load conditions were an IP load  $F_i = 5.45 F_0^{nom}$ , and an applied OP stress of  $0.201\sigma_y$ . The bridge gap was maintained at 40 mm. The fatigue specimen failed after 2,708 IP cycles and 1,354,000 OP cycles. The failure occurred from the lower set of contacts and by examination of the fracture surface, it was deduced that the crack nucleated from the left hand side of the rig.

### **4.3.5 BR1**

The previous tests all utilised the reference bridge gap of 40 mm, so an additional test was conducted with a bridge gap of 20 mm in order to

investigate the influence of this parameter. The applied IP load was  $F_i = 10.9 F_0^{nom}$ , and the maximum applied OP stress was  $0.201 \sigma_y$ . It was found that the test specimen failed from fretting fatigue after 1,426 IP cycles and 713,000 OP cycles. The failure occurred at the lower set of contacts. From examination of the fracture surface, it was seen that the critical crack nucleated at the left hand side of the rig from both contact surfaces, from which the critical crack was formed.

#### 4.3.6 Overall test observations

Inspection of the specimen failures can be useful in the investigation of the test results. In order to realise this, three orthogonal views are defined for the MRS in Figure 4.14. Accordingly, Figure 4.15 shows an optical image from test SC1 from view *A* of Figure 4.14. It is observed that the crack initiated at a small angle,  $\theta$ , in relation to the overall crack growth direction. This angle was measured as approximately  $15^\circ$  from the image. As crack propagation continues, the direction of crack growth orients itself normal to the OP load. It is noted that the crack follows this normal direction throughout the majority of the fatigue specimen. SEM allows further examination of the fracture surfaces from the fretting fatigue failures of the MRS. SEM images of the fracture surfaces from tests SC1 and SC2 are shown in Figure 4.16, where the applied OP (bulk) stress is normal to the image (view *B* of Figure 4.14). The images allow the locations of crack initiation to be identified. It is seen that crack initiation occurs at approximately  $x/a_2 = 0$  for both tests, at two separate locations, that correspond to two fretting contacts from the same fretting bridge. The two crack fronts then develop until the two fronts meet and form a single crack front until final specimen fast fracture. By comparing the two tests in Figure 4.16 it is seen that the location of crack initiation is similar, but test SC2 exhibits a significantly reduced fast fracture region, that is attributed to the lower OP stress in comparison with test SC1. From all the tests reported

in the previous sections, the critical crack was found to consistently nucleate close to the outer edge of the fretting pad at the specimen tip ( $x = 0$ ). It was also visually observed that the critical fretting fatigue cracks generally originated from the least worn regions. Fatigue striations on the fracture surface were not easily visible, even using SEM, although it was generally found that a crack formed at the two contact locations from the same bridge. Optical images of tests SC1 and SC2 are shown in Figure 4.17 from view C of Figure 4.14. The two tests had the same applied loading conditions. It is observed that the two tests produced similar fracture paths, demonstrating good repeatability of the results. It appears that crack initiation occurred at both edges of the fatigue specimen (upper and lower in the photographs). The two crack fronts eventually meet and continue propagation through the specimen. The angle of crack initiation may be estimated from the photographs, such as in Figure 4.18, which is a close-up of the SC1 test in Figure 4.17.

By examining the results of the test programme, it is clear that the bulk fatigue (OP) stress, that mimics the rotating bending moment of the splined shaft, is a key parameter in determining the fretting fatigue life of the MRS. Additionally, a decreased clamping load (IP load) was found to significantly increase the total fretting fatigue life e.g. from a mean life of 431,667 OP cycles for  $F_i = 10.9 F_0^{nom}$  to 1,354,000 OP cycles for an IP load of  $F_i = 5.45 F_0^{nom}$ . The reduced bridge gap of 20 mm (as opposed to 40 mm) also gave an increase in the number of cycles to failure. The effect was less pronounced than the effect of the IP load, leading to a life of 713,000 OP cycles for the shorter bridge gap. The OP stress-life (S-N) curve of the experimental results, including the results from Ref. [10] is shown in Figure 4.19.

#### 4.3.7 Relative displacements and wear

A new support fixture was designed and manufactured in order to attach an LVDT to the rig to measure the OP relative displacements, with the positions of the LVDTs shown schematically in Figure 4.20. The LVDT in the OP direction contacts with the upper surface of the fretting bridge. Measurements were taken for all of the applied OP loads of the experimental tests (cycled at  $R_\sigma = 0.1$ ), with the resulting displacement range determined as a function of applied OP load and shown in Figure 4.21. There is a linear relationship with applied OP load and good repeatability is observed.

Surface profilometry can be used to identify fretting wear that occurred from the tests. The axial surface profile for test SC2 at  $x/a_2 = 0$  is given in Figure 4.22. It can be seen that there is a maximum measured depth of  $55 \mu\text{m}$ , with a consistent wear profile across the axial contact dimension.

#### 4.3.8 Measurement of the friction force

With a strain gauge bonded to the mid-section of the fatigue specimen the total friction force can be determined. The strain gauge (temperature compensated) was statically calibrated using the rig servo-hydraulic actuator and the analogue voltage output from the control unit. The signal conditioning of the strain gauge output was conducted via an amplifier that allowed the balancing of the bridge circuit and the adjustment of the gain. The specimen was monotonically loaded (tensile) in order to determine the required amplifier gain. This was done in loading and unloading to capture possible hysteresis effects. An additional calibration was carried out in order to check that the dynamic behaviour of the gauge was stabilised. A plot of the measured OP force,  $F_o$ , and the force inferred from the strain gauge,  $F_g$ , after 500 OP cycles of test BR1 is shown in Figure 4.23. The sinusoidal waveforms indicate that there is a reduced force inferred from the strain gauge in

comparison with the applied force. This is due to the transmission of the friction force to the fretting pads. The shape of the strain gauge waveform also suggests that partial slip fretting conditions are attained. In partial slip, the actual COF is greater than the measured global ratio of  $Q/P$ . Therefore the traction coefficient,  $T_c$ , for the out-of-plane direction is defined as:

$$T_c = \frac{Q_{\text{minor}}}{N} \quad (4.1)$$

where  $Q_{\text{minor}}$  is the OP force generated by friction per contact and  $N$  is the normal load per contact. A free-body diagram of a half-section of the MRS fatigue specimen and fretting bridges is shown in Figure 4.24 and from static equilibrium (OP direction) considerations leads to:

$$T_c = \frac{F_o - F_g}{4N} \quad (4.2)$$

With a sliding condition for IP loading (a COF of  $\mu$ ), the normal clamping load per foot is given by:

$$N = \frac{P}{\sin \theta + \mu \cos \theta} \quad (4.3)$$

where  $P$  is the applied major load per foot and  $\theta = 25^\circ$  for the MRS specimen. The traction coefficient was calculated for the instant of maximum OP load and was found to be approximately 0.1 for all of the experimental tests. This value indicates partial slip, since it is substantially lower than the measured COF from Ref. [117] for the same material.

#### 4.3.9 Spline comparison

The test results from the MRS can be compared with the results of the scaled spline testing [7] that was previously conducted at the University of Nottingham. Table 4.4 reports the fretting fatigue results from the scaled spline test programme. The total life S-N curves from the MRS and scaled spline testing are subsequently plotted in Figure 4.25, where the number of cycles refers to the minor cycles for the scaled spline and the OP cycles for the MRS. The plain fatigue data are obtained from Ref. [9]. The stress levels of the scaled spline tests were obtained from finite element analyses of the spline, at a position of  $z/a_1 = 0.75$  at the spline root using the model from Ref. [11]. It is clear that the imposed fretting for both the MRS and scaled spline has a detrimental effect on the total fatigue life of the material. The average life reduction factor is approximately 4.0. It is also observed that the MRS results are in good agreement with the spline fretting fatigue data. Significantly, this provides an important validation of the representative specimen concept using the MRS.

#### 4.4 Discussion

The experimental tests with the URS highlighted that the coating on the titanium specimens was removed. This behaviour is attributed to delamination of the coating, as there is an elastic mismatch between the coating material and the substrate. Further work could investigate this delamination behaviour. The debris produced by the fretting action was not removed after the URS tests. Since it can be difficult for debris to escape in a conforming contact, as employed in this study, any compacted debris has consequently been included in the profile measurements. Therefore, the actual wear could be greater than that reported. The URS experimental programme was conducted at room temperature, whereas it is known that elevated temperatures can affect the material fretting behaviour. At increased

temperatures glaze formation provides surface lubrication [118], reducing the COF and resulting in increased fretting wear damage. The current generation of low pressure (LP) spline couplings in aeroengines, however, are unlikely to experience the temperatures required for glaze formation.

The MRS test programme demonstrated a good correlation with the fretting fatigue results from the scaled spline programme, although the MRS tests slightly underestimated the overall lives. This can be explained by examining the differences between the two. The externally splined component of the spline coupling was gas nitrided, whereas the MRS was not. Nitriding gives a higher surface hardness (although decreased ductility) [119], which will inhibit the crack initiation process. The beneficial residual stresses that the nitriding process introduces also inhibit crack initiation and crack propagation. Therefore, it would be expected that under fretting fatigue, nitriding would improve the total fretting fatigue life of the MRS. There are also inevitable differences between the simplified MRS test and the real spline coupling. For example, the spline coupling contact is initially lubricated, whereas the MRS tests are run in dry conditions.

## **4.5 Summary of chapter**

This chapter has presented the experimental results from the reintroduced uniaxial representative specimen (URS) and multiaxial representative specimen (MRS). The URS was successfully used to test various material combinations under representative spline conditions, generating valuable data to aid the selection of candidate spline materials. All of the specimens experienced fretting wear, which was quantified for each test using surface profilometry, allowing a material combination ranking to be created. It was found that Inconel 718 generally produced the least wear. The titanium specimens (both coated and un-coated) produced the highest wear, whether

tested against the harder materials or against each other. It was also observed that the coating on the titanium specimens was either partially or fully removed. This is attributed to the elastic mismatch between the coating and substrate material. Surface cracks were observed for the S/CMV vs. Inco combination, which experienced the least wear of the combinations. The surface cracking is believed to have occurred in the debris layer, as the cracks were seen to have “rubbed out” with the application of additional load cycles.

The results of the MRS test programme were outlined, providing multiaxial fretting fatigue data for the current spline material of choice for triple-spool gas turbine aeroengines. The scatter of the total fretting fatigue life was quantified. Additionally, the effect of the bridge gap and the normal clamping load on the total life was obtained. The failure location of the fatigue specimen was examined and out-of-plane (minor cycle) relative displacement measurements were also obtained across the load range. Significantly, a stress-life comparison of the MRS, scaled spline and plain fatigue test data highlighted the detrimental action of fretting for the spline. A good agreement was found between the MRS and scaled spline test results, providing a key validation of the representative specimen concept. In order to further interpret the experimental results presented in this chapter, the following chapter reports the detailed finite element modelling of the URS and MRS test rigs.

## 4.6 Tables

Table 4.1. Average wear volume per unit face width ( $\mu\text{m}^2$ ) of the primary material when in contact with the secondary material from the URS tests.

		Primary material				
		Ti-6/4	Ti-6/4c	S/CMV	AerMet	Inco718
Secondary material	Ti-6/4	5,299	18,080	824	-10,450	-14,391
	Ti-6/4c	24,253	9,694	-168	-5,428	-9,326
	S/CMV	15,606	46,827	6,675	6,062	1,175
	AerMet	20,450	30,454	6,905	16,890	1,260
	Inco718	25,508	20,809	-1,404	-9,474	2,595
	Average	18,223	25,173	2,566	-480	-3,737

Table 4.2. The measured displacement ranges using the LVDTs from the URS tests.

Test ID	Material Combination		Measured displacement range ( $\mu\text{m}$ )	
			Inner LVDT	Outer LVDT
1	Inco718	SCMV	59	80
2	Inco718	AerMet	56	97
3	Inco718	Inco718	60	74
4	Ti-6/4	Ti-6/4	68	99
5	AerMet	SCMV	66	149
6	SCMV	SCMV	64	95
7	SCMV	Ti-6/4	60	94
8	Ti-6/4c	Ti-6/4c	78	131
9	Inco718	Ti-6/4c	62	100
10	Inco718	Ti-6/4	62	108
11	AerMet	Ti-6/4c	75	86
12	AerMet	AerMet	101	257
13	Ti-6/4c	Ti-6/4	86	125
14	SCMV	Ti-6/4c	67	99

Table 4.3. The MRS test conditions and resulting fretting fatigue lives.

Test ID	In-plane load	Out-of-plane max. stress	Bridge gap (mm)	$N_f$ (out-of-plane cycles)
SC1	10.9 $F_0^{nom}$	0.201 $\sigma_y$	40	2.79x10 <sup>5</sup>
SC2	10.9 $F_0^{nom}$	0.144 $\sigma_y$	40	2.03x10 <sup>6</sup>
SC3	10.9 $F_0^{nom}$	0.201 $\sigma_y$	40	3.73x10 <sup>5</sup>
NL1	5.5 $F_0^{nom}$	0.201 $\sigma_y$	40	1.35x10 <sup>6</sup>
BR1	10.9 $F_0^{nom}$	0.201 $\sigma_y$	20	7.13x10 <sup>5</sup>

Table 4.4. Summary of scaled spline test conditions and the associated results of fretting fatigue damage [7].

Parameter	$B_n = 0.039$	$B_n = 0.087$	$B_n = 0.117$
Life (major cycles)	> 35,000	12,021	1490
Life (minor cycles)	> $1.75 \times 10^7$	$6.01 \times 10^6$	$7.45 \times 10^5$
Crack initiation location ( $x/a_2, z/a_1$ )	-	(0-1, 0.7-0.94)	(0-1, 0.7-0.87)

**Note:** All cases used design values of torque and axial load,  $T_n = 0.818$  and  $F_n = 0.032$ . Symbol '>' means that failure had occurred within the specified number of cycles, at which point the test was stopped.

## 4.7 Figures

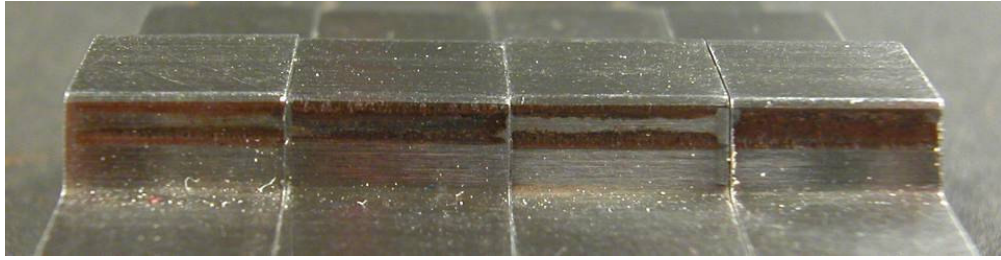
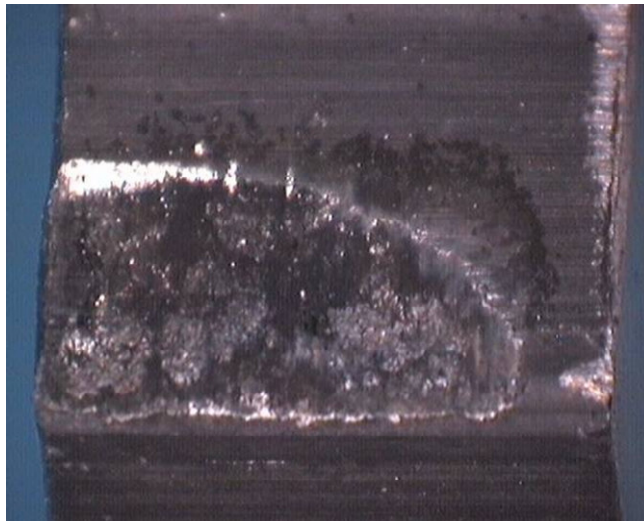


Figure 4.1. The four fretting wear scars from the S/CMV vs. S/CMV test.

a)



b)



Figure 4.2. The optical images from the Ti-6/4c against S/CMV combination, showing, a) partial removal of the coating on the Ti-6/4c specimen, and b) coating transfer onto the S/CMV specimen.

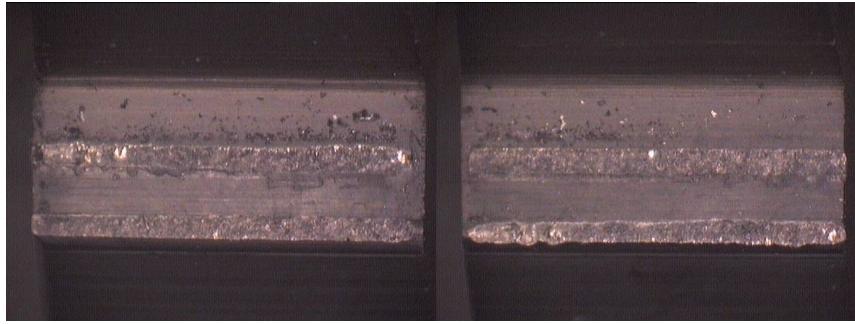


Figure 4.3. Optical images of the mating specimens from the Ti-6/4c vs. Ti-6/4c material combination.

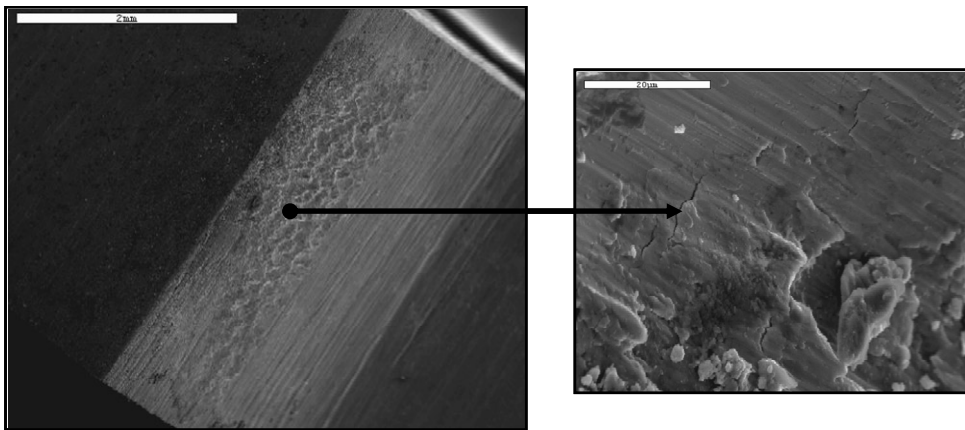


Figure 4.4. SEM micrograph of the Inco specimen from Inco vs. Ti-6/4 combination, showing the worn region.

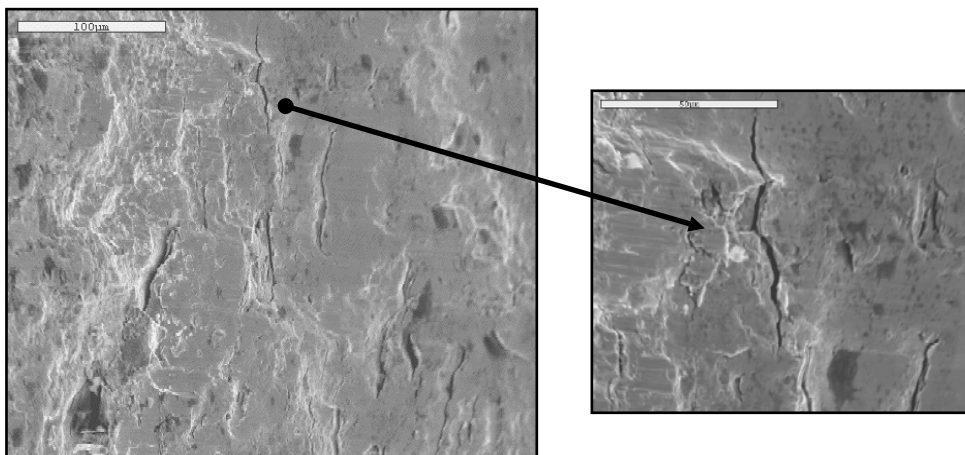


Figure 4.5. SEM micrographs from SCMV vs. Inco test showing surface cracking of the S/CMV sample at the centre of contact.

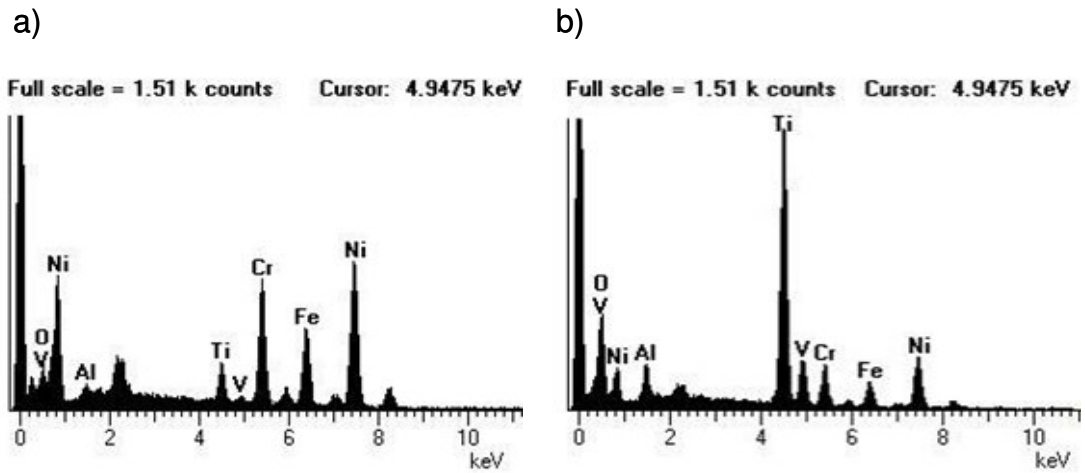


Figure 4.6. The EDX analyses to determine elemental composition of the Inco sample from Inco vs. Ti-6/4 combination for a) unfretted specimen, and b) fretted specimen.

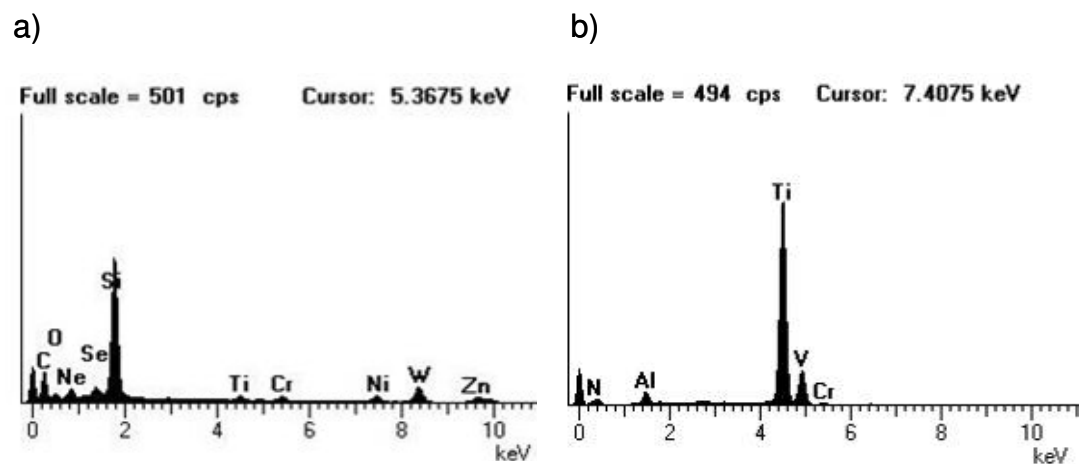


Figure 4.7. The EDX analyses to determine elemental composition of the AerMet sample from AerMet vs. Ti-6/4c combination for, a) unfretted material, and b) fretted material.

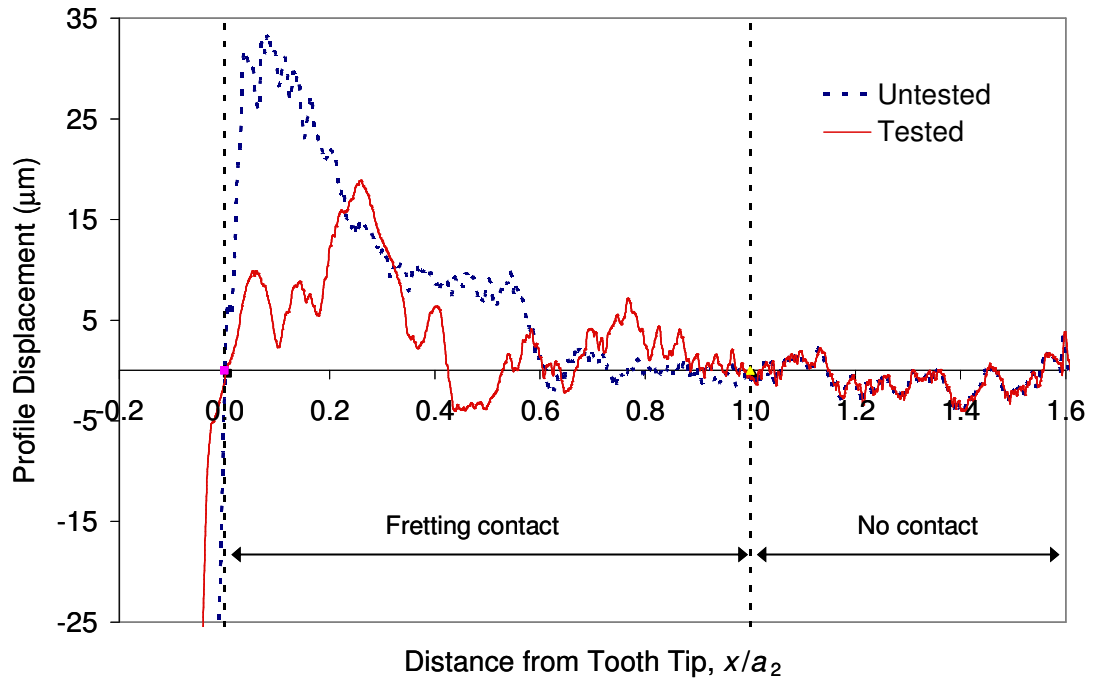


Figure 4.8. The measured surface profiles of tooth 1 (outer arm) from S/CMV vs. S/CMV test.

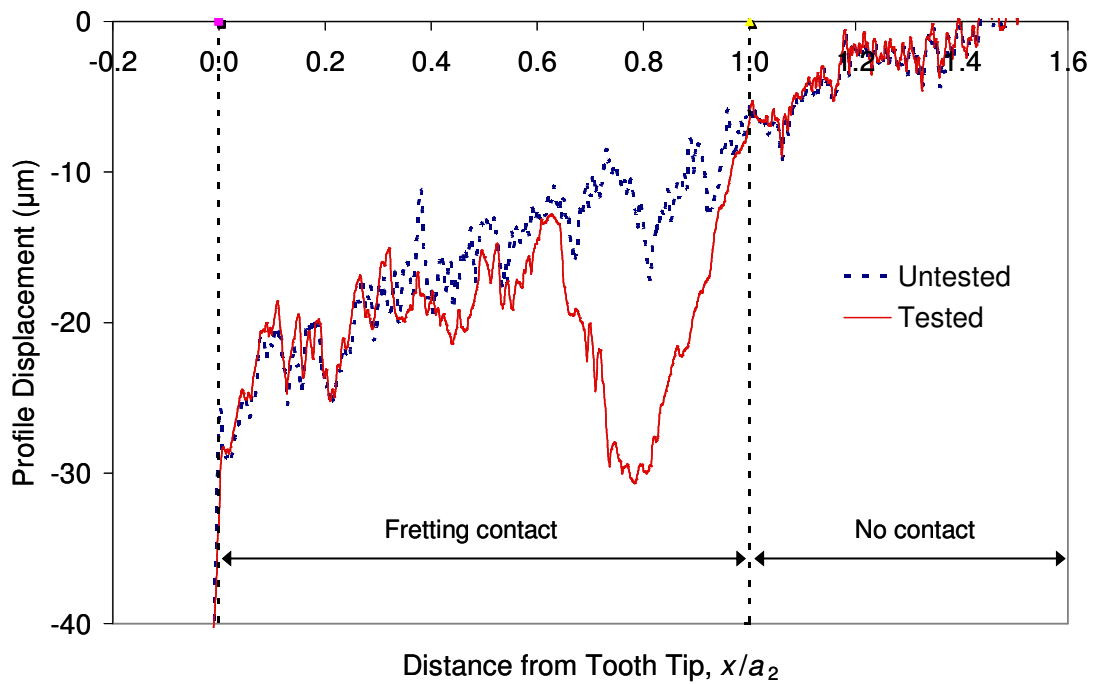


Figure 4.9. The measured surface profiles of tooth 2 (inner arm) from S/CMV vs. S/CMV test.

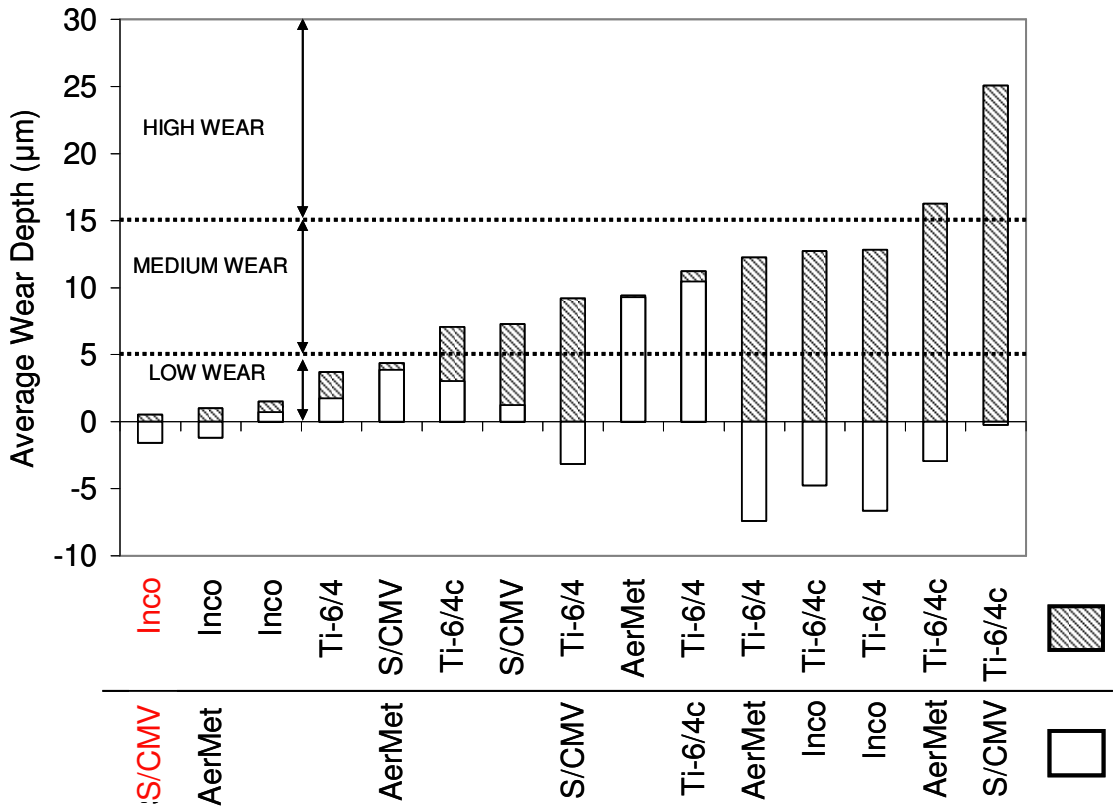


Figure 4.10. The average wear depths for the combinations after 20,000 cycles, ranked from least wear to most wear for the most worn specimen (hatched bars). For a load of  $F_i = 10.9 F_0^{nom}$ .

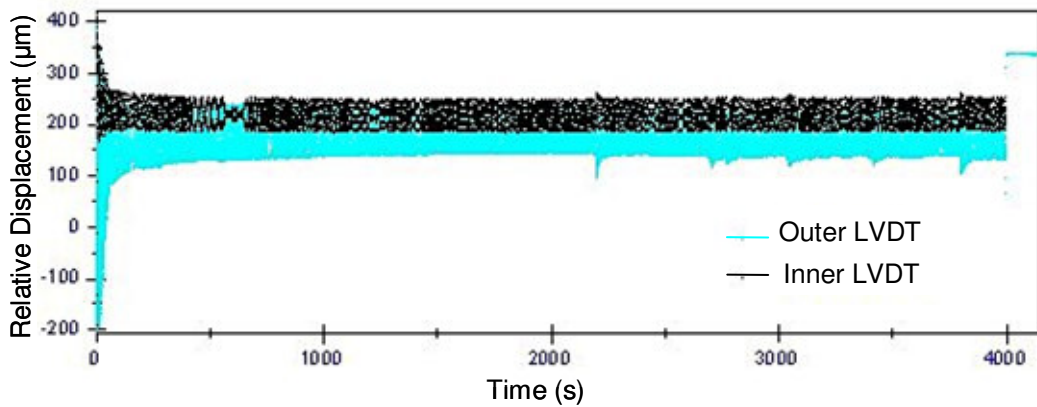


Figure 4.11. The recorded relative displacement data from the S/CMV vs. S/CMV test from the URS.

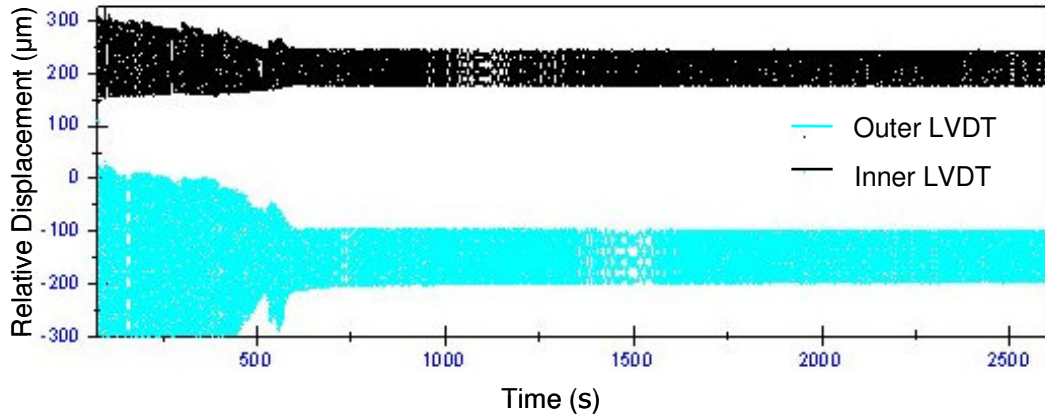


Figure 4.12. The recorded relative displacement data from the Ti-6/4c versus S/CMV test from the URS.

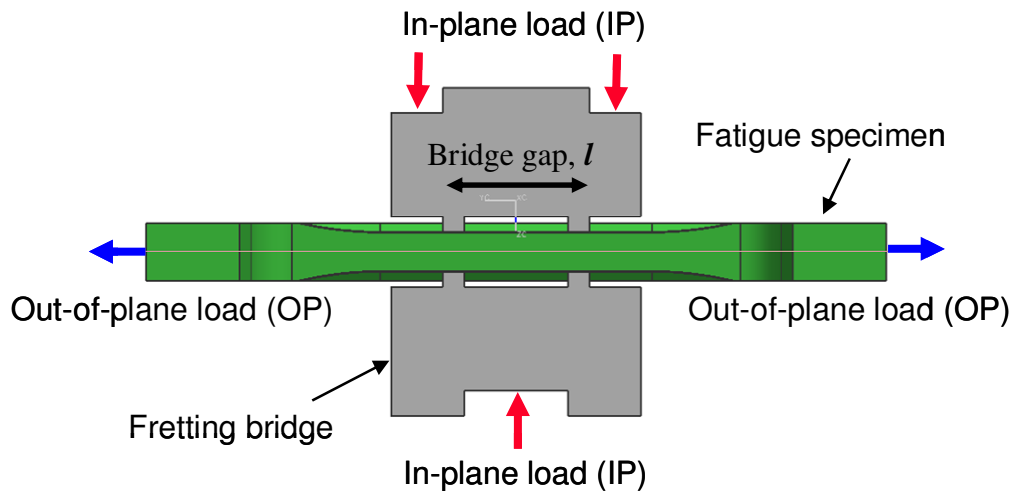


Figure 4.13. The definition of the bridge gap (20 mm bridge gap shown) and the position of loading of the MRS.

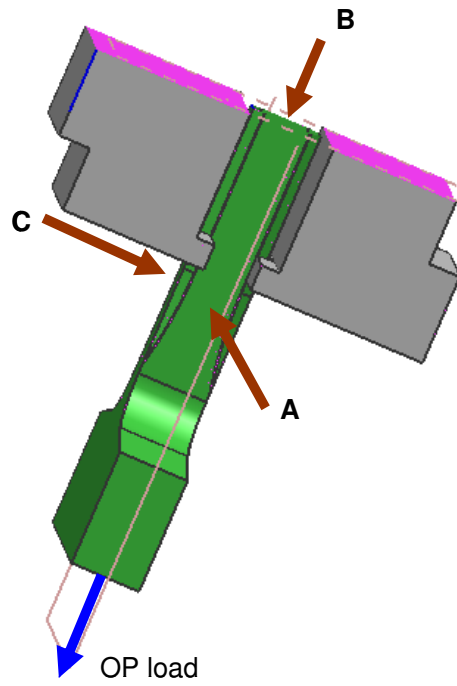


Figure 4.14. Section of the MRS, indicating the orthogonal views, where *A* is at the front of the experimental rig.

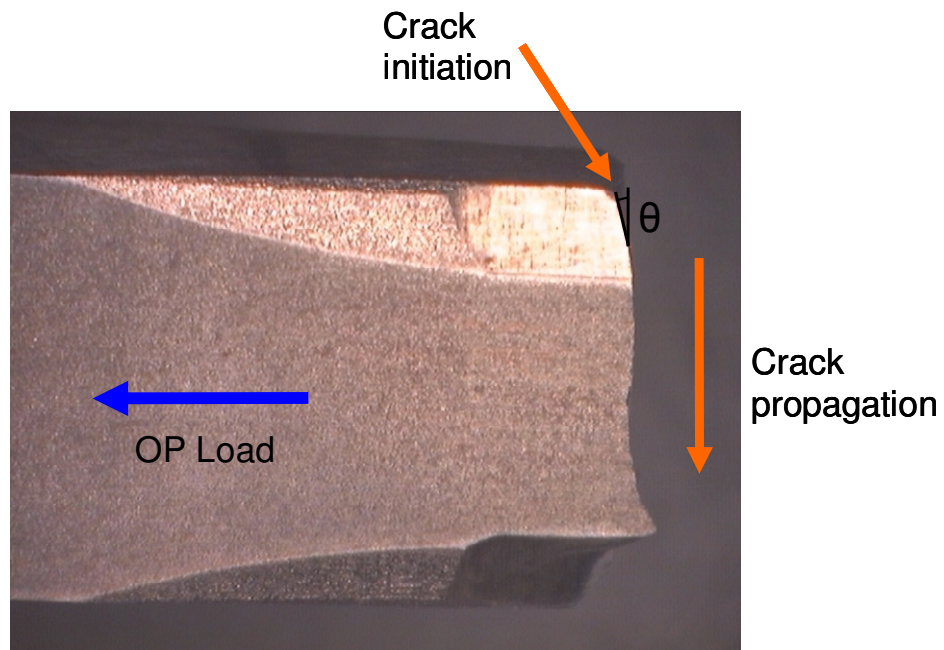
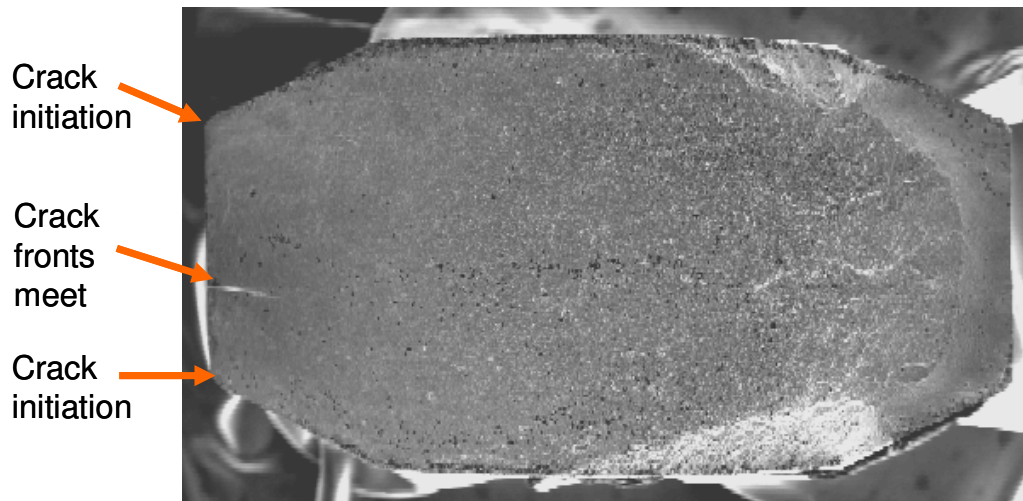


Figure 4.15. The optical image of test SC1 from view *A* (rotated) of Figure 4.14, highlighting the crack growth direction.

**Test SC1**



**Test SC2**

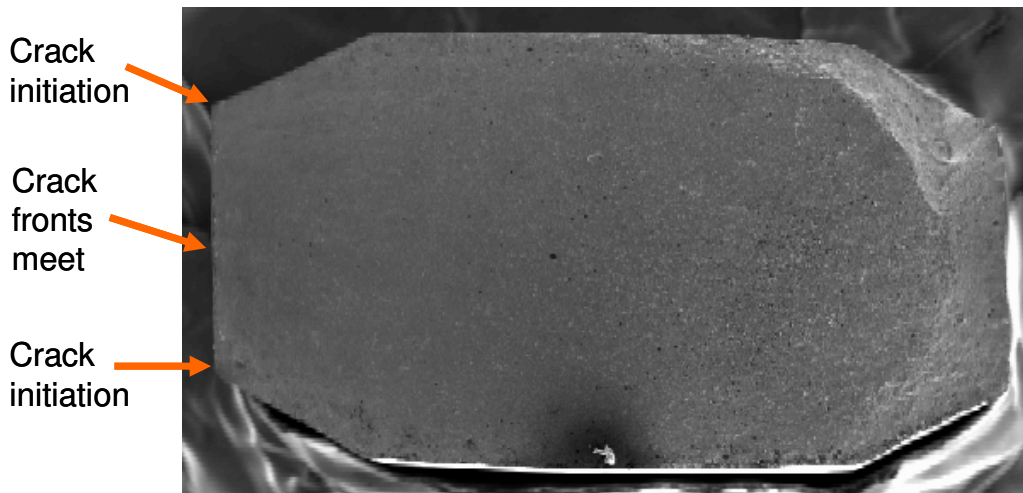
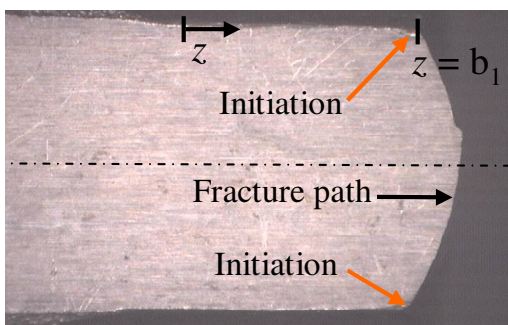


Figure 4.16. SEM images of the fracture surfaces of tests SC1 and SC2 (view B of Figure 4.14).

**Test SC1**



**Test SC3**

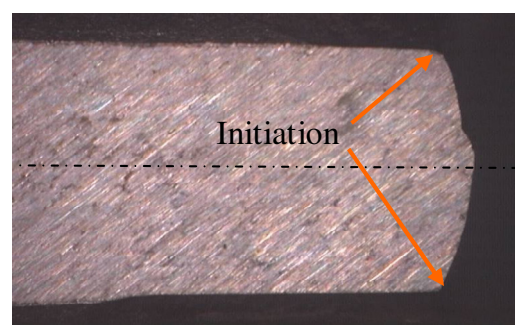


Figure 4.17. Images of the fracture paths (view C of Figure 4.14) of the fatigue specimens for an applied minor cycle load of  $\sigma_{\max}/\sigma_y = 0.20$  for tests SC1 and SC3.

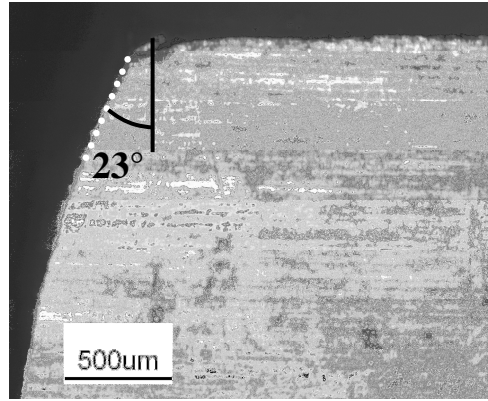


Figure 4.18. Close-up of the initiation of test SC1 (from view C of Figure 4.14) for an applied minor cycle load of  $\sigma_{\max}/\sigma_y = 0.20$ , indicating the nucleation crack angle.

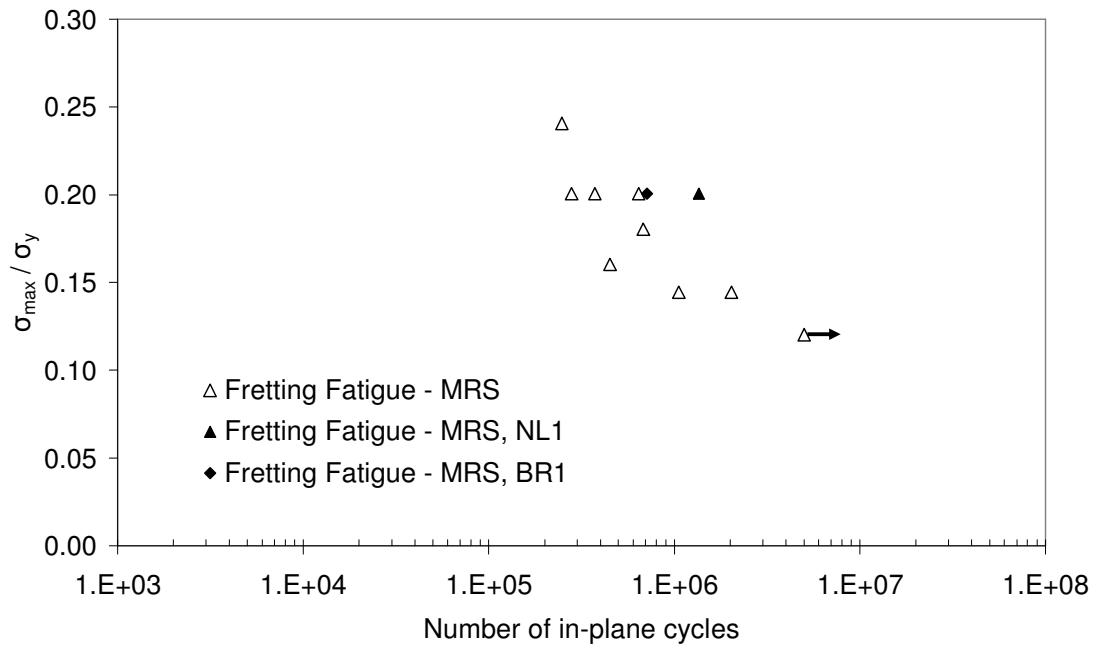


Figure 4.19. The in-plane S-N curve of the MRS tests, showing the effect of reduced IP load and reduced bridge gap. Including the results of Ref. [10].

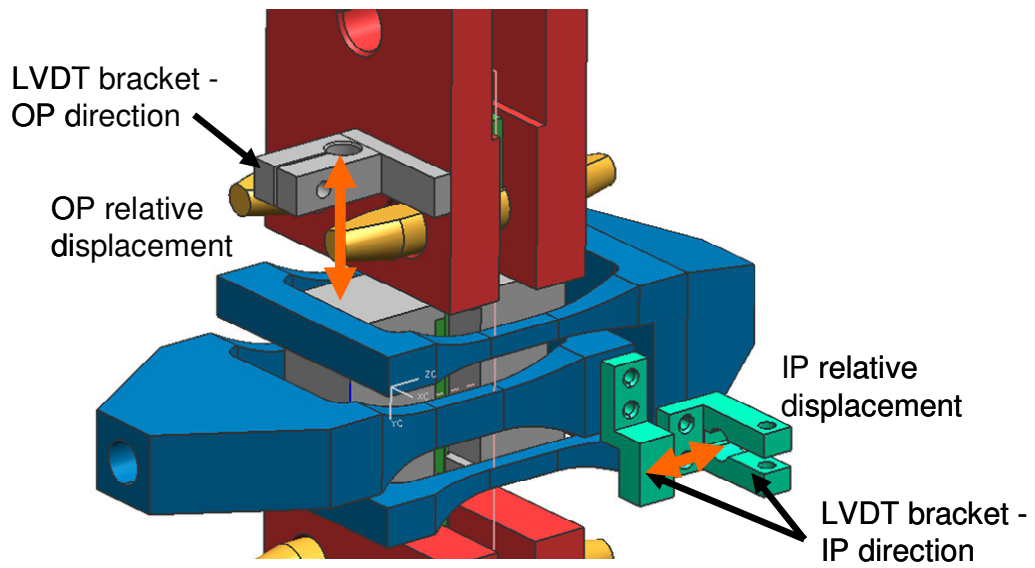


Figure 4.20. The location of the LVDT brackets and the definition of the relative displacements of the MRS.

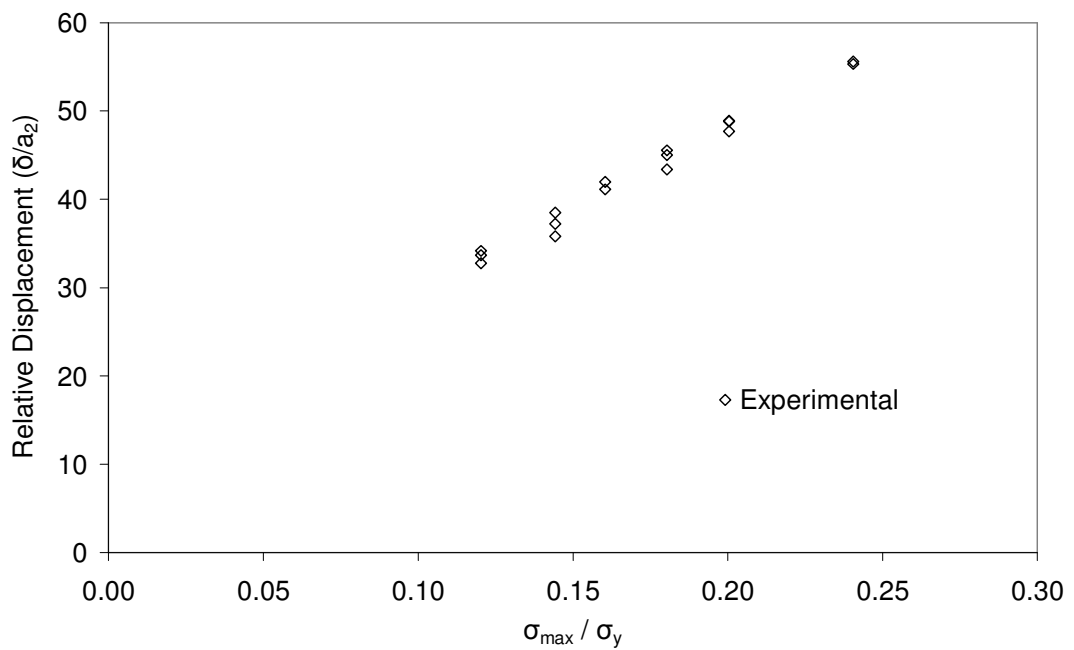


Figure 4.21. The measured OP relative displacement range (non-dimensionalised) against the maximum applied OP stress of the MRS.

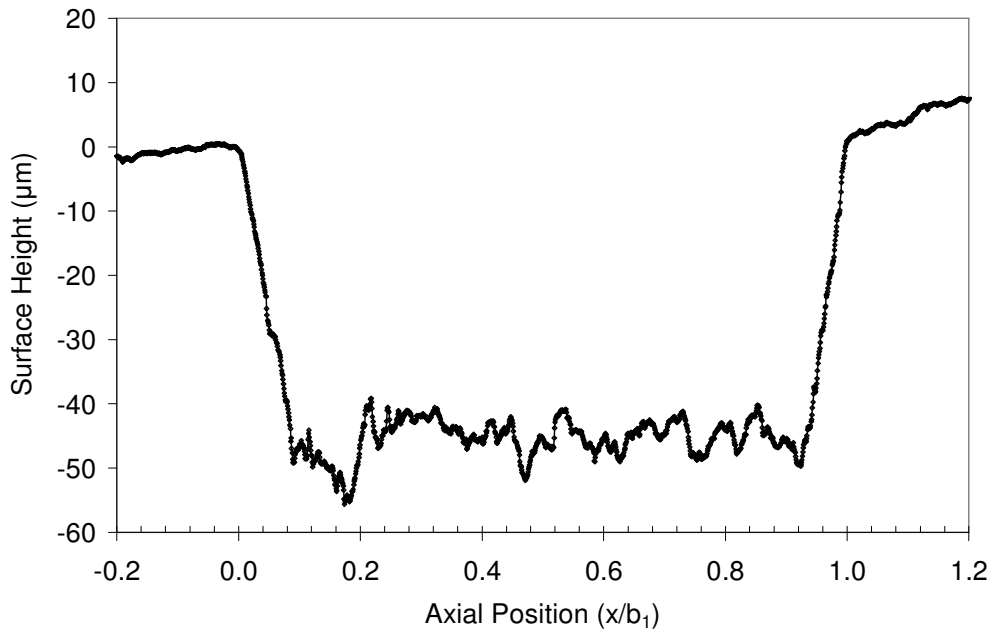


Figure 4.22. Axial surface profilometry trace at  $x/a_2 = 0$  from test SC2.

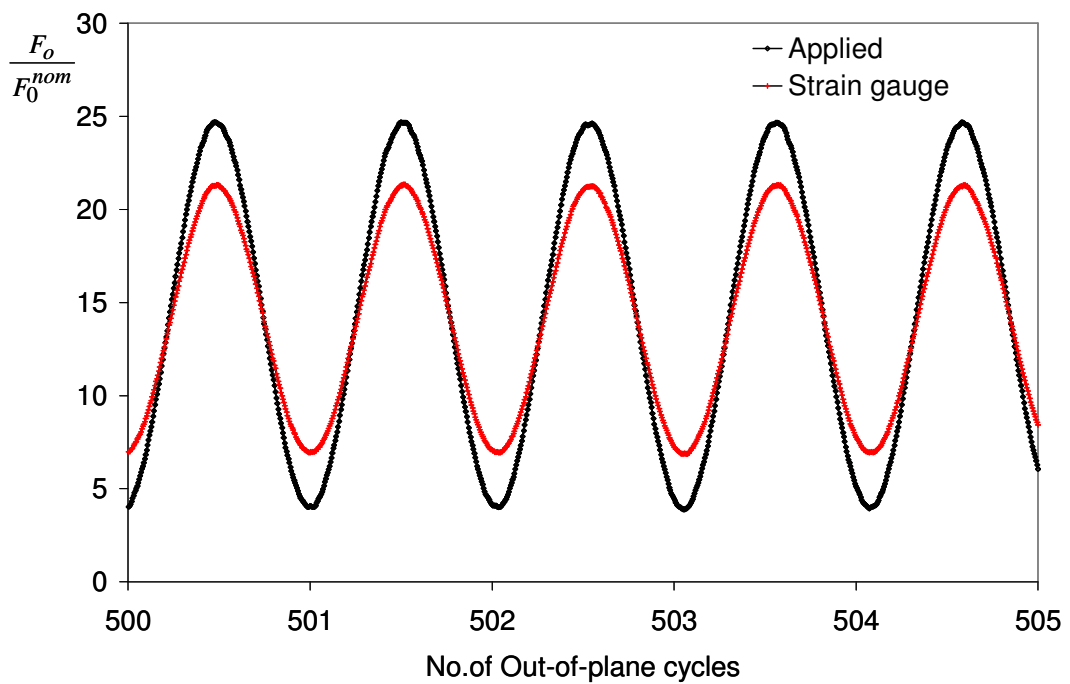


Figure 4.23. The measured (non-dimensionalised) applied OP force and measured strain gauge force after 500 OP cycles of test BR1.

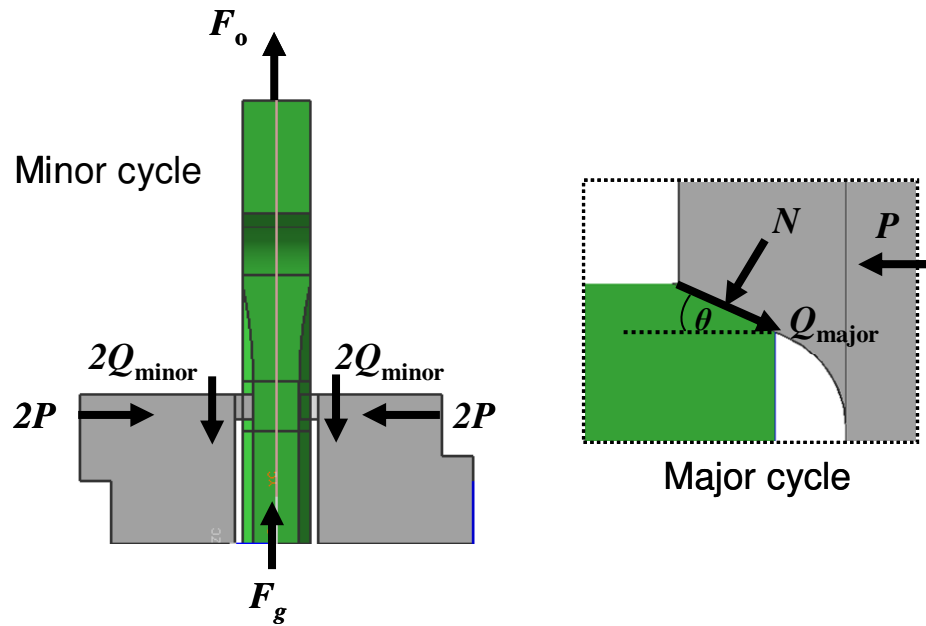


Figure 4.24. The half-section free-body diagram of the MRS.

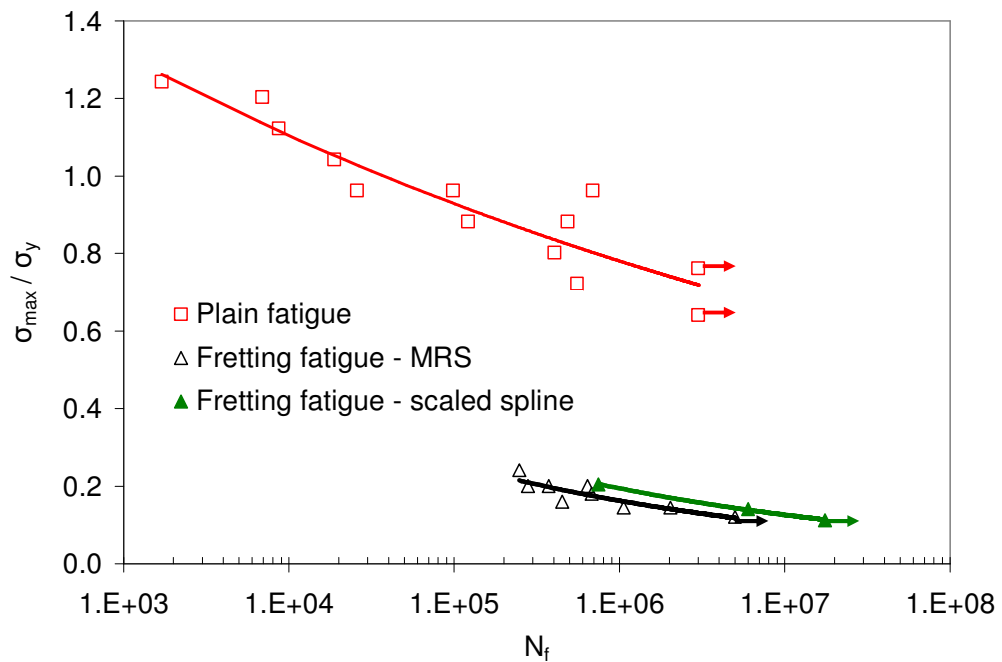


Figure 4.25. Comparison of (i) MRS fretting fatigue tests, (ii) scaled spline fretting fatigue tests and (iii) uniaxial ( $R_\sigma = 0.1$ ) plain fatigue stress-life data for the spline material, showing significant effect of fretting on fatigue life.

Arrows indicate test run-outs.

# Finite Element Modelling

## 5.1 Introduction

The experimental results from the representative testing allowed the fretting and fretting fatigue behaviour of the spline coupling to be explored. The uniaxial representative specimen (URS) facilitated the evaluation of candidate spline materials and the fretting fatigue lives from the multiaxial representative specimen (MRS) showed a good correlation with the scaled spline testing. In order to provide further insight with respect to these results, the finite element (FE) method will be applied to simulate the experimental behaviour. This will allow the key fretting fatigue variables experienced during the tests to be discerned, giving invaluable insight into the processes governing the fretting fatigue phenomenon.

The development of a global FE model of both the URS and MRS is first described. The model of the URS makes it possible to perform a comparison between the predicted and measured rig displacement data, permitting the inference of the coefficient of friction (COF) using an inverse method. The measured data from the MRS test rig allows the global model to be validated. A local sub-model is then introduced, that consists of a high mesh resolution. Finally, the sub-surface stress components of the fretting specimen of the MRS are presented, demonstrating the effect of various important parameters.

## 5.2 URS FE modelling and results

The global FE model of the URS was introduced in Chapter 3 and was used to show that a representative scaled spline contact pressure was obtained for the rig tests. The analysis techniques will now be further elucidated, followed by the presentation of the results.

In order to capture the fretting behaviour, frictional contact must be simulated between the contacting specimens. The contact can be solved in the ABAQUS FE code with the finite sliding or small sliding formulations. The general, finite sliding formulation is able to handle relative slip that is of a greater magnitude than the dimensions of the individual elements in contact. The small sliding assumption restricts the contact constraints to a single node at the beginning of the analysis, resulting in improved solution times over the finite sliding formulation, but can only be used with small slip magnitudes. Due to the large magnitude of the contact slip expected for the analyses of the URS, the finite sliding formulation was specified. In addition to the contact formulation, the method of enforcing the frictional constraints must be specified. This can be realised via the Lagrange or penalty method. The behaviour of the Lagrange and the penalty method are shown graphically in Figure 5.1. The Lagrange multiplier strictly enforces the condition of stick when the shear traction is below the critical value ( $Q < \mu N$ ). The discontinuity can cause convergence difficulties, especially for complex three-dimensional analyses. The penalty method was therefore implemented for the analyses presented here. The penalty method allows a finite slip when the shearing traction is below the critical value. The amount of slip allowed is termed the allowable elastic slip,  $\delta_{aes}$ , and must be specified for the analyses. It should be noted that a very small value of  $\delta_{aes}$  leads to an effectively converged solution with respect to the Lagrange multiplier. A value of  $\delta_{aes}/a_2 = 2.8 \times 10^{-4}$  was used

for the analyses, as utilised in Refs. [10, 116]. Furthermore, a convergence study of this parameter was conducted for the MRS (detailed later in the chapter) and convergence was attained with this magnitude of  $\delta_{aes}$ . More detailed results from the FE modelling of the URS will now be presented.

### 5.2.1 Inverse calculation of COF

Relative displacement data was acquired from the URS using linear variable differential transformers (LVDTs) for the rig tests and can aid characterisation of the fretting behaviour. In general, tests were conducted with two LVDTs to measure the relative displacement of the load-arms. The FE model of the URS includes the location of the LVDT measurement points (shown in Figure 3.11), facilitating a direct comparison between the experimental and computational results. These global relative displacements are principally influenced by the elastic deformation of the load arms and the relative contact slip between the fretting specimens. The contact slip (and therefore the COF) is typically difficult to quantify directly due to the small magnitude and difficulty of implementing experimental measurement techniques at the contact interface. An inverse method can therefore be applied to circumvent this difficulty. The inverse method involves correlating computationally predicted data with the equivalent experimental data. The test conditions can then be inferred from the parameters that were used as the inputs into the model. In the case of the URS, a range of FE analyses were run using the loads applied in the rig tests, with a variation in the specified COF, and the resulting predicted global displacements compared with the LVDT test data. This permits the deduction of the COF between the fretting specimens from the individual material combination tests. With two LVDTs it is not possible to independently obtain the displacement behaviour at each contact. It was therefore assumed that each pair experienced the same conditions.

The FE analyses were solved with the S/CMV material properties for the fretting specimens, therefore neglecting the effect of the different material properties. With the vast majority of the global relative displacement contributed to by the elastic deformation of the load arms (of the same material for all tests) this assumption is deemed valid. Additionally, with dissimilar material combinations an elastic mismatch is produced between the two contacting specimens. The mechanics of this situation were addressed in detail in Ref. [58], where it is stated that the elastic mismatch leads to different tangential displacements between the two bodies in contact and the tangential shear tractions also influence the relative normal surface displacement. This coupling of the normal and tangential behaviour is neglected in the present work, meaning that the inferred slip values for the dissimilar material combination tests are approximate.

The results of the FE analyses are shown in Figure 5.2, where the predicted global relative displacement data is presented as a function of the COF for the applied rig loads. The predicted displacements were obtained from the positions indicated on the model of Figure 3.11 and doubled in order to account for the symmetry boundary condition. The corresponding magnitude of the maximum FE-predicted contact slip between the fretting specimens is also plotted in Figure 5.2. For clarity, and to indicate that with a ramping up of the load the relative displacement of the inner LVDT decreases (i.e. the inner arms move towards each other), the curve of the inner LVDT has been assigned a negative magnitude. It is observed that the relative displacements decrease with an increase in the COF, which is attributed to decreasing contact slip. All three curves show a bi-linear trend. This is due to the transition from full sliding to partial slip with increasing COF, causing an increase in the global stiffness of the assembly. The predicted running fretting condition is indicated in Figure 5.2, signifying stick, partial slip or full sliding

states. For the particular geometry and loading studied, the transition from full sliding to partial slip occurs at a COF of 0.7.

Piecewise-linear functions were fitted to the results of Figure 5.2. The experimentally measured relative displacement ranges (tabulated in Table 5.1) were then compared to the curves. The procedure may be visualised by drawing a horizontal line that corresponds to the experimental measurement and finding the intersection with the curve of either the inner or outer load arm. The corresponding COF values may then be read off vertically and noted. As a sample calculation, a measured relative displacement range of 200  $\mu\text{m}$  for the outer LVDT leads to a predicted COF of 0.49. The method was conducted for both the inner and outer LVDT data for all of the material combinations, with the results tabulated in Table 5.1 (the material combinations in the table are ordered according to the wear ranking of Chapter 4, with the most wear resistant first). It is observed that the inner LVDTs consistently predict a higher COF than the outer LVDTs (by approximately 0.2 typically). An average of the inner and outer LVDT-based COF values was therefore calculated to the nearest 0.05 and given in Table 5.1. The greatest of the averaged COFs was found to be 0.90 for three of the combinations, and the lowest was found to be 0.50 for Aermet against itself. The S/CMV against S/SMV test gave a COF of 0.85. This value is significant for the analysis of the multiaxial representative specimen that will be conducted later in the present thesis. From the results of the inferred (average) COF, it is ascertained that three of the tests were run in the full sliding condition (Ti-6/4c against itself, Aermet against itself and Ti-6/4c against Ti-6/4) and the remaining tests in the partial slip state. No fretting fatigue cracks were observed from the tests in the full sliding regime.

Room temperature fretting wear tests have previously been conducted using the cylinder-on-flat geometry [118]. For the non-nitrided S/CMV versus non-nitrided S/CMV combination, test conditions consisted of a peak Hertzian contact pressure of 550 MPa and an applied tangential stroke of 50  $\mu\text{m}$  (full sliding) at a cyclic frequency of 20 Hz. After 18,000 cycles the COF was found to be 0.91 for S/CMV versus S/CMV. This is in good agreement with the value of 0.85 found here. For the Inco versus Inco combination, the COF was determined to be 0.94 in Ref. [118], with the same conditions as for the S/CMV versus S/SMV test but with a peak Hertzian pressure of 784 MPa and after 200,000 cycles. This is in excellent agreement with the value of 0.90 found in Table 5.1.

### 5.2.2 Wear coefficient for S/CMV

With the tests utilising the multiaxial representative specimen conducted on S/CMV, the Archard wear coefficient is estimated for this material from the measured wear volume,  $V$ , of the URS test (see Chapter 4). The Archard equation is given by:

$$k = \frac{V}{SP} \quad (5.1)$$

where  $k$  is the dimensional wear coefficient,  $S$  is the total accumulated sliding distance and  $P$  is the applied normal load. The dimensional wear coefficient represents the volume of material removed per unit sliding distance per unit normal load. The S/CMV against S/CMV test of the URS (with a representative spline normal load) gave a worn volume of 6,675  $\mu\text{m}^3$ . With a slip amplitude of 15  $\mu\text{m}$  determined from the inverse method (see Table 5.1), this gives  $k = 3.6 \times 10^{-8} \text{ MPa}^{-1}$ . This can be compared with the measured value of Ratsimba et al. [107], for the scaled spline coupling using a nitrided against non-nitrided combination. The results of Ratsimba et al. indicated a wear

coefficient of  $k = 7.0 \times 10^{-8} \text{ MPa}^{-1}$  for no added lubrication and  $k = 1.0 \times 10^{-8} \text{ MPa}^{-1}$  as a typical average for light lubrication. The coefficient found here is therefore in reasonable agreement with the previous findings; the slightly lower value could be due to the higher surface hardness of the nitrided material employed in the original study.

### 5.3 MRS major cycle FE analysis

The global FE model of the MRS was introduced in Chapter 3 and was used to show that a representative scaled spline contact pressure was obtained for the rig tests. More detail of the modelling will now be introduced, followed by examination of the results. As for the URS, frictional contact constraints under major cycle loading must be implemented for the MRS. The following section will determine a converged value of the allowable elastic slip ( $\delta_{aes}$ ) for the FE analyses, by examining the global major cycle force-displacement ( $F$ - $\delta$ ) hysteresis loops. For all of the analyses, the small sliding formulation was specified, as the relative slips were less than the element length in the contact. Contact was defined between the other rig components, e.g. the loading clasps to bridge interfaces as shown in Figure 5.3. The contacts between the loading pins were tied to ease the solution process. Both feet are permitted to slip in the global model (governed by  $Q > \mu P$ ) under major and minor cycle loading. For all of the analyses, the COF is assumed to be constant throughout the fretting contact zone.

#### 5.3.1 In-plane force-displacement loops

The MRS test rig has two LVDTs mounted onto the loading clasps. These allow the in-plane, or IP load (major cycle)  $F$ - $\delta$  loops to be obtained experimentally. The global FE model incorporates the LVDT fixtures (Figure 5.3), allowing a direct comparison of the measured and predicted  $F$ - $\delta$  loops, with the aim of validating the model. The model includes the deformations

and frictional behaviour of the loading components. Mesh refinement was conducted and the solution was deemed suitably converged according to the change in predicted IP relative displacements. Several analyses were run, with increasing mesh refinement, resulting in the converged model containing a total of 62,555 nodes and 215,336 elements, as shown in Figure 5.4. A total of 20 increments were solved per step, to adequately capture the non-linear response. The analysis was run for three complete cycles, as a frictional contact model experiences frictional shakedown (as discussed in Ref. [120]).

A comparison of the experimental (from Ref. [10]) and predicted IP relative (converged) displacements are plotted in Figure 5.5. It is observed that the analysis with a COF of 0.6 for both the specimen to pad and bridge to loading clasps interfaces predicts an overly stiff global response. The effect of the COF on the contact surfaces between the bridges and loading clasps was then investigated. As stated earlier, the contacts between the loading pins were tied to ease the solution process. With the COF for the bridge to loading clasps modified to a value of 0.3, it is seen that there is an increase in the predicted global compliance, which matches the experimental result.

For the penalty method, the allowable elastic slip must also be determined. A convergence study was pursued to determine a value of  $\delta_{aes}$ , extending down to values as low as  $\delta_{aes}/a_2 = 5.6 \times 10^{-5}$ . As seen in Figure 5.5, there is only a small increase in the predicted hysteresis loops between the two allowable elastic slip magnitudes. Therefore a value of  $\delta_{aes}/a_2 = 2.8 \times 10^{-4}$  was deemed to have converged and used for all of the subsequent FE analyses. This is in agreement with the previous study in Refs. [10, 116].

The final converged FE-prediction is shown in Figure 5.6, along with the FE-predicted curve of the previous study [10]. The new FE prediction captures the range well. This is due to the modelling of more of the rig support structures and their interfaces with the fretting bridges. It is also seen that the modelling of the hysteresis has been improved, although it has not been fully captured. Possible sources of this difference could arise from:

- Tolerances to allow for clearance fits at loading pins,
- Misalignments,
- Other sources of 'slack' in the system.

The use of a static and dynamic friction model, as discussed in Ref. [32], was investigated but found not to have a significant effect on the results.

### **5.3.2 Contact slip distributions**

The contour plot of contact slip for a specified in-plane COF of 0.6 (and clasp to bridge COF of 0.3) is given in Figure 5.7, where the magnitude is non-dimensionalised according to  $a_2$ . Full slip occurs across the entire contact, with the greatest magnitude occurring at the position of  $x/a_2 = 1.0$  and  $z/b_1 = 0$ . This is attributed to bending of the fretting bridges upon application of the IP load, causing the inner edge of the pad ( $z/b_1 = 0$ ) to 'dig in.'

## **5.4 MRS minor cycle FE analysis**

Experimental variations of the surface conditions (and hence COF) will inevitably arise between the different contacts in the MRS. It has been suggested that this could lead to accommodation of the load by some of the contacts, leading to contact sticking, whilst the remaining contacts slip [58]. Whilst this could occur, it is experimentally observed that surface wear occurs on all of the contacts, suggesting that similar conditions exist at all of the

contacts. Furthermore, the critical fretting fatigue crack of the specimen was also found to initiate at different contacts in the different experimental tests, supporting this assumption. As a result, all of the contacts in the FE model are permitted to slip under IP and OP cycling, governed by the Coloumb friction law when  $Q > \mu P$ . Following from the findings of the previous section, an out-of-plane COF of 0.9 will be used for the majority of the analyses. This is due to the steady-state COF of 0.85 inferred using the URS for S/CMV against S/CMV and the value of 0.91 for the same combination from cylinder-on-flat testing of Ref. [118]. The chosen value of 0.9 will therefore give slightly conservative results. The effect of the COF on the important variables will also be investigated later in this Chapter.

#### 5.4.1 Frictionless analysis

The accuracy of the solution can be investigated by employing frictionless contact, providing validation of the finite element mesh. The FE-predicted OP displacements can be compared with a one-dimensional Hooke's prediction (neglecting Poisson ratio effects) as given by:

$$\delta_{nom} = \frac{L(F_{max} - F_{min})}{AE} \quad (5.2)$$

where  $F$  is the applied bulk fatigue load,  $A$  is the cross-sectional area and  $E$  the Young's modulus of the fatigue specimen. With frictionless contact,  $L$  is the distance from the axial specimen constraint at the top of the specimen to the set of contacts to be examined. The numbering convention of the MRS contacts is given in Figure 5.8. The predicted relative displacements for the MRS tests for the lower set of contacts are plotted in Figure 5.9. These values give the bound of maximum slip. It can be seen that the FE results agree well with the Hooke's law predictions, providing a validation of the mesh. In reality, friction acts at the contact interface to restrain the relative motion.

### 5.4.2 Out-of-plane force-displacement loops

The relative displacements on the MRS rig caused by out-of-plane (minor cycle) loading were recorded and shown in Chapter 4. These experimental relative displacements may now be compared with the FE-predicted values. Firstly, it is important that the correct OP boundary conditions are applied to the FE model. Frictional force transfer occurs from the fretting specimen into the fretting bridges, meaning the loading clasps must be appropriately constrained. For the MRS test rig, the bridges are attached via loading arms to a motor and torque converter. This assembly rests on a greased bed that allows free movement in the surface plane. It is not fixed to the bed in the out-of-plane direction and therefore given sufficient force the assembly could be lifted off the surface. The FE model extends to the loading clasps but does not include all the fixtures up to the motor. The bridges can therefore be classed as floating. In order to ensure convergence of the FE model, an axial linear spring (SPRING1 in ABAQUS) attached to the end of the loading clasps will be able to model the rig boundary conditions. Spring stiffness' down to  $0.01 \text{ Nmm}^{-1}$  were run and found not to deviate from the solution with a spring stiffness of  $100 \text{ Nmm}^{-1}$  and therefore a stiffness of  $100 \text{ Nmm}^{-1}$  was used for the analyses presented here. A summary of the boundary and contact conditions of the MRS global FE model is shown in Figure 5.10.

The positions that the displacements were evaluated are labelled in Figure 5.11. The comparison of the measured (from Chapter 4) and predicted OP displacements is shown in Figure 5.12 for  $\delta_{A-B}$ . It is observed that a good correlation is obtained in relation to the slope of the curves, but there is an offset which gives lower FE-predicted displacements. This could arise from a number of sources, with the following factors deemed the most significant:

- Tolerances and clearances,

- Angular error due to misalignment of the LVDT bracket.

The COF of the bridge to fretting specimen contacts was found to have a negligible effect on the predicted OP relative displacements, due to the majority of the displacements being caused by elastic deformations.

### 5.4.3 Contact slip distributions

Figure 5.13 shows contour plots of the predicted out-of-plane slip for the minimum and maximum applied OP load cases for a COF of 0.9. It is observed that there is a region of stick at the inner edge-of-contact. This is attributed to bending of the bridges on application of the in-plane load. The increase in the OP load is seen to decrease this stick zone. As fretting fatigue failures were observed at the  $z/b_1 = 1$  position, the contact slip in this region plays a significant role in the initiation of the critical crack. Additionally, with reference to Figure 4.22 and with the prediction of full slip from IP cycling (major cycle) in Section 5.3.2, it is suggested that the majority of the wear on the fatigue specimen occurs from cycling of the IP load. This highlights the multiaxial nature of the problem.

## 5.5 Development of MRS FE sub-model

A fine mesh is not computationally practical for the global model of the MRS. Sub-modelling therefore, is a technique that allows a global model to be solved with a relatively coarse mesh. A sub-model of a region is then created that is significantly more refined than that of the global model [121]. A separate analysis is subsequently solved, with the complete boundary conditions for the sub-model interpolated from the displacement field of the global model. In ABAQUS, the nodes at the boundaries of the sub-model are specified as node sets, allowing identification of the displacements to be applied from the global model.

Due to geometric symmetry, a quarter section of the MRS specimen and one pad foot contact are modelled for the sub-model, as shown schematically in Figure 5.14. This assumes the same conditions for upper and lower contacts. The sub-model consists of linear brick elements (C3D8) with full integration, resulting in 61,845 nodes and 55,800 elements. The mesh is biased towards the contact edges, with the smallest element having dimensions of 33 x 29 x 18  $\mu\text{m}$ . The dimension into the depth of the specimen is kept constant at 33  $\mu\text{m}$  across the near-contact surface region. The transverse and axial sections of the mesh are shown in Figure 5.15 and Figure 5.16, respectively. The mesh was arrived at by the approximate matching of the smallest element size with the material grain size. This is discussed in more detail in the following chapter.

The sub-model has the displacement boundary conditions imposed from foot 1 (as shown in Figure 5.8) for the results presented below. The model was solved with isotropic elastic-plastic material properties, with the properties the same as used for the global model. Coulomb friction was also implemented using the penalty method as was done for the global model. When implementing frictional constraints using the penalty method, it is essential that the specified allowable elastic slip is the same for the global and sub-model analyses [122]. This ensures consistent contact compliances between the two analyses. As noted in Ref. [122], the default value of the allowable elastic slip in ABAQUS is determined as a fraction of the characteristic contact surface face dimension [115] and therefore will likely be different between the two analyses. The allowable elastic slip, therefore, should be specified directly as a magnitude.

## 5.6 MRS stress and strain distributions

It is known that the stress state is a key factor for the total fretting fatigue life of a component. The direct axial stress is commonly associated with

controlling fatigue crack initiation and propagation. Furthermore, the multiaxial nature of the stress and strain field of the MRS will influence the total life. Consequently, the other stress components will also be investigated. A three-dimensional coordinate transformation was conducted for the sub-model in order to align the axes with the contact flank. The transformed axes form a right-hand set and are shown in Figure 5.14. Consequently the transformed (local) stresses are presented in the remainder of this chapter. The axial stress distributions are determined at the tip of the fretting specimen ( $x/a_2 = 0$ ).

The response of the sub-model was checked to ensure consistency with the global model. Contour plots of the local variables for the global and sub-model were compared at the boundaries of the sub-model and were found to be consistent. Additionally, the contact pressure distribution from the global and sub-models were examined (at maximum applied IP load) and an example is shown in Figure 5.17. A good agreement is obtained between the two, although the sub-model shows an increased magnitude at the edge-of-contact, which is attributed to the finer mesh of the sub-model. It is also seen that there is almost lifting off of the edge of the pad at the  $z = b_1$  edge-of-contact position.

The FE global and sub-model analyses were solved across the out-of-plane loads corresponding to the experimental tests, with a COF of 0.9. Comparisons of the axial stress distributions of  $\sigma_{zz}$  for the maximum and minimum applied IP loads are shown in Figure 5.18 and Figure 5.19. It is seen that the maximum occurs at the inner edge of the pad ( $z/b_1 = 0$ ) for the maximum applied in-plane load. The peak then switches to the outer edge of the pad for the minimum applied load. Whilst the stress (and strain) state is complex, varying throughout the load cycle, a comparison of the stress state

gives insight into the failure location. The peak stress magnitude at the edge-of-contact, although similar in magnitude at the minimum and maximum applied IP load, is compressive at the maximum applied load and tensile at the minimum applied load. This tensile stress peak at the  $z/b_1 = 1$  position is in excellent agreement with the observed experimental failure location. It is also interesting to note that plasticity is predicted for the maximum applied IP load, but macroscopic elastic material behaviour is predicted for the minimum applied IP load.

## 5.7 The effect of varying the parameters

### 5.7.1 Bridge gap

One of the experimental tests reported in Chapter 4 was tested with a reduced bridge span of 20 mm, as defined in Figure 5.20. Consequently, The FE global model of the MRS was modified to include the new bridge geometry, and the position of the sub-model was translated axially to reflect this. The effect of the bridge span on the predicted stress distributions is shown in Figure 5.21. The axial  $\sigma_{zz}$  component is shown at the minimum applied IP load (for  $\sigma_{b\_max}/\sigma_y = 0.20$  and COF 0.9) and shows that there is a predicted decrease in the peak stress at the  $z/b_1 = 1$  position. This is attributed to the reduction in bending of the bridge for a span of 20 mm. This reduced stress for the reduced bridge span suggests that the critical fretting fatigue crack would initiate after an increased number of cycles. This is in agreement with the experimental test with this geometry, where the reduced bridge gap caused an increase in total fretting fatigue life.

### 5.7.2 COF

Figure 5.22 shows the effect of the COF on the  $\sigma_{zz}$  stress component at the specimen tip ( $x/a_2 = 0$ ) at the minimum applied in-plane load (load case of

$\sigma_{b\_max}/\sigma_y = 0.20$ ). It is observed that the distributions are qualitatively similar, but there is an increased peak stress at  $z/b_1 = 1$  with a COF of 0.9. As this is the observed axial position of failure, this highlights the importance of experimentally reducing the COF, which would be expected to lead to an increased number of cycles to initiate a crack. This could be done by ensuring a lubricated contact or by applying a low-friction coating. The same conditions are again plotted in Figure 5.23, but for the  $\sigma_{yz}$  stress component. As would be expected, the increased COF causes an increase in the predicted shear stress magnitude, particularly at the  $z/b_1 = 1$  edge-of-contact.

## 5.8 Summary of chapter

This chapter has described the detailed finite element modelling of the representative specimens. A number of FE analyses were solved to simulate the experimental tests of the uniaxial representative specimen, with a variation in the coefficient of friction. An inverse method was applied to the test results of URS, via comparison of the FE-predicted global relative displacements. This allowed the COF from the various material combination tests to be inferred. It was found that the inferred COF for S/CMV against S/CMV was 0.85. This value will be a significant parameter in the prediction of the fretting fatigue life of the URS and MRS tests. The AerMet against AerMet combination gave the lowest COF of 0.50. Additionally, full sliding conditions were predicted for a COF below 0.7, and partial slip for a COF greater than 0.7. For the multiaxial representative specimen, a global FE model was used to simulate the rig behaviour and an FE sub-model used to accurately predict the key fretting fatigue stress state. It was shown that the global model was able to capture the range of the experimental Force-displacement loop, validating the model. The stress distributions obtained from the sub-model indicate that the peak magnitude of the axial stress at the surface of the fatigue specimen occurs at  $z/b_1 = 1$ , in excellent agreement with

the experimental failure location. Additionally it was seen that the COF is a significant parameter for the predicted stress state in the MRS. The results from the FE analyses will now be used in the following chapter, where a total fretting fatigue lifing methodology is developed.

## 5.9 Tables

Table 5.1. The measured displacement range and inferred coefficient of friction (COF) and slip values, ordered according to the wear ranking.

Test ID	Material Combination		Inner LVDT		Outer LVDT		COF <sub>avg</sub>	FE-predicted slip (μm)
			Displacement range (μm)	Inferred COF	Displacement range (μm)	Inferred COF		
1	Inco718	SCMV	59	0.98	80	0.81	0.90	10
2	Inco718	AerMet	56	1.02	97	0.73	0.90	10
3	Inco718	Inco718	60	0.97	74	0.85	0.90	10
4	Ti-6/4	Ti-6/4	68	0.88	99	0.72	0.80	20
5	AerMet	SCMV	66	0.91	149	0.60	0.75	26
6	SCMV	SCMV	64	0.93	95	0.74	0.85	15
7	SCMV	Ti-6/4	60	0.97	94	0.74	0.85	15
8	Ti-6/4c	Ti-6/4c	78	0.78	131	0.63	0.70	31
9	Inco718	Ti-6/4c	62	0.95	100	0.71	0.85	15
10	Inco718	Ti-6/4	62	0.95	108	0.68	0.80	20
11	AerMet	Ti-6/4c	75	0.81	86	0.79	0.80	20
12	AerMet	AerMet	101	0.62	257	0.38	0.50	82
13	Ti-6/4c	Ti-6/4	86	0.69	125	0.65	0.65	42
14	SCMV	Ti-6/4c	67	0.90	99	0.72	0.80	20

Note: FE simulations assume S/CMV material properties for the fretting specimens, and neglect the elastic mismatch of dissimilar material combinations.

## 5.10 Figures

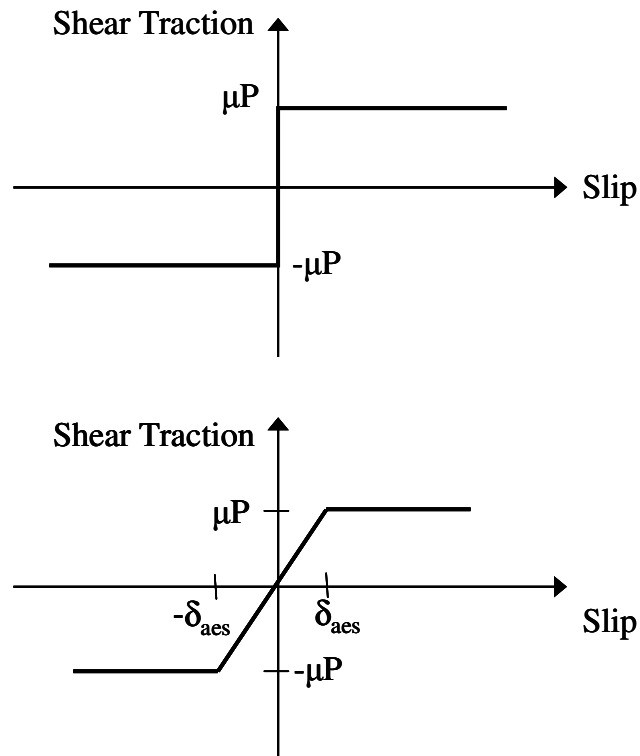


Figure 5.1. Comparison of the behaviour of the Lagrange and penalty method contact constraints.

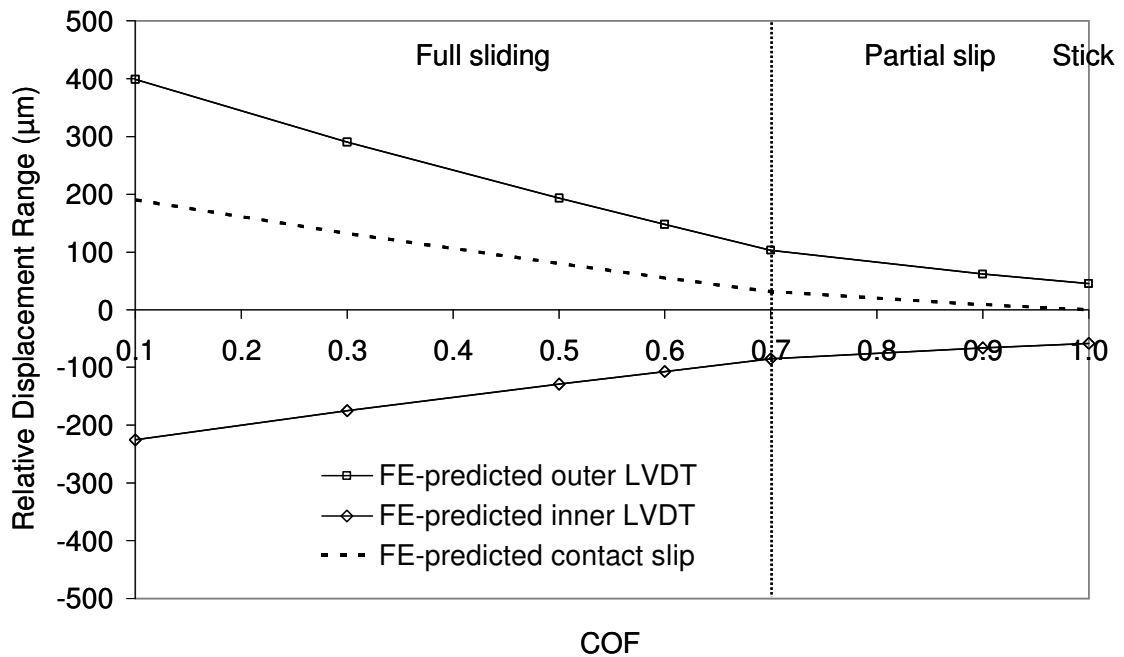


Figure 5.2. The FE-predicted global relative displacements and contact slip of the URS, allowing the application of the inverse method to determine the COF from the rig tests.

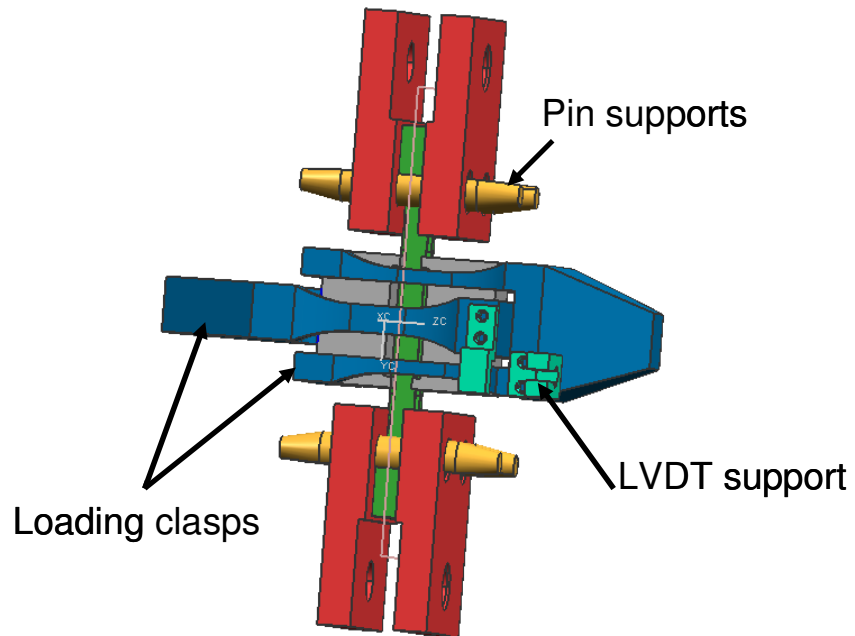


Figure 5.3. The global FE model of the MRS, with the support structures labeled.

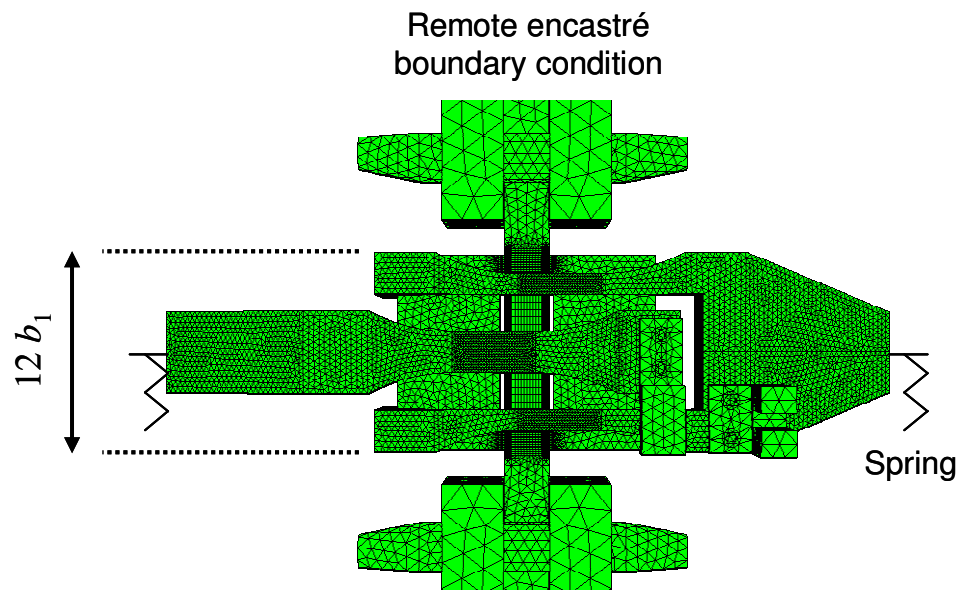


Figure 5.4. The refined mesh of the global FE model of the MRS.

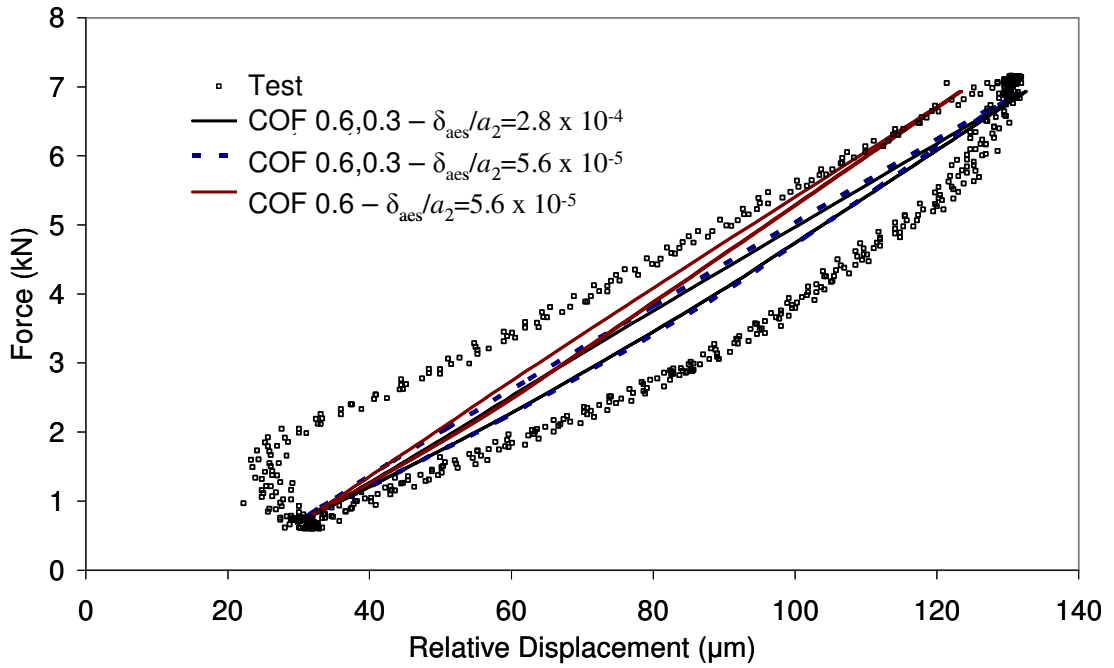


Figure 5.5. The effect of the COF (specimen to pad, loading clasps) and the allowable elastic slip on the global relative displacements.

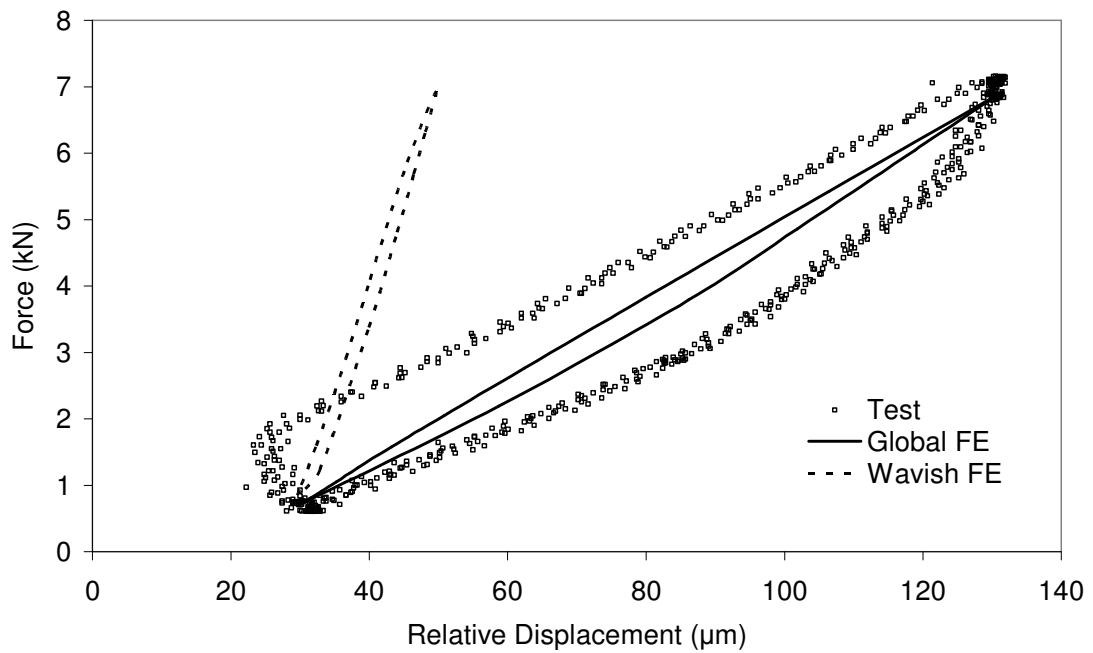


Figure 5.6. The measured and predicted stabilised IP force-displacement loops. The global FE-predicted loop utilises a COF of 0.6 and 0.3 between the other components. The result Wavish FE is from Ref. [10].

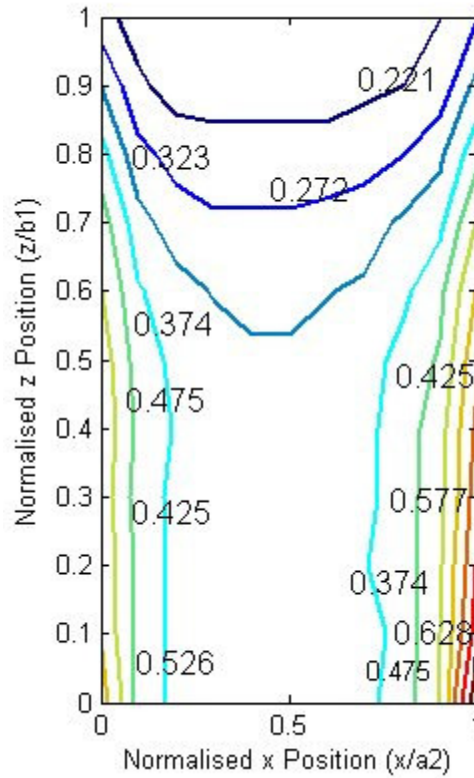


Figure 5.7. Contour plot of the in-plane (major cycle) contact slip for an applied load of  $F_i = 10.9 F_0^{nom}$ . Contact slip in  $\mu\text{m}$  is non-dimensionalised according to  $a_2$  (mm).

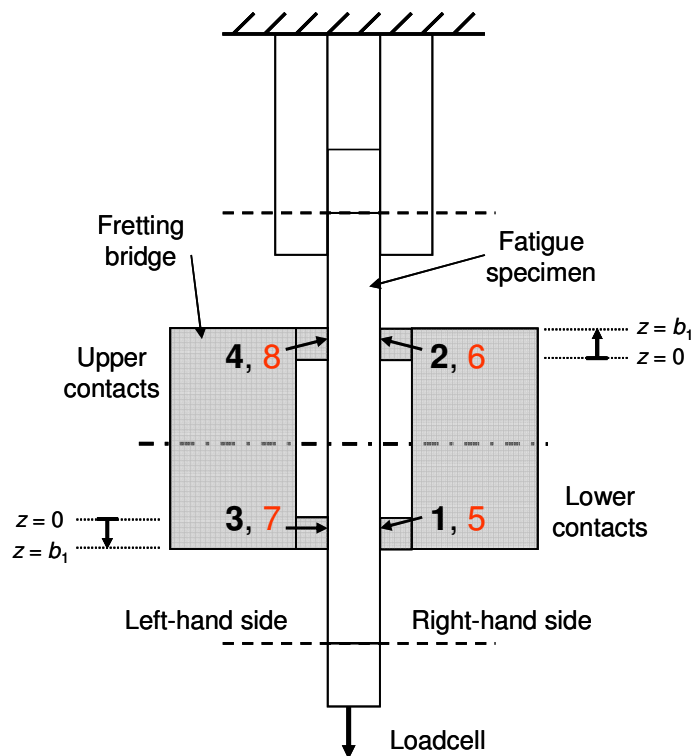


Figure 5.8. The tooth numbering convention of the MRS, where bold numbering indicates contact at the front of the rig.

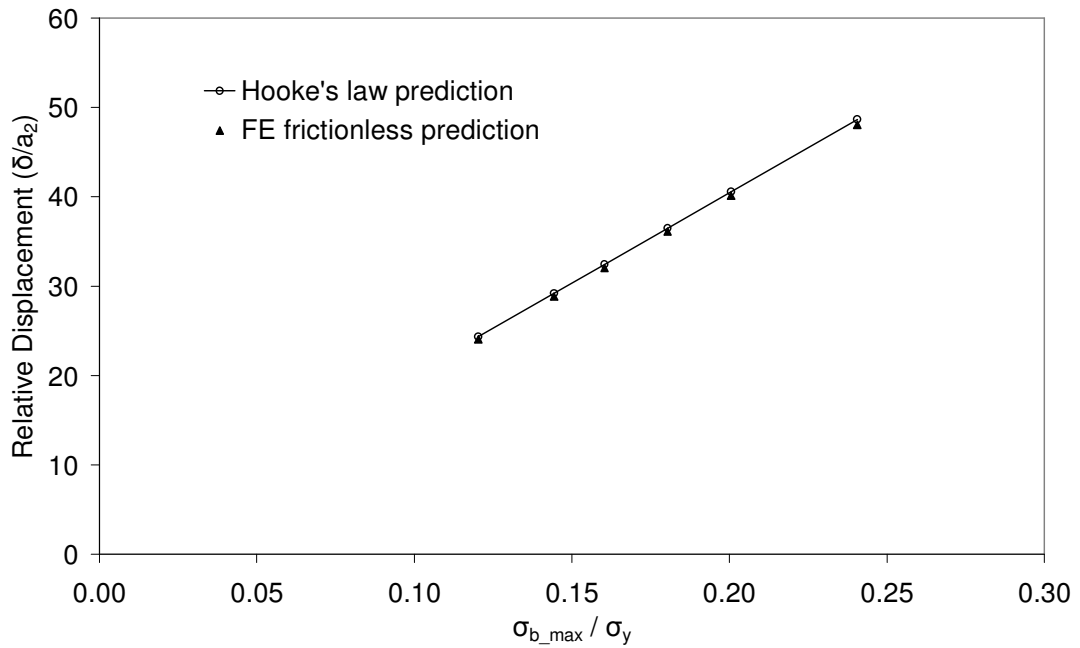


Figure 5.9. The Hooke's law predicted relative displacements against the maximum applied bulk stress, including the corresponding FE results for frictionless contact at the lower contacts (1, 3, 5 and 7).

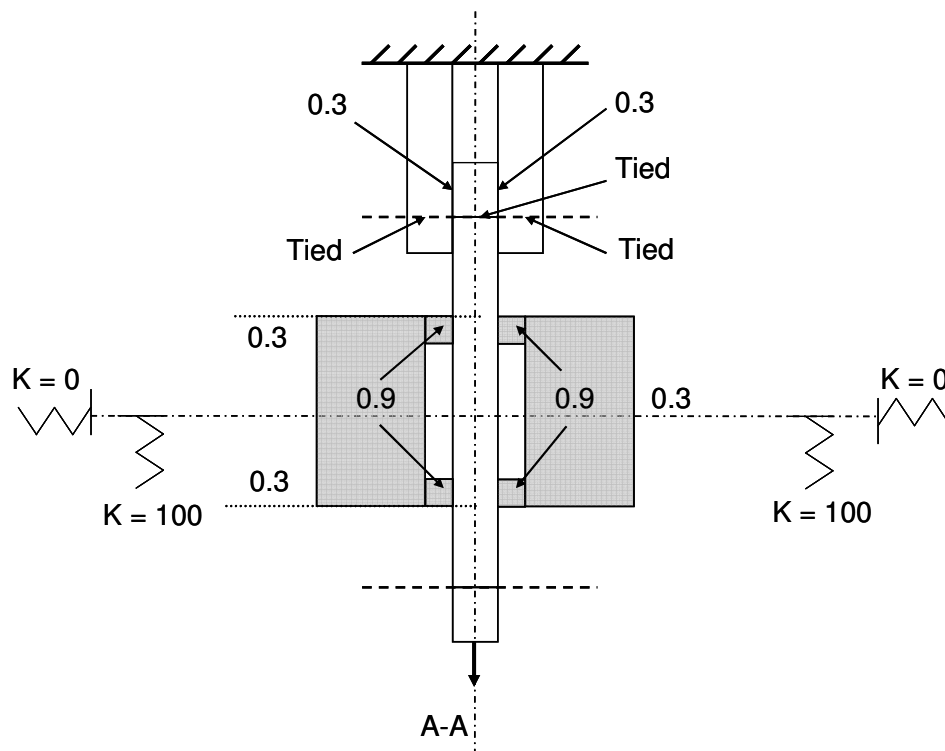


Figure 5.10. Schematic of the MRS, summarising the boundary and contact conditions.

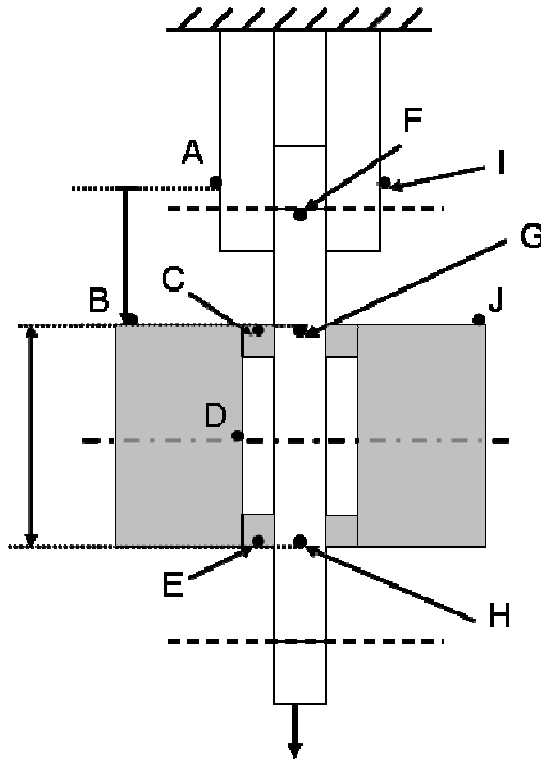


Figure 5.11. Schematic of the MRS, with the locations of displacements.

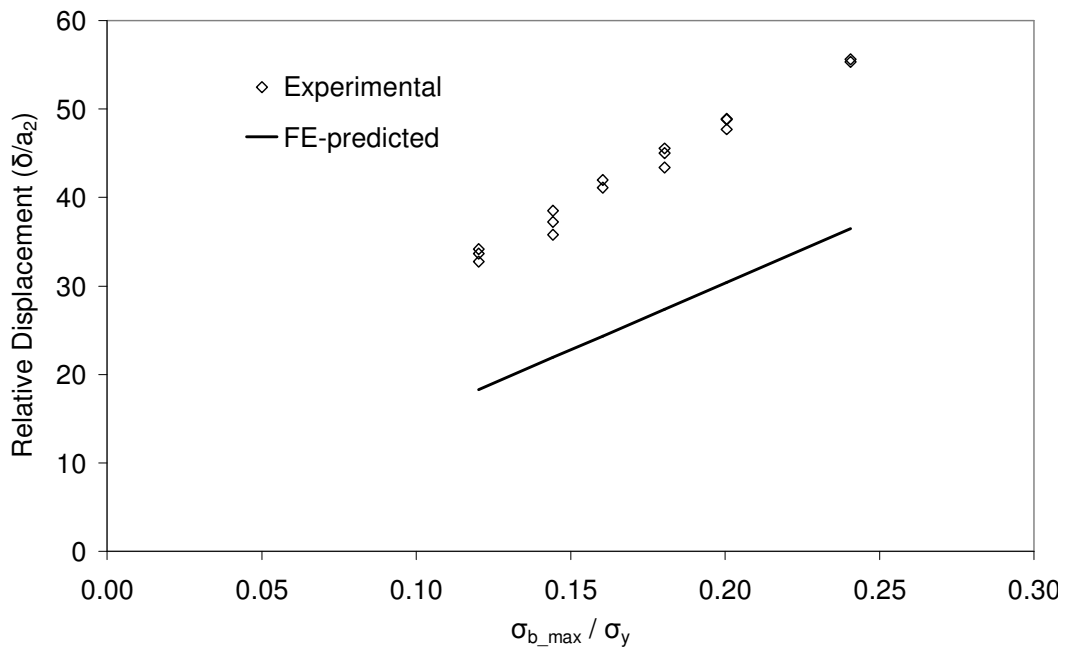


Figure 5.12. Comparison of the measured and predicted OP relative displacements. Predicted displacements from position A-B of Figure 5.11.

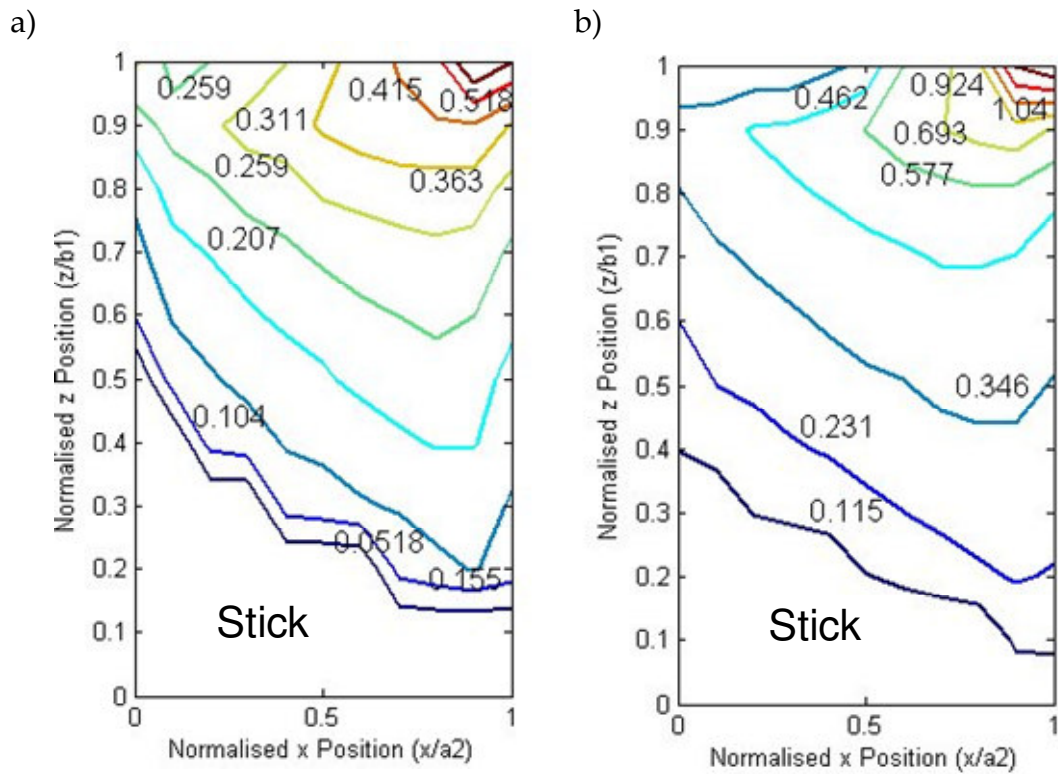


Figure 5.13. Contour plot of the out-of-plane (minor cycle) contact slip for: a)  $\sigma_{b\_max}/\sigma_y = 0.24$  and b)  $\sigma_{b\_max}/\sigma_y = 0.12$ . Contact slip in  $\mu\text{m}$  is non-dimensionalised according to  $a_2$  (mm).

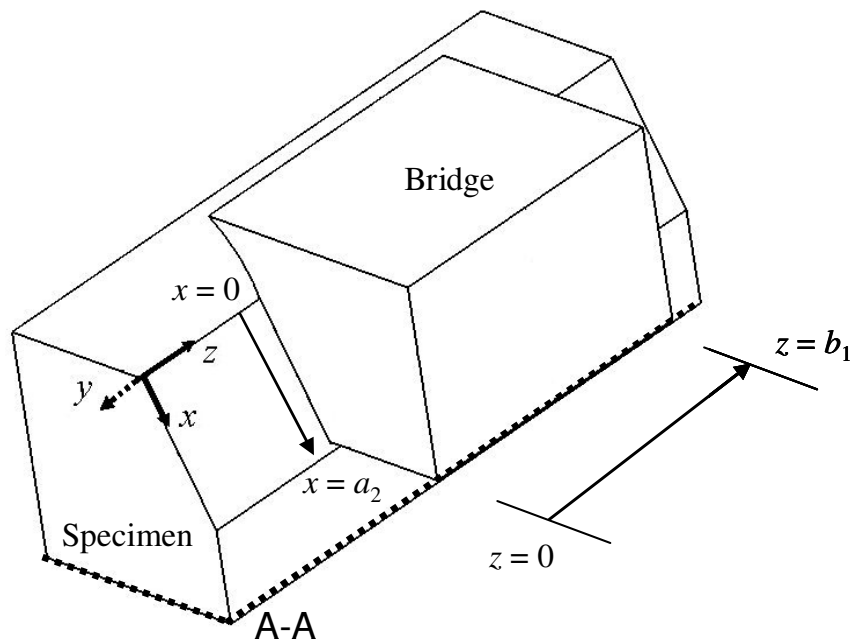


Figure 5.14. Schematic of the sub-model, including local coordinate conventions (on the specimen). The plane of symmetry A-A defined in Figure 5.10 is indicated by dashed lines.

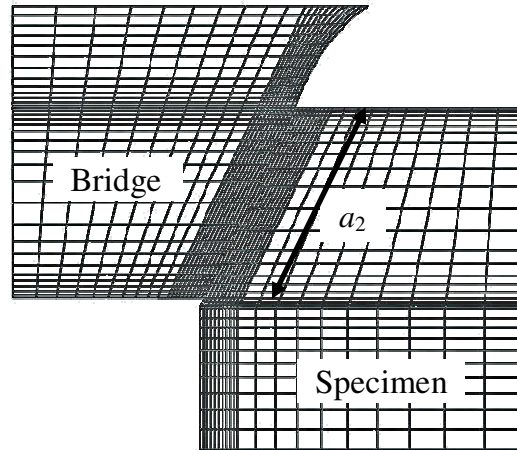


Figure 5.15. Transverse section of the refined sub-model mesh.

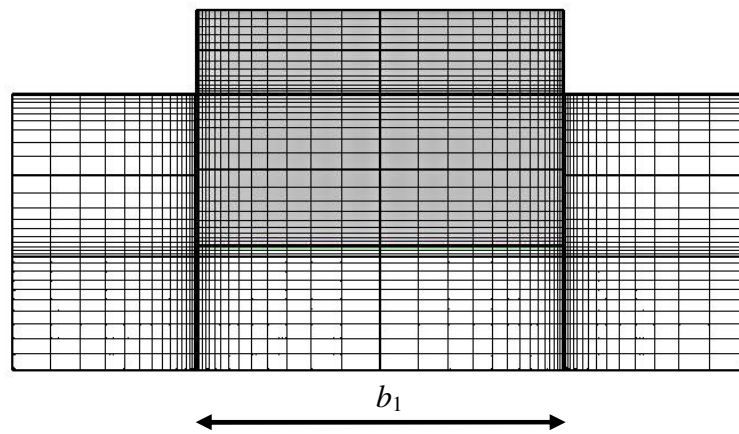


Figure 5.16. Axial section of the refined sub-model mesh (bridge is shaded in grey).

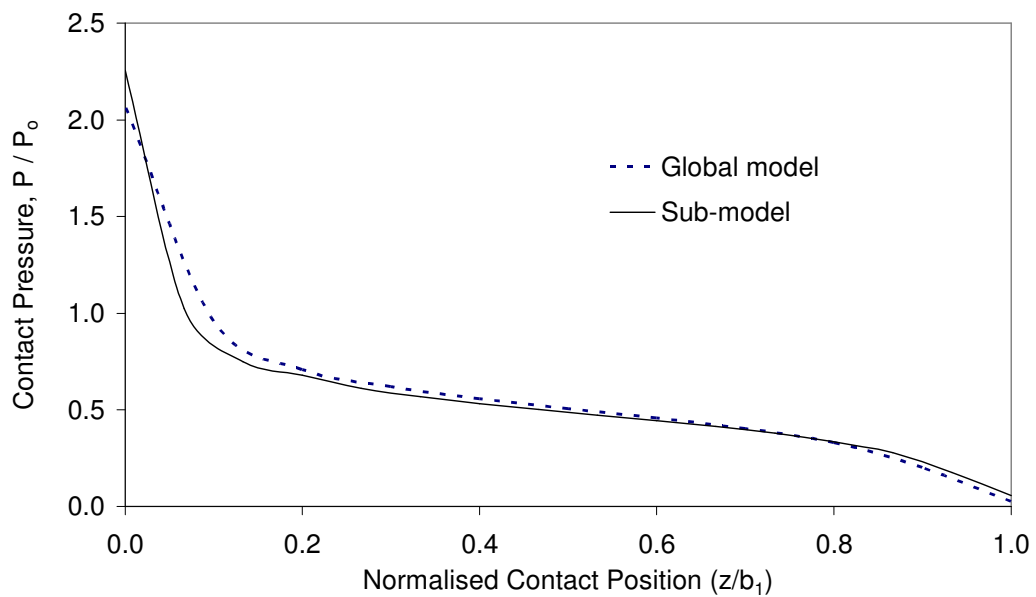


Figure 5.17. Example of the comparison of the contact pressure distributions for the global model and sub-model at  $x/a_2 = 0.5$ .

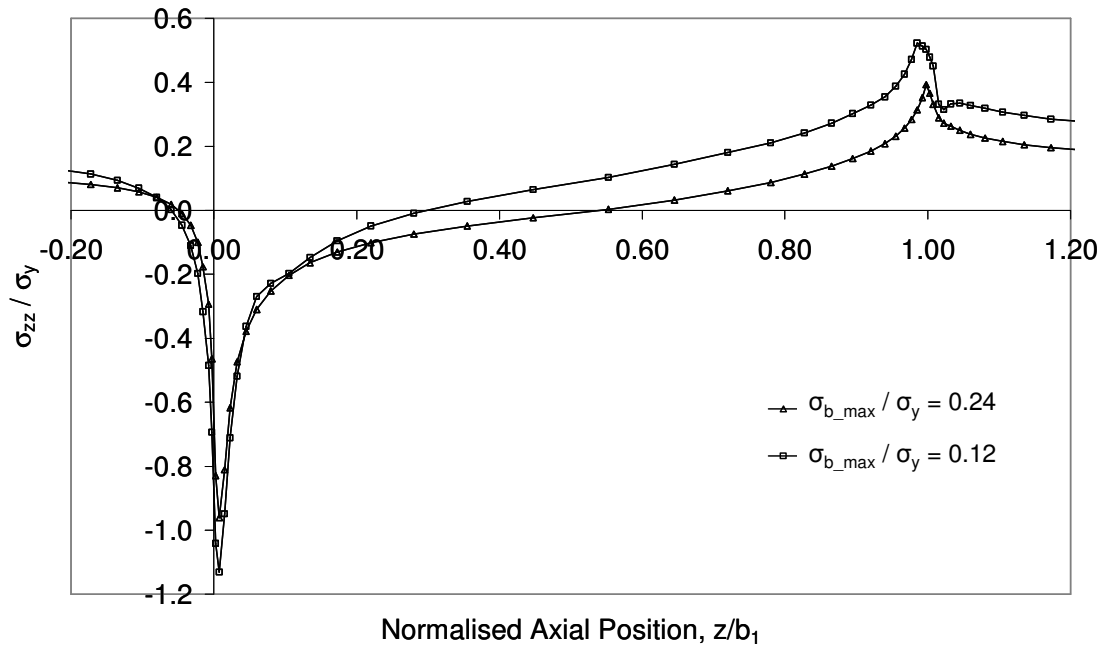


Figure 5.18.  $\sigma_{zz}$  stress component at specimen tip ( $x/a_2 = 0$ ) at maximum applied in-plane load.

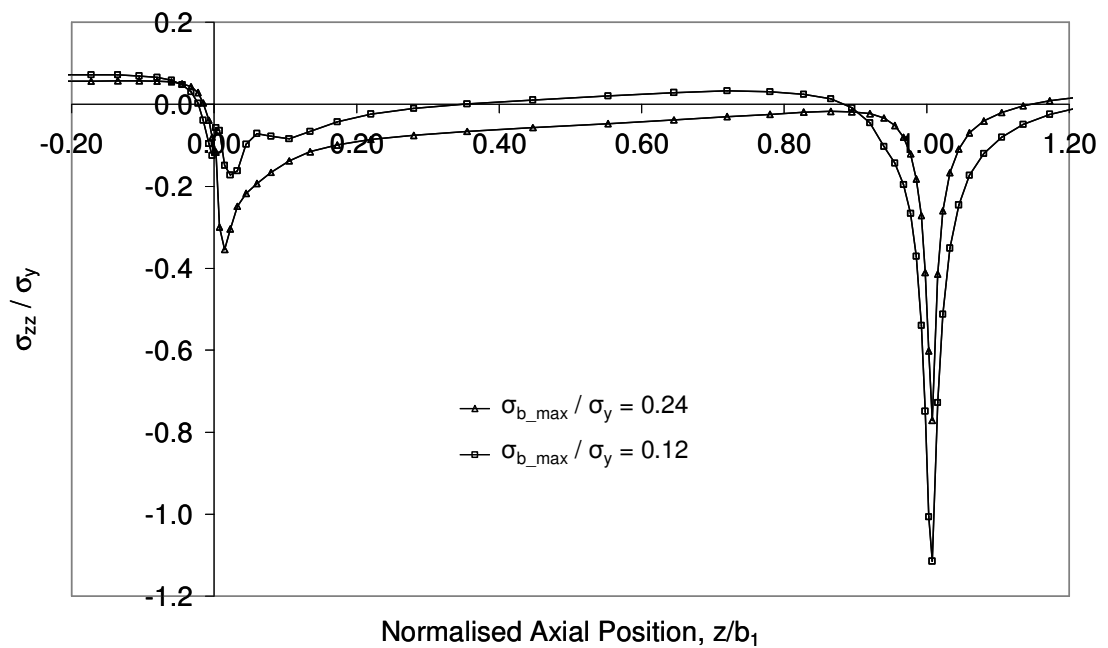


Figure 5.19.  $\sigma_{zz}$  stress component at specimen tip ( $x/a_2 = 0$ ) at minimum applied in-plane load.

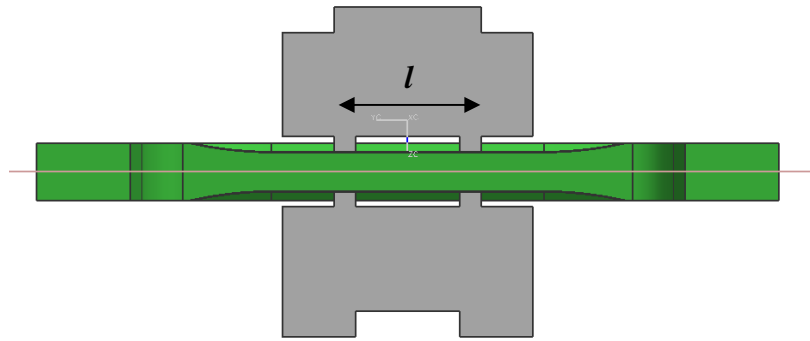


Figure 5.20. The axial side view of the MRS, indicating the bridge span definition.

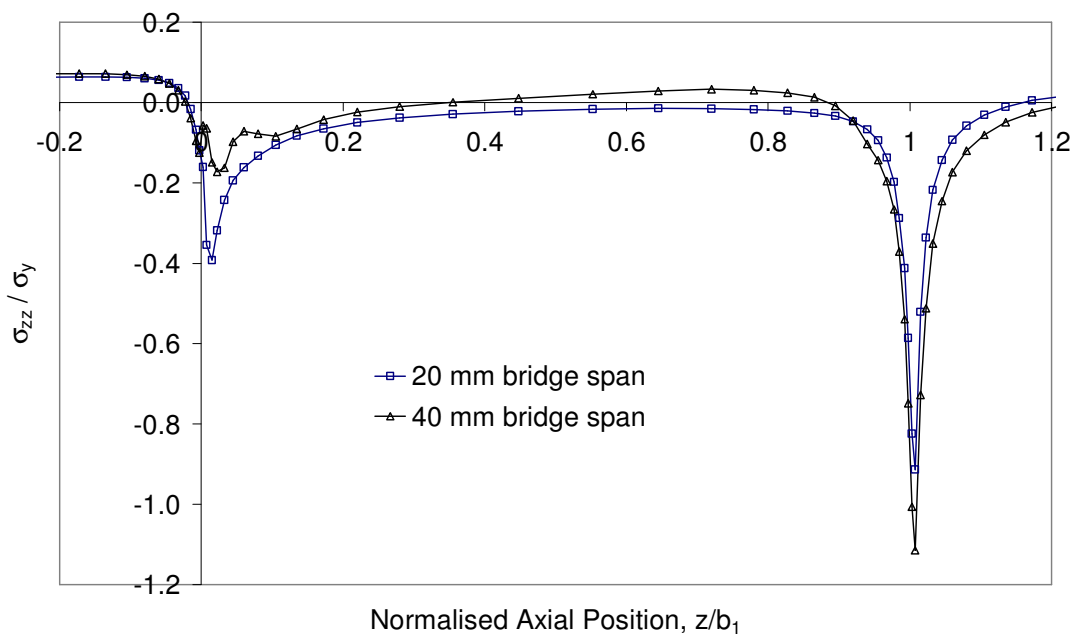


Figure 5.21. Comparison of the  $\sigma_{zz}$  stress component at specimen tip ( $x/a_2 = 0$ ) at minimum applied in-plane load for different bridge spans (load case of  $\sigma_{b\_max}/\sigma_y = 0.20$ ).

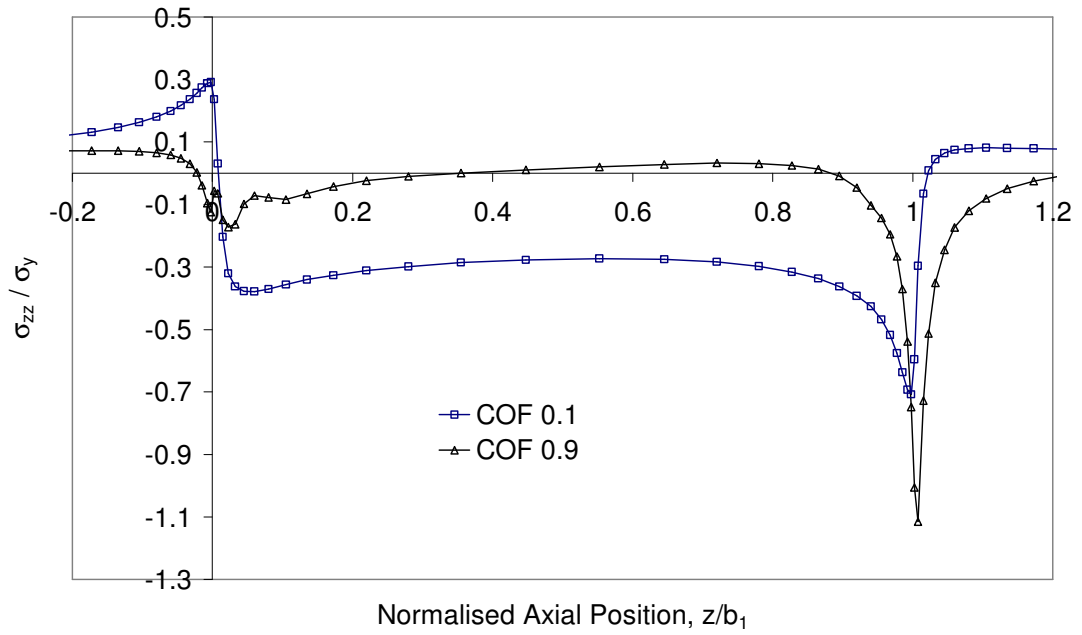


Figure 5.22. The effect of the COF on the  $\sigma_{zz}$  stress component at specimen tip ( $x/a_2 = 0$ ) at minimum applied in-plane load (load case of  $\sigma_{b\_max}/\sigma_y = 0.20$ ).

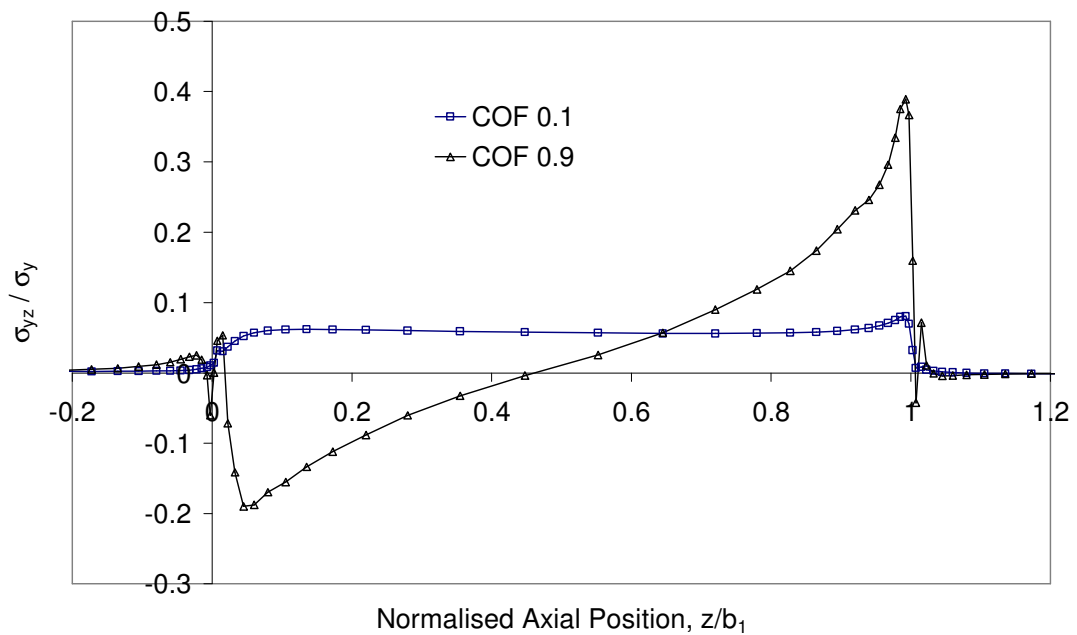


Figure 5.23. The effect of the COF on the  $\sigma_{yz}$  stress component at specimen tip ( $x/a_2 = 0$ ) at minimum applied in-plane load (load case of  $\sigma_{b\_max}/\sigma_y = 0.20$ ).

# Fretting Fatigue Lifting

## 6.1 Introduction

Finite element (FE) modelling was conducted in Chapter 5 in order to predict the local fretting contact variables of the uniaxial representative specimen (URS) and the multiaxial representative specimen (MRS). The sub-surface stress and strain state of the MRS was also shown, and the influence of the parameters investigated. The state of stress and strain is a critical factor controlling fretting fatigue life, with the near-surface condition being a major factor in the crack initiation (nucleation) process. Additionally, the crack propagation phase can be significant in determining the total fretting fatigue life of a component. This regime can be quantified via the calculation of crack tip stress intensity factors (SIFs), which are then correlated with empirical data.

This chapter will predict the total fretting fatigue life of the URS and MRS. The numerical method is based on the three-dimensional FE models of the test rig assemblies that were presented in Chapter 5, which include frictional contact effects. The sub-model of the MRS may then be used to provide detailed stress and strain distributions for use in a prediction methodology. A lifting methodology is presented that quantifies the crack initiation phase with a multiaxial critical-plane fatigue parameter, followed by crack growth prediction in the Paris regime using El Haddad small crack correction from linear elastic fracture mechanics (LEFM) principles.

## 6.2 Fretting fatigue lifing methodology

A methodology that is able to predict cracking location and the number of cycles to failure of fretted components would allow the optimisation of designs for components in contact. Fretting fatigue life is influenced by the complex interaction of varying mechanisms that must be accounted for and the unification of these is critical. There are various length scales that are important for the fretting fatigue process [65] and a lifing methodology should take account of behaviour at these different scales. Therefore with this in mind, the failure process can be separated into different regimes. The initiation of a critical crack occurs first, and if a crack is formed then propagation may occur. The propagation phase may be broken down into the short crack and conventional crack growth regimes. Therefore, the methodology adopted in the present work combines the failure regimes to predict the total number of cycles to failure,  $N_T$ , with the following relation:

$$N_T = N_i + N_{SCG} + N_p \quad (6.1)$$

where  $N_i$  is the number of cycles to initiate a crack of a specified dimension,  $N_{SCG}$  is the number of cycles of crack propagation in the short crack growth regime and  $N_p$  is the number of cycles of crack propagation in the conventional LEFM regime. Following from the work of Miller, it was suggested that the smallest microstructural barrier must be overcome for a crack to initiate [68]. This can be specified as the material grain size. For a CMV steel similar to the one tested with the URS and MRS, it was reported in Ref. [123] that the grain size was approximately 16  $\mu\text{m}$ . With S/CMV having a finer grain size, the initiation process will therefore be deemed to occur to a depth of 10  $\mu\text{m}$  for the analysis of the URS and MRS.

If a fretting fatigue crack initiates, then propagation first occurs in the short crack regime. For crack propagation to occur, the stress intensity factor range must be greater than the threshold stress intensity factor range, ( $\Delta K_{th}$ ). The critical crack length for the transition from short crack to conventional crack growth,  $a_0$ , may be found from the Kitagawa-Takahashi (K-T) diagram, leading to:

$$a_0 = \frac{1}{\pi} \left( \frac{\Delta K_0}{\sigma_e} \right)^2 \quad (6.2)$$

where  $\sigma_e$  is the fatigue limit and  $\Delta K_0$  is threshold in the LEFM regime. The threshold crack length is often termed the El Haddad dimension. For the CMV alloy steel studied here, the threshold stress intensity factor range,  $\Delta K_{th}$ , is measured as 4.52 MPa m<sup>0.5</sup>, with the plain fatigue limit determined from Ref. [9], leading to  $a_0 = 65 \mu\text{m}$ . Once this dimension is reached, crack growth is quantified using conventional LEFM techniques until final total fracture of the specimen. A summary of the total fretting fatigue lifing methodology is provided in Figure 6.1.

### 6.3 Initiation life prediction

The state of stress and strain is critical for the initiation of a fretting fatigue crack. The initiation process can be modelled on the continuum scale or at smaller scales, such as at the meso or micro-scales. The prediction of initiation at the continuum scale will be undertaken here, due to its ability to predict the severity of fretting and the crack location, whilst knowledge of the mechanics of initiation at the microscale is not sufficiently developed for the fretting problem. At the continuum level, research has been conducted into the application of asymptotic approaches, allowing a prediction to be made as to whether a crack will nucleate or not. The experimental data of Chapter 4

indicated that the majority of the MRS tests suffered complete failure under fretting fatigue, therefore it would be expected that the application of the asymptotic method would indicate the nucleation of a crack. The approach taken here, therefore, aims to quantify the number of cycles for a crack to nucleate in addition to the cracking location.

### 6.3.1 Smith-Watson-Topper (SWT) relation

Previous work has suggested that the failure mode of metallic materials is either tensile or shear driven [80]. The SWT parameter has been observed to give good life predictions for a range of materials failing under the tensile cracking mode, for example, it was shown in Ref. [87] that critical-plane SWT predictions gave a good correlation with measured plain fatigue lives for the laboratory-scale spline coupling made from the high-strength CMV steel studied here. The parameter is therefore applied in this chapter in order to predict the crack nucleation regime. Due to the complex, multiaxial stress and strain state that is developed in the fretting fatigue case as revealed in Chapter 5, a critical-plane implementation of the SWT parameter is required. The critical-plane approach originated from the work of Brown and Miller [19] that was introduced in Chapter 2.

Smith, Watson and Topper suggested a stress-strain function to correlate fatigue life data at different stress ratios [79]. The stress ratio,  $R_\sigma$ , is defined as:

$$R_\sigma = \frac{\sigma_{\min}}{\sigma_{\max}} \quad (6.3)$$

The proposed function was combined with the strain-life equation in order to correlate it with uniaxial fatigue data, leading to the Smith-Watson-Topper (SWT) relation, which is given as:

$$SWT = \sigma_{\max} \frac{\Delta \varepsilon}{2} = \frac{\sigma_f'}{E} (2N_f)^{2b} + \sigma_f' \varepsilon_f' (2N_f)^{b+c} \quad (6.4)$$

where  $\Delta \varepsilon$  is the total strain range,  $\sigma_f'$  is the fatigue strength coefficient,  $b$  is the fatigue strength exponent,  $\varepsilon_f'$  is the fatigue ductility coefficient,  $c$  is the fatigue ductility exponent and  $N_f$  the number of cycles to failure. In the critical-plane implementation of the SWT parameter,  $\sigma_{\max}$  is the maximum normal stress on the critical plane and  $\Delta \varepsilon$  is the normal strain range on the same plane.

The mean stress (and strain) influences the crack nucleation phase [124]. The maximum stress term ( $\sigma_{\max}$ ) in the SWT parameter attempts to include the effects of mean stress on fatigue life. This is based on the maximum stress being equal to the stress amplitude ( $\sigma_a$ ) for a fully reversed test. The fatigue constants, therefore, should be for a zero mean stress from a fully reversed load ( $R_\sigma = -1$ ) and a zero mean strain ( $R_\varepsilon = -1$ ). The mean strain is defined as:

$$R_\varepsilon = \frac{\varepsilon_{\min}}{\varepsilon_{\max}} \quad (6.5)$$

For compressive values of  $\sigma_{\max}$  the SWT parameter is set to zero. The Basquin high-cycle fatigue (HCF) constants were obtained from Ref. [9], where load-controlled uniaxial fatigue tests were conducted on non-nitrided and nitrided S/CMV material up to complete specimen failure. The tests were conducted at room temperature (20°), at a stress ratio ( $R_\sigma$ ) of 0.1 and test frequency of 10 Hz. More detail of the test procedure may be found by consulting Ref. [9]. The effect of test frequency is known to be small at the frequencies stated here, and therefore the results are deemed to be applicable to the MRS with minor cycling of 5 Hz. The constants were corrected for mean stress effects using the standard Goodman relation (e.g. see Ref. [12]), in order to determine the

constants for fully reversed loading ( $R_\sigma = -1$ ), where the Goodman correction for mean stress is given as:

$$\sigma_{am} = \sigma_a \left( 1 - \frac{\sigma_m}{\sigma_u} \right)^{-1} \quad (6.6)$$

where  $\sigma_{am}$  is the fatigue strength for a given life with zero mean stress,  $\sigma_a$  is the stress amplitude,  $\sigma_m$  is the mean stress and  $\sigma_u$  is the ultimate strength. The determination of the fully reversed constants from the original test data in Ref. [9] is shown in Figure 6.2 and the results tabulated in Table 6.1. The final crack front size was determined to be approximately 2.5 mm in depth by SEM examination of the fracture surfaces of the failed uniaxial fatigue specimens [9]. The constants are therefore denoted as the 2.5 mm constants in Table 6.1.

### 6.3.2 Back-calculating Basquin constants

The constants obtained in the previous section were for complete failure of the plain fatigue specimen, and therefore are not representative of crack nucleation at smaller length scales, such as in fretting fatigue. A methodology of modifying the SWT constants for the effects of a shorter nucleation length was offered in Ref. [125]. It was suggested that the crack propagation regime could be subtracted from the total fatigue life in order to determine the nucleation life at a smaller length scale. Nucleation was deemed to occur at a dimension of 10  $\mu\text{m}$ , which approximately equates to the material grain size.

The stress intensity factor,  $K_I$ , is required to quantify the crack propagation regime, and for a semi-elliptical surface crack in a long shaft under tension is given by Ref. [126]:

$$K_I = F_I \sigma \sqrt{\pi a} \quad (6.7)$$

where  $\sigma$  is the nominal crack driving stress,  $a$  is the crack length and  $F_1$  is a geometrical correction for finite specimen dimensions.  $F_1$  was as determined as a function of  $a/r$ , which was obtained from a polynomial fit of the data for a circular crack in Ref. [126] (for a Poisson's ratio of 0.3) as shown in Figure 6.3:

$$F_1 = 0.416\left(\frac{a}{r}\right)^2 - 0.012\left(\frac{a}{r}\right) + 0.66 \quad (6.8)$$

The effects of short crack growth must be incorporated as described in the following section.

### 6.3.3 Short crack behaviour

It has been observed that short cracks propagate at a faster rate than long cracks under the same nominal SIF range ( $\Delta K$ ) [12]. The Kitagawa-Takahashi (K-T) diagram [96] represents the variation of the threshold stress intensity factor range ( $\Delta K_{th}$ ) with short crack length, below the threshold value of crack length,  $a_0$ , that was defined in Eq. 6.2. The K-T approach sets  $\Delta K_{th} = \Delta K_0$  for  $a > a_0$  and  $\Delta \sigma_{th} = \sigma_e$  for  $a < a_0$  in a constant stress field, where  $\sigma_e$  is the fatigue limit and  $\Delta K_0$  is threshold in the LEFM regime. The K-T approach can also be formulated in terms of the SIFs, which is more convenient in a varying stress field. When considering the variation of the threshold SIF with crack length, this gives a discontinuous evolution. An alternative to the K-T method of including short crack propagation behaviour was suggested by El Haddad et al. [97]. It was suggested that the threshold (intrinsic) crack length,  $a_0$ , can be used to increase the crack driving force via the SIF, with the implicit assumption that the threshold is constant. The number of cycles of short crack propagation (up to  $a_0$ ) with the El Haddad approach is therefore predicted by the determination of the SIF via:

$$\Delta K_I = Y\sigma_{zz}\sqrt{\pi(a+a_0)} \quad (6.9)$$

where  $\Delta\sigma_{zz}$  is the crack driving stress range and  $Y$  is a geometrical correction factor for finite specimen dimensions.

Using the well-known Paris law [28] with the El Haddad short crack correction [97], the number of cycles for crack propagation from 10  $\mu\text{m}$  to 2.5 mm was subtracted from the uniaxial fatigue test data to obtain the nucleation Basquin fatigue constants. It is suggested that these constants are then more consistent for FE-based nucleation prediction based on integration point values of the critical-plane SWT parameter. The integration was conducted numerically and was found to have converged (within a  $\Delta N_p$  of  $< 5\%$ ) for an increment of 1000 cycles. Figure 6.4 shows a comparison of the nucleation and uniaxial fatigue test stress-life data. It can be seen that the difference is more significant at higher loads. The conventional Basquin fatigue constants (2.5 mm) are given in Table 6.1, along with the resulting 10  $\mu\text{m}$  nucleation constants obtained from a linear regression of the data in Figure 6.4.

#### **6.3.4 Strain-controlled fatigue tests**

The Coffin-Manson LCF constants for use in the SWT relation must be obtained from strain-controlled tests. This approach requires the cyclic stress-strain hysteresis loops to be stabilised once any elastic or plastic shakedown has occurred. If ratchetting occurs then the SWT fatigue constants vary with time, and cannot be applied in a stabilised state. The results of the uniaxial fatigue tests (non-nitrided S/CMV) were obtained from a personal communication with an industrial partner, where the tests were conducted at a strain ratio ( $R_\epsilon$ ) of zero at a temperature of 20°. Due to a lack of comprehensive data at different strain ratios, the constants at  $R_\epsilon = 0$  were assumed to be the same as for fully reversed loading ( $R_\epsilon = -1$ ). A similar reasoning was employed by Salerno et al. [124], whereby it was suggested that the SWT parameter with fully reversed constants would be the first

choice to characterise the fatigue behaviour under non-zero mean strain conditions due to its ease of use.

The total strain range,  $\Delta\varepsilon_T$ , was specified for each test and the following relation used to determine the plastic strain range,  $\Delta\varepsilon_p$ :

$$\Delta\varepsilon_p = \Delta\varepsilon_T - \Delta\varepsilon_e \quad (6.10)$$

where  $\Delta\varepsilon_e$  is the elastic strain range. A schematic of a typical stress-strain hysteresis curve for  $R_\varepsilon = 0$  is shown in Figure 6.5. By examination of Figure 6.5, the plastic strain range is given by:

$$\Delta\varepsilon_p = \Delta\varepsilon_T - \left( \frac{\Delta\sigma}{E} \right) \quad (6.11)$$

where  $E$  is the Young's modulus of the material in monotonic tension. The cyclic stress-strain curve is formed from the locus of the points from the stabilised stress and strain ranges and used to give  $\Delta\sigma$ . A straight line fit was used to determine the Coffin-Manson constants, and the non-dimensionalised values are tabulated in Table 6.1. The yield strain,  $\varepsilon_y$ , is determined from  $\sigma_y / E$ .

### 6.3.5 Critical-plane implementation of SWT

The three-dimensional implementation of the critical-plane analysis is conducted by the rotation of the coordinate system about the original two coordinate axes in the surface plane. For the local coordinate system utilised here and defined for the MRS sub-model in Chapter 5, this gives a rotation about the  $x$  and  $z$ -axes by the angles  $\theta_x$  and  $\theta_z$  respectively. Given a right-handed coordinate system ( $x$ - $y$ - $z$ ), the rotation matrices for the orthogonal transformations are given as follows:

$$R_z(\theta_z) = \begin{bmatrix} \cos\theta_z & 0 & -\sin\theta_z \\ 0 & 1 & 0 \\ \sin\theta_z & 0 & \cos\theta_z \end{bmatrix} \quad (6.12)$$

$$R_x(\theta_x) = \begin{bmatrix} 1 & 0 & 0 \\ 0 & \cos\theta_x & \sin\theta_x \\ 0 & -\sin\theta_x & \cos\theta_x \end{bmatrix} \quad (6.13)$$

By convention, the rotation matrices represent a positive rotation of the coordinate axes in the counter-clockwise direction when looking towards the origin. This rotation is shown diagrammatically in Figure 6.6 for the two-dimensional case, but also applies to the three-dimensional case. According to Euler's rotation theorem, any rotation can be represented as a composition of rotation about three axes and thus is able to be represented by a 3x3 rotation matrix,  $A$ , operating on a vector,  $r$  [127]:

$$r' = Ar \quad (6.14)$$

which, when the rotation  $R_x$  is conducted first, gives:

$$A = R_x(\theta_x)R_z(\theta_z) \quad (6.15)$$

which in this case leads to:

$$A = \begin{bmatrix} \cos\theta_z & \sin\theta_z & 0 \\ -\cos\theta_x \sin\theta_z & \cos\theta_x \cos\theta_z & \sin\theta_x \\ \sin\theta_x \sin\theta_z & -\sin\theta_x \cos\theta_z & \cos\theta_x \end{bmatrix} \quad (6.16)$$

This can be defined in terms of the direction cosines of the unit normal to the plane ( $y$ -axis), giving:

$$\begin{pmatrix} n_x \\ n_y \\ n_z \end{pmatrix} = \begin{pmatrix} \sin \theta_z \\ \cos \theta_x \cos \theta_z \\ -\sin \theta_x \cos \theta_z \end{pmatrix} \quad (6.17)$$

The normal stress and strain to the plane are then deduced via a three-dimensional transformation using the second order tensor transformation rule [128]:

$$\sigma = \sigma_{11}n_x^2 + \sigma_{22}n_y^2 + \sigma_{33}n_z^2 + 2\sigma_{12}n_xn_y + 2\sigma_{23}n_y n_z + 2\sigma_{13}n_x n_z \quad (6.18)$$

$$\varepsilon = \varepsilon_{11}n_x^2 + \varepsilon_{22}n_y^2 + \varepsilon_{33}n_z^2 + \varepsilon_{12}n_x n_y + \varepsilon_{23}n_y n_z + \varepsilon_{13}n_x n_z \quad (6.19)$$

With the residual stress deemed to be negligible due to the low-stress grinding manufacturing method employed, the FE-predicted stress and strain state will be used to determine the SWT parameter on the critical-plane for the various experimental tests. The resulting value can then be correlated with the nucleation life using the previously determined constants. The relation is solved via the Newton-Raphson numerical technique in order to obtain a prediction for the number of cycles to nucleate a fretting fatigue crack with the dimensions of the material grain size. This numerical integration was conducted using a FORTRAN program.

### 6.3.6 Stress gradient effects

The steep stress gradients encountered in fretting fatigue must be taken into account in the analysis of the problem. Volume averaging may be conducted in order to account for this effect. As discussed earlier, the grain size must be overcome for a crack to initiate and therefore averaging can be conducted over this dimension. This can be realised via:

1. Averaging of the stress and strain state,

2. Averaging of the predicted SWT parameter,
3. The finite element mesh.

When the predicted stress and strain state is obtained with a discretisation that is greater than that of the grain size, the averaging can be conducted with the first two methods mentioned above. An alternative technique is where the averaging process is indirectly realised with the mesh in FE analyses. The integration (Gauss) point stresses can be used and averaged according to the mesh size and required averaging dimension.

To the author's knowledge, there are currently no reports in the literature of volume averaging having been conducted for complete contact geometries. The averaging approach is realised in the present work for the URS and MRS by approximately matching the dimensions of the mesh (integration points) with the grain size. Due to the elemental shapes used in the FE meshes of both the URS and MRS models, this therefore gives a rectangular process zone over which the averaging is conducted.

### **6.3.7 SWT URS results**

A number of FE analyses were conducted in Chapter 5 using the global model of the URS, with a variation of the coefficient of friction (COF). The results of the analyses were subsequently used to furnish the FE-predicted critical-plane SWT parameter for the S/CMV versus S/CMV combination, with the findings tabulated in Table 6.2. The SWT calculation was performed on the specimen of the inner load arm. An example of the distribution of the predicted SWT parameter (at axial position  $z/b_2 = 0.5$ ) for a COF of 0.9 is shown in Figure 6.7. It is observed that the peak SWT value occurs at the edge of the fretting contact at  $x/a_2 = 1$ . The magnitude of the SWT parameter then reduces in the fillet of the tooth, as the influence of the contact diminishes. The fatigue

constants of Table 6.1 were used to predict the number of cycles to initiate a crack with the dimensions of the grain size, with the results tabulated in Table 6.2. It is seen that an increase in the COF leads to a decrease in the predicted crack initiation phase. For a COF lower than 0.9, there is an effectively infinite life predicted. It is also found that the number of cycles of the crack initiation phase for a COF of 0.9 and 1.0 is significantly greater than the 20,000 major cycles that were applied to the experimental tests (see Chapter 4). With the COF for the S/CMV against S/CMV combination inferred to be 0.85 from the URS tests, this suggests that no cracks would initiate in the experimental test. The test observations from this combination are in agreement with this prediction.

### 6.3.8 SWT MRS results

The analyses of the MRS using the FE sub-model may now be used to predict the SWT parameter for the experimental test conditions of Chapter 4. Stress and strain data for all 8 integration points of the elements nearest to the contact surface were used to obtain an averaged SWT parameter, therefore attaining an averaging dimension akin to that of the material grain size. With multiaxial loading, the contributions that the major and minor cycles make regarding fretting damage can be evaluated using damage accumulation rules. The linear Palmgren-Miner rule is the most commonly applied and is given as:

$$\sum_{i=1}^k \frac{n_i}{N_i} = C \quad (6.20)$$

where  $k$  is the number of load spectra,  $n_i$  is the number of completed cycles at a specific load magnitude,  $N_i$  is the number of cycles to failure at the prescribed stress amplitude, and  $C$  is experimentally determined (typically  $C = 1$  for design purposes). For the MRS this gives:

$$\frac{C}{N_{total}} = \frac{1}{N_{major}} + \frac{500}{N_{minor}} \quad (6.21)$$

FE analyses of the MRS were conducted with major cycling only. It was found that the predicted fatigue damage caused by the major cycles was insignificant in comparison with the applied constant major cycle load and fluctuating minor cycle load. The major cycling (IP load) was therefore neglected for the SWT analyses.

Figure 6.8 shows the contour plot of the SWT parameter for the OP loads of  $\sigma_{max}/\sigma_y = 0.12$  and  $\sigma_{max}/\sigma_y = 0.24$  at an IP load of  $F_i = 10.9 F_0^{nom}$ . The contact of the bridge pad is marked by the dimension  $b_1$ . There exists a similar distribution for the two load cases, with increased magnitudes for the higher applied OP load. The peak SWT value occurs close to the edge-of-contact with the bridge pad for both load cases, at a position of  $z/b_1 = 1.0$  and  $x/a_2 \approx 0.0$ . This corresponds to the outer axial edge of the bridge pad. There is a significant value of the SWT parameter across this edge ( $z/b_1 = 1$ ), which is attributed to the bending of the bridge pad. For the other axial edge-of-contact position of  $z/b_1 = 0$ , an SWT value of almost zero is predicted, due to the compressive axial stress state that was shown to occur at this position in Chapter 5. The SWT parameter at  $x/a_2 = 0.5$  is plotted for both load cases in Figure 6.9, highlighting the position of the axial peak. The variation of the SWT parameter in the  $x$ -direction is also plotted in Figure 6.10, indicating the peak location at the specimen tip.

The 10  $\mu\text{m}$  nucleation constants of Table 6.1 were used to furnish the predicted number of cycles to nucleate a fretting fatigue crack, with the results shown in the S-N curve given in Figure 6.11 (and summarised in Table 6.3). The minor cycle S-N curve is formed by plotting the applied OP stress

and the number of OP (minor) cycles. It is seen that the applied OP load significantly influences the crack initiation phase. For the highest applied OP load, crack nucleation is predicted to occur rapidly, whilst for the lowest applied OP load crack nucleation is predicted to occur after over 4 million cycles. Hence at high OP loads, the nucleation phase underestimates the total life, whilst at low OP loads a good agreement with the total life is observed. The inclusion of crack propagation effects would be expected to improve the predictions of the total fretting fatigue life.

With experimental tests conducted at  $\sigma_{\max}/\sigma_y = 0.20$  with a reduced IP load ( $F_i = 5.45 F_0^{nom}$ ) and a reduced bridge gap (20mm) in Chapter 4, the crack nucleation phase was predicted for these load cases as above, with the results plotted in the minor cycle S-N curve in Figure 6.12. It is seen that the methodology successfully captures the trend for both of these conditions, whereby there is an increase in the number of cycles to nucleate a crack that is consistent with the increased total life of both tests. Additionally it is seen that the approach correctly predicts that the reduction in the IP load is more significant than the reduction in the bridge gap.

### **6.3.9 FE-predicted critical-plane orientation**

Optical photographs of the fractured fretting specimens were documented in Chapter 4 in order to experimentally determine the crack initiation angle. In order to compare with the FE-predicted critical plane approach (as shown in Figure 6.13) a coordinate transformation was conducted to align the local axis with the global axis. The direction cosines of the normal to the plane were then used to determine the angle between the crack initiation plane and the global axis. With reference to Figure 4.15, the prediction gives an angle of  $\theta = 15.8^\circ$ , in excellent agreement with the FE-predicted (found to the nearest  $5^\circ$ ) value of  $15^\circ$ . Similarly, with reference to Figure 4.18, the predicted angle was

found to be 21°, in good agreement with the experimentally measured value. The excellent correlations of the predicted and observed angles of crack initiation validate the critical-plane approach employed.

#### 6.4 Fracture mechanics methodology

The application of fracture mechanics techniques has given increased understanding into fatigue and fretting fatigue processes [27]. With the FE-predicted crack initiation phase found to be a small proportion of the experimentally observed total life for the higher applied OP loads of the MRS, LEFM will be applied to predict the crack propagation phase of the MRS. Fracture mechanics methods will not be applied to the URS, as no propagating cracks were found to occur in the experimental test programme. For the analysis of the MRS, the fine grain size in combination with the contact width in comparison with the plastic zone size mean that LEFM (modified by the El Haddad correction for short cracks) techniques are applicable. A two-dimensional schematic of the MRS geometry is shown in Figure 6.14, where the applied bulk stress ( $\sigma_{zz}$ ) is normal to the plane. The location of crack nucleation is shown at  $x/a_2 = 0$ . It is assumed that propagation occurs normal to the contact surface ( $y$ -direction) across the width of the specimen,  $W$ . The dimension  $W$ , is approximately 10 mm.

The predicted stress distributions from the FE sub-model were presented in Chapter 5. In order to further examine the crack nucleation and propagation phases, additional results are presented below. The axial distributions into the depth of the specimen (at the failure position of  $z/b_1 = 1$ ) of the stress ranges are plotted in Figure 6.15 for one load case. The distributions are obtained along the line denoted in Figure 6.14. It can be seen that the axial stress ( $\sigma_{zz}$ ) is the dominant component. The shear stress components are significant for short crack lengths, highlighting their importance on the nucleation and short

crack processes. It is observed that the component  $\sigma_{yz}$  is the most sustained shear stress away from the contact surface. Therefore for the propagation of a fretting fatigue crack, it is deemed that the direct axial stress parallel to the surface ( $\sigma_{zz}$ ) and the shear stress ( $\sigma_{yz}$ ) are the key stress components. It is assumed that a tensile stress parallel to the surface promotes initiation, whilst a compressive stress retards initiation. The distributions of the  $\sigma_{zz}$  stress component for two loadcases are shown in Figure 6.16 at the maximum and minimum point in the load cycle. This variation in axial stress state results in the actual  $R_\sigma$  ratio local to the contact not being the same as the nominal ratio ( $R_\sigma = 0.1$ ). The  $R_\sigma$  ratio is plotted in Figure 6.17 for applied minor cycle loads of  $\sigma_{\max}/\sigma_y = 0.12$  and  $0.24$ . It is observed that  $R_\sigma$  is negative near to the contact interface, and tends towards the nominal ratio as the influence of the contact diminishes.

Neglecting the fast fracture region, the crack propagation phase can be estimated via the empirical Paris law [28], which is given by:

$$\frac{da}{dN} = C(\Delta K_{eff})^n \quad (6.22)$$

where  $da/dn$  is the crack growth rate,  $C$  and  $n$  are constants that are empirically determined and  $\Delta K$  is the stress intensity factor range, defined as:

$$\Delta K = K_{\max} - K_{\min} \quad (6.23)$$

For mixed mode fracture mechanics [129], to include modes I and II, the effective SIF range ( $\Delta K_{eff}$ ) is defined as [130]:

$$\Delta K_{eff} = \sqrt{\Delta K_I^2 + \Delta K_{II}^2} \quad (6.24)$$

In addition to the originally proposed Paris law, various modifications to the original law have been suggested, including the form that was used in Refs. [61, 131]. It was suggested that this is able to deal with near-threshold conditions better than the classical form, and is given as:

$$\frac{da}{dN} = C(\Delta K_{eff} - \Delta K_{th})^n \quad (6.25)$$

where  $\Delta K_{th}$  is the threshold stress intensity factor range. The Paris law constants must be experimentally determined and were obtained using a compact tension (CT) specimen based on tests reported in Ref. [132], with the fatigue crack growth rate measured using the potential drop method. The constants were modified, via a Walker equation, to correspond to  $R_\sigma = -1$ , resulting in  $m = 0.41$ ,  $n = 2.5612$  and  $C = 2.86 \times 10^{-12}$  ( $\Delta K$  units of MPa mm<sup>1/2</sup>). The same Paris law constants are used in both Eq. (6.22) and Eq. (6.25), as  $\Delta K_{th}$  has a negligible effect in modifying the constant  $C$ . A comparison of the behaviour of the Paris law and the modified form for near-threshold conditions is plotted in Figure 6.18. The conventional relation quantifies the linear stage II crack propagation regime but also approximates the near-threshold region as linear, whereas the modified form more closely replicates frequently observed empirical behaviour. Ideally, the near-threshold condition behaviour could be quantified by a separate empirical parameter, but the difficulty involved in determining the crack propagation behaviour at the scales involved makes this impractical. Therefore, the modified Paris law used here subtracts the threshold SIF from the calculated SIF and is raised to the same power.

The issue of crack growth prediction for fretting fatigue has been dealt with by numerous authors. Nicholas et al. [133] analysed mixed mode crack growth from the contact edge of a rounded-edge pad fretting fatigue test

arrangement for Ti-6Al-4V. The approach adopted involved the application of a weighted function method for evaluating the stress intensity factors parametrically as a function of crack length and direction, using mixed mode weight functions from the work of Beghini et al. [134] to deal with stress gradient effects (as seen in Figure 6.15 for example). It was shown that the crack growth direction beyond approximately 10  $\mu\text{m}$  could be treated as simply normal to the contact surface. Consequently in the present work, the SIFs will be determined with the following assumptions:

- After predicted initiation from the contact edge location at the predicted critical plane angle, it is assumed that growth takes place in a direction normal to the contact surface,
- Based on the observation that the crack appears to grow approximately uniformly across the width of the specimen, a two-dimensional fracture mechanics assumption is made,
- Local mode I and mode II SIF values are calculated by treating the locally-predicted (sub-model) normal stress ( $\sigma_{zz}$ ) as 'far-field' stresses in the weight function approach described below, using the expression for an edge-cracked plate under far-field loading. This neglects the effect of the presence of the crack on the stress state.

## 6.5 Determination of the SIFs

In order to quantify the crack propagation phase, the SIFs must be determined. There are a variety of methods of calculating the SIFs, which are listed below:

- Analytical,
- Weight functions,
- Distributed dislocation technique,

- Finite element analysis.

The SIFs are geometry dependent, meaning that analytical methods are limited to a small number of specific cases. The distributed dislocation and weight function techniques are numerical methods. Finite element analysis is a numerical technique that allows modelling of the crack via incremental re-meshing or meshless methods such as the extended finite element method (XFEM) that is an advanced technique still in development (e.g. see Ref. [135]). Due to the ability of the weight function method to handle steep stress gradients, the approach will be applied as described in the following section.

### 6.5.1 Weight functions

The weight function method, developed by Bueckner [136], is used to determine  $\Delta K_I$  and  $\Delta K_{II}$  from the following relations [137]:

$$\begin{aligned}\Delta K_I &= \int_0^a \Delta\sigma_{zz}(x)h_I(x,a)dx \\ \Delta K_{II} &= \int_0^a \Delta\sigma_{yz}(x)h_{II}(x,a)dx\end{aligned}\tag{6.26}$$

where  $\Delta\sigma$  is the crack driving stress range as a function of depth into the specimen. The integrating variable,  $x$ , begins at a zero crack length up to the crack tip. The Mode I weight function for the edge-cracked plate,  $h_I(x,a)$ , must be determined numerically and, with the ratio  $a / W$  denoted as  $\alpha$ , is (for  $\alpha < 0.85$ ) given as:

$$h_I = \sqrt{\frac{2}{\pi a}} \frac{1}{\sqrt{1-\rho}} \left[ 1 + \sum_{(v,\mu)} \frac{A_{v\mu} \alpha^\mu}{(1-\alpha)^{3/2}} (1-\rho)^{v+1} \right]\tag{6.27}$$

where  $\rho = x / a$ , and  $A_{v\mu}$  are the influence coefficients of the weight function [137]. For mode II loading ( $\alpha < 0.9$ ), the corresponding function is given as:

$$h_{II} = \sqrt{\frac{2}{\pi a}} \frac{1}{\sqrt{1-\rho}(1-\alpha)^{1/2}} \left[ (1-\alpha)^{1/2} + \sum_{(v,\mu)} A_{v\mu} (1-\rho)^{v+1} \alpha^\mu \right] \quad (6.28)$$

From experimental data, it is known that the  $R$  ratio affects the crack propagation rate, meaning that the Paris law constants are a function of stress ratio. Various models have been proposed to account for this effect. An empirical relation was suggested by Walker [29] and is applied here to the mode I SIF, to give  $\Delta K_{I,eff} = \Delta K_I (1-R)^{(1-m)}$ , where  $m$  is a material constant and  $0 < m < 1$ , leading to a modified version of Eq. 6.24 as follows:

$$\Delta K_{eff} = \sqrt{\Delta K_{I,eff}^2 + \Delta K_{II}^2} \quad (6.29)$$

For the material employed here, it was established that  $m = 0.41$  [132]. This is based on the gradient,  $m$ , being constant as a function of  $R$  ratios, whilst  $C$  varies.

From the modified version of the Paris law (Eq. 6.25), the increment in crack length,  $\Delta a$ , for a given  $\Delta N$  can be determined from:

$$\Delta a = C (\Delta K_{eff} - \Delta K_{th})^n \Delta N \quad (6.30)$$

As stated earlier, the initial crack length is specified as the dimension of the grain size, followed by an incremental approach until the final crack length is reached.

The observed negative  $R_\sigma$  near to the contact surface (Figure 6.17) suggests that the crack will be under compression at some point during the load cycle. Consequently, the crack faces will come into contact, and in this case it is often assumed that:

$$\Delta K = K_{\max} \quad (6.31)$$

This is because it has been suggested that under compression, there is transmission of contact pressure between crack faces, leading to no stress intensity factor being developed at the crack tip (therefore no crack growth). This is generally found to be valid, although is not the case for more ductile metals [138]. In the present work, the Walker parameter is only applied to positive  $R$  ratios.

In summary, the approach adopted here is to identify the relative contributions to total life from the initiation and propagation regimes, and is outlined as:

- Step 1:** Identify the location and orientation of crack nucleation with the peak SWT magnitude and specify initial crack length, in this case, as the grain size,
- Step 2:** Assume nucleated crack is perpendicular to surface (at  $z = b_1$ ),
- Step 3:** Determine modes I and II weight functions from Eqs. 6.27 and 6.28 respectively. Identify local stress ranges ( $\Delta\sigma_{zz}$  and  $\Delta\sigma_{yz}$ ) via interpolation from detailed (sub-model) predicted distributions, such as that in Figure 6.15, and determine  $\Delta K_{\text{I}}$  and  $\Delta K_{\text{II}}$  using Eq. 6.26 or, for short cracks, using  $(a + a_0)$  in place of  $a$  in Eq. 6.26,
- Step 4:** Determine  $\Delta K_{\text{eff}}$  from Eq. 6.29,

**Step 5:** Calculate increment in crack length for a given  $\Delta N$  using Eq. 6.30,

**Step 6:** Calculate new crack position and repeat steps 3-5 until  $\alpha > 0.85$ , at which point the accumulated number of cycles is taken to correspond to  $N_p$ .

A piece-wise linear interpolation was conducted in order to determine axial stress state with distance for use in the Paris law. A FORTRAN program was created to implement interpolation and the subsequent weight function method.

## 6.6 Fracture mechanics results

Figure 6.19 shows the evolution of  $(\Delta K - \Delta K_{th})$  with crack length for two OP load cases. The figure shows the mixed mode  $(\Delta K_{eff} - \Delta K_{th})$  and mode I  $(\Delta K_I - \Delta K_{th})$  distributions for both loads. It is observed that the inclusion of mixed mode effects increases the SIF in comparison with the mode I SIF. It is therefore noted that a solely mode I formulation will result in a more conservative crack propagation prediction. The mixed mode formulation has a greater influence on the SIF in the early-stage of crack propagation, followed by a convergence with the mode I solution. The mode mixity parameter as used by Sutton et al. [139] quantifies the degree of mode II loading:

$$\alpha_{mixity} = \tan^{-1} \left( \frac{K_{II}}{K_I} \right) \quad (6.32)$$

This parameter is plotted in Figure 6.20, and highlights the diminishing influence of the mode II component with crack length.

The SWT parameter predicted nucleation for an applied OP load of  $\sigma_{\max}/\sigma_y = 0.12$ , although at a similar number of cycles to the run-out of the experimental test. The run-out of the experimental test at this load suggests one of the following: i) that the test would have failed after further cycling; ii) that no fretting fatigue cracks were nucleated or; iii) that arrest of a nucleated crack occurred. By examination of Figure 6.19, crack arrest is almost predicted to occur for this load case at the transition from the short to conventional crack growth regime.

## 6.7 Total fretting fatigue life predictions

The predicted SIFs were used to predict the crack propagation regime, with the mixed mode results shown in Figure 6.21. It was found that the mixed mode predictions were not significantly different from the mode I predictions. This suggests that the simpler mode I analysis is adequate for the current application. The initiation and propagation (mixed mode) regimes were combined, as given by Eqn. 6.1 to give total fretting fatigue life predictions ( $N_T$ ) for the MRS, with the findings also plotted in Figure 6.21. There is a good agreement with the experimental results, although for higher applied bulk stresses the predictions are conservative. In the practical application of this method, the conservative predictions can be seen as advantageous. For lower applied bulk stresses, the predictions are more accurate. It is interesting to note that for higher loads, the total life is dominated by crack propagation, whilst for lower loads crack nucleation is predominant. This confirms the key importance of the bulk stress parameter in the analysis of fretting fatigue.

## 6.8 Discussion

The FE-based lifing methodology presented has been shown to give good predictions for the complex multiaxial fretting fatigue problem of the MRS studied. The generally conservative predictions may arise from a variety of

sources. Crack initiation was predicted using a critical-plane SWT parameter. This multiaxial fatigue criterion neglects the surface damage generated by the fretting action. To address this issue, the use of a fretting fatigue damage parameter,  $D_{\text{fret}}$ , will be investigated in the following chapter.

The fracture mechanics approach included mode II effects. By comparison with a pure mode I case, it was found that the inclusion of mode II effects had only a minor effect of decreasing the predicted number of cycles of propagation. This is in agreement with the findings of Faanes [61], who showed that for sharp-edged contact pads, akin to those of the present work, a mixed mode (modes I and II) effective SIF solution was not required to capture the measured crack growth behaviour, beyond an initial short crack length. It was also suggested that the assumption of the crack to be perpendicular to the surface generally gave good predictions, i.e. the use of kinked crack solutions showed little deviation from the straight crack results. For the prediction of the short crack behaviour, the El Haddad approach pursued is more conservative than the alternative Kitagawa-Takahashi method, and future work could compare the two approaches.

Crack closure effects, which were first noted by Elber [140], are postulated to originate due to a variety of mechanisms (e.g. plasticity) and can mean that a crack is partially closed even for an applied remote tensile load. These effects, which inhibit crack propagation, were neglected. In addition, contact of the crack faces leads to a frictional interaction. This is likely to inhibit mode II growth [61], increasing the dominance of mode I.

The stress ratio ( $R_{\sigma}$ ) is known to affect the crack propagation rate. For positive values, the Walker parameter was used, although it was not applied for negative values. There is disagreement in the literature about the effect of

negative  $R$  ratios on the total fatigue life. Contradictions have been reported in the literature for different materials, whereby some data suggests that compression effects are beneficial (reduced crack growth rate) [141], whilst others report detrimental results [142]. In order to overcome this difficulty, two-parameter models have been suggested that attempt to account for negative  $R$  ratio effects and their use may improve predictions. For example, a two-parameter model was suggested by Kujawski that includes  $\Delta K$  and  $K_{\max}$  [143].

Material wear also influences the fretting fatigue life. As a consequence of wear, the edge-of-contact pressure peaks would be expected to be relieved relatively early in the total life. Small manufacturing tolerances also mean that a perfect sharp-edged contact does not exist in reality. This would reduce the severity of the stress state, leading to increased life predictions, which would improve the prediction to test correlations, particularly at high fatigue loads.

## 6.9 Summary of chapter

A fretting fatigue lifing methodology was implemented in this chapter in order to obtain computational life predictions for the experimental load cases of the uniaxial and multiaxial representative specimens. The crack initiation phase was quantified using the critical-plane (multiaxial) SWT parameter. The  $S/CMV$  fatigue constants were modified in order to be consistent with the crack initiation at the scale of the grain size (10  $\mu\text{m}$ ). It was found that no fretting fatigue cracks were predicted to initiate for the URS tests, in agreement with the experimental findings. When the methodology was applied to the MRS, cracks were predicted at  $z/b_1 = 1.0$  and  $x/a_2 \approx 0.0$ , in excellent agreement with the experimental observations. It was also found that the crack initiation was predicted to occur relatively early in the total life for the load cases with a high bulk stress (OP or minor cycle load). On the

other hand, for lower OP loads, crack initiation was predicted to occupy the majority of the total fretting fatigue life. Therefore, a total life approach was adopted, where the initiation and propagation regimes were accounted for. Short crack propagation behaviour was included using the El Haddad formulation of the stress intensity factors (SIFs), along with the propagation in the Paris law regime quantified using a linear elastic fracture mechanics mixed mode formulation. A numerical weight function approach was used to determine the crack tip SIFs. The crack propagation results from the mixed mode formulation (mode I and II) were not significantly different from the mode I results, suggesting that the simpler mode I formulation can be adequate in the analysis of fretting fatigue. The computational methodology was shown to successfully capture the experimentally observed effect of the key fretting fatigue stress, which mimics the spline rotating bending moment, on the total fretting fatigue life. Good total life predictions were also found for the MRS results, with conservative predictions for higher applied bulk fatigue stresses. The conservative predictions may be regarded as advantageous in the practical application of the methodology. The following chapter presents a novel empirical fretting fatigue lifing parameter, which attempts to empirically capture the effect of surface damage on the fretting fatigue life.

## 6.10 Tables

Table 6.1. The non-dimensionalised Basquin and Coffin-Manson fatigue constants for the CMV steel used. With  $R_\sigma = -1$  and  $R_\epsilon = 0$ .

	$\sigma'_f / \sigma_y$	<b>b</b>	$\epsilon'_f / \epsilon_y$	<b>c</b>
2.5 mm constants	2.661	-0.1072	50.5708	-0.6525
10 $\mu\text{m}$ constants	2.291	-0.0978		

Table 6.2. The FE-predicted results for the S/CMV versus S/CMV combination from the global model of the URS, showing the effect of COF on the critical-plane SWT life predictions.

COF	SWT <sub>max</sub> (MPa)	$\theta_x$ (deg)	$\theta_z$ (deg)	Predicted Cycles to Failure
0.3	0.484	90	90	Infinite
0.5	0.934	85	90	Infinite
0.6	1.022	90	90	Infinite
0.7	1.124	90	90	Infinite
0.9	1.579	90	90	7,093,618
1.0	3.350	90	90	164,962

Table 6.3. The results of the SWT critical-plane analyses of the MRS.

OP stress $\sigma_{\text{max}}/\sigma_y$	SWT <sub>max</sub> (MPa)	Angle $\theta_x$ (deg)	Angle $\theta_z$ (deg)	Location, z z/b <sub>1</sub>	Location, x x/a <sub>2</sub>	Number of OP cycles to initiation
0.24	7.0794	70	170	1.00	0.06	5860
0.20	4.6392	70	170	1.00	0.06	35,446
0.18	3.5858	70	170	1.00	0.03	118,747
0.16	2.8028	70	175	1.00	0.03	395,710
0.14	2.3136	70	175	1.00	0.03	1,029,610
0.12	1.7040	70	175	1.00	0.03	4,819,019

\*Note: angles to nearest 5°.

## 6.11 Figures

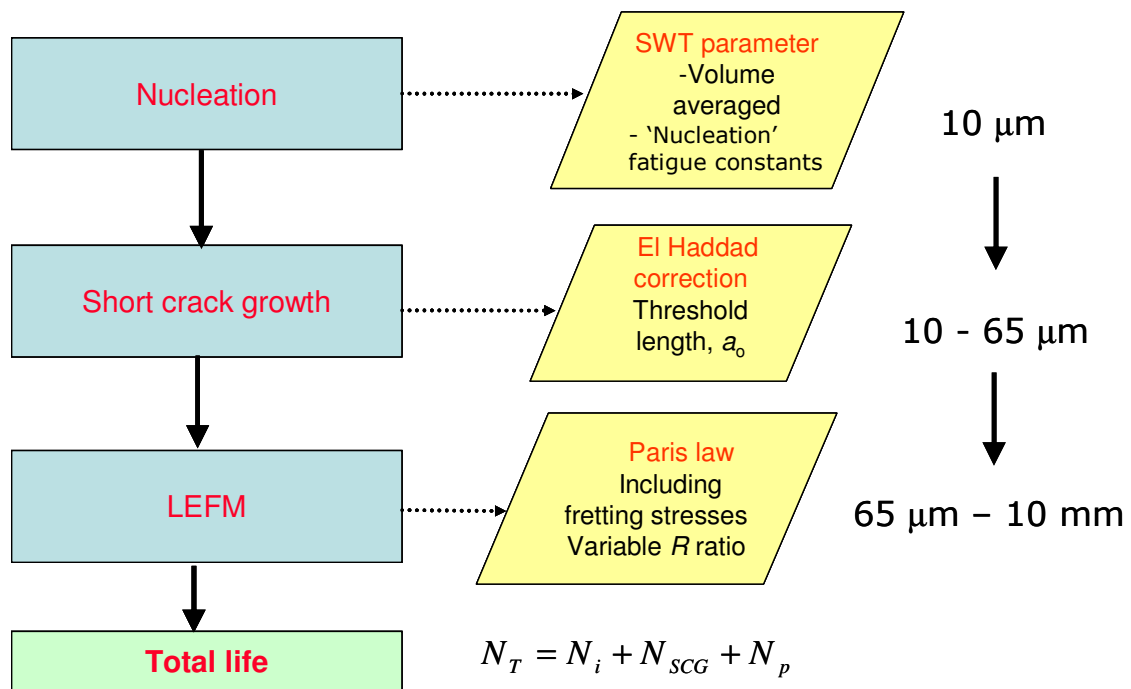


Figure 6.1. The fretting fatigue life methodology, with the associated length scales.

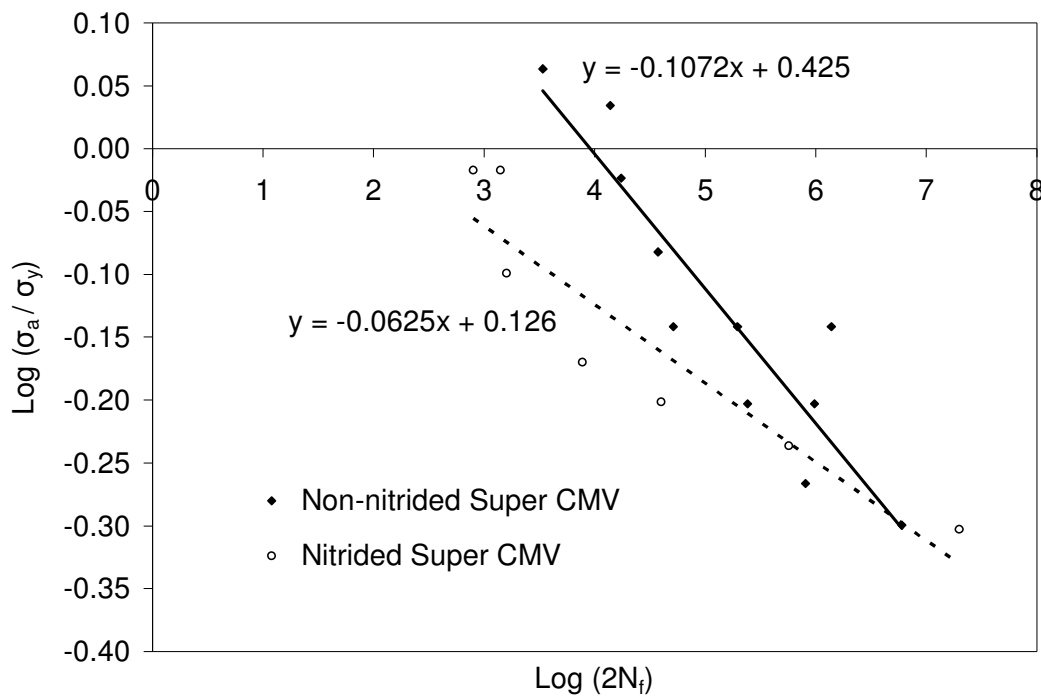


Figure 6.2. The determination of the Basquin fatigue constants (at  $R_\sigma = -1$ ) for CMV alloy steel, from test data in Ref. [9].

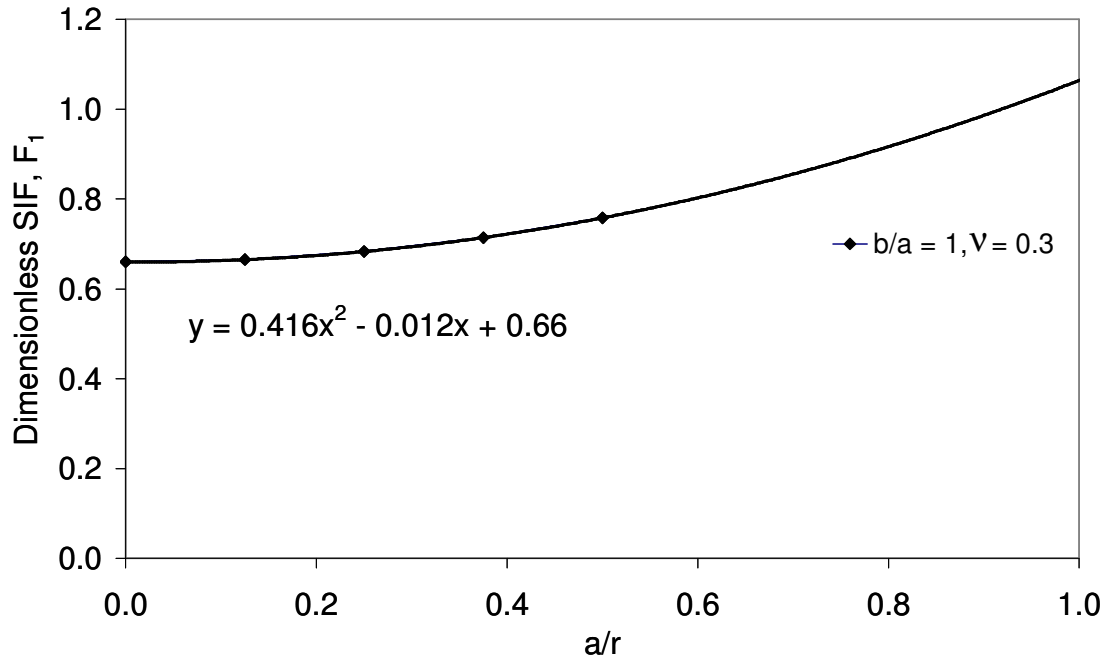


Figure 6.3 The dimensionless SIF,  $F_1$ , for a semi-elliptical surface crack in a long shaft under tension.

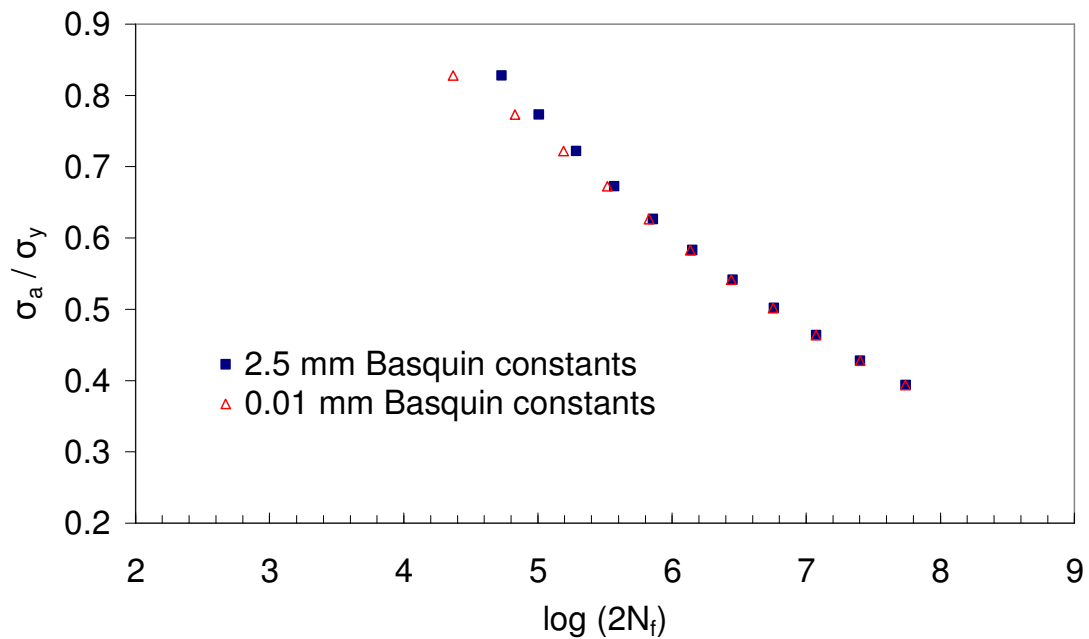


Figure 6.4. Stress-life data showing data for measured 2.5 mm fatigue cracks and estimated 10  $\mu\text{m}$  (nucleation) fatigue cracks.

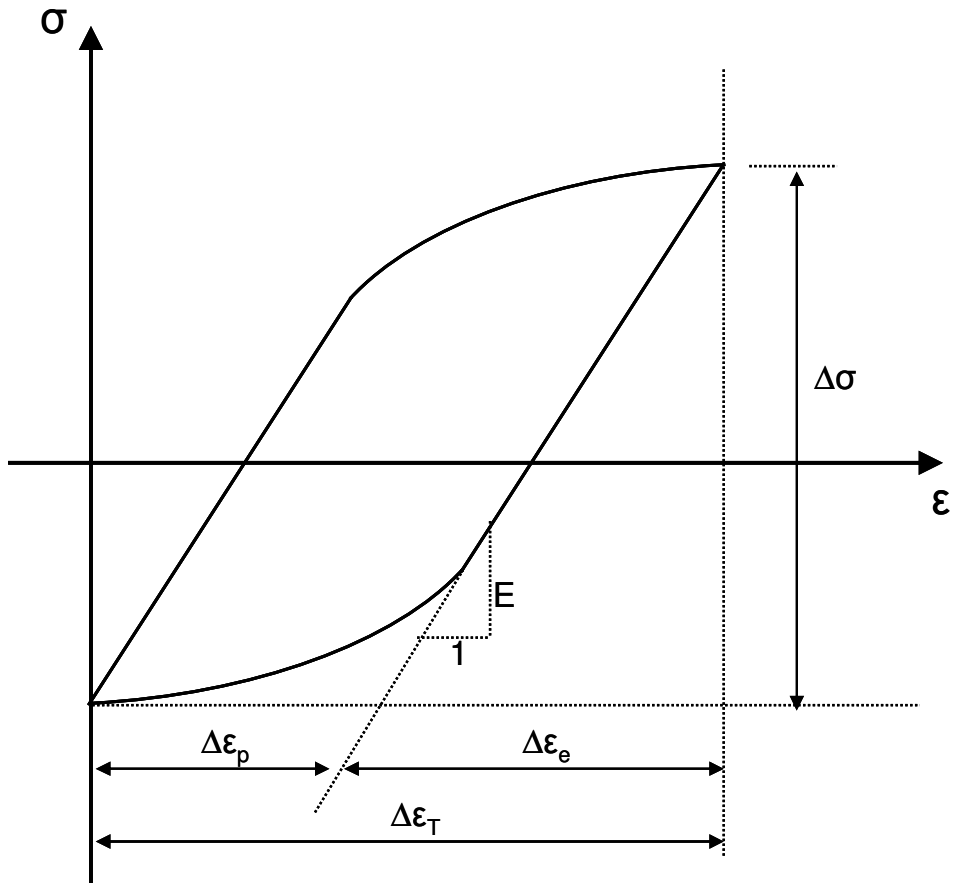


Figure 6.5. A typical hysteresis loop from strain-controlled testing (when  $R_\epsilon = 0$ ), including the definition of the stress and strain ranges.

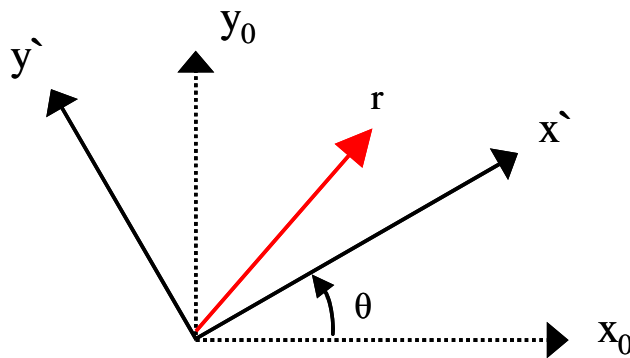


Figure 6.6. Rotation of the coordinate axes, being equivalent to a two-dimensional orthogonal transformation. Adapted from Ref. [127].

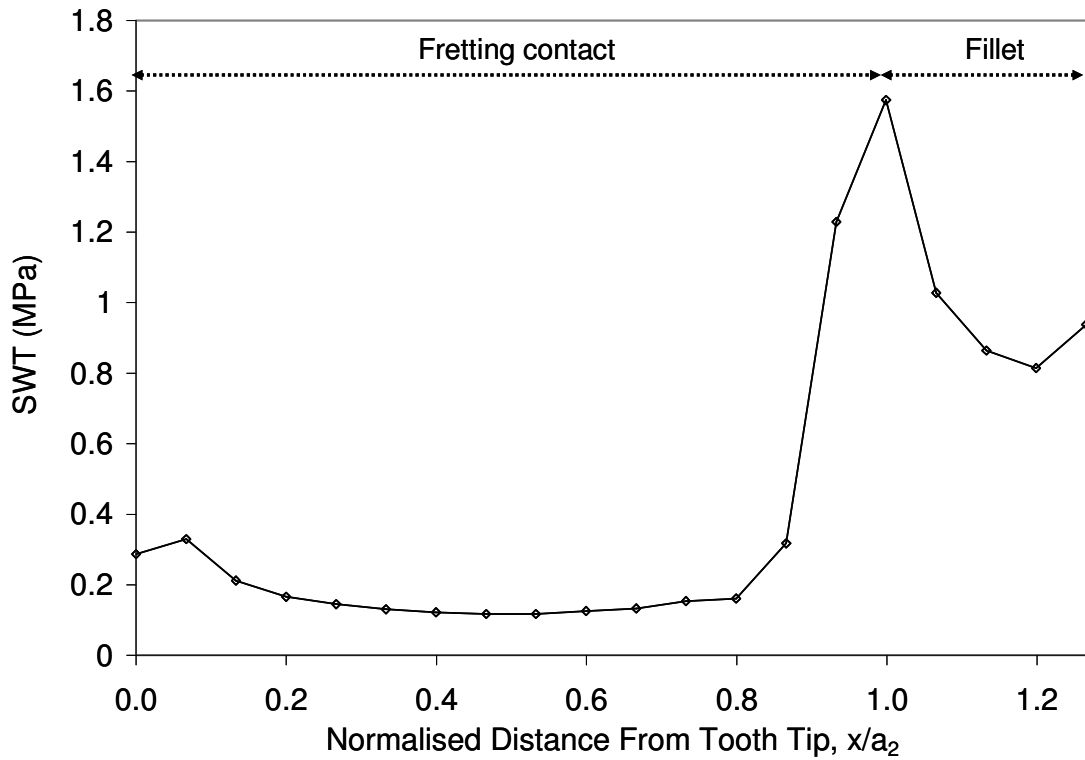


Figure 6.7. The FE-predicted SWT parameter for the URS at an axial position of  $z/b_2 = 0.5$  for a COF of 0.9.

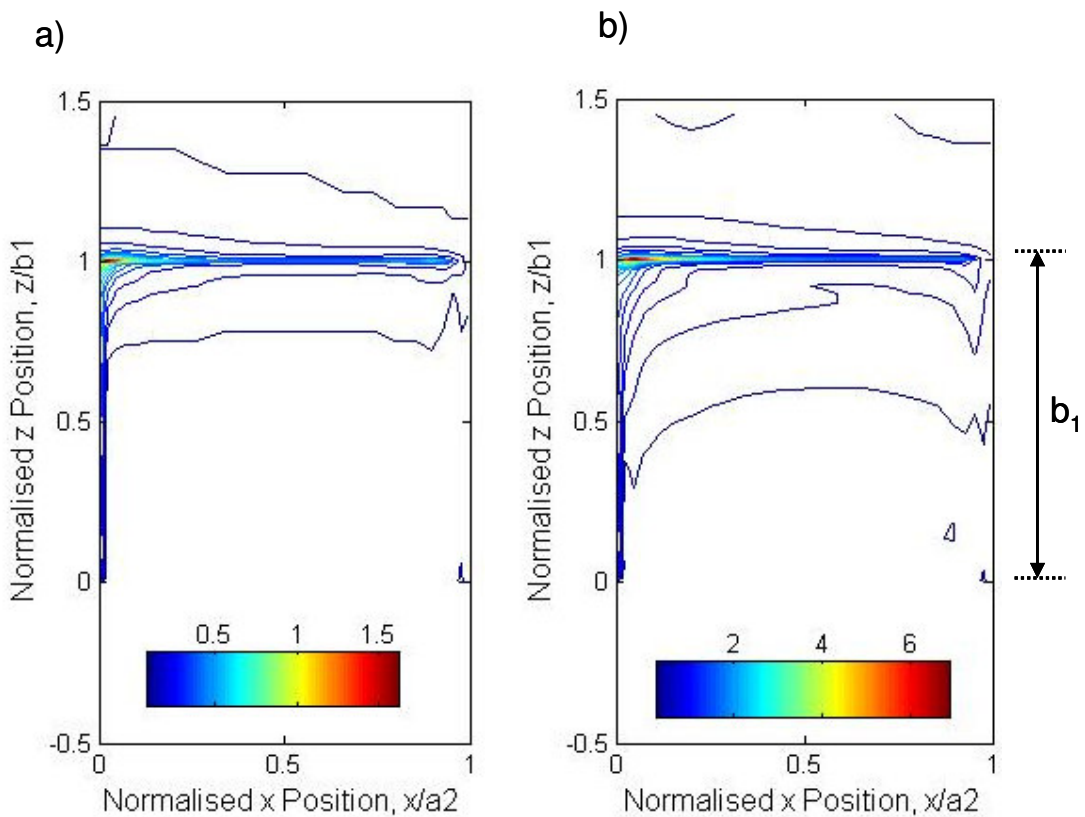


Figure 6.8. Contour plot of the averaged SWT parameter for: a)  $\sigma_{\max}/\sigma_y = 0.12$ , and b)  $\sigma_{\max}/\sigma_y = 0.24$ . The contact of the bridge is indicated by  $b_1$ .

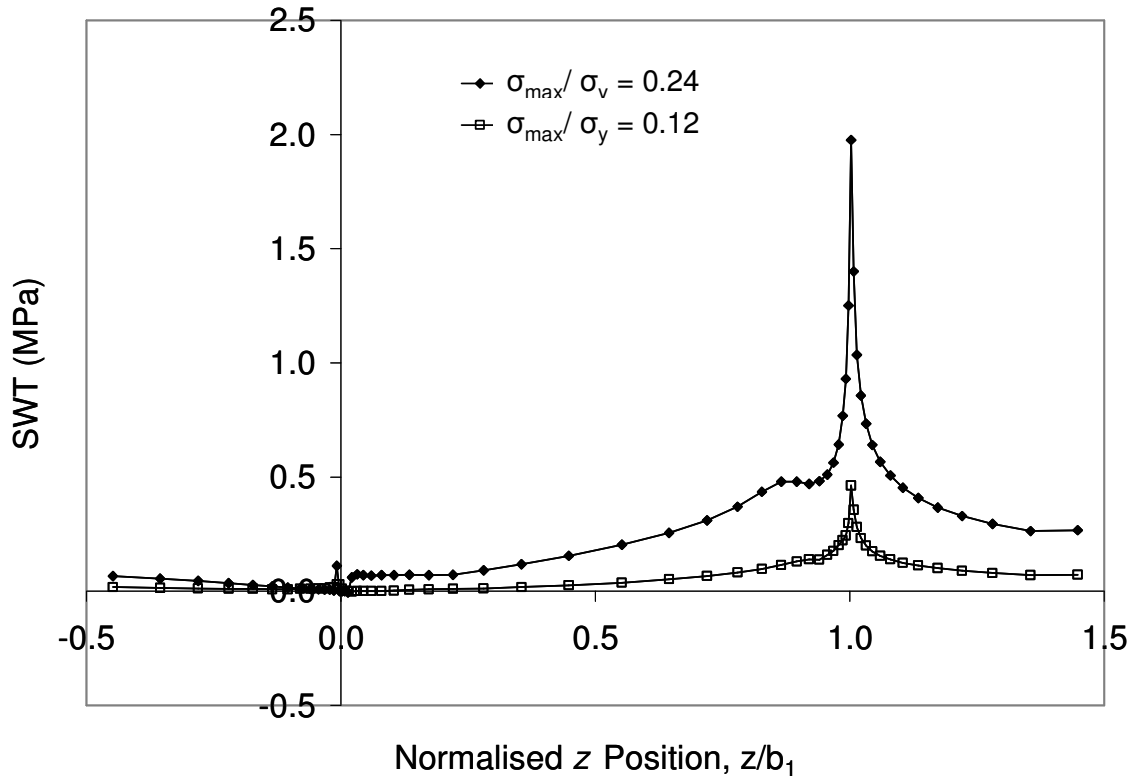


Figure 6.9. The averaged SWT parameter at  $x/a_2 = 0.5$  for two applied OP loads.

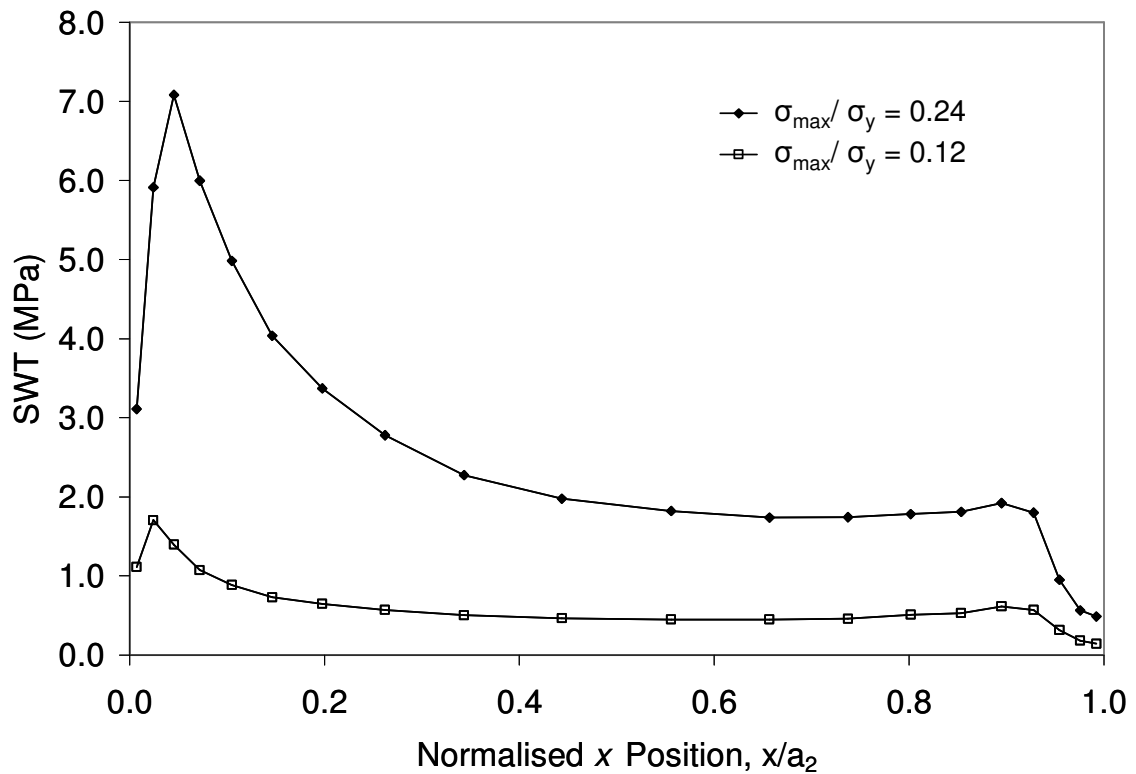


Figure 6.10. The averaged SWT parameter at  $z/b_1 = 1$  for two applied OP loads.

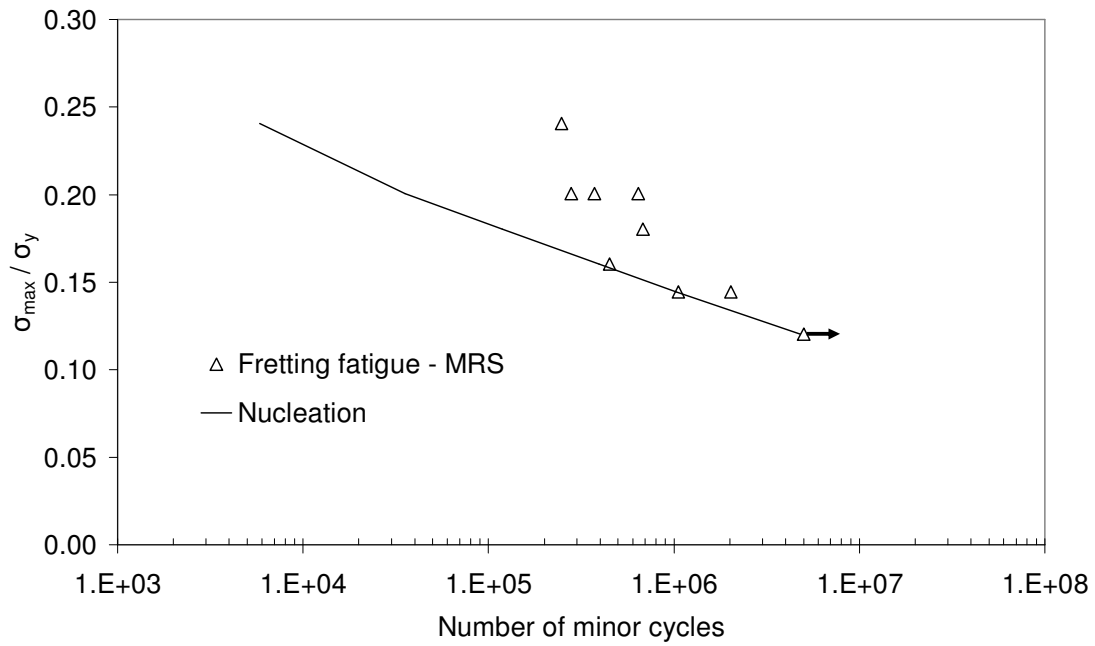


Figure 6.11. The minor cycle S-N curve of the MRS, showing a comparison of the predicted crack nucleation phase with the total number of cycles to failure of the experimental results.

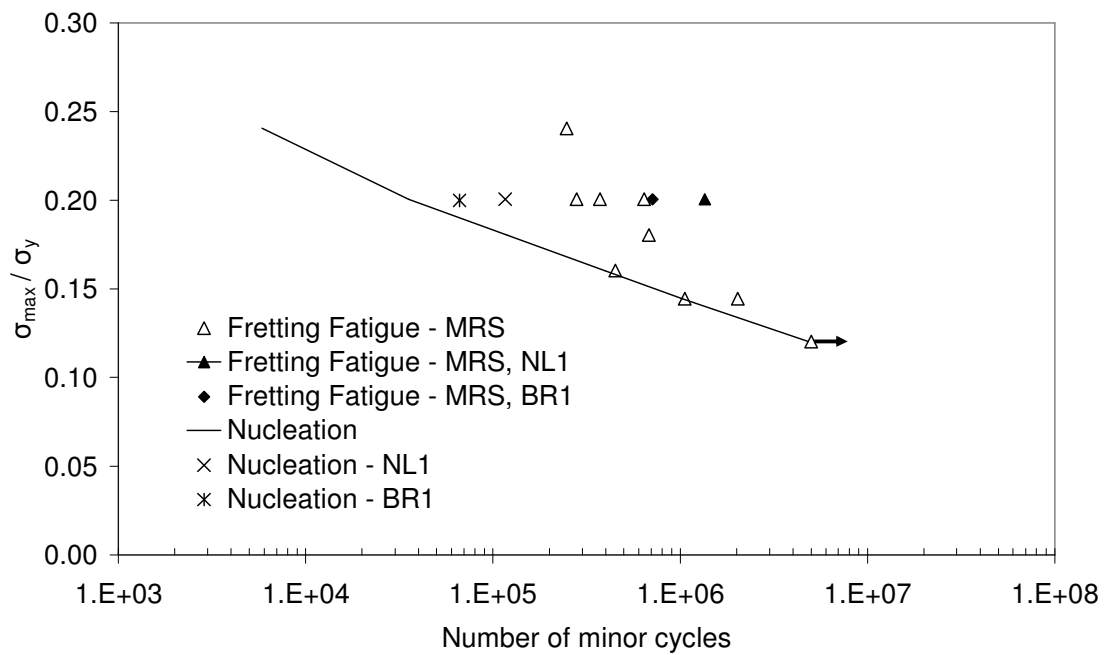


Figure 6.12. The minor cycle S-N curve, showing the effect of a reduced IP load (NL1) and a reduced bridge gap (BR1).

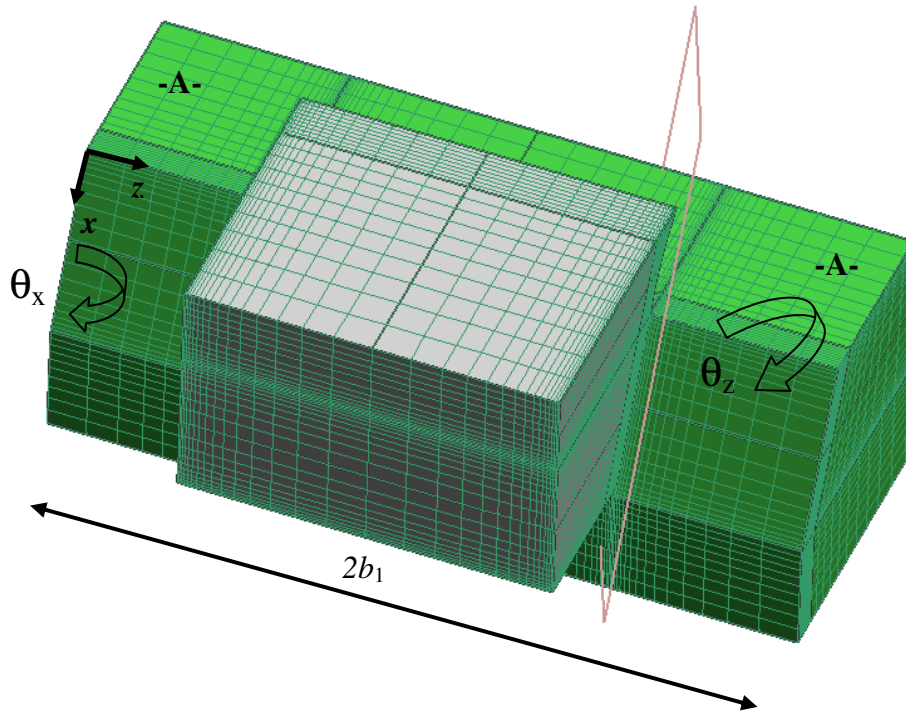


Figure 6.13. The sub-model with the definition of the critical-plane rotations.

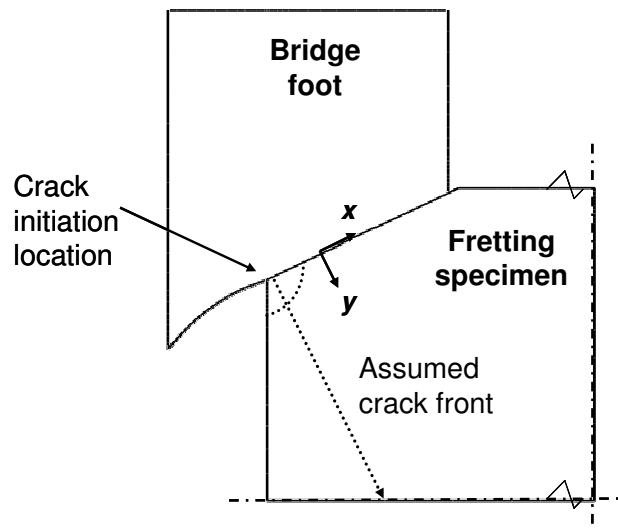


Figure 6.14. Two-dimensional schematic of the multiaxial RS. The applied bulk OP stress ( $\sigma_{zz}$ ) is normal to the plane.

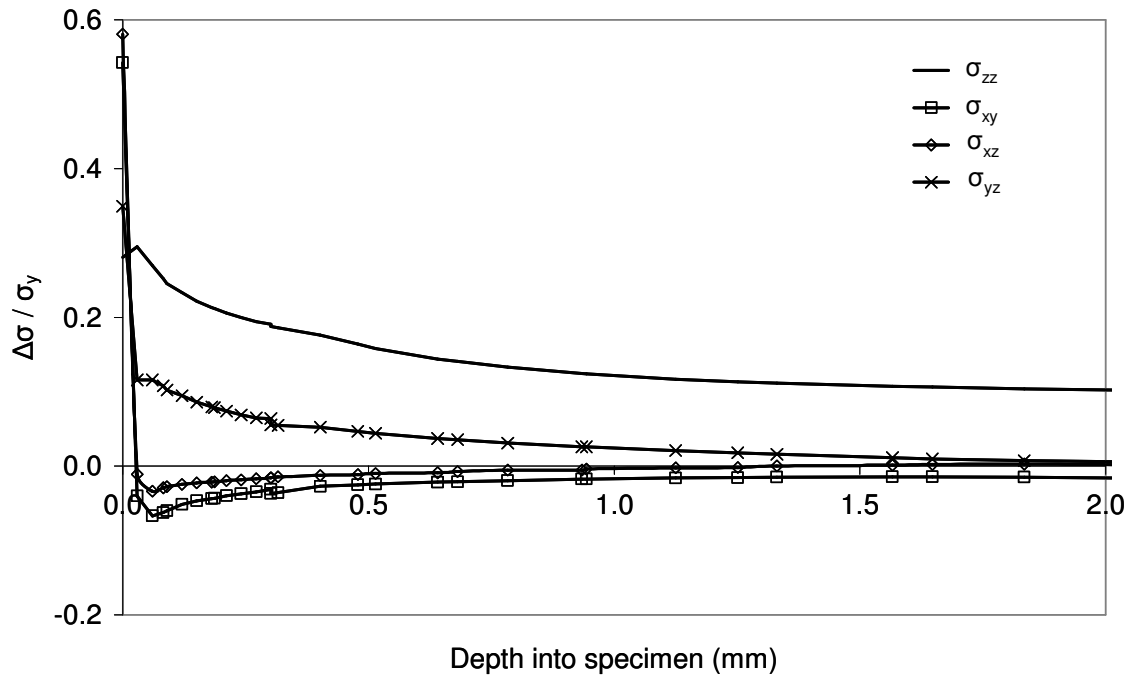


Figure 6.15. The axial and shear stress ranges into the depth of the specimen for an applied minor cycle load of  $\sigma_{\max}/\sigma_y = 0.12$  at the failure position of  $z/b_1 = 1.0$ .

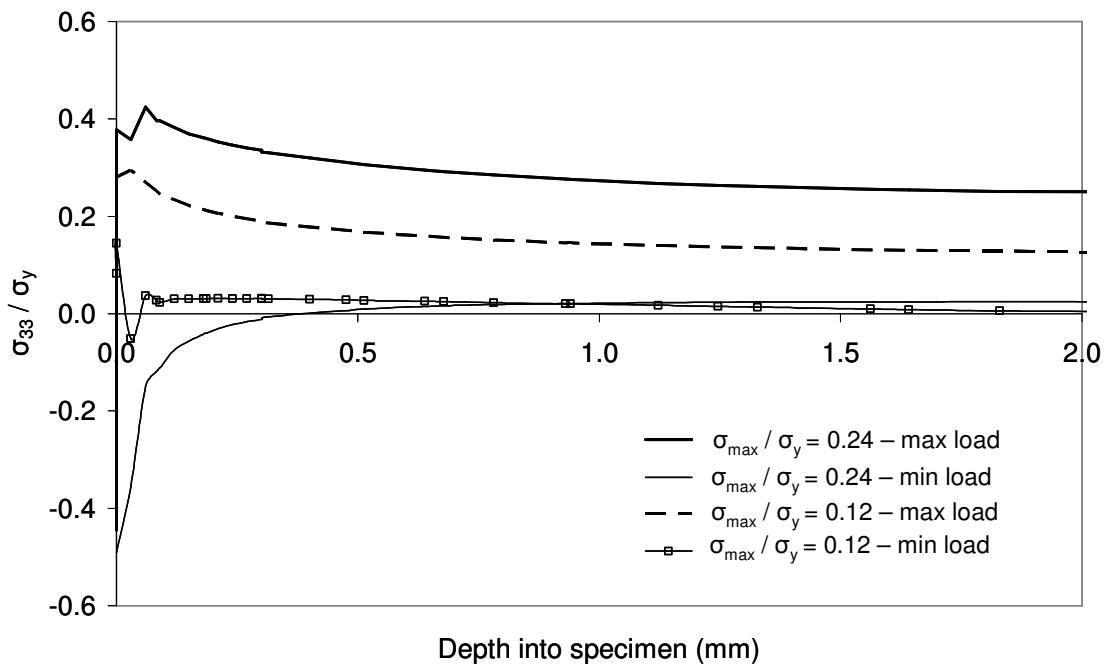


Figure 6.16. The axial stress ( $\sigma_{zz}$ ) at maximum and minimum loads for applied minor cycle loads of  $\sigma_{\max}/\sigma_y = 0.12$  and  $\sigma_{\max}/\sigma_y = 0.24$  at the failure position of  $z/b_1 = 1$ .

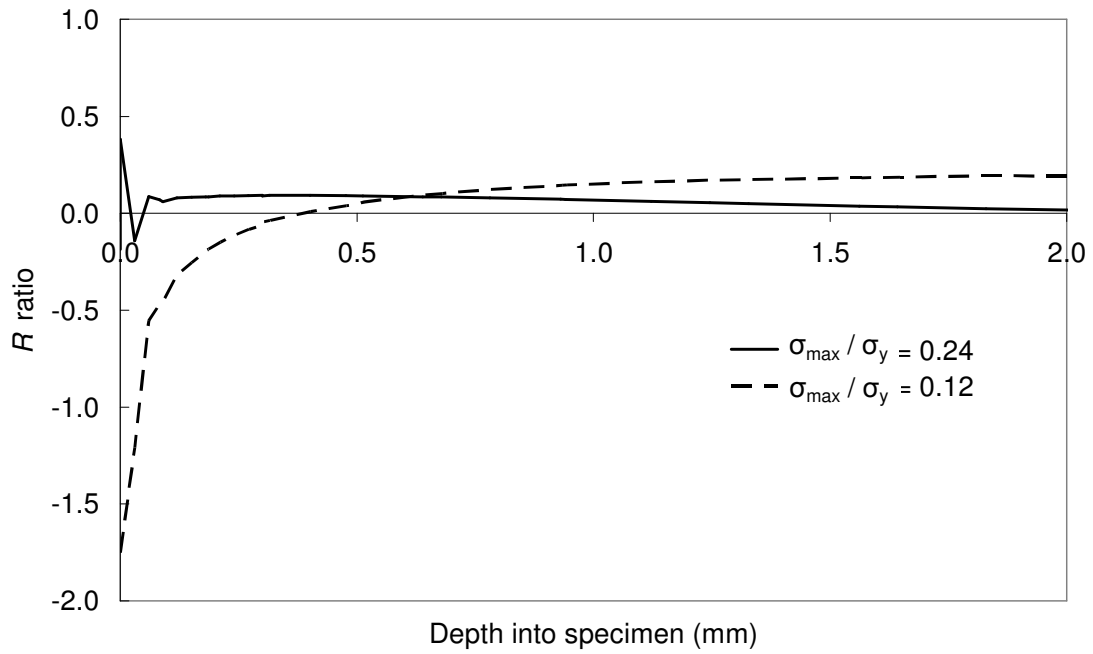


Figure 6.17. The variation of stress ratio,  $R_{\sigma}$ , with depth.

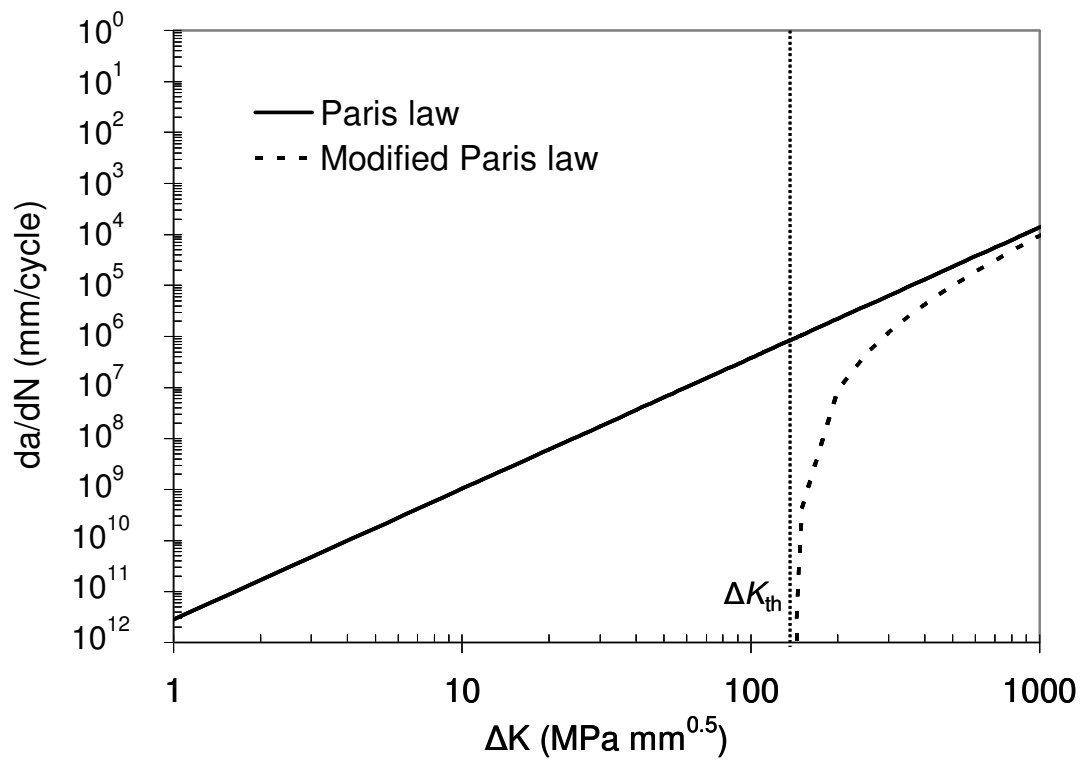


Figure 6.18. The Paris law and modified Paris law for near-threshold conditions.

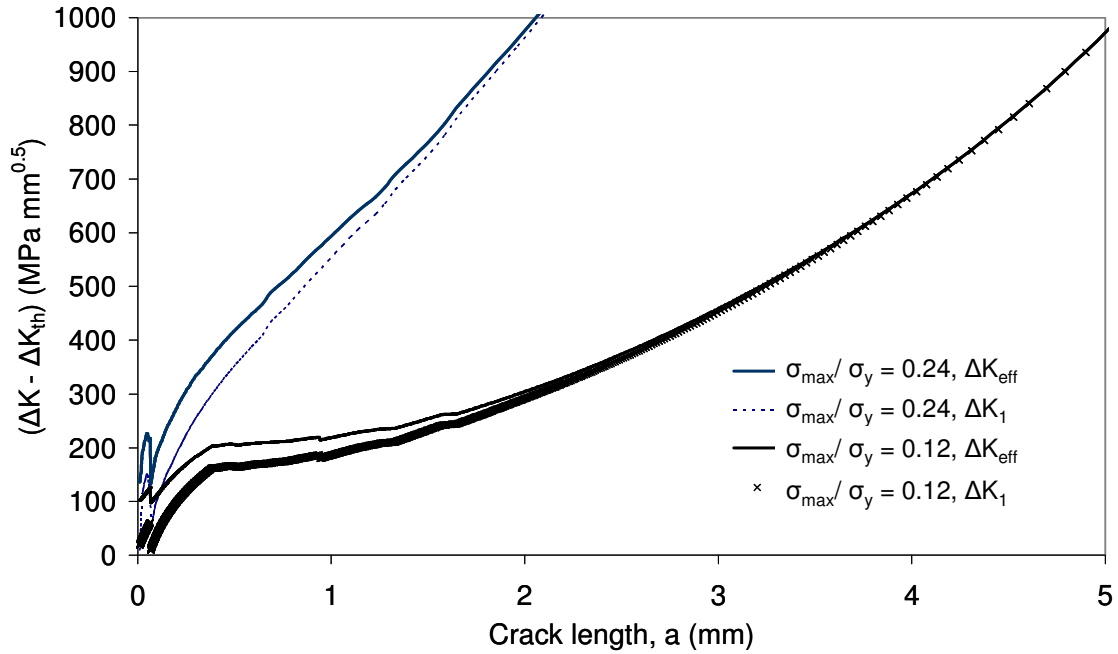


Figure 6.19. The variation of the mixed mode and mode I ( $\Delta K - \Delta K_{th}$ ) with crack length for two applied OP loads.

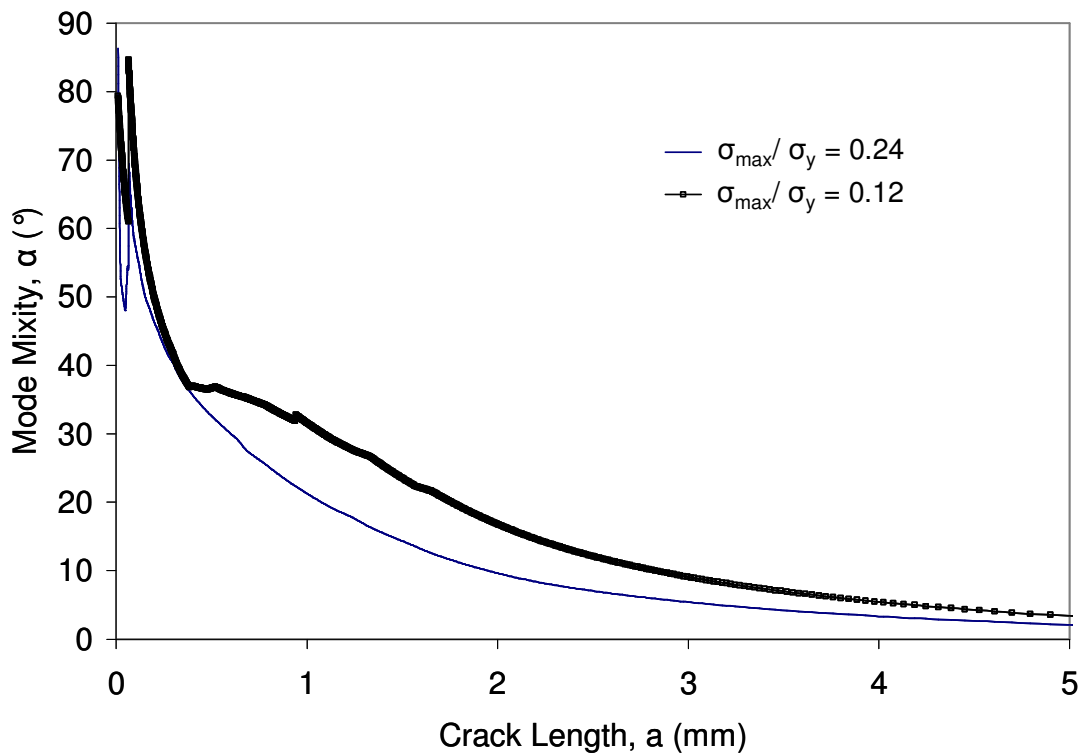


Figure 6.20. The mode mixity for the two OP load cases, as defined by  $\alpha_{mixity} = \tan^{-1}(\Delta K_{II} / \Delta K_I)$ .

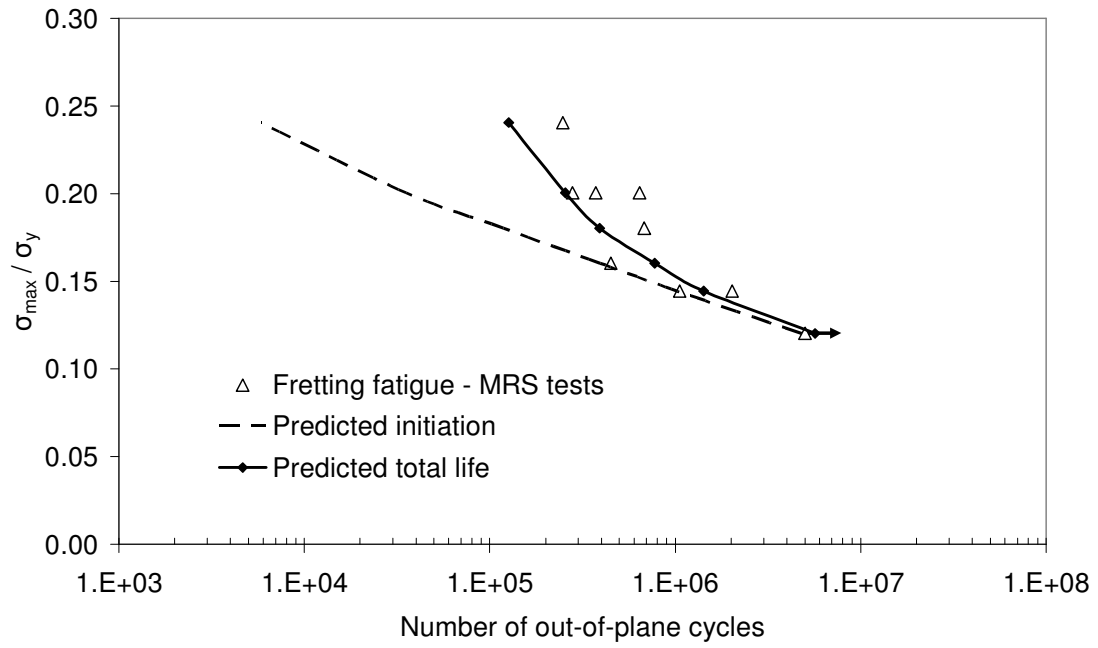


Figure 6.21. The experimental and predicted out-of-plane S-N curve of the MRS.

### Slip-based Lifting Parameters

#### 7.1 Introduction

The Smith-Watson-Topper (SWT) parameter was used to predict the crack nucleation phase of the uniaxial representative specimen (URS) and the multiaxial representative specimen (MRS) in the previous chapter. Fracture mechanics techniques were also used to predict the crack propagation phase of the MRS and the combined methodology was shown to capture the effect of the out-of-plane bulk fatigue stress (minor cycle load) on the total fretting fatigue (FF) life of the MRS. Additionally, it is known that contact slip is an important parameter influencing FF life. At low contact slips, fretting can be considered a plain fatigue case in the presence of a contact (stress gradient). With higher slip magnitudes, surface damage becomes the dominant failure mechanism. It is often observed that there is an increase in fretting fatigue life beyond a critical value of slip, which may be caused by the ‘rubbing’ out of early stage cracks before they have chance to propagate.

Most fretting fatigue lifting approaches are based on predicted stress and strain data only, neglecting the effects of surface damage and wear. This chapter shows the applicability of including a simple empirical surface damage parameter ( $D_{\text{fret}}$ ) into an existing critical-plane (multiaxial) SWT life prediction, in order to capture the effect of slip amplitude. With the predicted low magnitude of the contact slip and the predicted partial slip testing regime of the MRS tests, it is envisaged that no difference would have been predicted in lifting by using the multiaxial SWT fatigue approach (of Chapter 6) or the new  $D_{\text{fret}}$  approach. Therefore, the  $D_{\text{fret}}$  approach will be developed using the

simpler cylinder-on-flat geometry. The  $D_{\text{fret}}$  technique will also be applied as a potential explanation for the contact size effect in the cylinder-on-flat geometry.

## 7.2 Ruiz parameter

An attempt to include the effect of surface damage was made by Ruiz and co-workers [62], by creating a fretting fatigue damage parameter (FFDP). The resulting Ruiz parameter can be applied in order to predict the likely cracking location. One formulation of the parameter is given as:

$$F_1 = (\sigma_T)_{\max} (\tau\delta)_{\max} \quad (7.1)$$

where  $\tau$  is the surface shear stress and  $\delta$  is the cyclic slip amplitude. The term  $(\tau\delta)$  is a quantification of the frictional work and  $\sigma_T$  is the stress component parallel to the surface as it was hypothesised that a direct tensile stress ( $\sigma_T$ ) is required to propagate a crack. A modification to the parameter was made, leading to:

$$F_2 = \sigma_T \tau\delta \quad (7.2)$$

The  $F_2$  parameter has been shown to give a successful prediction of the likely cracking location for a dovetail connection made from Ti-6Al-4V material, but gives no quantification of the FF life. The physical interpretation of the Ruiz parameter is also not clear.  $F_2$  includes the product of the frictional work ( $\tau\delta$ ) and a crack driving term ( $\sigma$ ), but it is questionable as to whether the uniaxial stress term,  $\sigma_T$ , is able to capture the complex multiaxial stress state in fretting fatigue. Due to these limitations, a new FFDP, first suggested by Ding et al. [11], is investigated in the following sections.

### 7.3 Surface damage parameter $D_{\text{fret}}$

In addition to the state of stress and strain, the magnitude of contact slip is known to influence fretting fatigue life. The relative movement between two bodies inevitably leads to modification of the surface profiles due to fretting wear. This modification leads to a load (stress) distribution that differs from the initial un-worn case. It is also believed that 'rubbing out' of early stage cracks occurs, with a competition between fatigue cracking and fretting wear processes. Recent studies by Madge et al. [51, 125, 144], demonstrated the application of an FE-based methodology that incorporated the effects of wear and it was found that the approach could predict the more damaging effect of partial slip and beneficial action of large amplitude gross slip on FF life. The technique, however, requires considerable computational resources, therefore currently making it a specialised method. As well as the surface damage caused by the contact slip, there are also other features that exist during the fretting process, e.g. oxidation, near-surface plasticity, and heating, which influences cracking. To further improve prediction of fretting fatigue, these phenomena should be investigated and incorporated into a lifing methodology.

Traditional fatigue parameters applied to the fretting situation neglect the additional factors involved in fretting. In order to incorporate the previously mentioned surface damage effects on fretting fatigue, Ding et al. [11] recently suggested a modified SWT approach, which introduced the empirical fretting damage parameter  $D_{\text{fret}}$ . The addition of the FFDP to the SWT relation emphasises the importance of frictional work,  $\tau\delta$ , for the crack nucleation process, especially in a small volume close to the contact surface. The dimensionless  $D_{\text{fret}}$  parameter is formulated as:

$$D_{fret} = (1 + C\tau\delta) \left\langle 1 - \frac{\tau\delta}{(\tau\delta)_{th}} \right\rangle^n \quad (7.3)$$

where the constants  $C$ ,  $n$  and  $(\tau\delta)_{th}$  are to be empirically determined and the symbol  $\langle \rangle$  is defined by  $\langle u \rangle = u$  if  $u > 0$  and  $\langle u \rangle = 0$  if  $u \leq 0$ . The product  $(\tau\delta)$  is the frictional work during one fretting cycle for a given local contact position. The term  $(1 + C\tau\delta)$  is an empirical estimation of the enhanced possibility of crack formation under the frictional work  $\tau\delta$ . Finally, the term  $\left\langle 1 - \frac{\tau\delta}{(\tau\delta)_{th}} \right\rangle^n$  is introduced to characterise the consequence of fretting wear. A threshold,  $(\tau\delta)_{th}$ , is incorporated that is the limit of  $\tau\delta$  beyond which wear becomes dominant and there is no crack formation. The modified SWT approach is therefore expressed as:

$$\sigma_{max} \Delta \varepsilon_a D_{fret} = \frac{(\sigma'_f)^2}{E} (2N_f)^{2b} + \sigma'_f \varepsilon'_f (2N_f)^{b+c} \quad \tau\delta \leq (\tau\delta)_{th}. \quad (7.4)$$

When  $\tau\delta$  is greater than the threshold,  $(\tau\delta)_{th}$ , no failure is predicted. A key aspect that remains to be solved in the fretting problem is the separation of surface damage and stress gradient effects, and their relative contributions to fretting fatigue damage. It is expected that the development of the  $D_{fret}$  methodology will help to serve this goal.

## 7.4 Application of $D_{fret}$

### 7.4.1 Effect of slip

The effect of slip amplitude on fretting fatigue life for a titanium alloy (Ti-6Al-4V) was investigated by Jin and Mall [46] by conducting a range of experiments using the cylinder-on-flat geometry, with the test configuration

shown in Figure 7.1. A constant Hertzian peak pressure was maintained during the test (with a pad radius of 50.8 mm), along with an applied pad displacement and bulk fatigue stress in the specimen. The experimental findings are shown in Figure 7.2, along with the predictions from the FE-based methodology with evolving contact geometry (i.e. with wear) from Ref. [51]. It can be seen that beyond a critical slip amplitude, there is a significant increase in the fretting fatigue life. This is attributed to the increase in the contact width in the gross slip regime, which redistributes the contact load, leading to reduced local stress magnitudes. The computational predictions of Madge et al. [51] show good agreement with the experimental results but are computationally expensive to obtain.

In order to pursue a simpler, alternative method to that of the wear modelling technique, finite element analyses were conducted on the test geometry. The plane strain FE model is shown in Figure 7.3, in which the near-contact region mesh has a uniform element size, with a width of 10  $\mu\text{m}$  and depth of 3.6  $\mu\text{m}$ . An elastic material model for Ti-6/4 is used, with a Young's modulus of 126 GPa and Poisson's ratio of 0.30 [46], since macroscopic yielding was not expected to occur for the loading conditions investigated. A constant coefficient of friction (COF) of 0.8 is used throughout the analyses, according to the experimental measurement for the same test configuration reported in Ref. [145]. The frictional constraints were enforced via the exact Lagrange multiplier approach, where sticking is strictly enforced when the shear traction is less than the critical value as dictated by the Coulomb friction law.

The model was solved for a range of load cases, encompassing a range of slip amplitudes in the partial slip and gross slip regimes, with the conditions summarised in Table 7.1. For the FE analysis, a normal load,  $P$ , of 208  $\text{Nmm}^{-1}$  is applied to the cylinder in the first step, resulting in a peak Hertzian contact

pressure of 302 MPa. In the next step, the specimen is loaded by a cyclic fatigue load,  $\sigma(t)$ , with a maximum value of 550 MPa and a stress ratio ( $R_\sigma$ ) of 0.03. The pad is also loaded with a cyclic displacement,  $\delta_{app}(t)$ , with a maximum value of  $\delta_{app}^*$ . Different magnitudes of  $\delta_{app}^*$  lead to the slip conditions as given in Table 7.1. The applied displacement has been corrected to remove the effect of machine compliance, using the methodology in Ref. [51], with the following:

$$\delta = \delta_{global} \frac{C_{COF}}{C_{rig}} \quad (7.5)$$

where the constant  $C_{COF} / C_{rig}$  was determined to be 16 in Ref. [51].

The typical distributions of  $\tau\delta$  and the SWT parameter for the partial slip regime are shown in Figure 7.4 for  $\delta_{app}^* = 22 \mu\text{m}$  (test 8), where the shear traction is obtained at  $\delta_{app}(t) = \delta_{app}^*$  and where  $\delta$  is the FE-predicted relative slip amplitude per cycle. The plots are normalised with respect to the contact half-width,  $a$ . The distribution of  $\tau\delta$  shows non-zero values in both slip zones, with a peak magnitude located at  $x/a = 0.82$ . The maximum value of the SWT parameter appears at the trailing edge-of-contact ( $x/a = 1$ ). It is therefore clear that the predicted location of conventional fatigue cracking (via the SWT parameter) is at a different location to the position of maximum surface damage (from  $\tau\delta$ ). In the studies of Madge et al. [144], it has been reported that wear gives an attenuation of contact-edge SWT peak, shifting the cracking location steadily towards the stick-slip interfaces. Cracking in the slip zone is also commonly observed experimentally. Since the evolution of contact geometry reduces the SWT magnitudes near the contact edges, the significance of  $\tau\delta$  on the fretting fatigue crack nucleation around this region will be raised. Therefore as a first step, it is postulated in this study that

fretting fatigue cracking occurs at the location of maximum  $\tau\delta$ . Although Ruiz predicted in Ref. [62] that the cracking location could be predicted for a dovetail connection with the  $F_2$  parameter, a possible further enhancement of this could be to combine the frictional work and SWT parameter to include multiaxial effects, forming a new parameter:

$$F_3 = (\tau\delta)\sigma_{\max}\Delta\varepsilon_a \quad (7.6)$$

The cracking location would then be predicted by the maximum location of this parameter. Although not undertaken here, the location of  $x/a = 0.82$  used for test 8 is not significantly different from the maximum location of the  $F_3$  parameter, that occurs at  $x/a = 0.88$  for test 8. The fretting fatigue life is subsequently determined by the combination of the frictional work and the SWT parameter (at  $x/a = 0.82$  for test 8), as given by Eq. 7.4. Using peak SWT values for the different load cases, the total life can be predicted using the fatigue constants given in Table 7.2 (from Ref. [138]), and the resulting predictions are compared with the experimental results in Figure 7.5. It is clear that the conventional SWT approach, which is based on the peak SWT at the contact edge, significantly underestimates the test results, and also fails to capture an increase in life beyond a critical value of slip amplitude. This is because once the gross slip condition is reached, the predicted stress magnitudes, predominantly controlled by shear traction which has saturated at the critical value of  $\tau(x) = \mu p(x)$ , where  $p(x)$  is the local contact pressure as a function of position, do not increase with an increase in applied displacement. The life predictions based on the SWT values at the location of maximum  $\tau\delta$  are also plotted in Figure 7.6. It is found that the results are closer to the experimental tests than the peak SWT approach, and only slightly underestimate them up to  $\delta_{app}^*$  of 5  $\mu\text{m}$ . The approach, however, fails to capture the increase in life beyond a contact slip of 5  $\mu\text{m}$ , where gross slip

conditions prevail. The  $D_{\text{fret}}$  approach is therefore applied and the constants determined (based on the SWT at position of maximum  $\tau\delta$ ), with the implementation summarised as follows:

**Step 1:** The value of  $\tau\delta$  corresponding to the transition from partial slip to gross slip is identified from the finite element analyses of the test configuration in Figure 7.1. For the case studied here, the transition to gross slip was identified at  $\tau\delta = 0.58$  MPa mm. The threshold,  $(\tau\delta)_{\text{th}}$ , was therefore set as 0.60 MPa mm, due to the results of Ref. [144] indicating a recovery of total fretting fatigue life slightly beyond the contact regime transition,

**Step 2:** The FE-predicted SWT values across a range of slips were combined with  $D_{\text{fret}}$ , varying  $C$  and  $n$  to obtain the  $C$  and  $n$  values which optimise the fit. This was conducted using the least squares method and implemented to minimise the following objective function with respect to the unknown constants  $C$  and  $n$ :

$$F(C, n) = \sum_i \left\{ N_i^p(C, n) - N_i^e \right\}^2 \quad (7.7)$$

where  $N_i^p(C, n)$  is the FE-predicted life using  $\text{SWT} \cdot D_{\text{fret}}$  for data point,  $i$ , and  $N_i^e$  is the experimental life corresponding to the same data point. This allows the best fit to be obtained to the experimentally-observed results as a function of slip amplitude. For the test conditions of Table 7.1, this gives  $C = -0.350$  and  $n = 0.038$ .

The resulting  $D_{\text{fret}}$  with SWT life prediction is therefore shown in Figure 7.6 and is seen to capture the experimental trend well.  $D_{\text{fret}}$  as a function of the frictional work,  $\tau\delta$ , is plotted in Figure 7.7. For this case,  $D_{\text{fret}}$  is always less than 1, and it decreases monotonically with increasing  $\tau\delta$ . Therefore,  $D_{\text{fret}}$  results in an overall beneficial effect in terms of fatigue life for the investigated test conditions of Table 7.1.

#### 7.4.2 Application of $D_{\text{fret}}$ to the size effect

In fretting contacts there are high stress fields caused by the presence of the contacting body, which leads to steep stress gradients due to the rapidly decaying stress magnitude with distance away from the contact. This is especially apparent at the trailing edge-of-contact and at the stick-slip interfaces due to the high tractions present at these locations. This leads to the existence of a size effect that is also observed in notch fatigue studies (e.g. see Taylor [146]). In fretting, the size effect means that a variation in fretting fatigue life is observed with contact width for the Hertzian geometry when the ratio  $Q/P$  is maintained constant. This constant ratio ensures that the stress magnitude is maintained, whilst the extent of the stress field is varied [110].

The size effect was investigated for an aluminium alloy (Al4%Cu) with the Hertzian (cylinder-on-flat) geometry by Araújo and Nowell in Ref. [77], by varying the pad radius and the applied contact load. The static load,  $P$ , was first applied followed by an oscillatory shear force of peak magnitude  $Q_{\text{max}}$ . The bulk fatigue stress was applied in phase with the shear force at an amplitude of  $\sigma_b$ . Tests were conducted in the partial slip regime, with a constant  $Q/P$  of 0.45 across the tests. It was found that there were no fretting fatigue failures (test run-outs) at small contact sizes, as shown in Figure 7.8. With an increase in contact width beyond the critical size, it is observed that

there is a sudden decrease in total fatigue life. Araújo and Nowell explained the size effect with a process volume approach, which consists of averaging the stress and strain state in a micro-volume of material prior to applying the multiaxial fatigue criterion. It was argued that the dimensions of this could be equated to the grain size of the material. The approach improved prediction in relation to the experimental results, although a consistent averaging dimension was not found to fit the experimental results across the contact sizes. The analysis neglected the effect of slip amplitude on the fretting fatigue life, which is a possible explanation of the discrepancy. Therefore, for the analysis of the experimental results of Ref. [77], averaging of the SWT parameter in the process zone (grain size) will firstly be conducted in the present work. This will then followed by the application of the  $D_{\text{fret}}$  with SWT approach. This allows the averaging dimension to be kept constant along with the  $C$ ,  $n$  and  $(\tau\delta)_{\text{th}}$  values, for the different contact sizes.

A two-dimensional elastic plane strain (CPE4 elements) FE model was created in ABAQUS for the analysis of the experimental results. It was shown in Ref. [147] that three-dimensional effects for this geometry are small, justifying the plane strain assumption. The Al4%Cu mechanical and fatigue properties can be found by consulting Ref. [77], giving a Young's modulus of 74 GPa and Poisson's ratio of 0.33 and the fatigue constants as given in Table 7.2. The loading and boundary conditions were then applied, with 5 steps in the analysis, as seen in Figure 7.9. Analyses were carried out for different pad radii ( $R=25, 50$  and  $75$  mm). The mesh used for  $R = 50$  mm can be seen in Figure 7.10 (the origin of the  $x$ -coordinate is at the centre of contact). There is a uniform element size of  $7.8 \times 7.8 \mu\text{m}$  around the region of contact, which is finer than the grain size ( $50 - 100 \mu\text{m}$ ) in order to adequately capture the stress and strain state. Frictional constraints were enforced via the exact

Lagrange multiplier approach. The COF was previously determined to be 0.75 from Ref. [77], via a semi-analytical method that involved the experimental determination of the transition from partial slip to gross slip.

Figure 7.11 shows the contact pressure distributions for the three contact geometries. It is clear that, although the peak magnitude is constant, the extent of the contact increases with increasing contact radius. This gives identical contact pressure distributions when normalised against the contact half-widths,  $a$  (contact half-widths of 0.19, 0.38 and 0.57 mm from the radii of 25, 50 and 75 mm, respectively). Similarly, as shown in Figure 7.12, the normalised shear traction distributions are almost identical across the geometries. Figure 7.13 compares the predicted contact slip distributions. It is observed that with increasing contact size, there is an increase in the contact slip. As a result, the behaviour of the  $\tau\delta$  distributions is similar to the contact slip, with the distributions plotted in Figure 7.14. The peak value of  $\tau\delta$  is located at approximately  $x/a = -0.8$  in all cases. This difference in surface damage with increasing contact size is argued to influence the fretting fatigue cracking process and this will be captured via the predicted variation in the  $D_{\text{fret}}$  parameter.

The averaging in the process zone can be conducted via averaging of the SWT parameter or of the stress and strain state. Previous studies conclude that both methods give similar results [77, 148], and therefore averaging of the SWT parameter is conducted here. The averaging is realised with the following formula:

$$SWT_{\text{avg}} = \frac{1}{N} \sum_{i=1}^N SWT_i \quad (7.8)$$

where  $N$  is the total number of points where the SWT was determined and  $i$  is the value at a given integration point. A value of  $80\ \mu\text{m}$  is used for the averaging dimension, which matches the grain size for the aluminium alloy of  $50\text{-}100\ \mu\text{m}$ .

With the averaging of the SWT parameter realised, the  $D_{\text{fret}}$  approach may then be conducted. The critical value of  $\tau\delta$  for transition from partial slip to gross slip varies with pad radius (and contact half-width), as highlighted by the linear relationship in Figure 7.15. In order to demonstrate the approach, a value of  $(\tau\delta)_{\text{th}} = 0.4$  was chosen, which approximately corresponds to the value at a pad radius of  $R = 150\ \text{mm}$  (not shown in Figure 7.15 as the FE simulation of this contact size was not conducted). This was the largest contact size investigated in the original study, and there was not a significantly observed increase in the cycles to failure (due to wear processes becoming more dominant) for this geometry compared with the smaller contact sizes. This was therefore chosen as the critical value of  $(\tau\delta)_{\text{th}}$ .

Figure 7.16 plots the experimental results as a function of contact slip, along with the computational predictions. It is seen that the conventional SWT prediction methodology significantly underestimates the number of cycles to failure in comparison with the experimental results. When these predictions are averaged in the process zone, the resulting predictions over-predict the total fretting fatigue life. This same over-prediction was obtained by Araújo and Nowell in Ref. [77] using volume averaging. With  $(\tau\delta)_{\text{th}} = 0.4$ , the least squares optimisation according to STEP 2 in Section 7.4.1 (Eq. 7.7) can be conducted to obtain the  $D_{\text{fret}}$  constants. This gives  $C = 14.449$ ,  $n = 2.655$ , and it is observed in Figure 7.16 that the predictions with the  $D_{\text{fret}}$  approach are able

to match the experimental results. Subsequently, the behaviour of  $D_{\text{fret}}$  as a function of the frictional work,  $\tau\delta$ , is shown in Figure 7.17.

### 7.4.3 Effect of COF

Knowledge of the response of the fretting fatigue life with a change in the COF is useful for the assessment of fretting fatigue palliatives, such as surface coatings, that principally affect the crack initiation phase, for optimisation of fretting fatigue life for a given application. With fretting fatigue behaviour argued here to be governed by the combination of the surface damage (frictional work) and the stress and strain state (critical-plane SWT), it is implicit that a change in the COF will alter the total number of cycles to failure of a component. However, the effect of a change in the COF for a contact in partial slip is not immediately apparent. For example, the value of the shear traction would be expected to increase with an increase in the COF, whereas the contact slip will decrease. Therefore, a number of FE analyses were run to investigate this, using the  $R = 75$  mm model from Section 7.4.2. Analyses were solved with a variation in the COF whilst maintaining  $Q/P$  at 0.45. The findings for a variation of  $\tau\delta$  with the COF are given in Figure 7.18. The non-linear relationship shows that with a reduction in the COF, there is an increase in the surface damage (as quantified by  $\tau\delta$ ), indicating an increase in the severity of fretting. To further investigate this behaviour, the individual components can be examined, and are shown in Figure 7.19. The plot shows the percentage variation of the parameters compared with their respective values at a COF of 0.45. It is seen that with decreasing COF, the shear traction reduces rapidly, while the contact slip increases, indicating that contact slip effects become more significant. This suggests that with a reduction in the COF, wear processes (arguably related more to  $\delta$  than  $\tau$ ) become relatively more significant. This knowledge is useful in the separation of stress gradient and surface damage effects.

After examining the sensitivity of the surface damage ( $\tau\delta$ ) with COF, the fatigue crack initiation process may also be investigated, as quantified by the SWT parameter. Figure 7.20 shows the percentage variation of the FE-predicted number of cycles to failure obtained from the averaged SWT parameter (variation from the results with a COF of 0.45) with the COF, along with the variation of  $\tau\delta$  as found in Figure 7.19. It is seen that the FE-predicted number of cycles to failure is significantly more sensitive to the COF than the value of the surface damage according to  $\tau\delta$ . Both curves show a decrease from their respective values at a COF of 0.45 with increasing COF. Clearly, the predicted reduction (from a multiaxial fatigue viewpoint) in the number of cycles to failure is undesirable, but in the partial slip regime the decrease in the magnitude of  $\tau\delta$  is beneficial to the total fretting fatigue life. This highlights the competition between the surface damage and fatigue cracking processes. It also suggests that the crack initiation process induced from a stress and strain standpoint becomes relatively more significant than crack initiation induced from surface damage effects. In the analysis of fretting fatigue for practical applications, it is therefore likely that a reduction in the COF will lead to improved fretting fatigue resistance. Consequently, the use of surface lubrication or coatings that reduce the COF will be beneficial for fretting fatigue life. Attention must then be focused on the analysis of the increased wear that would occur. In the fundamental study of fretting fatigue, the separation of surface damage and stress (including steep gradients) effects is critical to understanding and solving the fretting fatigue problem, as the relative importance of the two factors has yet to be fully determined. The use of empirical parameters, such as  $D_{\text{fret}}$ , is expected to aid in reaching this goal. Future experimental testing could examine the effect on the fretting fatigue life of varying the COF. The varying COF across different tests (with the same load conditions) could be realised by using dry, lubricated and coated

specimens. In combination with FE modelling and the  $D_{\text{fret}}$  parameter, this could allow the relative importance of stress gradient and surface damage effects to be determined.

## 7.5 Discussion

Although the approach demonstrated in this chapter introduces three additional variables, the importance of empirical parameters in the study of fretting fatigue should not be underestimated. Future testing is undoubtedly required to validate the approach, e.g. investigation of the experimental sensitivity of the parameters and of their application across a wide-range of fretting conditions. It will also be of use to ascertain if  $(\tau\delta)_{\text{th}}$  is the critical parameter that governs the pick-up in life with increased slip amplitude.

Future work could investigate the further development of the  $D_{\text{fret}}$  methodology, with the following as a possible example. With a positive value of  $D_{\text{fret}}$ , the maximum value of the parameter gives the position of maximum surface damage and minimum fatigue life. The maximum value of the  $D_{\text{fret}}$  function (denoted as  $y$  below) can be obtained by differentiation with respect to  $\tau\delta$  and finding the stationary point. To simplify the expression, a substitution is conducted, where  $x$  represents  $\tau\delta$  and  $K$  represents  $(\tau\delta)_{\text{th}}$ . This leads to the expression:

$$\frac{dy}{dx} = C \left(1 - \frac{x}{K}\right)^n - \frac{n}{K} (1 + Cx) \left(1 - \frac{x}{K}\right)^{n-1} \quad (7.9)$$

The stationary point is found by setting the expression to zero:

$$0 = C \left(1 - \frac{x}{K}\right)^{n-1} \left[ \left(1 - \frac{x}{K}\right) - \frac{n}{K}(1 + Cx) \right] \quad (7.10)$$

This is satisfied for the trivial solution of  $x = K$ , or when:

$$x = \frac{KC - n}{C(1 + n)} \quad (7.11)$$

Substituting the constants into the previous expression yields the stationary point (SP) value of  $\tau\delta$ ,  $(\tau\delta)_{sp}$ , as:

$$(\tau\delta)_{sp} = \frac{C(\tau\delta)_{th} - n}{C(1 + n)} \quad (7.12)$$

The minimum of the  $D_{fret}$  function could then be equated to the experimentally found value of  $\tau\delta$  that corresponds to the worst fretting fatigue life. The application of this requires a suitable algorithm to optimise the function, whilst adhering to this constraint. Additionally, advanced mathematical programming or optimisation techniques could be applied to the problem to further optimise the procedure and investigate the behaviour of the function.

In the analysis of the contact size effect, all of the tests were conducted in the partial slip regime. With further increases in the pad radius (beyond the value of  $R = 150$  mm that was tested in Ref. [77]) a 'pick-up' in the experimental life to failure may not be observed. Whilst this is recognised, this work aims to demonstrate the general approach and may lead to future refinement of the technique; for example, by modification of the functional form of  $D_{fret}$ .

## 7.6 Summary of chapter

A recently suggested fretting fatigue lifing parameter has been implemented in this chapter. The approach combines multiaxial fatigue-cracking phenomena as quantified by the SWT parameter, with a fretting fatigue damage parameter,  $D_{\text{fret}}$ , that is used to include surface damage effects (such as wear, oxidation, heating etc.). The formulation of  $D_{\text{fret}}$  includes terms that quantify the effects of surface damage caused by the frictional work  $\tau\delta$ .

It has been shown that the  $D_{\text{fret}}$  approach is able to capture the variation in fretting fatigue life with contact slip, providing more accurate life predictions. The methodology was also used to capture the contact size effect in fretting fatigue. The approach advances fretting fatigue lifing of components with the inclusion of surface damage effects via parameters determined from simple experimental tests. This potentially circumvents the need for computationally intensive wear simulations. Further tests are required to validate the method.

## 7.7 Tables

Table 7.1 The loadcases for the FE analyses of the experimental results of Ref. [46].

Load case	Applied displacement, $\delta_{app}^*$ ( $\mu\text{m}$ )	FE-predicted slip in contact, $\delta$ ( $\mu\text{m}$ )	FE-predicted Slip regime
1	38	0.8	p.s
2	35	1.2	p.s
3	30	1.9	p.s
4	26	2.5	p.s
5	25	2.6	p.s
6	24	2.9	p.s
7	23	3.1	p.s
8	22	3.3	p.s
9	17	5.2	g.s
10	16	6.2	g.s

where p.s. is partial slip and g.s is gross slip.

Table 7.2. The 1 mm fatigue constants for Ti-6Al-4 [138] and Al 4%Cu [77].

Material	$\sigma_f'$ (MPa)	$b$	$\epsilon_f'$	$c$
Ti-6Al-4V	2030	-0.104	0.841	-0.688
Al 4%Cu	1015	-0.11	0.21	-0.52

## 7.8 Figures

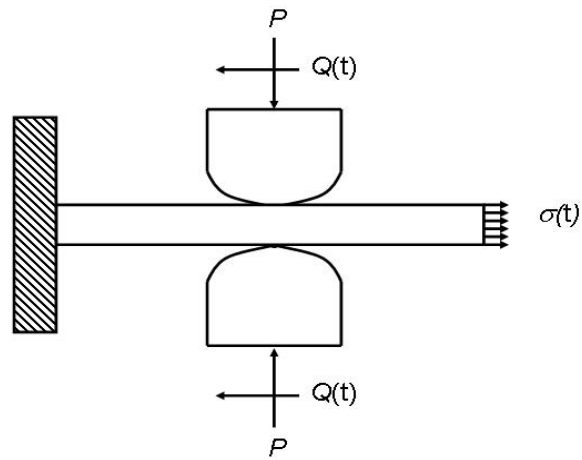


Figure 7.1. Schematic of the fretting fatigue test configuration of Ref. [46].

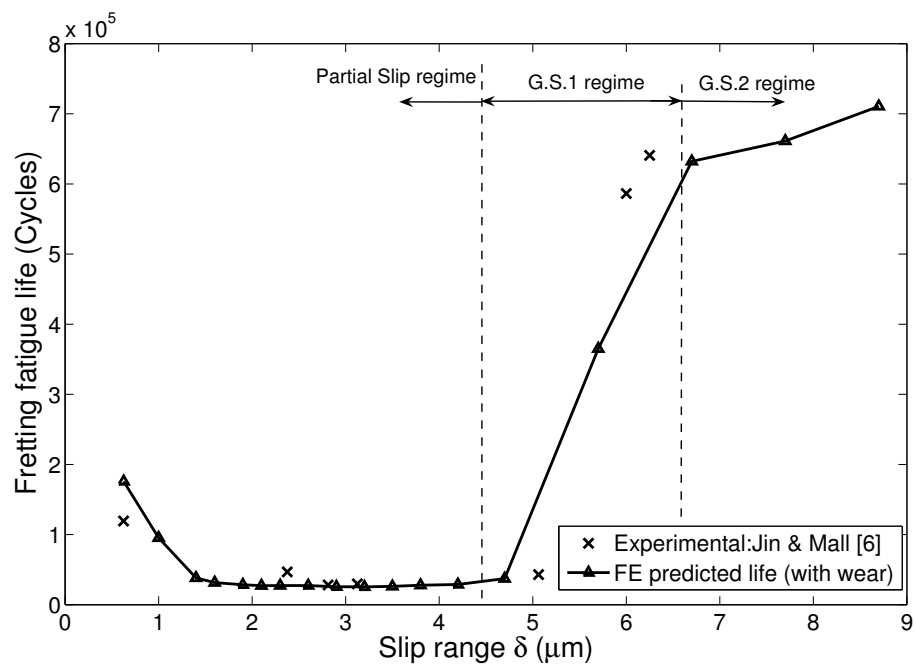


Figure 7.2. The correlation between contact-evolution based fatigue predictions and experimental data, from Ref. [144].

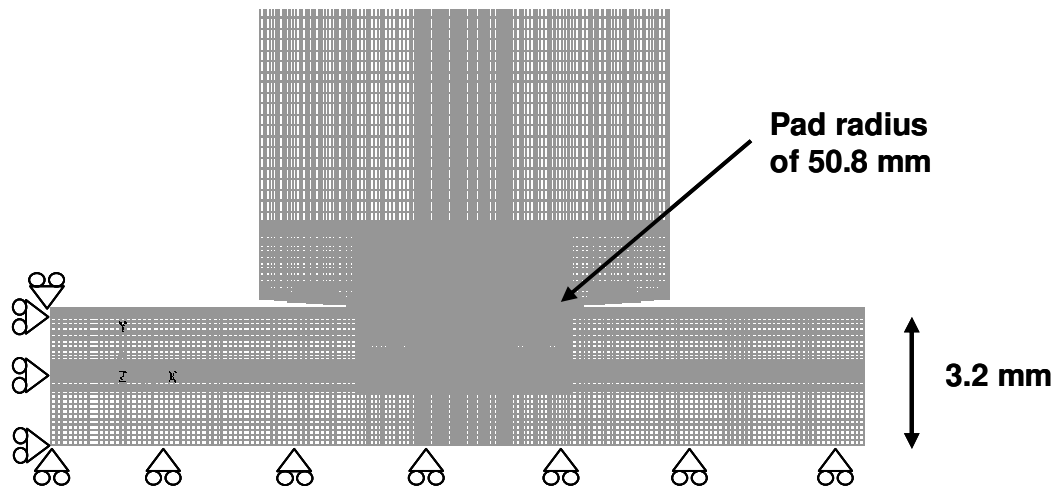
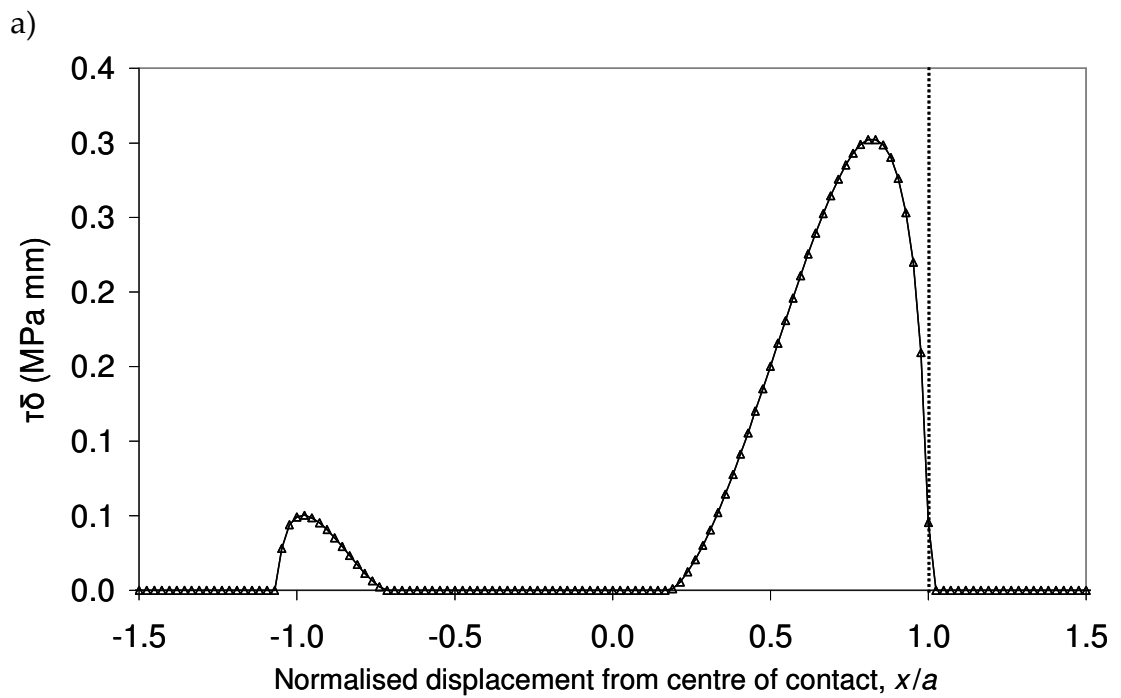


Figure 7.3. The cylinder-on-flat FE mesh used for the simulation of the experimental results of Jin and Mall [46].



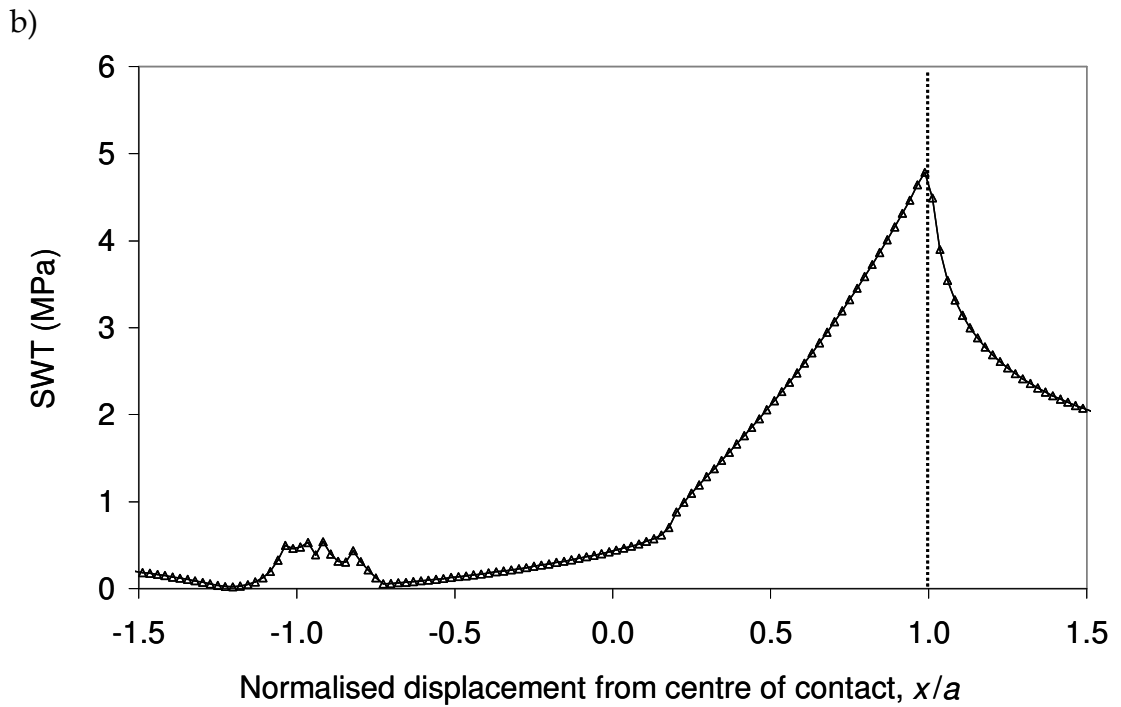


Figure 7.4. The normalised distribution of a)  $\tau\delta$  and b) SWT parameter for test 8 under the partial slip condition, with the critical edge-of-contact position indicated.

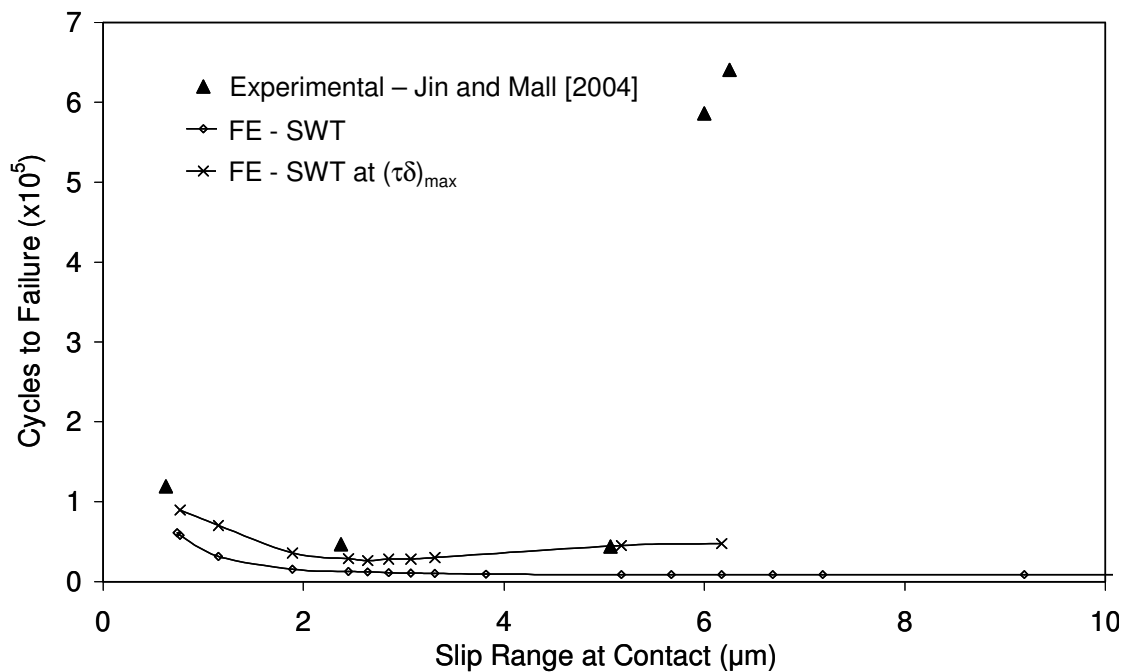


Figure 7.5. The predicted effect of slip amplitude on fretting fatigue life with the SWT approaches for the experimental results of Ref. [46].

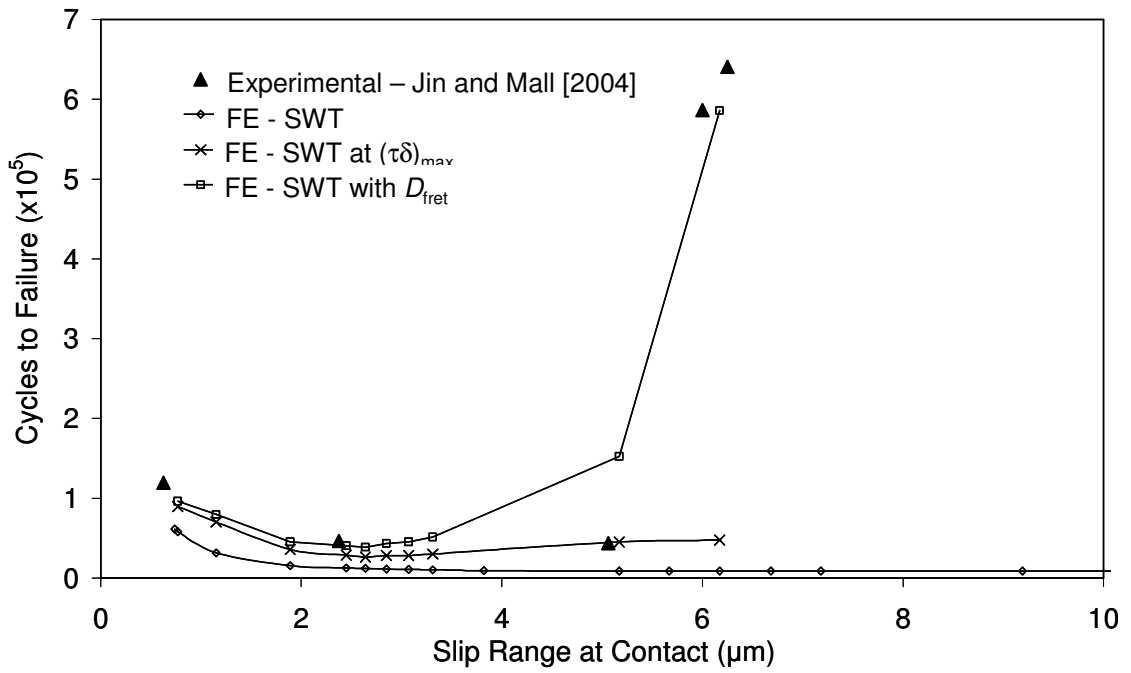


Figure 7.6. Comparison of the predicted effect of slip amplitude on fretting fatigue life from the different approaches with the experimental results [46].

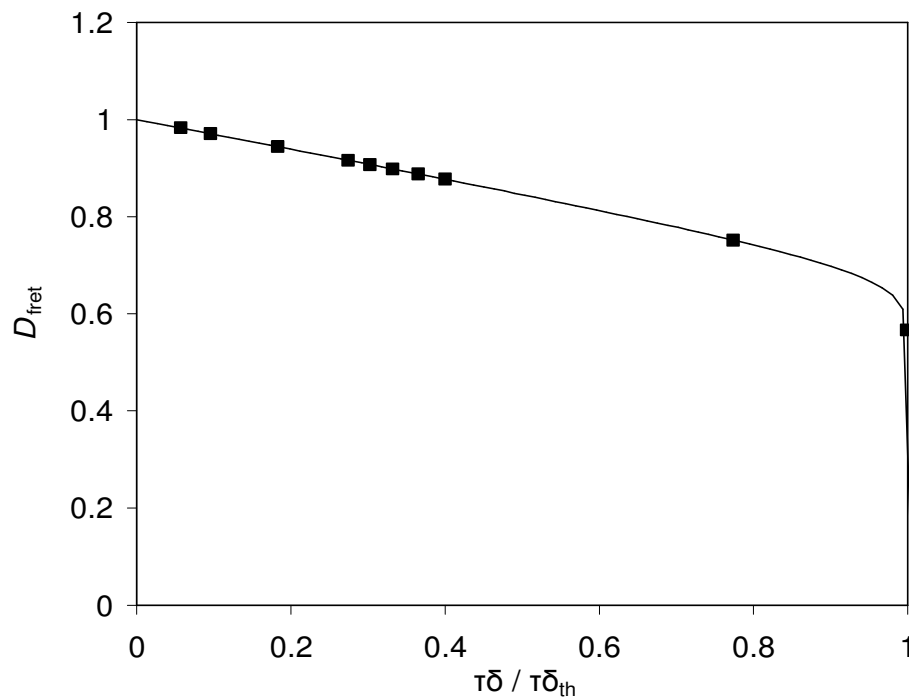


Figure 7.7. The predicted distribution of  $D_{fret}$  as a function of  $\tau\delta$ . The data points represent the values from the FE analyses.

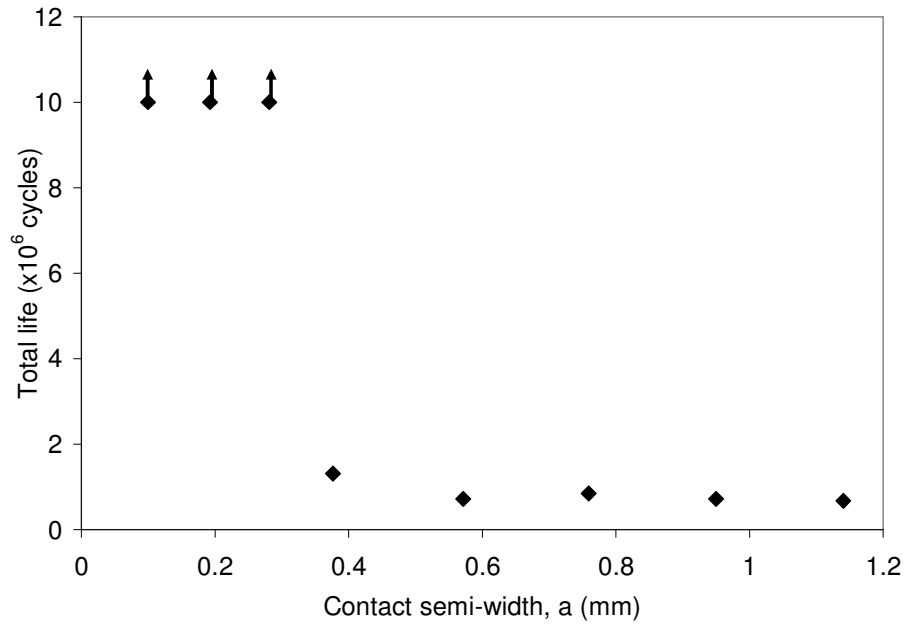


Figure 7.8. The experimental results for the contact size effect for a Hertzian contact for Al4%Cu [77].

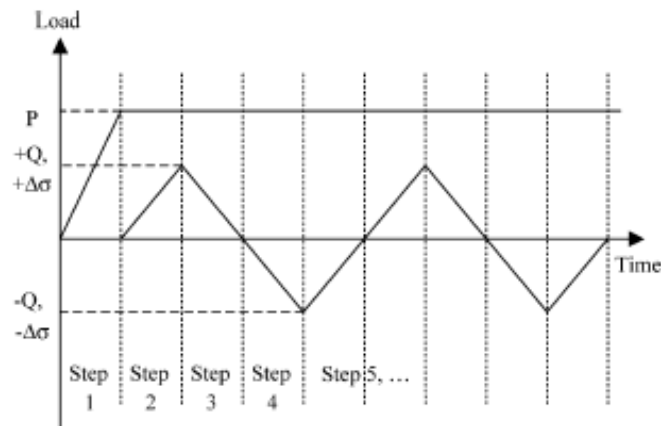


Figure 7.9. The steps simulated in the FE analysis for the cyclic loading.

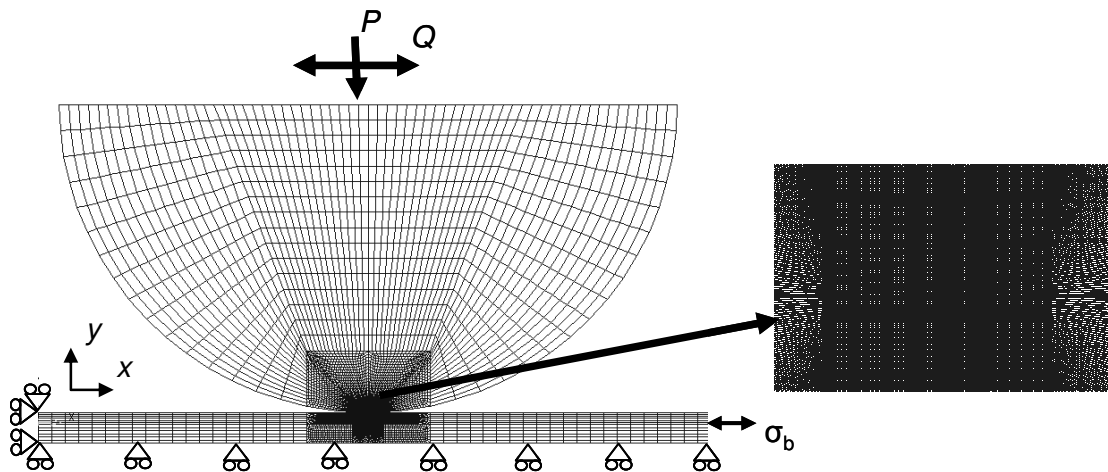


Figure 7.10. The  $R = 50$  mm mesh in the region of contact, showing the uniform element size.

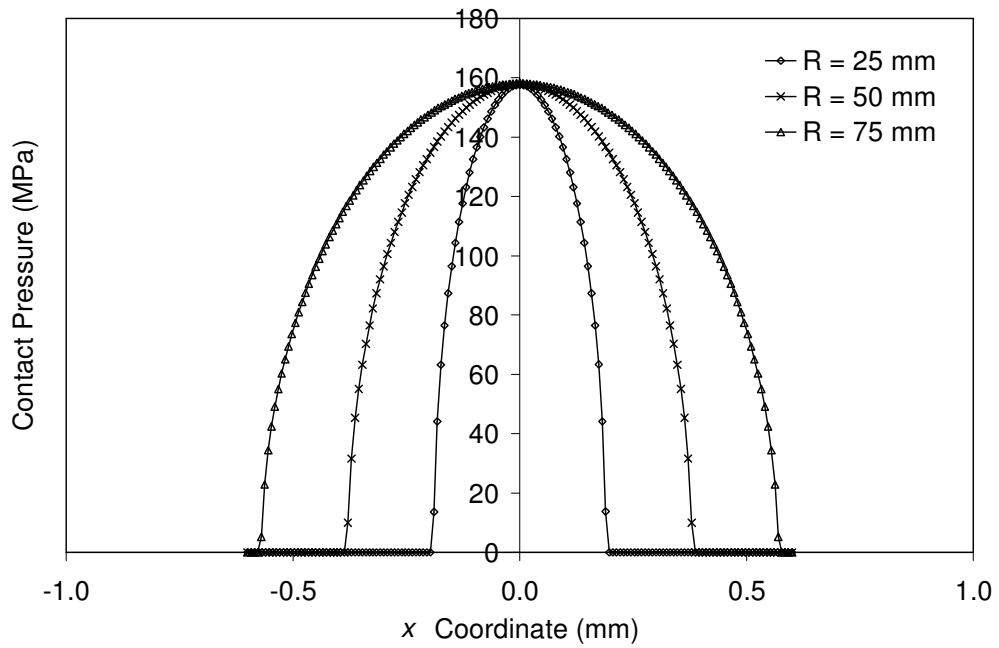


Figure 7.11. The contact pressure distributions for the three radii.

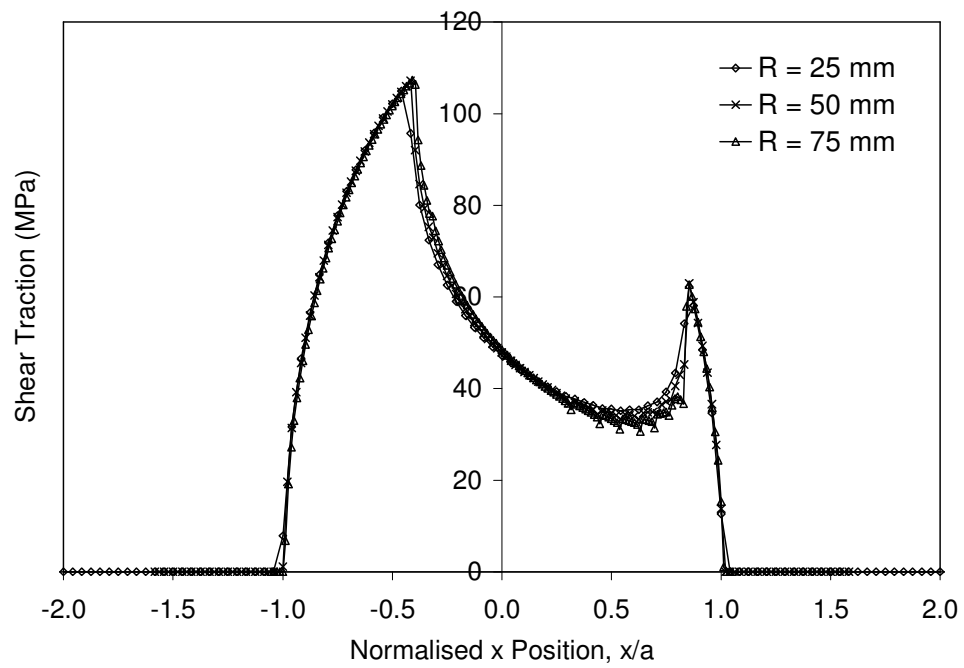


Figure 7.12. The normalised shear traction distributions for the three radii.

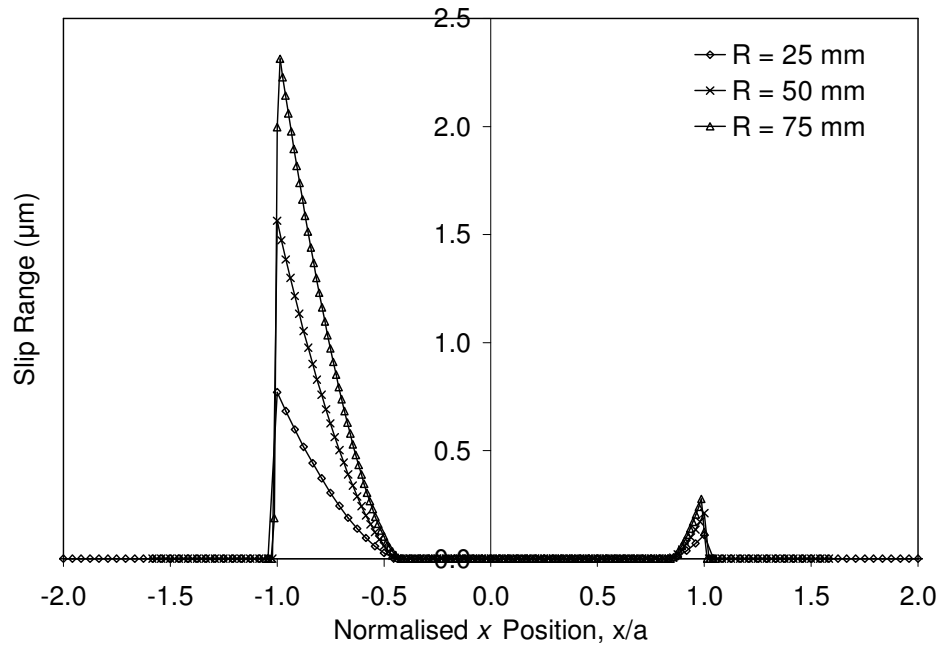


Figure 7.13. The contact slip distributions for the three radii.

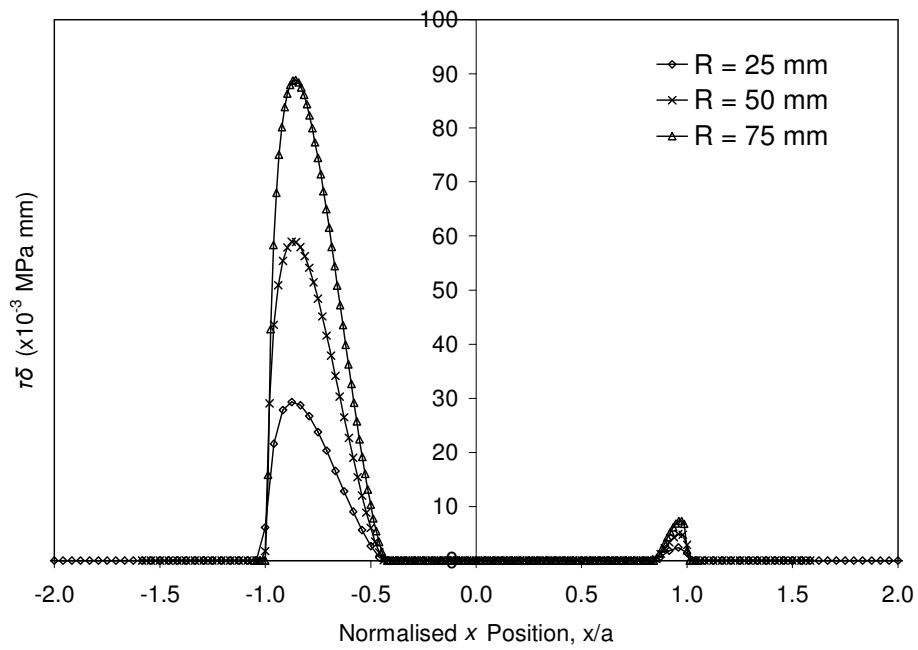


Figure 7.14. The  $\tau\delta$  distributions for the three radii.

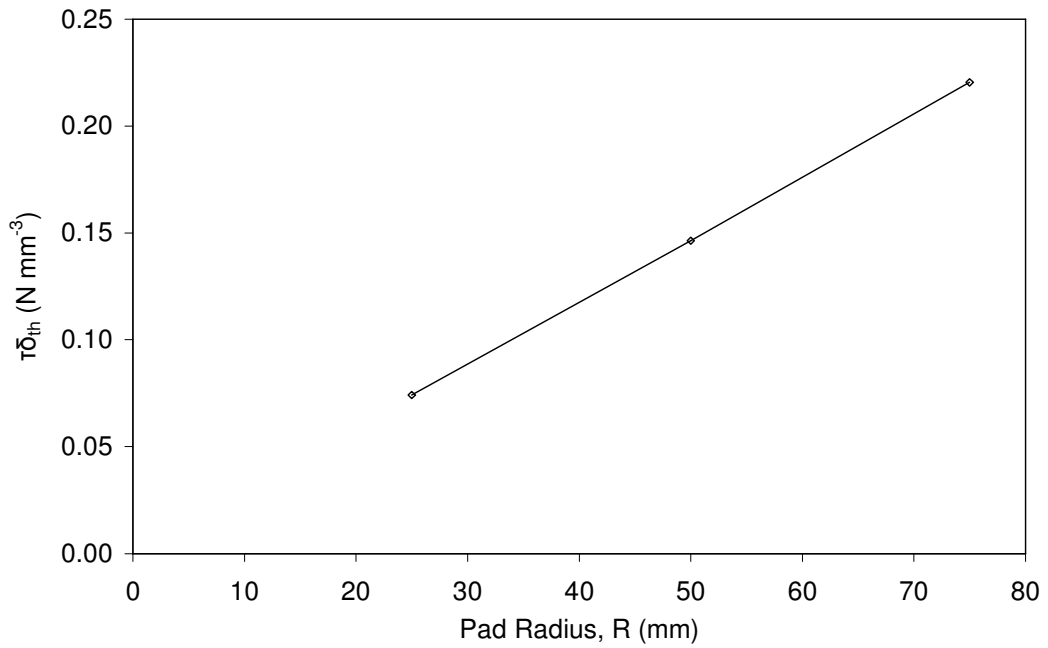


Figure 7.15. The FE-predicted variation of  $(\tau\delta)_{th}$  with pad radius for the experimental arrangement of Ref. [77].

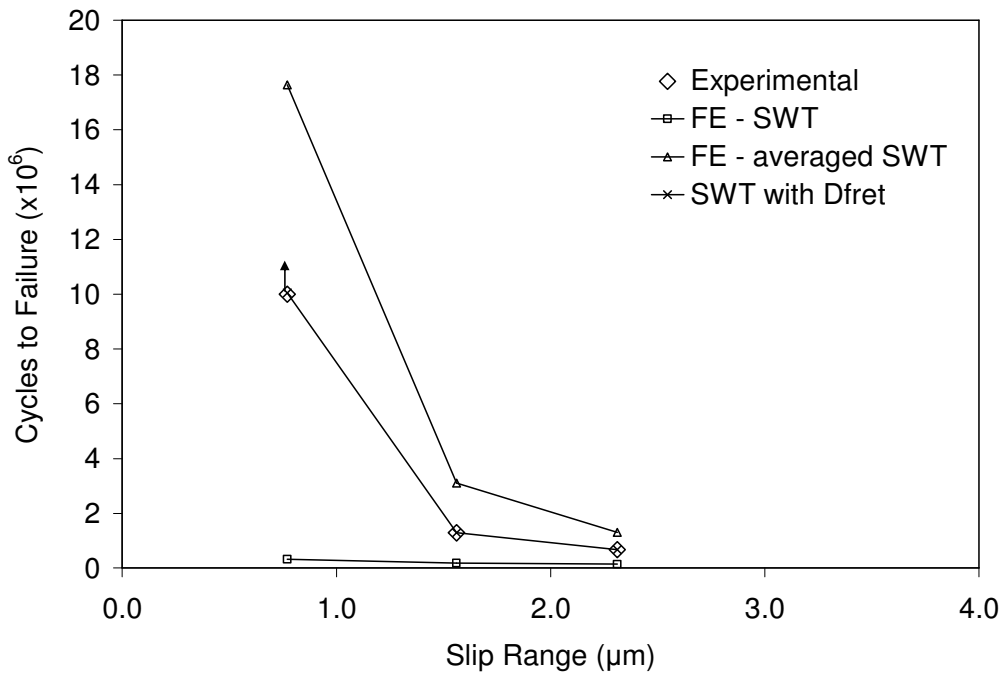


Figure 7.16. The experimental and computational predictions of the size effect on fretting fatigue life, using the combined SWT and  $D_{fret}$  approach.

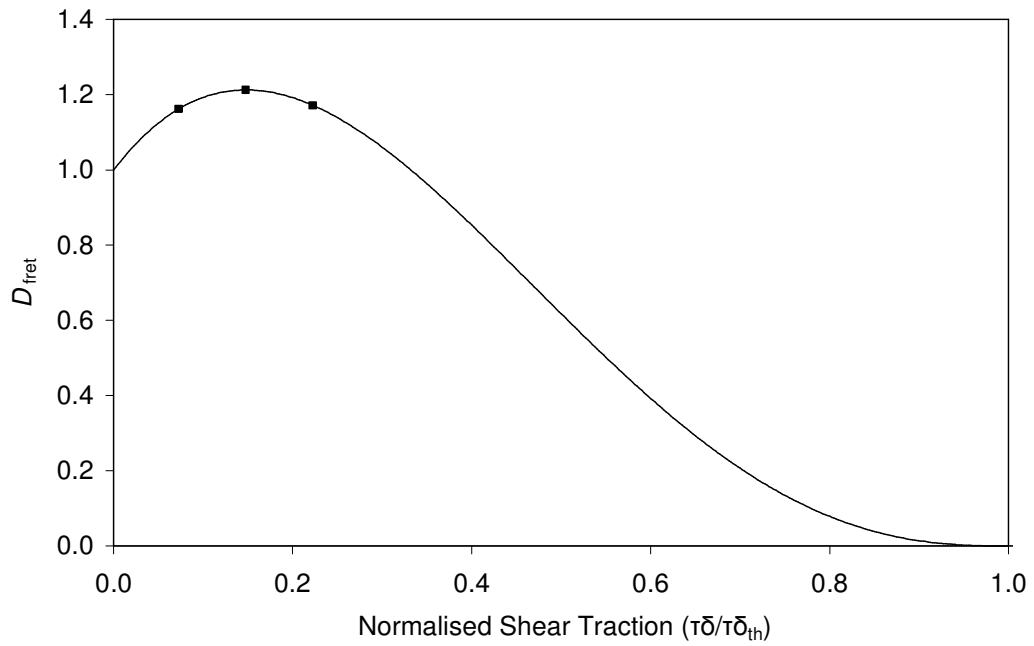


Figure 7.17.  $D_{fret}$  as a function of  $\tau\delta / (\tau\delta)_{th}$  for the contact configuration in Ref. [77]. The data points represent the values from the FE analyses.

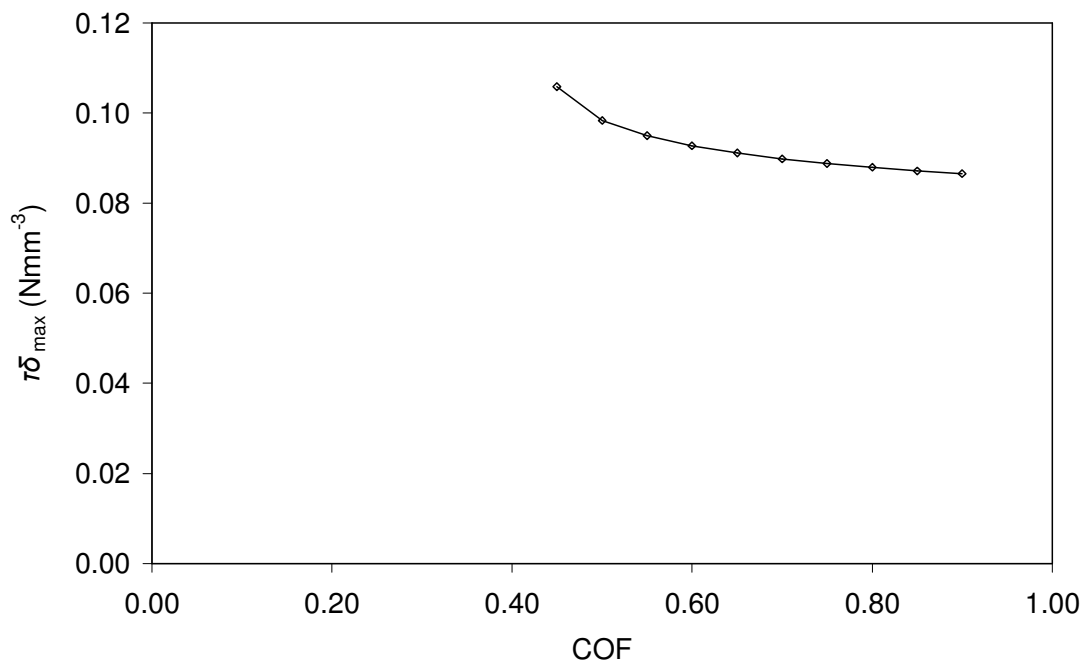


Figure 7.18. The variation of  $(\tau\delta_{max})$  with COF for  $a = 0.57$  mm ( $Q/P$  maintained at 0.45).

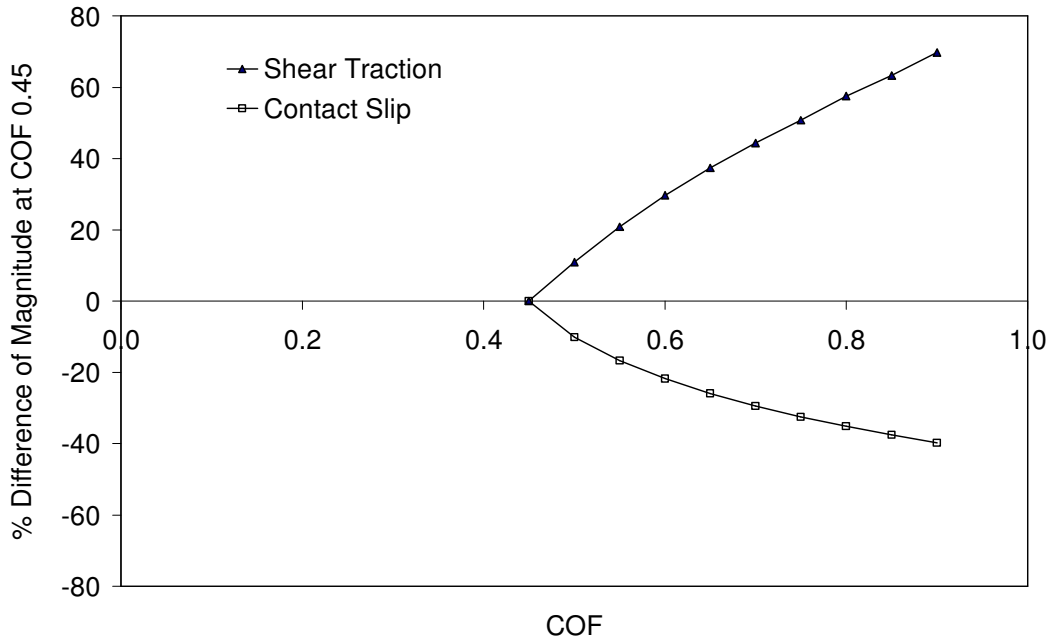


Figure 7.19. The percentage variation of shear traction ( $\tau$ ) and contact slip ( $\delta$ ) with COF as compared with the values at a COF of 0.45 (for  $Q/P = 0.45$ ).

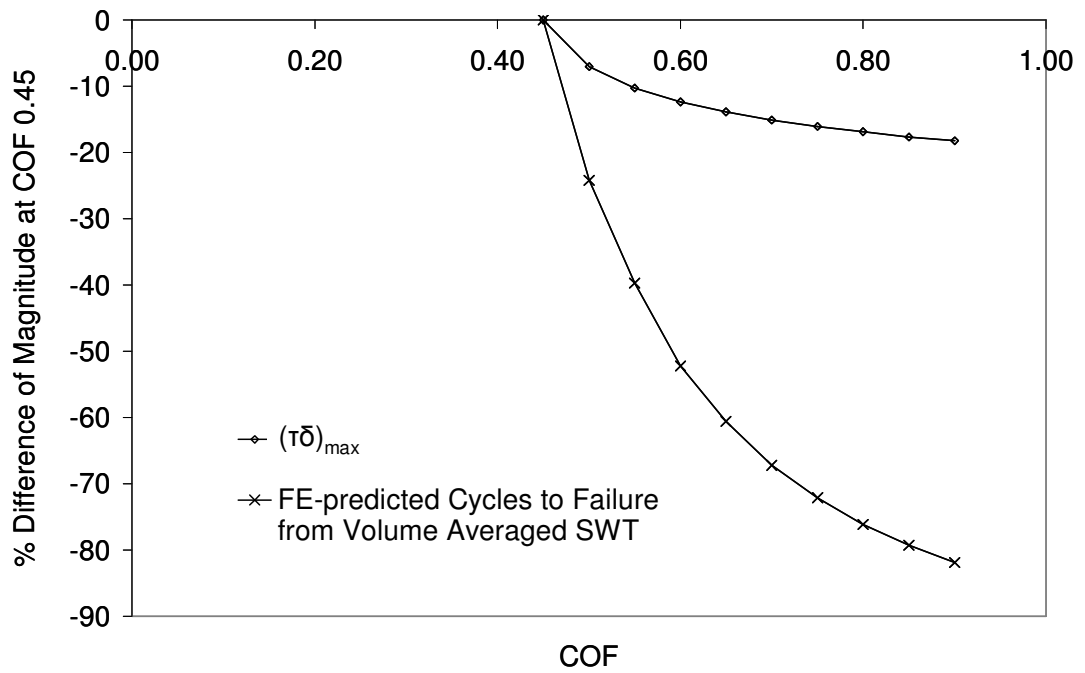


Figure 7.20. The percentage variation of  $(\tau\delta)_{\max}$  and SWT parameter with the COF, as compared with the respective values at a COF of 0.45 (for  $Q/P = 0.45$ ).

### Conclusions and Recommendations

#### 8.1 Conclusions

This thesis has advanced the understanding of fretting fatigue in complex spline couplings with the use of representative specimens. The specimens mimic the behaviour of a scaled spline coupling, which itself reproduces the key phenomena associated with fretting fatigue in aeroengine spline couplings. With the fretting fatigue failure behaviour of such couplings not fully understood, the representative specimen (RS) methodology pursued provided a cost-effective approach to further spline development. This combined experimental and computational approach utilised a uniaxial representative specimen (URS) and a multiaxial representative specimen (MRS). The URS was designed to replicate spline major cycle loading, whilst the MRS replicates combined major and minor cycle loading. The representative nature of the specimens with respect to the scaled spline coupling was demonstrated by using the finite element (FE) method.

The URS of Ref. [9] was redeveloped and enhanced in the present work. Subsequently, a number of fretting tests were conducted with the new URS on each of the different material combinations from the following:

- High strength CMV steel,
- Ti-6Al-4V (Ti-6/4),
- Ti-6Al-4V with a surface coating of Balinit C Star (Ti-6/4c),
- AerMet 100,
- Inconel 718 (Inco).

This provided an effective tool to evaluate the fretting performance of the material combinations, which was not conducted in the original study. No complete fretting fatigue failures occurred, but differing levels of fretting wear between the material combinations was measured. Following from this, a ranking of the wear performance was made, aiding the choice of future spline materials. For example, it was found that the combinations with Inco experienced the least wear and titanium the most wear. It was also generally observed that dissimilar material combinations experienced more wear than the similar material combination tests. In conjunction with the experimental tests, FE analyses were used to simulate the mechanical response. Significantly, an inverse technique enabled the coefficient of friction (COF) of the combinations to be inferred. This was realised via comparison of the predicted relative displacements from the FE model with the respective experimental measurements. The global FE model featured the position of the experimental measurements, thus enabling a direct comparison. The COF was then deduced according to the input value that gave the same displacements as the experiments. It was found that the inferred COF for S/CMV against S/CMV was 0.85. Knowledge of this COF is critical for the prediction of the fretting fatigue life of spline couplings. The AerMet against AerMet combination gave the lowest COF of 0.50. Additionally, full sliding conditions were predicted for a COF below 0.70, and partial slip for a COF greater than 0.70.

The MRS approach of Ref. [10] was pursued to study the fretting fatigue behaviour of S/CMV under representative spline conditions. An extensive multiaxial fretting fatigue test programme was conducted using the MRS. This helped to quantify the scatter and investigated the influence of the in-plane (major cycle) load and the bridge gap on total fretting fatigue life. It was found that a reduction in both of these parameters increased the total life to

failure. The MRS tests that represent the tests of the scaled spline were identified and plotted in the form of a stress-life curve, highlighting the detrimental effect of fretting on total life. In addition to the experimental tests, detailed FE modelling was conducted in order to simulate the MRS tests. This involved the creation of a global model, followed by a local sub-model. The global model included more of the rig components than previous studies and was shown to be able to capture the range of the experimental force-displacement loop, providing validation. The sub-model was used to accurately predict the key fretting fatigue stress components, indicating the location of likely fretting fatigue failure at  $z/b_1 = 1$ . The model was also used to show the important influence of the COF on the predicted stress state.

A fretting fatigue lifing methodology was developed in order to obtain computational life predictions for the experimental load cases of the URS and MRS. The crack initiation phase was quantified using the critical-plane (multi-axial) SWT parameter. The  $S/CMV$  fatigue constants were modified in order to be consistent with the crack initiation at the scale of the grain size (10  $\mu\text{m}$ ). It was found that no fretting fatigue cracks were predicted to initiate for the URS tests, in agreement with the experimental findings. When the methodology was applied to the MRS, cracks were predicted at  $z/b_1 = 1.0$  and  $x/a_2 \approx 0.0$ , in excellent agreement with the experimental observations. It was also found that crack initiation was predicted to occur relatively early in the total life for the load cases with a high bulk stress (OP or minor cycle load). On the other hand, for lower OP loads, crack initiation was predicted to occupy the majority of the total fretting fatigue life. Therefore, a total life approach was adopted, where the initiation and propagation regimes were accounted for. Short crack propagation behaviour was included using the El Haddad formulation of the stress intensity factors (SIFs), along with the propagation in the Paris Law regime quantified using a linear elastic fracture

mechanics mixed mode formulation. A numerical weighted function approach was used to determine the crack tip SIFs. The crack propagation results from the mixed mode formulation (mode I and II) were not significantly different from the mode I results, suggesting that the simpler mode I formulation can be adequate in the analysis of fretting fatigue. The computational methodology was shown to successfully capture the experimentally observed effect of the key fretting fatigue stress, which mimics the spline rotating bending moment, on the total fretting fatigue life. Good total life predictions were also found for the MRS results, with conservative predictions for higher applied bulk fatigue stresses. The conservative predictions may be regarded as advantageous in the practical application of the methodology.

In summary, the methodology was shown to successfully:

- Predict no fretting fatigue cracking for the URS tests,
- Predict the location of cracking of the fatigue specimen of the MRS,
- Predict the effect of the key fretting fatigue stress, which mimics the spline rotating bending moment, on the total fatigue life of the MRS,
- Predict the effect of the major cycle load and bridge gap on total fretting fatigue life of the MRS,
- Determine the relative contributions of the crack initiation and crack propagation phases of the MRS.

In addition to the state of stress and strain, other effects can influence the fretting fatigue life of a component. With this in mind, a recently suggested fretting fatigue lifing parameter was implemented. The approach combined

multiaxial fatigue-cracking phenomena as quantified by the SWT parameter, with a fretting fatigue damage parameter,  $D_{fret}$ , with the formulation given as:

$$D_{fret} = (1 + C\tau\delta) \left\langle 1 - \frac{\tau\delta}{(\tau\delta)_{th}} \right\rangle^n \quad (8.1)$$

where  $C$ ,  $n$  and  $(\tau\delta)_{th}$  are empirical constants and the symbol  $\langle \rangle$  is defined by  $\langle u \rangle = u$  if  $u > 0$  and  $\langle u \rangle = 0$  if  $u \leq 0$ . The formulation of the  $D_{fret}$  parameter was used to include surface damage effects (such as wear, oxidation, heating etc.) caused by the frictional work  $\tau\delta$ . It was shown that the  $D_{fret}$  approach captured an experimentally observed variation in fretting fatigue life with contact slip, providing more accurate life predictions. The methodology was also used to provide an explanation of the contact size effect in fretting fatigue. The approach advances fretting fatigue lifing of components with the inclusion of surface damage effects via parameters determined from simple experimental tests. This potentially circumvents the need for computationally intensive wear simulations.

The URS and MRS have been shown to be effective tools for experimentally simulating fretting fatigue in aeroengine spline couplings, generating invaluable data. With reference to the RS concept in Figure 3.1 in Chapter 3, significantly this thesis has shown that the lifing methodology is successfully capable of predicting the fretting fatigue life of the MRS, and therefore of the scaled spline. The representative specimens and life prediction methodology may also be applied more generally to other complex geometries in contact. The RS approach can also be used to provide further development and validation of the computational life prediction methodology.

## 8.2 Recommendations for future research

This thesis has shed further light on the fretting fatigue behaviour of splined couplings, but it has also raised areas that merit additional research. With the URS and MRS shown to be cost-effective tools, more experimental testing could be undertaken. This could be focused on:

- Determination of the  $D_{\text{fret}}$  constants for various materials and conditions,
- The influence of nitriding,
- Investigation of different surface coatings,
- The effect of surface lubrication.

A key area of future work concerns the separation of surface damage effects and stress gradient effects in fretting fatigue. The representative specimens can contribute to this fundamental problem in the understanding of fretting, by serving to generate the empirical constants for use in the  $D_{\text{fret}}$  with SWT approach. This could also yield insights into the competition between fretting fatigue and fretting wear processes.

The use of fracture mechanics techniques were important in understanding the behaviour of the MRS. More advanced approaches could be investigated, such as the use of weighted functions for cracks inclined at an angle.

Further advances in knowledge could be obtained by the application of additional computational simulation techniques to compare with the results of this thesis. For example, FE crack growth modelling, FE-based wear simulations and FE analysis of coatings are all techniques currently in development.

## REFERENCES

---

- [1] Rolls-Royce. The jet engine. Rolls-Royce Technical Publications; 5th edition, 2005.
- [2] Ford T. Mainshafts for the Trent. *Aircraft Engineering and Aerospace Technology* 1997;69:555-560.
- [3] Leen SB, McColl IR, Ratsimba CHH, Williams EJ. Fatigue life prediction for a barrelled spline coupling under torque overload. *Proceedings of the Institution of Mechanical Engineers, Part G: Journal of Aerospace Engineering* 2003;217(3):123-142.
- [4] Volfson BP. Stress Sources and Critical Stress Combinations for Splined Shaft. *Journal of Mechanical Design, Transactions of the ASME* 1982;104(3):551-556.
- [5] Tjernberg A. Load distribution in the axial direction in a spline coupling. *Engineering Failure Analysis* 2001;8(6):557-570.
- [6] Tjernberg A. Load distribution and pitch errors in a spline coupling. *Materials and Design* 2001;22(4):259-266.
- [7] Leen SB, Hyde TH, Ratsimba CHH, Williams EJ, McColl IR. An investigation of the fatigue and fretting performance of a representative aero-engine spline coupling. *Journal of Strain Analysis for Engineering Design* 2002;37(6):565-583.
- [8] Leen SB, Hyde TR, Williams EJ, Becker AA, McColl IR, Hyde TH, Taylor JW. Development of a representative test specimen for frictional contact in spline joint couplings. *Journal of Strain Analysis for Engineering Design* 2000;35(6):521-544.
- [9] Hyde TR. Development of a Representative Specimen for Fretting Fatigue of Spline Joint Couplings. PhD thesis, University of Nottingham, UK, 2002.
- [10] Wavish PM. Representative Specimen for Multiaxial Fretting Fatigue in a Splined Coupling. Vol. PhD thesis: University of Nottingham, UK., 2006.
- [11] Ding J, Sum WS, Sabesan R, Leen SB, McColl IR, Williams EJ. Fretting fatigue predictions in a complex coupling. *International Journal of Fatigue* 2007;29(7):1229-1244.

- [12] Suresh S. *Fatigue of Materials*. Cambridge, UK: Cambridge University Press, 1998.
- [13] Albert WAJ. Über treibseile am Harz. *Archive für Mineralogie Geognosie Bergbau und Hüttenkunde* 1838;10:215-234.
- [14] Fairbairn W. Experiments to determine the effect of impact, vibratory action, and long continued changes of load on wrought iron girder. *Philosophical Transactions of the Royal Society, London* 1864;154:311.
- [15] Wöhler. Experiments on the Strength of Metals - English summary. *Engineering* 1967;4:160-161.
- [16] Gerber H. Bestimmung der zulässigen spannungen in Eisenkonstruktion. *Zeitschrift des Bayerischen Architekten und Ingenieur-Veriens* 1984;6:101-110.
- [17] Goodman J. *Applied to Engineering*, Longmans Green, London 1899.
- [18] Basquin OH. The exponential law of endurance tests. *Proc ASTM* 1910;ASTEA 10:625-630.
- [19] Brown MW, Miller, K.J. A theory for fatigue failure under multiaxial stress-strain conditions. *Proc Instn Mech Engrs* 1973;187:65-73.
- [20] Coffin CF. A study of the effects of cyclic thermal stresses on a ductile metal. *Trans ASME* 1954;76:931-950.
- [21] Manson SS. Behaviour of materials under conditions of thermal stress. In: TN 2933, NACA, 1954.
- [22] Palmgren A. Lebensdauer von Kugellagern. *ZDVDI* 1924;68(14):339.
- [23] Miner MA. Cumulative Damage in Fatigue. *Trans ASME, J Appl Mech* 1945;67:A159.
- [24] Jin O, Lee H, Mall S. Investigation into cumulative damage rules to predict fretting fatigue life of Ti-6Al-4V under two-level block loading condition. *Journal of Engineering Materials and Technology, Transactions of the ASME* 2003;125(3):315-323.
- [25] Matsuiski M, Endo T. Fatigue of metals subjected to varying stress. In: Kyushu District meeting of the Japan Soc Mech Engrg Fukuoka, 1968, pp. 37-40.

- [26] Stephens RI, Farnetti A, Stephens RR, Fuchs HO. Metal fatigue in engineering. Wiley-IEEE, 2001.
- [27] Newman Jr JC. The merging of fatigue and fracture mechanics concepts: A historical perspective. *Progress in Aerospace Sciences* 1998;34(5-6):347-390.
- [28] Paris PC, Erdogan, F. A Critical Analysis of Crack Propagation Law. *Trans ASME, J Basic Eng* 1963;85(4):528.
- [29] Walker K. The effect of stress ratio during crack propagation and fatigue for 2024-T3 and 7075-T6 aluminium. *Effects of Environment and Complex Load History on Fatigue Life* 1970;ASTM STP 462:1-14.
- [30] Eden EM, Rose, W.N., Cunningham FL. The endurance of metals. *Proc IMechE* 1911;4:139.
- [31] Hutchings IM. *Tribology: Friction and Wear of Engineering Materials*. Sevenoaks: Edward Arnold, 1992.
- [32] Olsson H, Astrom KJ, De Wit CC, Gafvert M, Lischinsky P. Friction models and friction compensation. *European Journal of Control* 1998;4(3):176-195.
- [33] Bowden FP, Tabor D. *The friction and lubrication of solids*. Parts 1 and 2. Oxford: Clarendon Press, 1954.
- [34] Dini D, Nowell D. Prediction of the slip zone friction coefficient in flat and rounded contact. *Wear* 2003;254(3-4):364-369.
- [35] Wang RH, Jain VK, Mall S. A non-uniform friction distribution model for partial slip fretting contact. *Wear* 2007;262(5-6):607-616.
- [36] Dobromirski JM. Variables of Fretting Process: Are There 50 of Them? In *Standardization of Fretting Fatigue Test Methods and Equipment - ASTM STP 1159*. Attia MH, Waterhouse RB, editors.: American Society for Testing and Materials, Philadelphia, 1992, pp. 60-66.
- [37] Vingsbo O, and Soderberg, D. On Fretting Maps. *Wear* 1988;126:131-147.
- [38] Zhou ZR, Nakazawa K, Zhu MH, Maruyama N, Kapsa P, Vincent L. Progress in fretting maps. *Tribology International* 2006;39(10):1068-1073.

- [39] Shinde S, Hoepfner DW. Quantitative analysis of fretting wear crack nucleation in 7075-T6 aluminum alloy using fretting maps. *Wear* 2005;259(1-6):271-276.
- [40] Sato K. Determination and control of contact pressure distribution in fretting fatigue. Attia M, Waterhouse R, editors.: American Society for Testing and Materials, Philadelphia, 1992, pp. 85-100.
- [41] Iyer K, Mall S. Analyses of contact pressure and stress amplitude effects on fretting fatigue life. *Journal of Engineering Materials and Technology, Transactions of the ASME* 2001;123(1):85-93.
- [42] Waterhouse RB. *Fretting Corrosion*. Oxford: Pergamon, 1972.
- [43] Hyde TR, Leen SB, McColl IR. A simplified fretting test methodology for complex shaft couplings. *Fatigue and Fracture of Engineering Materials and Structures* 2005;28(11):1047-1067.
- [44] Wittkowsky BU, Birch PR, Dominguez J, Suresh S. Apparatus for quantitative fretting fatigue testing. *Fatigue and Fracture of Engineering Materials and Structures* 1999;22(4):307-320.
- [45] Jin O, Mall S. Effects of independent pad displacement on fretting fatigue behavior of Ti-6Al-4V. *Wear* 2002;253(5-6):585-596.
- [46] Jin O, Mall S. Effects of slip on fretting behavior: Experiments and analyses. *Wear* 2004;256(7-8):671-684.
- [47] Nishida T, Kondoh K, Xu JQ, Mutoh Y. Observations and Analysis of Relative Slip in Fretting Fatigue. Y. Mutoh SEKaDWH, editor.: American Society for Testing and Materials International, West Conshohocken, PA, 2003.
- [48] Sabelkin V, Mall S. Investigation into relative slip during fretting fatigue under partial slip contact condition. *Fatigue and Fracture of Engineering Materials and Structures* 2005;28(9):809-824.
- [49] M. Varenberg IEaGH. Slip Index: A New Unified Approach to Fretting. *Tribology Letters* 2004;17(3):569-573.
- [50] Ding J, Leen SB, McColl IR. The effect of slip regime on fretting wear-induced stress evolution. *International Journal of Fatigue* 2004;26(5):521-531.

- [51] Madge JJ, Leen SB, McColl IR, Shipway PH. Contact-evolution based prediction of fretting fatigue life: Effect of slip amplitude. *Wear* 2007;262(9-10):1159-1170.
- [52] Nowell D. *An Analysis of Fretting Fatigue*. Vol. D.Phil: University of Oxford, UK, 1988.
- [53] Nowell D, Dini D. Stress gradient effects in fretting fatigue. *Tribology International* 2003;36(2):71-78.
- [54] Waterhouse RB. *The problems of Fretting Fatigue Testing*. Waterhouse MHAaRB, editor.: American Society for Testing and Materials, Philadelphia, 1992, pp. 13-19.
- [55] Hills D, Mugadu A. An overview of progress in the study of fretting fatigue. *The Journal of Strain Analysis for Engineering Design* 2002;37(6):591-601.
- [56] Switek W. Early stage crack propagation in fretting fatigue. *Mechanics of Materials* 1984;3(3):257-267.
- [57] Lindley TC. Fretting fatigue in engineering alloys. *International Journal of Fatigue* 1997;19(Suppl 1):39-49.
- [58] Hills DA, Nowell D. *Mechanics of Fretting Fatigue*. Kulwer Academic Publishers, 1994.
- [59] Nishioka K, Hirakawa, K. *Bull JSME* 1972;15:135-144.
- [60] Fouvry S, Elleuch K, Simeon G. Prediction of crack nucleation under partial slip fretting conditions. *Journal of Strain Analysis for Engineering Design* 2002;37(6):549-564.
- [61] Faanes S. Inclined cracks in fretting fatigue. *Engineering Fracture Mechanics* 1995;52(1):71-82.
- [62] Ruiz C, Boddington, P.H.B., Chen, K.C. An investigation of fatigue and fretting in a dovetail joint. *Exp Mech* 1984;24:208-217.
- [63] Mugadu A, Hills DA, Nowell D. Modifications to a fretting-fatigue testing apparatus based upon an analysis of contact stresses at complete and nearly complete contacts. *Wear* 2002;252(5-6):475-483.
- [64] Golden PJ. Development of a dovetail fretting fatigue fixture for turbine engine materials. *International Journal of Fatigue* 2009;31(4):620-628.

- [65] Nowell D., Hills D.A., R. M, editors. Length Scale Considerations in Fretting Fatigue. West Conshohocken, PA: American Society for Testing and Materials, 2000.
- [66] Mutoh Y, Xu J-Q. Fracture mechanics approach to fretting fatigue and problems to be solved. *Tribology International* 2003;36(2):99-107.
- [67] Lykins CD, Mall S, Jain V. Evaluation of parameters for predicting fretting fatigue crack initiation. *International Journal of Fatigue* 2000;22(8):703-716.
- [68] Miller KJ. Materials science perspective of metal fatigue resistance. *Materials Science and Technology* 1993;9:453-462.
- [69] Goh CH, Wallace JM, Neu RW, McDowell DL. Polycrystal plasticity simulations of fretting fatigue. *International Journal of Fatigue* 2001;23(SUPPL 1):423-435.
- [70] Johnson KL. *Contact Mechanics*. Cambridge University Press, 1984.
- [71] Hertz H. *J reine und angewandte Mathematik* 1882;92:156-171.
- [72] Fellows LJ, Nowell D, Hills DA. Contact stresses in a moderately thin strip (with particular reference to fretting experiments). *Wear* 1995;185(1-2):235-238.
- [73] Mindlin RD. *J App Mech* 1949;16:259-268.
- [74] Cattaneo C. Sul Contatto di due corpi elastici: distribuzione locale degli sforzi. *Rend Accad Naz Lincei* 1938;27(6):342,434,474.
- [75] Muskhelishvili NI. *Some Basic Problems of the Mathematical Theory of Elasticity*. 1953.
- [76] Bramhall R. *Studies in fretting fatigue*. Vol. D.Phil.: University of Oxford. UK, 1973.
- [77] Nowell D, Araujo JA. The effect of rapidly varying contact stress fields on fretting fatigue. *International Journal of Fatigue* 2002;24(7):763-775.
- [78] Sackfield A, Truman CE, Hills DA. The tilted punch under normal and shear load (with application to fretting tests). *International Journal of Mechanical Sciences* 2001;43(8):1881-1892.
- [79] Smith KN, Watson, P., Topper, T.H. A stress strain function for the fatigue of metals. *J Mat, JMLSA* 1970;5:767-778.

- [80] Fatemi A, Socie D. A critical plane approach to multiaxial fatigue damage including out of phase loading. *Fatigue Fract Eng Mater Struct* 1988;11(3):149–165.
- [81] Lykins CD, Mall S, Jain VK. Combined experimental-numerical investigation of fretting fatigue crack initiation. *International Journal of Fatigue* 2001;23(8):703-711.
- [82] Navarro C, Munoz S, Dominguez J. On the use of multiaxial fatigue criteria for fretting fatigue life assessment. *International Journal of Fatigue* 2008;30(1):32-44.
- [83] Dang Van K, Griveau, B., Message, O. On a new multiaxial fatigue criterion limit criterion: theory and application, biaxial and multiaxial fatigue. *Mechanical Engineering Publications*, London, 1989.
- [84] Peridas G, Korsunsky AM, Hills DA. The relationship between the Dang Van criterion and the traditional bulk fatigue criteria. *Journal of Strain Analysis for Engineering Design* 2003;38(3):201-206.
- [85] Mall S, Naboulsi S. Fretting fatigue crack initiation behavior using process volume approach and finite element analysis. *Tribology International* 2003;36(2):121-131.
- [86] Bernardo AT, Araujo JA, Mamiya EN. Proposition of a finite element-based approach to compute the size effect in fretting fatigue. *Tribology International* 2006;39(10):1123-1130.
- [87] Sum WS, Williams EJ, Leen SB. Finite element, critical-plane, fatigue life prediction of simple and complex contact configurations. *International Journal of Fatigue* 2005;27(4):403-416.
- [88] Hills DA, Dini D. A new method for the quantification of nucleation of fretting fatigue cracks using asymptotic contact solutions. *Tribology International* 2006;39(10):1114-1122.
- [89] Dini D, Hills DA. Bounded asymptotic solutions for incomplete contacts in partial slip. *International Journal of Solids and Structures* 2004;41(24-25):7049-7062.
- [90] Cotterell B, Rice JR. Slightly curved or kinked cracks. *International Journal of Fracture* 1980;16(2):155-169.

- [91] Kondo Y, Sakae C, Kubota M, Yanagihara K. Non-propagating crack at giga-cycle fretting fatigue limit. *Nippon Kikai Gakkai Ronbunshu, A Hen/Transactions of the Japan Society of Mechanical Engineers, Part A* 2004;70(8):1066-1071.
- [92] Giannakopoulos AE, Lindley TC, Suresh S. Aspects of equivalence between contact mechanics and fracture mechanics: Theoretical connections and a life-prediction methodology for fretting-fatigue. *Acta Materialia* 1998;46(9):2955-2968.
- [93] Conner BP, Lindley TC, Nicholas T, Suresh S. Application of a fracture mechanics based life prediction method for contact fatigue. *International Journal of Fatigue* 2004;26(5):511-520.
- [94] Ciavarella M. A 'crack-like' notch analogue for a safe-life fretting fatigue design methodology. *Fatigue and Fracture of Engineering Materials and Structures* 2003;26(12):1159-1170.
- [95] Atzori B, Lazzarin P, Meneghetti G. Fracture mechanics and notch sensitivity. *Fatigue and Fracture of Engineering Materials and Structures* 2003;26(3):257-267.
- [96] Kitagawa H, Takahashi, S Applicability of Fracture Mechanics to Very Small Cracks or the Cracks in the Early Stage. *Second International Conference on Mechanical Behavior of Materials American Society for Materials, Metals Park, Ohio, 1976, pp. 627-631.*
- [97] El Haddad MH, Topper, T.H., Smith, K.N. Prediction of nonpropagating cracks. *Engineering Fracture Mechanics* 1979;11:573-584.
- [98] Kauzlarich JJ, Williams JA. Archard wear and component geometry. *Proceedings of the Institution of Mechanical Engineers, Part J: Journal of Engineering Tribology* 2001;215(4):387-398.
- [99] Archard JF. Contact and rubbing of flat surfaces. *J Appl Phys* 1953;24:981-988.
- [100] Vidner J, Leidich E. Enhanced Ruiz criterion for the evaluation of crack initiation in contact subjected to fretting fatigue. *International Journal of Fatigue* 2007;29(9-11):2040-2049.
- [101] McColl IR, Ding J, Leen SB. Finite element simulation and experimental validation of fretting wear. *Wear* 2004;256(11-12):1114-1127.

- [102] Madge JJ, Leen SB, Shipway PH. A combined wear and crack nucleation-propagation methodology for fretting fatigue prediction. *International Journal of Fatigue*; In Press, Accepted Manuscript.
- [103] Ding J, McColl IR, Leen SB, Shipway PH. A finite element based approach to simulating the effects of debris on fretting wear. *Wear* 2007;263(1-6):481-491.
- [104] Adey RA, Baynham J, Taylor JW. Development of analysis tools for spline couplings. *Proceedings of the Institution of Mechanical Engineers, Part G: Journal of Aerospace Engineering* 2000;214(6):347-357.
- [105] Medina S, Olver AV. An analysis of misaligned spline couplings. *Proceedings of the Institution of Mechanical Engineers, Part J: Journal of Engineering Tribology* 2002;216(5):269-279.
- [106] Ding J, McColl IR, Leen SB. The application of fretting wear modelling to a spline coupling. *Wear* 2007;262(9-10):1205-1216.
- [107] Ratsimba CHH, McColl IR, Williams EJ, Leen SB, Soh HP. Measurement, analysis and prediction of fretting wear damage in a representative aeroengine spline coupling. *Wear* 2004;257(11):1193-1206.
- [108] Ding J, Leen SB, Williams EJ, Shipway PH. Finite element simulation of fretting wear-fatigue interaction in spline couplings. *Tribology - Materials, Surfaces and Interfaces* 2008;2(1):10-24.
- [109] Limmer L, Nowell D, Hills DA. A combined testing and modelling approach to the prediction of the fretting fatigue performance of splined shafts. *Proceedings of the Institution of Mechanical Engineers, Part G: Journal of Aerospace Engineering* 2001;215(2):105-112.
- [110] Nowell D, Dini D, Hills DA. Recent developments in the understanding of fretting fatigue. *Engineering Fracture Mechanics* 2006;73(2):207-222.
- [111] Leen SB, Richardson IJ, McColl IR, Williams EJ, Hyde TR. Macroscopic fretting variables in a splined coupling under combined torque and axial load. *Journal of Strain Analysis for Engineering Design* 2001;36(5):481-497.
- [112] <http://www.specialmetals.com>. Special Metals, 2008.

- [113] <http://www.matweb.com/>. Matweb material datasheet, 2009.
- [114] Karuppanan S, Hills DA. Frictional complete contacts between elastically similar bodies subject to normal and shear load. *International Journal of Solids and Structures* 2008;45(17):4662-4675.
- [115] ABAQUS. In: User's and Theory Manuals Providence, RI, USA: Simulia, 2007.
- [116] Wavish PM, Houghton D, Ding J, Leen SB, Williams EJ, McColl IR. A multiaxial fretting fatigue test for spline coupling contact. *Fatigue & Fracture of Engineering Materials & Structures* 2009;32(4):325-345.
- [117] Ding J. Modelling of fretting wear. University of Nottingham, UK, 2003.
- [118] Soh HP. Fretting wear studies of aeroengine materials. Vol. PhD: University of Nottingham, 2006.
- [119] Hyde TR, Leen SB, McColl IR. A methodology for modelling the effects of nitriding on fatigue life. *Proceedings of the I MECH E Part L Journal of Materials:Design and Applications* 2008;222(1):1-14(14).
- [120] Barber JR, Klarbring A, Ciavarella M. Shakedown in frictional contact problems for the continuum. *Comptes Rendus Mecanique* 2008;336(1-2):34-41.
- [121] Cormier NG, Smallwood BS, Sinclair GB, Meda G. Aggressive submodelling of stress concentrations. *International Journal for Numerical Methods in Engineering* 1999;46(6):889-909.
- [122] Rajasekaran R, Nowell D. On the finite element analysis of contacting bodies using submodelling. *Journal of Strain Analysis for Engineering Design* 2005;40(2):95-106.
- [123] Fellows LJ, Nowell, D. and Hills, D.A. Analysis of crack initiation and propagation in fretting fatigue: the effective initial flaw size methodology. *Fatigue and Fracture of Engineering Materials and Structures* 1997;20(1):61-70.
- [124] Salerno G, Magnabosco R, Moura Neto Cd. Mean strain influence in low cycle fatigue behavior of AA7175-T1 aluminum alloy. *International Journal of Fatigue* 2007;29(5):829-835.

- [125] Madge JJ, Leen SB, Shipway PH. A combined wear and crack nucleation-propagation methodology for fretting fatigue prediction. *International Journal of Fatigue* 2008;30(9):1509-1528.
- [126] Murakami Y. *Stress intensity factors handbook*. Pergamon Press, 1988.
- [127] Goldstein H, Poole C, Safko J. *Classical Mechanics*. Upper Saddle River, N.J.: Pearson Education International, 2002.
- [128] Boresi AP, Schmidt J. *Advanced mechanics of materials*. New York: John Wiley & Sons, 2003.
- [129] Qian J, Fatemi A. Mixed mode fatigue crack growth: A literature survey. *Engineering Fracture Mechanics* 1996;55(6):969-990.
- [130] Chen W-R, Keer LM. Fatigue crack growth in mixed mode loading. *Journal of Engineering Materials and Technology, Transactions of the ASME* 1991;113(2):222-227.
- [131] Navarro C, Muñoz S, Domínguez J. Propagation in fretting fatigue from a surface defect. *Tribology International* 2006;39(10):1149-1157.
- [132] Sabesan R, Leen SB, J. WE. *Fatigue crack growth in aeroengine shafts using the finite element method*. Fatigue 2007 Cambridge, UK, 2007.
- [133] Nicholas T, Hutson A, John R, Olson S. A fracture mechanics methodology assessment for fretting fatigue. *International Journal of Fatigue* 2003;25(9-11):1069-1077.
- [134] Beghini M, Bertini L, Fontanari V. Stress intensity factors for an inclined edge crack in a semiplane. *Engineering Fracture Mechanics* 1999;62(6):607-613.
- [135] Giner E, Sukumar N, Denia FD, Fuenmayor FJ. Extended finite element method for fretting fatigue crack propagation. *International Journal of Solids and Structures* 2008;45(22-23):5675-5687.
- [136] Bueckner HF. A Novel principle for the computation of stress intensity factors. *Z Angew Math Mech* 1970;50(9):529-546.
- [137] Fett T, Munz D. *Stress Intensity Factors and Weight Functions*. Southampton: Computational Mechanics Publications, 1997.
- [138] Dowling NE. *Mechanical Behaviour of Materials*. Upper Saddle River, NJ, USA: Prentice-Hall Inc, 1998.

- [139] Sutton MA, Deng X, Ma F, Newman Jr JC, James M. Development and application of a crack tip opening displacement-based mixed mode fracture criterion. *International Journal of Solids and Structures* 2000;37(26):3591-3618.
- [140] Elber W. The significance of fatigue crack closure. *American Society for Testing and Materials, Philadelphia, 1971, pp. 230-242.*
- [141] Noroozi AH, Glinka G, Lambert S. A two parameter driving force for fatigue crack growth analysis. *International Journal of Fatigue* 2005;27(10-12):1277-1296.
- [142] Zhang J, He XD, Du SY. Analysis of the effects of compressive stresses on fatigue crack propagation rate. *International Journal of Fatigue* 2007;29(9-11):1751-1756.
- [143] Kujawski D. A new  $(\Delta K + K_{\max})^{0.5}$  driving force parameter for crack growth in aluminum alloys. *International Journal of Fatigue* 2001;23(8):733-740.
- [144] Madge JJ, Leen SB, Shipway PH. The critical role of fretting wear in the analysis of fretting fatigue. *Wear* 2007;263(1-6):542-551.
- [145] Sabelkin V, Mall S. Relative slip on contact surface under partial slip fretting fatigue condition. *Strain* 2006;42(1):11-20.
- [146] Taylor D. *The theory of critical distances: A new perspective in fracture mechanics.* Oxford, UK: Elsevier Science Ltd., 2007.
- [147] Kim HS, Mall S. Investigation into three-dimensional effects of finite contact width on fretting fatigue. *Finite Elements in Analysis and Design* 2005;41(11-12):1140-1159.
- [148] Magaziner R, Jin O, Mall S. Slip regime explanation of observed size effects in fretting. *Wear* 2004;257(1-2):190-197.